TÉCNICO LISBOA

UNIVERSIDADE DE LISBOA

INSTITUTO SUPERIOR TÉCNICO

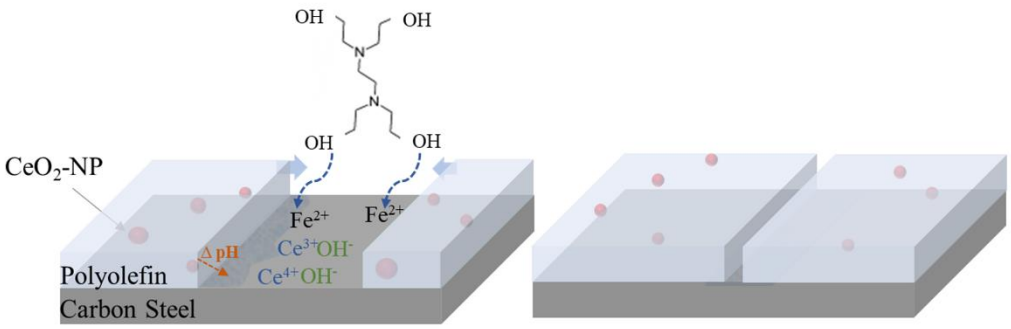

Development of Self-Healing Coatings for Corrosion Protection of Carbon Steel

Mahboobeh Attaei

Supervisor: Doctor Maria de Fátima Grilo da Costa Montemor
Co-Supervisor: Doctor Ana Clara Lopes Marques

Thesis approved in public session to obtain the PhD Degree in Chemical Engineering

Jury final classification: Pass with Distinction

2022

UNIVERSIDADE DE LISBOA

INSTITUTO SUPERIOR TÉCNICO

Development of Self-Healing Coatings for Corrosion Protection of Carbon Steel

Mahboobeh Attaei

Supervisor: Doctor Maria de Fátima Grilo da Costa Montemor
Co-Supervisor: Doctor Ana Clara Lopes Marques

Thesis approved in public session to obtain the PhD Degree in Chemical Engineering

Jury final classification: Pass with Distinction

Jury

Chairperson: Doctor Maria Filipa Gomes Ribeiro, Instituto Superior Técnico, Universidade de Lisboa

Member of the Committee:

Doctor Verónica Cortés de Zea Bermudez, Escola de Ciências da Vida e do Ambiente, Universidade da Trás-os-Montes e Alto Douro

Doctor Maria de Fátima Grilo da Costa Montemor, Instituto Superior Técnico, Universidade de Lisboa

Doctor João Carlos Salvador Santos Femandes, Instituto Superior Técnico, Universidade de Lisboa

Doctor Susana Paula dos Santos Carvalho Piçarra, Escola Superior de Tecnologia do Barreiro, Instituto Politécnico de Setúbal

Doctor Maryna Taryba, Instituto Superior Técnico, Universidade de Lisboa

2022

Abstract

Steel is widely used in industrial and engineering structures due to its excellent mechanical properties and competitive cost. However, steel structures are highly susceptible to corrosion, particularly when exposed to aggressive environments. Significant financial losses and environmental issues have been caused by the relatively high corrosion tendency of steels. Therefore, corrosion protection has become an issue of fundamental importance to minimize the economic losses and any ecological damage that corrosion might cause. One of the most effective ways to prevent steel´s corrosion is applying protective coatings. Over the years, organic coatings have been the most used thanks to their inherent features such as high barrier properties, availability, ease of processing, and their flexibility to customize formulations for specific applications. However, the protective performance of organic coatings deteriorates over time and many key strategies have been identified to mitigate this problem. In recent years, the concept of smart, self-healing coatings has been gaining critical importance. Incorporation of carriers loaded with corrosion inhibitors or other healing species, despite of the challenges, is one of the most effective routes to create "smart" organic coatings.

This Doctoral Thesis focuses on the modification of epoxy, and polyolefin coatings by adding encapsulated self-healing agents and/or corrosion inhibitors, with the objective of healing the coating matrix and repairing damaged areas, to control the corrosion propagation. Isocyanate compounds, and particularly isophorone diisocyanate serve efficiently as self-healing agents to heal the polymeric matrix. Thus, small, efficient, chemically stable, and long shelf-life microcapsules were synthesized to be added to the epoxy formulation to improve the healing ability of the epoxy coating for corrosion protection of carbon steel.

Cerium containing species, and in particular Ce (III) ions are also considered to be interesting species to inhibit corrosion, mostly for aluminium and magnesium alloys. Some cerium-based compounds have been reported to be effective to protect steel, as well. Therefore, in this Thesis two different corrosion inhibitors were employed to modify the epoxy-based and polyolefin-based coatings. First a novel cerium tri(bis(2-ethylhexyl)phosphate inhibitor was added together with isophorone diisocyanate microcapsules into an epoxy formulation to boost the protection properties of epoxy, thanks to multilevel protective effect of both particles. Then, CeO_2 nanoparticles (synthesized by author of this Thesis), were used to improve the corrosion protection

properties of polyolefin coatings. The CeO_2-containing polyolefin coating was applied to carbon steel and demonstrated improved barrier properties and healing of corrosion sites, in comparison to the unmodified reference coating. Electrochemical techniques revealed that the global and localized anti corrosion properties of the polyolefin coating increased drastically when CeO_2 nanoparticles were previously treated with N,N,N',N'-Tetrakis(2-hydroxyethyl)ethylenediamine (an organic inhibitor compatible with polyolefin matrix).

Keywords: Carbon steel, Organic Coating, Self-healing, Corrosion Inhibition Electrochemical Techniques.

Resumo

O aço é amplamente utilizado em estruturas industriais e de engenharia devido às suas excelentes propriedades mecânicas e custo competitivo. No entanto, as estruturas de aço são altamente suscetíveis à corrosão, principalmente quando expostas a ambientes agressivos. A elevada sensibilidade à corrosão do aço tem sido responsável por perdas financeiras significativas e também por graves problemas ambientais. Assim, a proteção contra a corrosão tornou-se uma questão de fundamental importância para minimizar as perdas económicas e danos ecológicos que a corrosão possa causar. Uma das formas mais eficazes de prevenir a corrosão do aço é a aplicação de revestimentos protetores. Ao longo dos anos, os revestimentos orgânicos (tintas) têm sido os mais utilizados graças às suas propriedades inerentes, como elevada barreira de proteção, disponibilidade, facilidade de processamento e flexibilidade para personalizar formulações para aplicações específicas. No entanto, a capacidade protetora dos revestimentos orgânicos deteriora-se com o tempo e muitas estratégias têm vindo a ser investigadas para mitigar esse problema. Nos últimos anos, o conceito de revestimentos inteligentes, com propriedades de autorregeneração tem vindo a ganhar importância. A adição de partículas transportadoras, impregnadas com inibidores de corrosão, ou outras espécies regenerativas, apesar de desafiante, é uma das estratégias mais eficazes para criar revestimentos orgânicos "inteligentes".

Esta tese doutoral foca-se na modificação de revestimentos epoxídicos e poliolefínicos através da incorporação de agentes de autorregeneração encapsulados e/ou inibidores de corrosão, com o objetivo de regenerar a matriz do revestimento e reparar áreas danificadas, para controlar a propagação da corrosão. Para o efeito foram utilizados compostos de isocianato, em particular diisocianato de isoforona, que atuam como agentes capazes de regenerar, eficientemente, a matriz polimérica. Assim, foram sintetizadas microcápsulas pequenas, eficientes, quimicamente estáveis e de longa vida útil que foram posteriormente adicionadas a uma formulação de epóxi, de forma a melhorar a capacidade de regeneração do revestimento epoxídico utilizado para proteção contra a corrosão de aço carbono.

Os compostos de cério e, em particular, os iões de Ce(III) são também considerados interessantes para inibir a corrosão, principalmente em ligas de alumínio e magnésio. Alguns compostos à base de cério também foram relatados como sendo eficazes na proteção de aço. Portanto, nesta tese foram estudados dois inibidores de corrosão, à base de cério, que foram utilizados para modificar revestimentos à base de epóxi e de

poliolefina. Primeiro, foi testado um novo inibidor de fosfato de cério tri(bis(2-etilhexil) que foi adicionado à formulação de epóxi juntamente com microcápsulas de diisocianato de isoforona para aumentar as propriedades de proteção do revestimento, graças ao efeito protetor multinível de ambas as partículas. De seguida, nanopartículas de CeO_2 (sintetizadas pela autora desta tese), foram usadas para melhorar as propriedades de proteção contra a corrosão do revestimento de poliolefina. A poliolefina contendo CeO_2 foi aplicada em aço carbono e demonstrou propriedades de barreira melhoradas, bem como a regeneração de zonas em corrosão. Através da utilização de técnicas eletroquímicas verificou-se que as propriedades anticorrosivas globais e localizadas de poliolefina melhoraram significativamente quando as nanopartículas de CeO_2 foram previamente tratadas com N,N,N',N'-Tetrakis(2-hidroxietil)etilenodiamina (um inibidor orgânico compatível com a matriz de poliolefina).

Palavras-chave: Aço Carbono, Revestimento Orgânico, Autorregeneração, Técnicas Eletroquímicas, Inibição de Corrosão.

Extended Abstract

Carbon steels are important engineering material in our daily life. Their physical and mechanical properties can be simply tuned by changing the carbon content and selection of proper heat treatment. Being also the cost effective and easy recyclable material, they are widely used in preparing countless products, mostly in construction, transportation, mining, energy, and oil & gas industries, among others. Despite of their fundamental role in human life, corrosion is a critical drawback of carbon steel. The predictable and unpredictable repair, maintenance, and replacement of corroded components specially in oil & gas industries represents substantial costs. Corrosion is also responsible for major concerns regarding personal safety and environmental issues. Therefore, several different protection methods have been reported to protect carbon steel from being corroded, such as cathodic and anodic protection, and modification of environment by addition of corrosion inhibitor. However, organic coatings are considered the most effective way to protect carbon steel from corrosion, and many different coating chemistries are used as effective barriers to protect steel components. During the last decades, intensive work has been devoted to the development and evaluation of more effective organic coatings for corrosion protection. One important research stream has been dedicated to the development of self-healing coatings containing smart anti-corrosion additives loaded with specific corrosion inhibitors or healing agents that confer corrosion protection. Smart coatings, with healing ability, may repair the polymeric network due to the presence of polymerizable agents or may passivate/inhibit the areas under corrosion thanks to the controlled delivery of corrosion inhibitors. Encapsulation of polymerizable species into micro or nano carriers, sensitive to external stimuli has been considered a viable and attractive smart route for introducing healing functionalities into the polymeric matrix. Among different possible healing strategies, application of one-component materials, which do not require addition of catalyst for their reactions have attracted considerable interest. These materials can be easily transformed into a polymeric protective layer via activation and reaction with moisture without needing any other chemicals. Encapsulation of isocyanates as healing agent, gives the possibility to prepare autonomous self-healing systems in water/moisture-containing environments, due to the extreme reactivity of the isocyanate chemical group. While encapsulation of isophorone diisocyanate as an efficient self-healing agent has been already reported in literature, the development of small, efficient, chemically stable, and long shelf-life microcapsules faces several issues,

and it is still considered a challenging field of research. Therefore, the first part of this PhD work, reported in chapter 3, was dedicated to the synthesis and characterization of microcapsules which can satisfy these conditions. The second part of the work involved the modification of an epoxy-based coating with the isocyanate-containing microcapsules, to be applied on carbon steel (also reported in chapter 3).

The self-healing ability of coatings containing isocyanate microcapsules can be explained by the slow release and diffusion of isophorone diisocyanate from microcapsules, followed by further reaction of isocyanate groups with water or OH groups, and formation of protective polymeric layer. Part of the work presented in Chapter 3 was published in Applied Polymer Science, 2019, 137, 48751 and Progress in Organic Coatings, 2020, 139, 105445.

In the third part of this Thesis, reported in chapter 4, the protective properties of coating modified with isocyanate microcapsules were further enhanced by addition of corrosion inhibitors. To this end, novel cerium tri(bis(2-ethylhexyl)phosphate inhibitor and isocyanate microcapsules were simultaneously added into the epoxy-based coating. Global electrochemical techniques evidenced a relevant synergistic effect when both additives are combined, resulting in significantly higher and more stable coating barrier properties. Localized electrochemical techniques revealed an important and stable corrosion inhibition phenomenon over defects formed in the coating containing the mixture of both additives. Part of the work presented in Chapter 4 was published in Progress in Organic Coatings, 2020, 147, 105864.

In chapter 5 of this Thesis, corrosion protection properties of a polyolefin coating were improved by addition of blank CeO_2 nanoparticles, and CeO_2 nanoparticles treated with N,N,N',N'-Tetrakis(2-hydroxyethyl)ethylenediamine as an organic corrosion inhibitor. To the author's best knowledge, neither CeO_2 nanoparticles, nor N,N,N',N'-Tetrakis(2-hydroxyethyl)ethylenediamine were previously reported to impart corrosion inhibition properties to polyolefin coatings to protect carbon steel. Therefore, this work unveils a new and very effective corrosion inhibition additive that is highly compatible with polyolefin coatings. Global electrochemical technique showed improved barrier properties and increased pore resistances of the modified coatings, in comparison to reference. The pore resistance of the modified coatings was up to four orders of magnitude higher than the reference ones. Results from evaluation of coatings by localized techniques revealed that blank CeO_2 nanoparticles were able to reduce the corrosion activity, while inhibitor treated CeO_2 nanoparticles fully suppressed the corrosion

activities over artificially made defect. Moreover, in most of the publications in the field, the precise corrosion protection mechanism of CeO_2 is not clearly discussed. Here, two characterization techniques, Micro-FTIR ATR, and EDS mapping, were combined to identify the corrosion protection mechanism in place. The obtained results revealed that two different mechanisms participate synergistically in the corrosion protection imparted by the inhibitor treated CeO_2 nanoparticles. On one hand, reaction of hydroxyl and amine groups of organic inhibitors with iron forms a protective complex layer that hinders the access of aggressive species to the steel surface, and on the other hand, a delayed dissolution of the CeO_2 nanoparticles followed by further reaction of cerium cations with OH^-, forms a protective cerium-containing layer at the cathodic sites. Part of the work presented in Chapter 5 was published in Corrosion Science, 2022, 198, 110162.

Resumo Alargado

O Aço carbono é um material de engenharia de elevada importância. As suas propriedades físicas e mecânicas podem ser facilmente ajustadas alterando o teor de carbono e selecionando o tratamento térmico adequado. Por serem materiais de baixo custo e facilmente recicláveis, são amplamente utilizados na produção de inúmeros produtos, principalmente nas indústrias da construção, transporte, mineração, energia, óleo e gás, entre outras. Apesar do seu papel fundamental, a corrosão é uma desvantagem crítica do aço carbono. A reparação, manutenção e substituição, tanto previsíveis como imprevisíveis, de componentes danificados através da corrosão, especialmente nas indústrias do petróleo e gás, acarretam custos substanciais. A corrosão é também responsável por grandes preocupações em relação à segurança pessoal e a questões ambientais. Assim, podem ser utilizados vários métodos de proteção para proteger o aço carbono da corrosão, tais como proteção catódica e anódica, e modificação da superfície material através da ação de inibidores de corrosão que são adicionados no meio líquido envolvente ou em revestimentos. Os revestimentos orgânicos são considerados a forma mais eficaz de proteger o aço carbono da corrosão, e a sua composição baseia-se em químicas distintas que se se caracterizam por formar barreiras de proteção eficientes sobre os componentes de aço. Nas últimas décadas, tem sido desenvolvido um intenso trabalho focado no desenvolvimento e avaliação de revestimentos orgânicos mais eficazes para proteção contra corrosão. Uma parte substancial desta investigação tem sido dedicada ao desenvolvimento de revestimentos de autorregeneração contendo aditivos anticorrosivos inteligentes carregados com inibidores de corrosão específicos ou agentes que conferem proteção contra a corrosão. Os revestimentos inteligentes, com capacidade de regeneração, podem envolver a reparação da rede polimérica devido à presença de agentes polimerizáveis ou a passivação/inibição das áreas sob corrosão graças à libertação controlada de inibidores de corrosão. O encapsulamento de espécies polimerizáveis em micro ou nanopartículas de transporte, sensíveis a estímulos externos, tem sido considerado uma estratégia inteligente, viável e atraente para a introdução de funcionalidades de regeneração na matriz polimérica. De entre as diferentes estratégias de regeneração possíveis, a aplicação de materiais mono componente, que não requerem a adição de catalisador para as suas reações, tem despertado um interesse considerável. Esses materiais podem ser facilmente transformados numa camada protetora polimérica via a ativação e reação com humidade sem precisar de nenhum outro produto químico. O

encapsulamento de isocianato como agente de regeneração, permite a preparação de sistemas de autorreparação autónomos em ambientes contendo água/humidade, devido à extrema reatividade do grupo químico isocianato. Embora o encapsulamento de diisocianato de isoforona como um agente de autorreparação eficiente já tenha sido relatado na literatura, o desenvolvimento de microcápsulas pequenas, eficientes, quimicamente estáveis e de longa vida útil enfrenta vários problemas e ainda é considerado um campo de investigação com grandes desafios. Portanto, a primeira parte deste trabalho de doutoramento, reportada no Capítulo 3, foi dedicada a sintetizar e caracterizar microcápsulas que satisfaçam tais condições. A segunda parte do trabalho envolve a modificação de um revestimento à base de epóxi com microcápsulas contendo isocianato, e sua aplicação em aço carbono (também relatado no Capítulo 3).

A capacidade de autorreparação dos revestimentos contendo microcápsulas de isocianato pode ser explicada pela lenta libertação e difusão de diisocianato de isoforona das microcápsulas, seguindo-se a reação dos grupos isocianato com água ou grupos OH, e formação de uma camada protetora polimérica. Esta parte da tese (apresentada no Capítulo 3) foi publicada nas revistas Applied Polymer Science, 2019, 137, 48751 e Progress in Organic Coatings, 2020, 139, 105445.

Na terceira parte desta tese, reportada no Capítulo 4, as propriedades protetoras do revestimento modificado com microcápsulas de isocianato foram reforçadas pela adição de inibidores de corrosão. Para este fim, um novo inibidor de fosfato de cério tri(bis(2-etilhexil) e microcápsulas de isocianato foram adicionados simultaneamente ao revestimento à base de epóxi. Os ensaios eletroquímicos evidenciaram um efeito sinérgico relevante quando ambos os aditivos são combinados, resultando em propriedades de barreira de revestimento significativamente mais elevadas e estáveis. As técnicas eletroquímicas localizadas confirmaram uma importante e estável inibição da corrosão, conferida pela formação de uma camada protetora sobre defeitos formados artificialmente no revestimento contendo a mistura de ambos os aditivos. Este trabalho, apresentado no Capítulo 4, foi publicado em Progress in Organic Coatings, 2020, 147, 105864.

No Capítulo 5 desta tese, as propriedades de proteção contra a corrosão de um revestimento de poliolefina foram melhoradas pela adição de nanopartículas de CeO_2 sem qualquer tratamento, e tratadas com N,N,N',N'-Tetrakis(2-hidroxietil)etilenodiamina como inibidor de corrosão orgânico. Tanto quanto é do conhecimento da autora, não há qualquer trabalho na literatura que reporte a inibição da corrosão em aço carbono através

da aplicação de revestimentos de poliolefina contendo nanopartículas de CeO_2, ou N,N,N',N'-Tetrakis(2-hidroxietil)etilenodiamina. Assim, este trabalho apresenta um novo aditivo inibidor de corrosão muito eficaz e altamente compatível com revestimentos de poliolefina. As técnicas eletroquímicas globais mostraram propriedades barreira melhoradas e maior resistência dos poros nos revestimentos modificados, em comparação com as referências. A resistência dos poros dos revestimentos modificados foi cerca de quatro ordens de grandeza superior comparativamente à referência. Os resultados da avaliação de revestimentos por técnicas localizadas revelaram que as nanopartículas sem tratamento foram capazes de reduzir a atividade de corrosão, enquanto que as nanopartículas de CeO_2 tratadas com inibidor suprimiram totalmente a atividade de corrosão em defeitos artificiais. Além disso, a maioria das publicações na área não discute claramente o mecanismo de proteção contra corrosão de CeO_2. Assim, neste trabalho foran utilizadas duas técnicas de caracterização, Micro-FTIR ATR, e mapeamento por EDS para evidenciar detalhes do mecanismo de proteção. Os resultados obtidos revelaram a participação de dois mecanismos diferentes na proteção contra a corrosão conferida pelas nanopartículas de CeO_2 tratadas com inibidor. Por um lado, a reação de inibidores orgânicos dos grupos hidroxietil e amina com os iões ferro leva à formação de uma camada protetora complexa que dificulta o acesso de espécies agressivas à superfície do aço e, por outro lado, a dissolução retardada das nanopartículas de CeO_2, seguida pela reação adicional de catiões de cério com OH^- forma uma camada protetora contendo cério nos locais catódicos. A parte da tese apresentada no Capítulo 5 foi publicada em Corrosion Science, 2022, 198, 110162.

Acknowledgments

It has been a long journey, a long learning process, and a special and unique experience with many people involved, directly and indirectly. Therefore, I would like to express my sincere appreciation to those who have contributed to this PhD work.

I am incredibly thankful to my supervisors, Professor Fátima Montemor and Professor Ana Clara Marques, for the opportunity they have given to me and for accepting me as a PhD student. Thank you for your guidance, priceless suggestions, scientific support, encouragement, and emotional support, especially during the pandemic lockdown!

Apart from scientific learning, I learned many other good things from Professor Fátima, as I had the honor of working more closely with her: patience and respecting diversity.

I want to thank her also for allowing me to be the corresponding author of scientific papers published during this work. It helped me to get critical insight into my work.

I will forever be grateful to Professor Ana, as a person who introduced me initially as a potential candidate to do this work.

I want to thank all co-authors of scientific articles published in the framework of this PhD Thesis in CSSE group, CERENA group, and Qatar University. I appreciate all collaborations and efforts which made these publications possible.

I want to express my gratitude to all members of the Corrosion Science and Surface Engineering research group, for their social and technical support, for sharing happy and sad moments, and for sharing lunchtimes or coffee breaks! I am particulary greatful to Professor João Salvador, Professor Alda Simoes, Dr. Maryna Taryba, Dr. Lénia Calado, Dr. Yegor Morozov, Dr. Pablo Arévalo-Cid, Dr. Katarzyna Siwek, Dr. Marta Alves, Dr. Jéssica Nardeli, Caterina Alves, Roma Raj, Joana Madeira, Mário Almeida, Gabriel Carvalho, and my special friend Mafalda Macatrão.

I would also like to thank Professor Luis Santos for agreeing to be my supervisor for the "Advanced Experimental Technique and methodology" subject, for his time, and his precious scientific advice.

I would like to thank, Professor Rui Galhano dos Santos, Mónica Loureiro, and Mário Vale from CERENA group for all supports they have given me. I would like to put a short note for Mário Vale: "Without any doubt, you are the best person I met in IST!".

I would like to thank Dr. Ana Cristino (Faculdade de Ciências da Universidade de Lisboa) for conducting the XRD tests.

I would also like to acknowledge the Qatar National Research Fund (a member of the Qatar Foundation) for NPRP Grant numbers 9-080-2-039, 11S-1226-170132 and NPRP13S-0120-200116. I also thank Centro de Química Estrutural and CERENA through the strategic project FCT-UID/QUI/00100/2019, UID/ECI/04028/2019, UIDB/00100/2020, UIDP/00100/2020, and UID/ECI/04028/2019 and for providing necessary equipment to carry out my research work. I also acknowledge Sherwin-Williams for providing the model formulation of the epoxy coating, VoestAlpine AG for providing the steel samples, Dow Chemical Company for providing the polyolefin-based coating formulation.

I am genuinely grateful to my best friend Merita, and my friend Raquel, for their friendship, all their support, and encouraging me to finish and close this chapter of my life. I am constantly being listened to by them, and I am delighted to have them.

I have no word to thank Maria Abrantes enough for giving a hand in translating abstract and extended abstract to Portuguese on such short notice.

To my beloved husband, Dr. Eshagh Movahed, I have no word to thank you enough for your being, your kind support, and your patience when I dedicated most of my time to my Thesis. Having you beside me is God's greatest gift, and I am thankful for that.

To my family, friends, and my ex-colleagues in Iran: I am sorry for ignoring you during my PhD! You are extraordinary persons, true friends, like stars. As the saying goes," TRUE friends are like STARS. you don't always see them, but you know they are there. Thank you!"

In the memory of my beloved brother "Mohamad Attaei", who helped many impoverished children to have access to the basic education.

May God Bless his Soul

Table of Contents

List of Figures

List of Tables

Abbreviations and Acronyms

3LPO	Three-Layer Polyolefin
8-HQ	8-hydroxyquinoline
ac	Alternating current
aminosilane	3-(2-aminoethylamino) propyltrimethoxysilane
BI	Benzimidazole
BTA	Benzothiazole
CC	Conversion Coating
Ce(DEHP)3	Cerium tri(bis(2-ethylhexyl)phosphate)
CHS	Carbon Hollow Sphere
CNT	Carbon Nanotubes ()
CPE	Constant Phase Element
CSP	Crude Steel Production
DEHP	bis(2-ethylhexyl)phosphate
DETA	Diethylenetriamine
DCPD	Dicyclopentadiene
DDA	Dodecylamine
DRFE	Desmodur RFE
EDA	Ethylenediamine
EDS	Energy Dispersive X-ray Spectroscopy
EEC	Equivalent Electrical Circuit
EIS	Electrochemical Impedance Spectroscopy
EU	European Union
FEG-SEM	Field Emission Gun Scanning Scanning Electron Microscopy
FTIR-ATR	Fourier Transform Infrared Spectroscopy - Attenuated Total Reflectance
GA	Gum Arabic
GO	Graphene Oxide
HDI	Hexamethylene diisocyanate
HDMS	Hexadecyltrimethoxysilane (HDMS**)**
HHNs	Hybrid halloysite tubes
HMZS	Hollow mesoporous zirconia nanosphere
IPDI	Isophorone diisocyanate
IPES	Isocyanate silane (3-isocyanatopropyltriethoxysilane)
L-CAR	L-Carnosine
LEIS	Localized Electrochemical Impedance Spectroscopy
LDH	Layered double hydroxide

MBI	2-Mercaptobenzimidazole
MBT	2-Mercaptobenzothiazol
MC	Microcapsule
MDI	Methylene Diphenyl diisocyanate
MSN	Mesoporous silica nanoparticle
n-OTES	Triethoxy(octyl)silane
NP	Nanoparticle
OCP	Open Circuit Potential
O/W	Oil-in-Water
SIET	Scanning Ion-Selective Electrode Technique
SVET	Scanning Vibrating Electrode Technique
TA	Tannic Acid
THEEDA	N,N,N',N'-Tetrakis(2-hydroxyethyl)ethylenediamine
PEI	Poly(ethyleneimine)
PF	Phenol-formaldehyde
PLC	Poly(ε-caprolactone)
PU	Polyurethane .
PUa	Polyurea
PUF	Polyurea-formaldehyde
RT	Room Temperature
TEOS	Tetraethyl orthosilicate
UF	Urea-Formaldehyde
W/O	Water-in-Oil
XRD	X-ray Diffraction
ZIF	Zeolitic Imidazolate Frameworks

Symbols

$\|Z\|$	Impedance modulus
$\|Z\|_{LF}$	Low-frequency impedance modulus
$\|Z\|_{0.005\ Hz}$	Impedance modulus taken at 0.005 Hz

Research Motivation

Research Motivation

Steel is a strategic material for industrial infrastructures, especially in the oil & gas industry, namely in pipelines, piping and main oilfield infra structures [1-6]. Corrosion is one of the primary mechanisms that lead to failure of these metallic facilities. For pipelines, corrosion can cause leaks, unexpected shutdowns, fire, and explosion, resulting in serious environmental and economic consequences [2,3]. In the oil & gas industry, it was estimated that the total annual cost of corrosion is 1.2 billion €, the number increases drastically, and running into tens billions of euros every year, considering the associated losses due to lost income and remediation measures [2]. Therefore, corrosion protection has been of immense importance for structural integrity management and production assurance.

Coatings generally, and organic coating specifically are the efficient and often most used method for protection of steel structures against corrosion. Although a high performance can be achieved in terms of adhesion, mechanical properties or durability, harsh service conditions lead to formation of microcracks and premature failure of organic coatings [7]. Maintenance and repair of the damaged coatings on large steel structures like offshore oil rigs, sea ships, etc. are extremely expensive [5]. However, costs of structural failures, subsequent environmental pollution and sometimes even loss of human lives are dramatically higher than that. Looking for solutions to prolong service life of anticorrosive coatings, scientists referred to self-healing coatings.

Although healing has been, for a long time, a quality of living organisms, lately self-healing materials have been developed, mimicking the healing ability of living organism, in such a way that they react upon the certain triggers with an automated repair mechanism [8]. Research on this concept attracted attentions and has been developing very fast in a wide range of industrial applications [9,10].

Self-healing coatings for corrosion protection are one group of these interesting materials that are designed to protect the underlying metallic substrate. These special coatings can restore their protective properties after a damage event, as opposed to conventional coatings [7,11].

Self-healing coatings can be classified in two main groups according to extrinsic and intrinsic self-healing functionalities [9,12]. In extrinsic self-healing coatings, reactive agents such as monomers, polymers, corrosion inhibitor or superhydrophobic agents can be stored in microcapsules or nano containers before incorporation into the coating. These

containers can recover the protection properties of coatings or coating's functionalities, in response to specific stimulus, that trigger the healing process [9,13–16]. For intrinsic self-healable coatings, the healing process may achieve by the polymeric matrix itself. This type of self-healing requires an external trigger such as heat, UV light or other stimuli [16].

Most recently, self-healing strategies for corrosion protection have been focused on multilevel and/or synergistic self-healing. In self-healing coatings this can be achieved by combining both intrinsic and extrinsic healing mechanisms to improve the corrosion protection properties of organic coatings [17–19].

In fact, during this PhD Thesis combination of both extrinsic and intrinsic self-healing concepts were employed to develop a highly protective, and highly stable self-healing system, beyond the state of the art.

This work had been conducted in the framework of two research projects: SMART-Coat, and S^2 Coat. These two projects are interconnected, since both aim at developing novel concepts of self-healing for organic coatings used for protection of steel [20,21].

SMART-Coat project aimed at tailoring protective organic epoxy primers with multilevel functionalities for autonomous corrosion protection of steel piping exposed to the marine atmospheres [21].

To meet this goal, a model epoxy coating, based on a commercial formulation was selected as a reference coating. A smart, self-healing coating was developed with addition of relatively small (≈ 20 μm), high efficiency, and long shelf-life microcapsules. Furthermore, a multifunctional self-healing system, was developed by simultaneous addition of microcapsules, and a pH sensitive corrosion inhibitor cerium organophosphate.

The second part of this PhD work addressed the development of polyolefin-based smart self-healing coatings, in the framework of S^2Coat project. The anti-corrosion performance of a commercial polyolefin coating, which has been reported to possess self-healing ability by itself, was further improved by addition of CeO_2 nanoparticles as a corrosion inhibitor. Furthermore, CeO_2 nanoparticles were treated with N,N,N',N'-Tetrakis(2-hydroxyethyl)ethylenediamine as an organic corrosion inhibitor, to develop a smart multilevel self-healing system. It is worth mentioning that despite their importance and potential benefits, polyolefin-based coatings have been rarely addressed [22].

References

[1] T. Skoczkowski, E. Verdolini, S. Bielecki, M. Kochański, K. Korczak, A. Węglarz, Technology innovation system analysis of decarbonisation options in the EU steel industry, Energy. 212 (2020) 118688. https://doi.org/10.1016/j.energy.2020.118688.

[2] L.T. Popoola, A.S. Grema, G.K. Latinwo, B. Gutti, A.S. Balogun, Corrosion problems during oil and gas production and its mitigation, Int. J. Ind. Chem. 4 (2013) 1–15. https://doi.org/10.1186/2228-5547-4-35.

[3] A. Popoola, O. Olorunniwo, O. Ige, Corrosion Resistance Through the Application of Anti-Corrosion Coatings, in: Dev. Corros. Prot., n.d.: pp. 241–270. https://doi.org/10.5772/57420.

[4] European Commission, Action Plan for a competitive and sustainable steel idustry in Europe, (2013) 1–23.

[5] S. Rio, O. D´Albuquerque, In-Service Pipeline Rehabilitation, in: Prot. Maint. Transm. Pipline, Technology Publishing Company, 2012: pp. 50–56. http://www.eia.gov/pub/oil_gas/natural_gas/analysis_publications/ngpipeline/transsys_design.html.

[6] G. Koch, Cost of corrosion, Trends Oil Gas Corros. Res. Technol. Prod. Transm. (2017) 3–30. https://doi.org/10.1016/B978-0-08-101105-8.00001-2.

[7] A.E. Hughes, Self-healing coatings, in: Recent Adv. Smart Self-Healing Polym. Compos., Elsevier Ltd, 2015: pp. 211–241. https://doi.org/10.1016/B978-1-78242-280-8.00008-X.

[8] R. A. t. M van Benthem, W. Ming, G de With, self-healing Polymer Coating, in S.V.D. Zwaag (Ed), Self Healing Materials an Alternative Approach to 20 Centuries of Materials Science, Springer, Dordrecht, Netherlands, 2007.

[9] M.F. Montemor, Hybrid nanocontainer-based smart self-healing composite coatings for the protection of metallic assets, in: Smart Compos. Coatings Membr., Elsevier Ltd, 2016: pp. 183–210. https://doi.org/10.1016/B978-1-78242-283-9.00007-5.

[10] D.G. Bekas, K. Tsirka, D. Baltzis, A.S. Paipetis, Self-healing materials: A review of advances in materials, evaluation, characterization and monitoring techniques, Compos. Part B Eng. 87 (2016) 92–119. https://doi.org/10.1016/j.compositesb.2015.09.057.

[11] M.F. Montemor, Functional and smart coatings for corrosion protection: A review of recent advances, Surf. Coatings Technol. 258 (2014) 17–37. https://doi.org/10.1016/j.surfcoat.2014.06.031.

[12] P. Vijayan, M. Al-Maadeed, Self-repairing Composites for Corrosion Protection: A Review on Recent Strategies and Evaluation Methods, Materials (Basel). 12 (2019) 2745. https://doi.org/10.3390/ma12172754.

[13] U. Eduok, E. Ohaeri, J. Szpunar, Self-healing composite coatings with protective and anticorrosion potentials: Classification by healing mechanism in Self-healing Composite Materials from Design to Applications, A. Khan, M. Jawaid, A. M. A., Asiri, S. N. Raveendran (Ed) , Elsevier Ltd, 2019. https://doi.org/10.1016/B978-0-12-817354-1.00008-9.

[14] M.F. Montemor, Functional and smart coatings for corrosion protection: A review of recent advances, Surf. Coatings Technol. 258 (2014) 17–37. https://doi.org/10.1016/j.surfcoat.2014.06.031.

[15] D.G. Shchukin, D. Borisova, H. Mohwald, Self-Healing Coatings, in: Wolfgang H. Binder (Ed.), Self-Healing Polym. From Princ. to Appl., First, 2013: pp. 381–399. https://doi.org/10.1002/9783527670185.ch6.

[16] D.Y. Wu, S. Meure, D. Solomon, Self-healing polymeric materials: A review of recent developments, Prog. Polym. Sci. 33 (2008) 479–522. https://doi.org/10.1016/j.progpolymsci.2008.02.001.

[17] A. Hassanein, A. Khan, E. Fayyad, A.M. Abdullah, R. Kahraman, B. Mansoor, R.A. Shakoor, Multilevel Self-Healing Characteristics of Smart Polymeric Composite Coatings, ACS Appl. Mater. Interfaces. 13 (2021) 51459–51473. https://doi.org/10.1021/acsami.1c14406.

[18] Y. Huang, L. Deng, P. Ju, L. Huang, H. Qian, D. Zhang, X. Li, H.L. Terryn, J.M.C. Mol, Triple-Action Self-Healing Protective Coatings Based on Shape Memory Polymers Containing Dual-Function Microspheres, ACS Appl. Mater. Interfaces. 10 (2018) 23369–23379. https://doi.org/10.1021/acsami.8b06985.

[19] Y. Huang, T. Liu, L. Ma, J. Wang, J. Zhang, X. Li, Saline-responsive triple-action self-healing coating for intelligent corrosion control, Mater. Des. 214 (2022) 110381. https://doi.org/10.1016/j.matdes.2022.110381.

[20] M.F. Montemor, A.C. Marques, Smart Single Layer Polyolefin Coating for Corrosion Protection of Steel Parts, (2017), NPRP11S-1226-170132.

[21] M.F. Montemor, A.C. Marques, Smart corrosion protection strategies for steel materials in the oil and gas industry- Smart Coat, (2018) 1–12.

[22] R. Raj, M.G. Taryba, Y. Morozov, R. Kahraman, R.A. Shakoor, M.F. Montemor, On the synergistic corrosion inhibition and polymer healing effect of polyolefin coatings modified with Ce-loaded hydroxyapatite particles on steel, Electrochim. Acta. 388 (2021) 138648. https://doi.org/10.1016/j.electacta.2021.138648.

Chapter 1

State of the art in “Smart self-healing coatings for protection of carbon steel”

This chapter provides an overview in the state-of-art of development of smart coatings for corrosion protection of steel. A literature review of the most important research related to this work is described.

1.1 Introduction

Metals possess distinctive characteristics such as high melting point, good conductivity, high ductility, relatively high hardness, and excellent tensile strength. These unique characteristics made them an integral part of human life since 1200 B.C. Among the wide variety of metals and alloys, steel is widely used in construction, transportation, mining, energy, and oil & gas industries due to its competitive cost and the ability to be recycled repeatedly [1]. Steel industries are vitally important for the world´s economy with almost steady increasing production. For society, steel industries' benefits include local jobs, durable products and conservation of raw materials for the future [2].

Figure 1.1a shows the world crude steel production (CSP) between 2000-2020 and the geographical share of each region in 2020 (Figure 1.1b). Although the regional share of CSP for the European Union (EU) was reported to be 7.4 %, the apparent steel use per capita in 2020 around the EU region was reported to be 273.9 kg which is significant (Figure 1.1c) [2]. Even by the influence of the pandemic, steel industries suffered only a minor shrinkage in steel demand. Despite the fundamental role of iron and steel in human life, a principal issue called **corrosion** is the main drawback of iron and steel.

Corrosion, defined as an irreversible interfacial reaction of a material with its environment [3], is a global challenge that affects many industries, including steel industries. It is estimated that, annually, the global cost of corrosion reaches to 2.1 trillion €, which is equivalent to 3.4% of the world´s gross domestic products [4].

By employing the available corrosion control practices, the annual savings of 15-35% is estimated on a global basis [5]. Besides the problems associated with the negative impact on the world economy, corrosion also represents major concerns regarding personal safety and environmental issues. For instance, uncontrolled corrosion could induce leak, fire, and explosion in pipelines, among other consequences [6].

Therefore, tremendous efforts have been made to develop and implement corrosion prevention solutions. The following subsections will describe a detailed classification of most effective efforts for corrosion protection of metals and, in particular, steels. Before that, it is necessary to discuss the corrosion mechanism of steel, and specifically, those reactions involved in corrosion of carbon steel used during this PhD work.

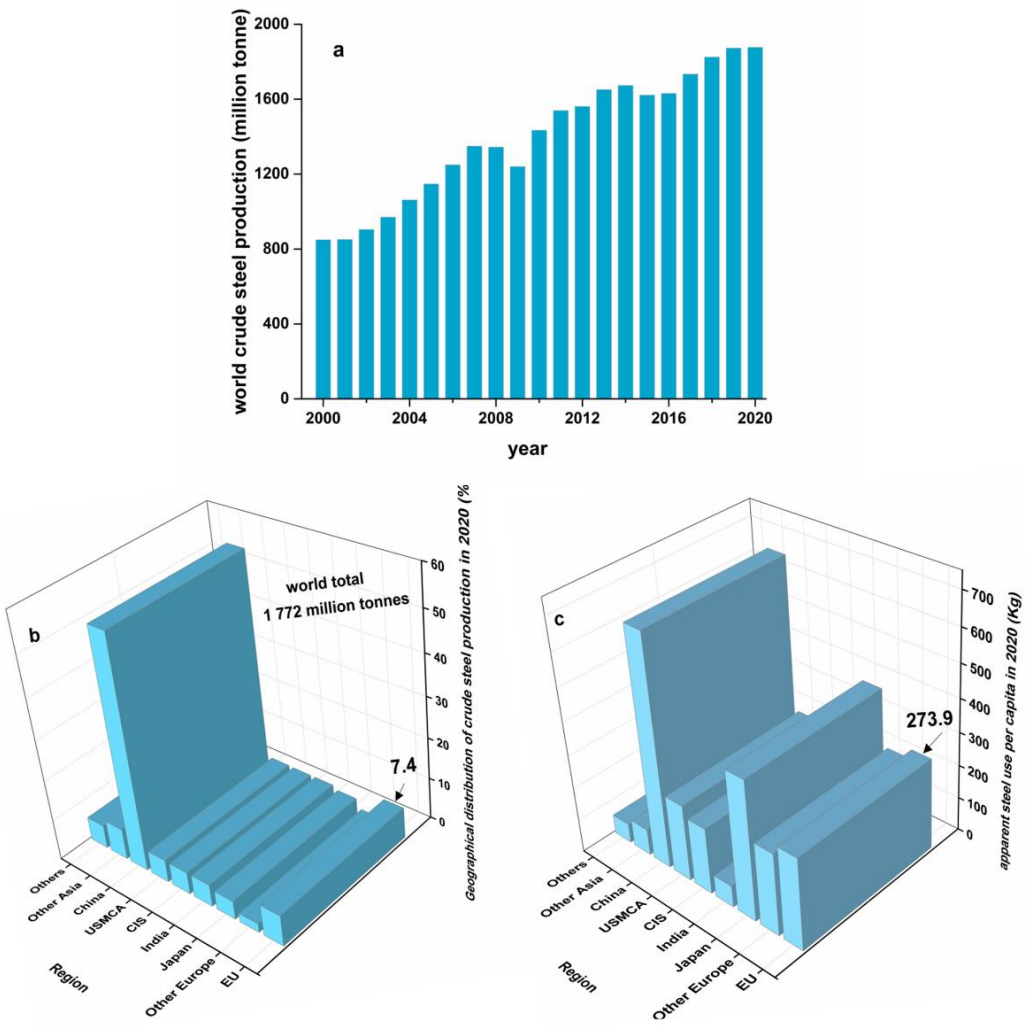

Figure 1.1 a) World CSP, b) regional share of CSP in 2020, c) the regional apparent steel use per capita in 2020. Information extracted from [2].

1.2 Corrosion mechanism in carbon steel

Carbon steel is an iron-based alloy containing less than 2 wt% of carbon. It can be classified into three main groups of high, medium, and low carbon steel, with carbon content of (> 0.5 wt%), (0.25-0.55 wt%), and (< 0.25 wt%) respectively [7]. Table 1.1 shows the chemical composition of low carbon steel used during this PhD work.

Table 1.1 Elemental composition of carbon steel used in this work.

Element	**C**	**Mn**	**P**	**S**	**Fe**
wt%	0.12	0.6	0.045	0.045	balance

Corrosion mechanisms in carbon steel, on the one hand, depends strongly on chemical composition of steel especially carbon content, and on another hand, depend on chemical composition of the corrosive environment (air pollution by gases, acid vapors or seawater aerosols) [8–10].

The presence of C, Mn, P, and S aims to improve the mechanical properties, forgeability, and machinability but is less effective in corrosion protection of low carbon steel [11].

Corrosion of carbon steel in aqueous solution proceeds by simultaneous oxidation and reduction reactions which can be accompanied by other chemical reactions in which the corrosion products may participate.

In general, these reactions occur in four steps as following:

i) dissolution of the iron occurs at the anodic sites initially from Fe into Fe^{2+} and further to Fe^{3+} and can be written according to equations 1.1, and 1.2:

$$Fe \rightarrow Fe^{2+} + 2e^{-} \qquad \text{Eq. 1.1}$$

$$Fe^{2+} \rightarrow Fe^{3+} + e^{-} \qquad \text{Eq. 1.2}$$

oxygen, which is highly soluble in the aqueous solution, as a possible oxidizing agent, accelerates the consumption of produced electrons and reduces at the cathodic sites according to equation 1.3 [12]:

$$\tfrac{1}{2}\, O_2 + H_2O + 2e^{-} \rightarrow 2(OH)^{-} \qquad \text{Eq. 1.3}$$

ii) OH^- ions react with Fe^{2+} ions to form ferrous hydroxides (equation 1.4). This reaction is provoked by further absorption of water molecules on the surface, followed by the formation of hydroxide, which is known to have diffusion barrier properties [10,13].

$$Fe^{2+} + 2\,(OH)^{-} \rightarrow Fe(OH)_2 \qquad \text{Eq. 1.4}$$

iii) although the formation of $Fe(OH)_2$ can temporarily reduce the rate of oxidation reaction of iron at the anodic site, by the time elapsed, further diffusion of oxygen following by its reaction with $Fe(OH)_2$, produces ferric hydroxide and hydrated oxides according to equations 1.5, and 1.6:

$$2Fe(OH)_2 + H_2O + 1/2\, O_2 \rightarrow 2\, Fe(OH)_3 \qquad \text{Eq. 1.5}$$

$2Fe(OH)_2 + 1/2\ O_2 \rightarrow 2FeOOH + H_2O$ Eq. 1.6

iv) then, the unstable FeOOH transforms into $Fe_2O_3.H_2O$ according to equation 1.7:

$4\ Fe(OH)_2 + O_2 \rightarrow 2\ Fe_2O_3 + 4\ H_2O$ Eq. 1.7

The hydrated oxide can also lose its water and revert to the anhydrous ferrous and ferric oxide. The major corrosion products formed during the corrosion of carbon steel in an aqueous solution are listed in Table 1.2.

Table 1.2 Major corrosion products formed during the corrosion of carbon steel in an aqueous solution (information extracted from [13], and [17])

Name	Formula
Goethite	α-FeOOH
Akaganeite	β-FeOOH
Lepidocrocite	γ-FeOOH
Feroxyhite	δ-FeOOH
Magnetite	Fe_3O_4
Maghemite	γ- Fe_2O_3
Hematite	α-Fe_2O_3
-	$Fe(OH)_2$
Bernalite	$Fe(OH)_3$

However, the corrosion mechanism of carbon steel in contact with the solutions containing a high concentration of chloride ions (e.g., marine atmosphere or via direct contact of NaCl solution) is slightly different. In such a condition, the dissolution of iron into Fe^{2+} cations occurs in various steps, according to equations 1.8, 1.9, 1.10, 1.11 [12]:

$Fe + H_2O \rightarrow Fe(OH)_{ads} + H^+$ Eq. 1.8

$Fe + Cl^- \rightarrow Fe(Cl^-)_{ads}$ Eq. 1.9

$Fe(OH)_{ads} + Fe(Cl^-)_{ads} \rightarrow Fe + FeOH^+ + Cl^- + 2e^-$ Eq. 1.10

$FeOH^+ + H^+ \rightarrow Fe^{2+}_{aq} + H_2O$ Eq. 1.11

Apart from the corrosion products listed in Table 1.2, corrosion products containing chloride may be found in Cl^-- contains ambient, as detailed in Table 1.3.

Table 1.3 Corrosion products formed during the corrosion of carbon steel in Cl^--containing aqueous solution. (Information extracted from [17]).

Name	Formula
Lawrencite	$FeCl_2$
Molysite	$FeCl_3$
Ferric oxychloride	β-$Fe_2(OH)_3Cl$
Green rust	GR1

When the corrosion condition like pH, temperature, oxygen, and chloride ion availability changes, various iron oxide, oxyhydroxides, and hydroxides can be formed during the corrosion of carbon steel [14–16]. A comprehensive study on the formation mechanism and evolution of the surface rust layer of carbon steel can be found elsewhere [17–19]. In general, in an aqueous solution, goethite and feroxyhyte are the major corrosion products formed at the surface [15]. In such a condition, diffusion of oxygen through these oxide and hydroxide layers controls the corrosion rate of carbon steel [17].

In an aqueous solution containing a high concentration of chloride ions, akaganeite, lepidocrocite, and magnetite are the major corrosion products detected at the metallic surface. In such a condition, diffusion of Cl^- through the rust layer controls the corrosion progress and results in a high corrosion rate [15,18].

It is believed that the corrosion products form during the corrosion of carbon steel at the initial stage of corrosion are loose, porous and have an uneven structure with a weak adhesion to the carbon steel [10,19,20]. Therefore, they provide a poor barrier property against the diffusion of electrolyte and corrosive species towards the metallic substrate [10,14]. Although the protection properties of the rust layer formed at the surface of carbon steel was reported, this may happen only in two conditions: i) a long-term exposure of the substrate to the aggressive environment and the formation of a thick rust layer [18,19]; or ii) by initial formation of magnetite in highly Cl^--concentrated environment (with strong adhesion into the substrate) [20].

Therefore, other effective strategies should be employed to protect carbon steel from corrosion attacks.

1.3 Corrosion protection of carbon steel

1.3.1 Implementation of a corrosion management system

As mentioned before, successful corrosion prevention and protection need enormous efforts. These efforts start by implementing a corrosion management system to achieve the desired level of service at a minimum cost. Although implementation of a corrosion management system is costly, optimization can be done by combining it with corrosion protection technologies. A two-by-two matrix shown in Figure 1.2 helps to picture the benefit of this combination. With a poor management system and a short corrosion protection technology, corrosion is neither controlled nor managed (i.e., it is unsafe). With a sound corrosion protection technology, corrosion is controlled but not optimized (i.e., it is expensive). A mature management system without proper corrosion protection technology cannot be effective (i.e., it is unsound). Combining a mature management system with sound corrosion protection technology is ideal for effective and efficient corrosion control of a steel structure [4].

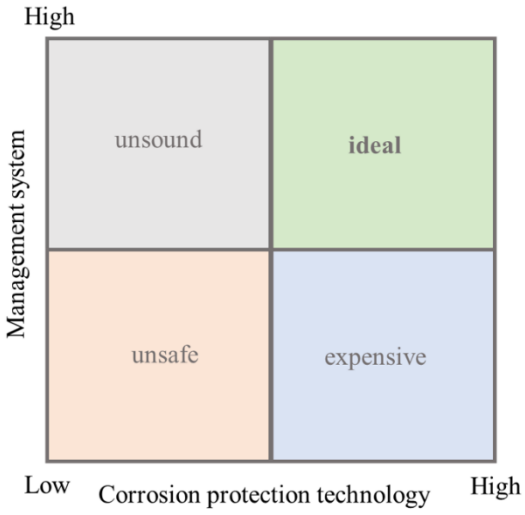

Figure 1.2 A two-by-two matrix depicting the benefit of combining a mature management system with a sound corrosion protection technology. Image adapted from [4].

Therefore, corrosion management in a system begins from the system´s policy, strategy, and objective of an organization to control the corrosion [4]. Risk management, documentation, training, communication, management review, and continuous improvement are critical factors in successfully monitoring and managing the corrosion

[4]. The output of these actions leads to the road map and a practical plan to combat the corrosion menace.

Practically, corrosion protection of steel is based on suppression, elimination, and control of those parameters involved in the corrosion. These practices start from i) design and material selection following by ii) electrochemical (cathodic and anodic) protection, iii) modification of environment (addition of corrosion inhibitor), and v) coating [21,22].

1.3.2 Design and Material selection

Design and material selection are preliminary but essential steps for corrosion prevention, and these two parameters seem to be interconnected [4,23]. In this respect, design may start from the production of an alloy by adding a different percentage of alloying elements to make them more resistive against corrosion and more competent for a particular application [23,24]. Alloying with various metallic elements improves iron and steel's corrosion resistance by forming a protective layer or densification of corrosion products [25–28]. For instance, addition of Chromium (Cr) to the steel improves the corrosion resistance of steel by forming a compact layer of Cr_2O_3 which protects the underlayer metal [27]. Another study showed that adding Cr and Cu to carbon steel promotes the formation of $FeCO_3$ as a protective corrosion product in the CO_2 environment and decreases the corrosion rate [26].

Moreover, addition of other elements like Al, Ti, V, Nb, Si, and Mo into carbon steel improves the corrosion protection properties of this alloy [24]. For the two latest elements (Si, and Mo), improvement of corrosion resistance due to the presence of these elements is a secondary effect [24]. However, the material selection for corrosion prevention depends on the corrosive environment, working temperature, expected lifetime, and the probability of employing the secondary corrosion protection methods (e.g., corrosion inhibitor, and coating).

An intelligent design also prevents corrosion or at least reduces the corrosion rate. The major design parameters affecting the corrosion rate are stress on the material during the service, the relative velocity of the medium, bi-metallic contacts, inhomogeneous surfaces, and sharp corners [23].

1.3.3 Cathodic Protection

Cathodic protection is an electrochemical process used to control the corrosion of a metallic structure surface, exposed to a conductive environment. Cathodic protection can be achieved by using a galvanic anode (sacrificial anode) or by impressing a current [29]. Using these methods, the structure's electrochemical potential value will fall down below the potential value of the protection criteria of (-800 mV) vs Ag/AgCl [30]. Cathodic protection by sacrificial anodes is achieved by connecting a less noble metal to the metal to be protected. For instance, Magnesium is employed to protect the steel in contact with soil, while Aluminum and Zinc are typically used to protect steel structures in contact with sea water [29]. The sacrificial metal then corrodes instead, generating a current to protect the metallic system.

A DC power source, which can supply current, with the positive pole connected to an anode (made of graphite or activated titanium) and a negative pole connected to the structure to be protected, can be used as an impressed current system [29,31].

1.3.4 Anodic Protection

Like Cathodic protection, anodic protection is an electrochemical technique used to protect metals that exhibit passivation. This method is used only when cathodic protection and other protective methods are not the preferred corrosion protection methods [32]. The technique is usually used to protect carbon steel storage tanks in an acidic environment, like sulfuric acid. The material to be protected should display an active-passive behavior, possess a wide range of passive potential, and have a very low passive current compared to the corrosion current [5,32]. Thus, the formation of a protective-insoluble oxide film results in corrosion protection of metallic structure by anodic polarization [32]. Adequate anodic protection depends on the quality of protective, insoluble oxide film, which is affected by the applied potential and environmental parameters [32].

1.3.5 Corrosion Inhibitors

Corrosion inhibitors are chemical substances or a combination of substances, that when added in a very low concentration into a corrosive media, effectively prevents or reduces the metal corrosion without significant reaction with the components of the environment [33]. Inhibitors play a critical role in closed systems such as cooling water recirculation

systems, oil production, and oil refining facilities, where a suitable and controlled inhibitor concentration is ensured [34]. Inhibitors can interact with a metallic surface to effectively reduce the corrosion rate [35,36]. Selection of corrosion inhibitors is a challenging task. Corrosion mechanisms and environmental parameters are the most important factors affecting a proper inhibitor selection. However, secondary factors like regulations, health issues, toxicity, disposal, and cost can complicate the selection of corrosion inhibitors [34,36]. Inhibitors can be classified according to their inhibition mechanism: anodic (or passivating) inhibitors; cathodic inhibitors, mixed inhibitors, and volatile corrosion inhibitors [36]. While the latest are considered out of scope of this work, others will be discussed in brief.

1.3.5.1 Anodic Inhibitors

Anodic inhibitors are generally oxidizing substances that react with the metallic ions produced at the anodic sites and provide corrosion protection by suppressing the anodic reaction. Anodic inhibitors should be available in the system above the specific critical concentration. To achieve anodic passivation, one or several mechanisms may be involved as following [36]: i) ability to shift the corrosion potential towards more positive values, therefore forcing the metallic surface into the passive range, ii) stabilization of passive oxide layers, iii) repair of damaged protective (oxide) layers, iv) enhancement of the passive ability by incorporation of species into the passive layer, v) decrease of the probability of absorption of aggressive ions, such as chloride ions, vi) formation of insoluble hydroxides which are deposited on the metal surface [37]. The most commonly used anodic corrosion inhibitors for steel are calcium nitrate, sodium nitrite, sodium benzoate, and sodium chromate [33].

1.3.5.2 Cathodic Inhibitors

Cathodic inhibitors, which commonly contain metal ions, can slow down the rate of the cathodic reaction in alkaline pH (due to hydroxyl release at the cathodic zone), raising the local impedance and hindering the diffusion of reducible species into these areas. These inhibitors work by different mechanisms that include: i) decreasing the reduction reaction rates (cathodic poisons), and ii) selective precipitation on the cathodic areas (cathodic precipitators). Well-known examples are rare earth elements, namely cerium cations, that can form stable hydroxides or oxides on the cathodic areas [36].

1.3.5.3 Mixed Corrosion Inhibitors

Mixed corrosion inhibitors are mainly organic compounds and can affect both anodic and cathodic reactions involved in a corrosion process. Thus, many of these inhibitors are more effective in suppressing redox reactions than the other reactions. This group of inhibitors can adsorb on the metal surface. The effectiveness of a mixed inhibitor depends on: i) the chemical composition and structure of the inhibitor, ii) the chemical structure and physical condition of the metal surface [36], and iii) the operational parameters like pH, temperature, and chlorine ion concentration [38]. Organic inhibitors like 8-hydroxyquinoline (8-HQ), salicylaldoxime [36], thiols (compounds containing -SH groups) [39], a large group of green corrosion inhibitors [38], surfactants [40,41], and ionic liquids [42] classify under the group of mixed inhibitors. A detailed review of the state of the art of effective corrosion inhibitors for steel will be presented later in subsection 1.4.4.2.

1.3.6 Coatings

One of the most suitable corrosion protection strategies is the application of coatings [43]. A coating acts as a physical barrier to isolate the metal from aggressive media or to functionalize the metal surface for corrosion protection [44]. Coatings for corrosion protection are generally classified into conversion coatings, inorganic, and organic coatings. Although in some classifications, conversion coatings are included in the group of inorganic coating, in the author's point of view, considering it as a separate subsection seems to be more convenient.

1.3.6.1 Conversion coatings

Conversion coatings (CCs) form as a consequence of the surface-based chemical reactions in which the metal surface and other ions present in a solution are involved [45]. Being a direct consequence of surface reactions differentiates a CC from other coatings. Hexavalent chromium (Cr(VI)) and phosphate treatments are probably the oldest and most economical choices of CC for the protection of carbon steel, and both can provide good adhesion and corrosion protection properties to the substrate [46]. Chromates-based conversion coatings are considered the most effective corrosion protection system for many metals and alloys [47]. In most cases, these coatings promote the formation of protective species by reaction of hexavalent chromium with the metallic substrate (for

example in Aluminum alloys it reinforces the passive film). In fact, oxidation of the metallic substrate produces electrons to reduce the hexavalent Cr of dichromate ion ($Cr_2O_7^{2-}$) that forms a protective hydrated three valence $Cr(OH)_3$ films [48]. This corrosion protective layer also improves the mechanical properties of the bare material. Despite of the promising self-healing properties of chromate-based coatings, due to major health issues and environmental hazards, the use of Cr(VI) containing compounds has been seriously restricted [47]. Therefore, most recently, a tendency towards the use of eco-friendly elements, has shifted the research streams in CCs toward the less toxic elements, namely: trivalent chromium (Cr(III)), molybdate, rare earth elements (e.g., Ce, La, Nb, Y), Ti, and Zr contains chemicals. These elements have been intensively studied as green CCs as reported elsewhere [45,49].

1.3.6.2 Inorganic coatings

Inorganic coatings are defined as the non-hydrocarbon-based coatings. Two groups of metallic and ceramic coatings fall into this subdivision. Essential metallic coatings for steel components are Cr-diffusion coating, Al-diffusion coating, and MCrAlY (M denotes for Ni, Co, Fe alone or mixture) coatings [50]. Anodizing, galvanizing, and thermal spray coating also fall in this group [51]. Ceramic coatings, known mostly as thermal barrier coatings (TBCs) also can provide corrosion protection against hot gases and molten metals, and meantime act as a thermal barrier to reduce the actual temperature of the metallic surface in contact with a hot environment up to the100 ^{o}C. The most important coating in this group is zirconia -7% yttria applied on top of the MCrAlY (M= Ni, Co, or NiCo) bond coat used for vehicle engines, gas turbines, and airplane components [50].

1.3.6.3 Organic coatings

Organic coatings are the most used coatings for protection of carbon steel, thanks to their inherent lightweight, abundance, flexibility, ease of processing, low ionic conductivity, flexibility to customize formulations for specific applications, and cost-effectiveness [44,52]. They can be divided into three main groups of: water-based, solvent-based, and 100% organic material [52]. The chemical formulation of these organic (polymeric) coatings, used for corrosion protection of steel differs from epoxy [53], polyurethane (PU) [54], polyvinyl [55], polyacrylate [56], polyester [57], polyolefin [58,59], alkyd [60] to silane-based coatings [61,62].

Generally, organic coatings can provide an efficient barrier layer between the environment and the corrosion-susceptible metal. Among these chemicals, epoxy-based coatings are widely used for corrosion protection of steel. Epoxies contain more than one epoxide group, which is the reactive group that enables polymerization and film formation [63]. The corrosion protection provided with an epoxy-based coating is a combination of two factors: a crosslinked epoxy polymer matrix with aromatic groups which form an excellent barrier to corrosion, and hydroxyl groups that provide strong adhesion to the metallic substrate [63]. However, the protective performance of these coatings can deteriorate over time due to their permeability to water, aggressive ions, and oxygen [52]. Therefore, many key strategies have been searched to mitigate this problem. The most used and probably oldest strategy to improve the performance of an organic coating is the application of multi-layer coatings. These multilayered coatings generally consist of a CC, a primer, and several topcoats (depending on application). In such a system, each layer has a specific role in protecting metallic substrate, namely reducing the diffusion of aggressive ions, humidity and UV, reducing the temperature on the metallic surface, and reducing the mechanical damage, among others [52,64]. Figure 1.3 shows a typical three-layer polyolefin (3LPO) coating used to protect pipelines in the oil & gas industry. This specific system is composed of a fusion-bonded epoxy with an approximate thickness of 150 µm as a corrosion protection primer, a co-polymer adhesive (125 µm) as a tie layer (avoiding any sharp and well-defined interface between primer and topcoat), and a thick layer (500 µm) of polyolefin (polyethene or polypropylene) as a topcoat [59,64].

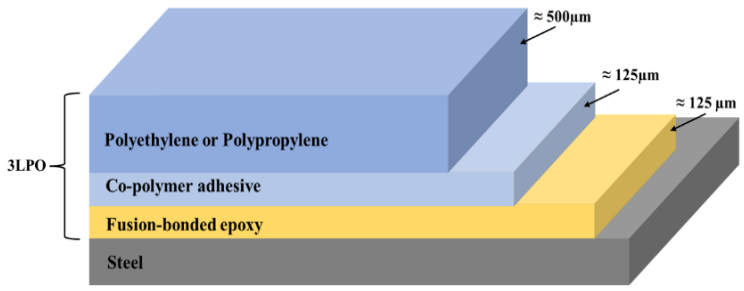

Figure 1.3 A simplified scheme of a 3LPO coating used in oil and gas industry for protection of steel. Information extracted from [59], and [64].

Although in such a multilayer system, each layer has its specific role in protection of the metallic substrate, every single layer can be irreversibly attacked by an external factor

[1]. Therefore, adding anti-corrosion pigments (corrosion inhibitors) to the primer layer is considered an excellent strategy to extend the lifetime of this coating system [44]. A wide range of corrosion inhibitors has been explored and suggested for carbon steel. Metallic flakes (i.e., zinc) [65], phosphates, carbonates [66], nitrates [67], silanes [68], amines [69], amides [70], and green inhibitors included, essential oils [71], surfactants [72], amino acids [73], ionic liquids [42], and rare earth corrosion inhibitors [72,74], among others. Although these inhibitive pigments can significantly improve coating functionality, early leaching of inhibitors may happen due to UV irradiation, matrix degradation, or other ageing events. Consequently, the protection properties of coatings can decrease drastically, leading to early and costly maintenances.

1.3.7 Self-healing coating

In the last decades, the concept of ”smart” and “self-healing” coatings has been gaining pace [1,44]. While the replacement of such a multilayer coating shown in Figure 1.3 with a one-layer smart coating seems impossible, the concept of self-healing can be applied to every single layer; therefore, a more sustainable protective system can be developed.
In polymer chemistry, the term “self-healing” is related to the filling up a gap by polymer, where the material was removed [75]. The same quality is expected for a self-healing coating and usually it refers to the intrinsic self-healing ability of a coating. In this case, repairing the polymeric matrix begins with ionomeric arrangements, molecular diffusion, or reversible hydrogen bonding without any external trigger [76]. The recovery of coatings´ functionality is also considered a self-healing property of a coating, which refers to the extrinsic self-healing ability of a coating [44]. The extrinsic self-healing strategy will be feasible by the addition of carriers like hollow glass fibers [77,78], capillaries [79], microcapsules (MCs) or nanocontainers [80,81], containing chemicals capable of recovering the coating´s functionality or to heal coating´s defects. Carriers may also be loaded with corrosion inhibitors to suppress the corrosion activities at the metallic surface.

1.3.7.1 Self-healing systems by recovery of coating functionality

The easier dispersion of microcapsules and nanocontainers in a polymeric matrix is an advantage of these systems over glass fibers and capillaries [76]. The encapsulation of polymerizable species into micro or nanocarriers, sensitive to external stimuli, has been

considered a viable and attractive smart route for introducing healing functionalities into the polymeric matrix [43,82]. Capsule-based self-healing materials are attracting the interest of the coating industries. They have been broadly investigated thanks to the versatility of available encapsulation technologies and a wide variety of active agents, which offer many possibilities to design self-healable coatings tailored for a specific purpose [83].

For the first time, the concept of self-healing based on MCs containing a self-healing agent was adopted by White et al. in 2001 [81]. The authors encapsulated Dicyclopentadiene (DCPD) monomer into a urea-formaldehyde (UF) shell. MCs then were added to the epoxy composite containing Grubb's catalyst. Whereby, mechanically rupture of MCs´ shell, released DCPD monomer, filled the crack, and polymerized in contact with the catalyst. The crack was healed, with a reported 75% recovery of the original strength of the epoxy composite [81] and improved later tile 90% by fine-tuning MC's size and catalyst percentage [84]. Although the DCPD-based/Grubb's catalyst self-healing system, was attracted tremendous attention toward the self-healing systems, two main shortcomings of this system can be addressed: i) Grubb's catalyst is costly and sensitive to temperature and humid conditions; ii) the dispersion of the relatively large MCs into the polymer matrix is not easy task, as the MCs tend to be aggregated in the polymeric matrix [76]. The same research group then developed another self-healing system based on the tin-catalyzed polycondensation of phase-separated droplets containing hydroxy polydimethylsiloxane and polydiethoxysiloxane. This time, the di-n-butyltin di-laurate, as a catalyst, was encapsulated, while a siloxane-based healing agent was incorporated into the vinyl ester matrix by phase separation [85]. The authors declared several advantages of the later system compared to the first one: simplicity, higher stability of healing agent inside the matrix, and the cost-effectiveness of the newly developed system. In another approach, they developed a self-healing system by encapsulating both the catalyst and the healing agent. From the authors' point of view, this latest system would be preferable to avoid early reaction of matrix with both catalysis and healing agent [86]. Salt immersion corrosion testing also showed that the last approach is the most promising among others [86].

Inspired by White et al. recent work, several other systems have been suggested. The new proposed systems are often based on the addition of two microcapsules: a healing agent and a curing agent or hardener. A dual-shell MCs like polyurea/polyurea-formaldehyde (PUa-PUF) also was suggested to overcome the problems of agglomeration [87,88].

A two-parts self-healing system based on epoxy as a healing agent, encapsulated in poly(methyl methacrylate) and encapsulated polyether amine as a hardener, was also reported by several groups [88–95]. Epoxy is cured in contact with amine and heals the polymeric matrix if only the temperature and time control appropriately [96]. The low chance of encountering both components at the defect site and the proper ratio to form a protective layer can be addressed as a main shortage of two-component self-healing systems [97].

Another branch of research was focused and is still focused on application of plant oils as a self-healing agent, namely linseed [98–103], and tung oil [104–106]. Being cost-effective and eco-friendly, these species are very attractive materials in this field. The encapsulation process can be easily achieved by using a surfactant, usually polyvinyl alcohol and a PUF polymer. Despite the promising self-healing ability of tung oil and linseed oil, illustrated by the salt spray test, the protective properties of intact coatings containing these types of MCs were reported to be reduced even by the addition of a low quantity (3-5 wt%) of relatively small (8-53μm) MCs [106,107].

Therefore, silane treatment, with ability to interact with both polymeric matrix and MCs´ outer shell was suggested to improve the mechanical properties of coatings modified with plant oil-filled MCs [108,109]. However, the very low drying rate of plant-based oils after releasing from MCs is considered a major drawback of these systems [76].

Another interesting approach, also proposed for the first time by White and his co-worker, was the encapsulation of isocyanate compounds as healing agents [110]. Encapsulation of isocyanates enables an autonomous self-healing system in water/moisture-containing environments due to the extreme reactivity of the isocyanate chemical group (NCO), which can form a chemical bond with any chemical group containing an active hydrogen atom (H). These MCs can also be triggered by mechanical pressure, release their core content, and protect the bare metal in contact with the aggressive environment by forming a protective polymeric layer over the defect [111].

A literature review revealed that the most relevant research works focus on the encapsulation of isocyanate compounds as self-healing agents, with particular emphasis to methylene diphenyl diisocyanate (MDI) [112,113], hexamethylene diisocyanate (HDI) [114–117] and isophorone diisocyanate (IPDI) [110,114,115,117–120]. While MDI-MCs have their application only in self-healing of cements and concretes [112,113], HDI-MCs, and IPDI-MCs are mostly incorporated in polymeric matrices (mostly epoxy), to protect steel.

Research into the encapsulation of HDI, and IPDI has gained pace in recent years, but just a few works report on the introduction of HDI-MCs [114,116,121,122], and IPDI-MCs [111,123,124] into polymeric matrices to develop smarter coatings. The healing performance of developed coatings containing different quantities of MCs were evaluated by salt spray or salt solution immersion tests, often in the presence of artificial scratches. For coatings which contain MCs, authors reported the successful filling of scratches thanks to the release of self-healing species from MCs; identical scratches made in reference coatings (without MCs) remained un-filled. This process is illustrated in Figure 1.4 [111].

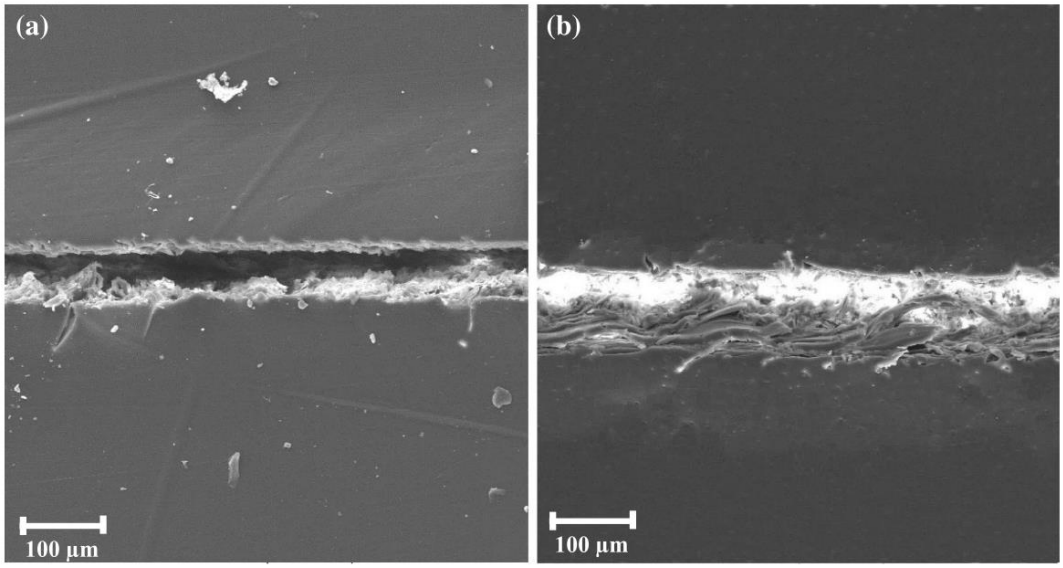

Figure 1.4 SEM micrographs of a scratched area: a) reference epoxy, b) epoxy coating containing 10 wt% IPDI-MCs. Image reprinted from [111] with permission.

Table 1.1 summarizes in detail the most relevant efforts made for the development of self-healing coatings by adding HDI-MCs and IPDI-MCs. Among these works, Haghayegh et al. comprehensively studied several systems by encapsulation of IPDI, and isocyanate-terminated prepolymer based on IPDI. They prepared MCs with various mean diameter, starting from 250 ± 18.1 µm and going down to the 45 ± 1.8 µm by increasing emulsification rate, quantity of solvent, and drastically increased in the amount of surfactant from 11 to 22 wt%.

Additionally, they developed several coatings by adding 1, 3, 5, 10, 15, and 20 wt% of IPDI-MCs into the epoxy coating. Several important results can be extracted from this work: i) the reduction of MCs´ diameter is a critical point in the development of self-

healing coatings, ii) the addition of a higher quantity of MCs to the polymeric matrix seems to favour of the self-healing ability of the coating, as the best healing performance was obtained by a system containing 20 wt% of MCs, iii) the addition of more than 5 wt% of MCs decreases the mechanical properties of the coatings drastically [121], probably due to formation of voids and aggregated particles, into the coating matrix, as reported elsewhere [125].

Table 1.4 Most important developed self-healing systems based on isocyanate-MCs.

No.	Coating	Healing Agent	MCs´ diameter (µm)	MCs added (wt%)	Reference
MC1	epoxy	HDI	106	10	[116]
MC2	epoxy	HDI	88 ± 22	10	[121]
MC3	epoxy	HDI	5-350	10	[114]
MC4	epoxy	HDI	57-328	10	[122]
MC5	epoxy	IPDI	75.8	15	[124]
MC6	epoxy	IPDI	40-87	Na	[126]
MC7	epoxy	IPDI	5-200	1, 3, 5, 10, 15, 20	[111,127]

Figure 1.5 summarizes several major issues that need to be addressed, particularly in the design of a self-healing coating by encapsulation of isocyanate-based species.

The self-healing agent should present low viscosity to flow easily into the defect and should be highly reactive to effectively heal the defect. MCs should be large enough (50-200 µm) to enable easy rupture and ensure high loading capacity [82]. However, in what concerns anti corrosion coatings, it is worth to stress that the size of MCs is constrained by the dry coating thickness and the size of the MCs shall be at least 3 times lower than that coating thickness. Additionally, MCs' shell is expected to fulfil additional requirements, most importantly: i) chemical stability during coating formulation and application, ii) enough rigidity to maintain integrity during mixing and application process, and iii) sufficient brittleness to allow rupture upon mechanical damage.

Therefore, considering that selection of a proper self-healing agent is the first step for the successful design of a self-healing coating, the second step would be to select a viable encapsulation route to meet the optimum properties of MCs (small MCs with a high

encapsulation yield). Moreover, MCs´ shell should satisfy all the conditions mentioned before as well as having the full compatibility with the polymeric matrix.

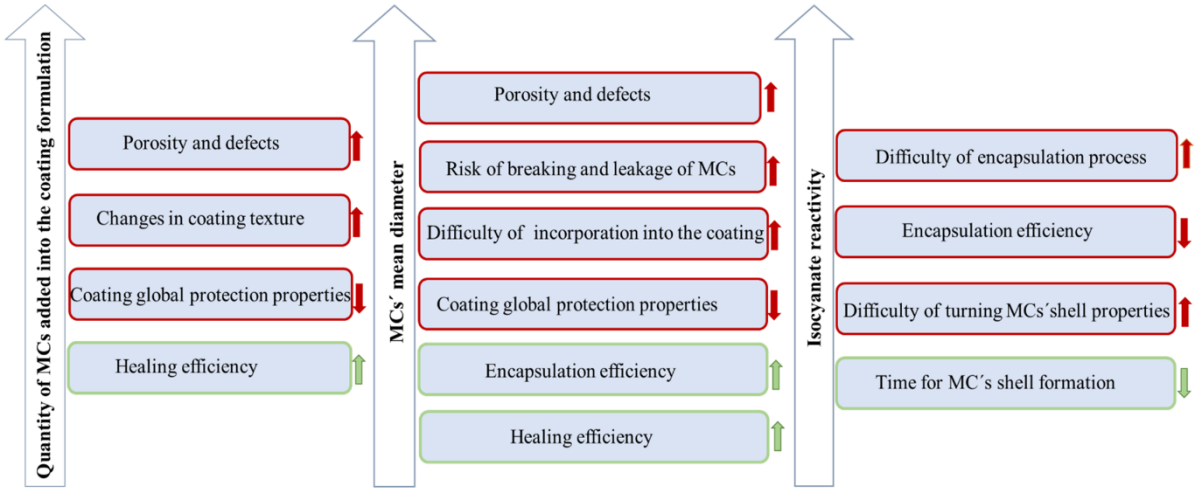

Figure 1.5 Issues that can be addressed in successful design of a self-healing coating.

In general, microencapsulation methods can be grouped into three major categories: i) physico-mechanical (e.g., spray-drying, and spray-congelation), ii) physico-chemical (e.g., supercritical fluid, coacervation, layer by-layer, sol-gel, and solvent evaporation), and iii) chemical methods (e.g., emulsion polymerization, in-situ polymerization, and interfacial polymerization) [128]. Selection of a certain microencapsulation technique is strongly dependent on the nature of the active reagent to be encapsulated, application, and expected properties of MCs [128]. Still, complexity, production capacity, and cost effectiveness of each method are other factors contributing to select the proper encapsulation method, as shown in Figure 1.6 [129]. Amongst the large variety of encapsulation techniques, interfacial polymerization is the most used technique for encapsulation of self-healing agents e.g., isocyanate [76]. In-situ polymerization and solvent evaporation have been also employed. Therefore, these three methods will be explained briefly here, while the detailed description of other methods can be found elsewhere [128,131].

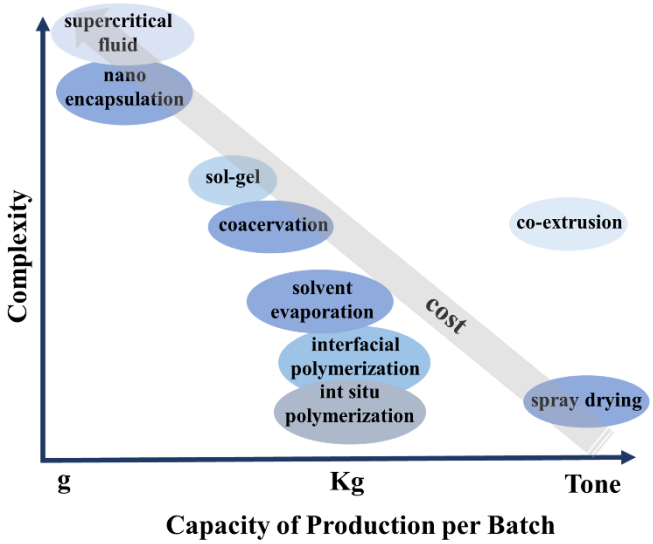

Figure 1.6 Comparison between the different encapsulation methods. Re-printed from [129] with permission.

In solvent evaporation technique, a polymer as shell former, together with the material to be encapsulated are dissolved in a volatile organic solvent like dichloromethane. The resulting emulsion, or solution, is dispersed in the water phase, composed of an aqueous solution including a proper stabilizer e.g., poly (vinyl alcohol) or polyvinylpyrrolidone, to form small polymeric particles, or core-shell capsules containing the encapsulated material. MCs' shells form during several hours when the system is left under mechanical stirring, by removal of the solvent from the polymer droplets [131]. Loureiro et al. reported encapsulation of IPDI in biodegradable, temperature-responsive poly(ε-caprolactone) (PCL), aimed to be applied as cross-linking agents for the development of green adhesives, which potentially can be used to provide self-healing properties [132]. The biodegradable PCL MCs were formed via the solvent evaporation method in combination with an oil-in-oil-in-water (O/O/W) double-emulsion system as shown in Figure 1.7 [132]. Despite of interesting approach to obtain high encapsulation efficiency (60 wt%), the large MCs´ mean diameter (225-525 μm), tendency of droplets to coalescence during the fabrication [132], and tendency to form polynucleated MCs [76], make this approach less interesting for designing self-healing coatings for corrosion protection.

Interfacial polymerization is one of the most important routes to fabricate isocyanate-based MCs. As compared to bulk polymerization, interfacial polymerization is a type of step-growth polymerization that takes place at the interface of two immiscible phases.

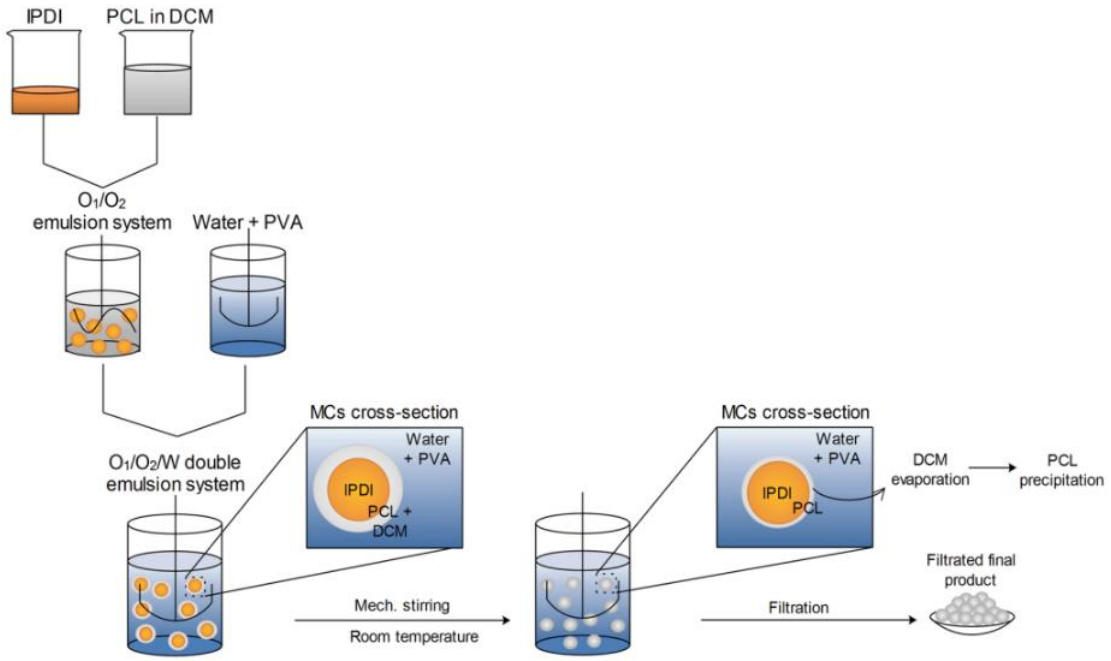

Figure 1.7 Schematic representation of the PCL MCs´ fabrication process. Image reprinted from [132] with permission.

Microencapsulation of isocyanate is typically achieved by an oil-in-water (O/W) microemulsion system combined with interfacial polymerization, which involves adding at least two reactants in a pair of immiscible liquids. One of the liquids is preferably an aqueous solution, forming the continuous phase (W phase) and the other, the dispersed phase, is composed of the isocyanate to be encapsulated and a shell former reagent (O phase). A suitable stabilizer (surfactant) is added to the continuous phase, preventing the droplets from coalescing or particles from coagulating during the polycondensation process. The two immiscible phases were then vigorously mixed to form a stable emulsion. Finally, MCs´ shell forms by diffusion of the reactants, which become in contact at the oil droplets' interface, followed by interfacial polymerization at the interface of both phases to form MCs (Figure 1.8) [128].

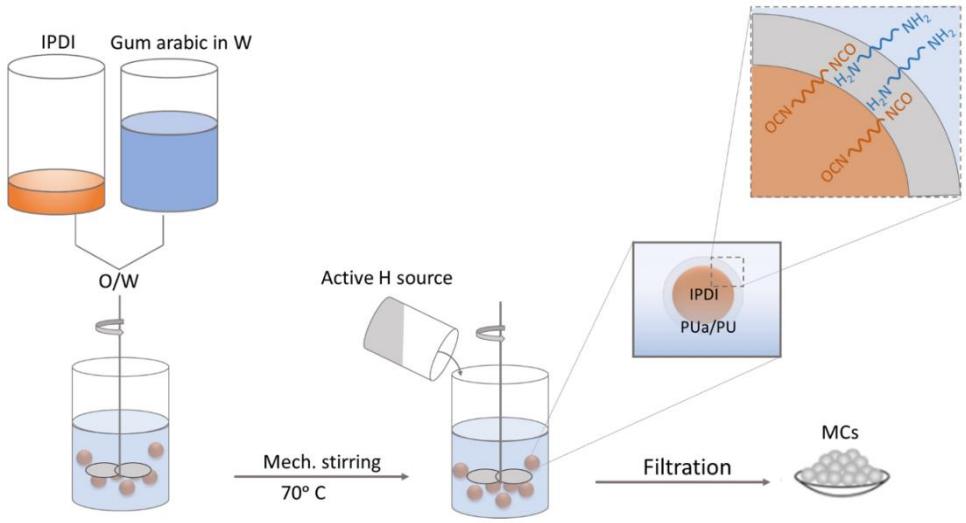

Figure 1.8 Schematic illustration of the IPDI-loaded MCs´ fabrication via O/W emulsion formation, following by interfacial polymerization.

In-situ polymerization technique is quite identical to the interfacial polymerization technique. In this technique monomers, which form the MC´s shell, are dissolved in continuous phase, and polymerization occurs at the core surface to form MC´s shell [76]. The major attempts to encapsulate isocyanate-based MCs have been made by one of these two latest methods. In most cases, encapsulation of isocyanate by interfacial polymerization ended in the formation of PU, and/or PUa shell-MCs [110,111,114,133]. However, a combination of interfacial polymerization and in-situ polymerization was also reported [112,118,130,131] and led to the formation of double layered MC´s shell, offering higher thermal and chemical stability, and a longer shelf life [134]. This approach still suffers from some of the drawbacks mentioned before: large MCs´ mean diameter, the tendency of droplets to coalescence during the fabrication, a tendency to form polynucleated MCs, higher complexity, and longer duration of synthesis in comparison with interfacial polymerization [76,132].

Recently, we reported high-loaded IPDI-MCs encapsulated in PUa/PU-silica hybrid shell, via O/W microemulsion combined with interfacial polymerization [135]. In that work, incorporating a multifunctional isocyanate silane (3-isocyanatopropyltriethoxysilane) (IPES), in the oil phase, as “latent” active H source, led to the formation of impermeable PUa/PU-silica hybrid shell MCs with more than 60 wt% of pure encapsulated IPDI. These PUa/PU-silica hybrid shell MCs with the mean diameter of 82 ± 7 µm exhibited approximately the same isocyanate content after three months, demonstrating an effective

barrier capacity of their shell, therefore long shelf-life of these MCs. Two more active H sources were tested on that work, namely diethylenetriamine (DETA), and combination of 3-(2-aminoethylamino)propyltrimethoxysilane (aminosilane) and tetraethyl orthosilicate (TEOS), both added to the continuous (W) phase, and showing promising results [135]. In another work, our group focused on the encapsulation of commercial MDI (Ongronat® 2500) and the effect of amine-based active H sources, namely ethylenediamine (EDA), aminosilane, branched poly(ethyleneimine) (PEI), and triethoxy(octyl)silane (n-OTES) was studied in terms of encapsulation efficiency, shelf life, and chemical and thermal stability of MC´s shell [136]. From this latest work, it is possible to conclude that the NH-based active H sources, EDA and PEI, were the ones that led to the achievement of higher encapsulation efficiency, possibly related to a faster shell formation. However, the best overall performance was achieved by combining the PEI and the silane n-OTES, obtaining MCs with bimodal size distribution with the maximum at 75, and 146 µm, and a shell thickness of 15.86 ± 2.09 µm [136].

Knowledge, we obtained from these recent works encouraged us to go beyond the state of the art and try to design small and highly efficient MCs targeting coatings for corrosion protection.

To summarize, self-healing species encapsulated by polymeric, or hybrid shells can partially or totally recover the protective properties of the organic coatings by releasing the healing agent mostly in response to mechanical pressure. Among various self-healing agents, isocyanate-based ones are considered some of the most promising ones and interfacial polymerization is considered a viable, fast, and flexible method to encapsulate these compounds. Although some reversible healing systems have been reported [135], in most cases, the healing agent is typically released in a single event and can block the pathways of corrosive species partially. However, this repaired polymeric protective layer always contains pores and small defects that serve as paths for the diffusion of electrolyte and corrosive ions, which can reach the metallic surface. Thus, the coating's protective properties need to be further enhanced by adding corrosion inhibitors.

1.3.7.2 Self-healing systems targeting the corrosion inhibition

To suppress corrosion activity at the coating-metal interface often the corrosion inhibitors are directly added to the polymeric matrix. These systems are still considered self-healing, since the corrosion protection functionality of the coating is recovered [97]. A wide variety of corrosion inhibitors like organic compounds [137], chromates and inorganic

complexes [138] are proposed for corrosion protection of steel and intensively reviewed elsewhere [137,138].

Among wide variety of organic compound reported as corrosion inhibitor, 8-HQ [139,140], 2-mercaptobenzothiazol (MBT) [141,142], benzothiazole (BTA) [143,144], tannic acid (TA) [145,146], molybdate ion [147,148], amines [92,149,150], and surfactants [72], were reported as effective corrosion inhibitors for steel and some other alloys. Organic inhibitors form a protective film over the metallic surface by offering their free lone pair of electrons to the vacant orbital of the metal ion [137]. Some of them, like surfactants, are composed of a polar head which interacts with the metal surface and a hydrophobic group that extends away from the surface and that can form an additional protective layer against the diffusion of aggressive species [137]. Although direct addition of organic inhibitors is an effective way to enhance corrosion protection properties of organic coatings, this approach suffers several drawbacks, mainly leaching or fast depletion of the corrosion inhibitor [97], possible side reactions between polymeric matrices and inhibitors (e.g., amine inhibitors within epoxy resin) [151], and poor distribution of low-soluble corrosion inhibitors within polymeric matrix [152].

Inorganic materials like metal oxides, metal nano powders, nitrides and carbides, and nano-calcium carbonates have significant potential to act as corrosion inhibitors, enhancing polymer coatings' barrier performance [138].

Metallic nanoparticles (NPs) such as Zn, Ti, and Al with corrosion potential more negative than steel substrates can provide sacrificial protection and barrier protection for steel substrates. When Zn NPs are added to the epoxy coatings, the corrosion resistance significantly improves by enhancing the cathodic protection performance of polymer coatings [153]. Nano-Ti powder enhances the barrier properties of organic coatings by decreasing the diffusion coefficient and decreasing the permeation of corrosive ions in the organic coating matrix [154]. Nano-Al, when added to the epoxy coatings, can provide multiple effects and enhanced barrier performance. Initially, nano-Al decreases the coating porosity and the diffusion of corrosive agents inside the polymeric coating. Then after diffusion of corrosive ions through the coating, Al particles participate in the electrochemical reactions and can provide cathodic protection. Finally, Al corrosion products such as hydroxide and oxide of Al are formed and precipitate within the coating pores and act as a barrier against further diffusion of corrosive agent [155,156].

Various metal oxides such as SiO_2, TiO_2, Al_2O_3, ZnO, ZrO_2, CeO_2, and iron oxides (Fe_2O_3/Fe_3O_4) have been used as anti-corrosion nanofillers in polymeric coatings. In the

first place, most of these compounds, when incorporated into the polymeric matrix, act as a filler and can physically delay the diffusion of corrosive ions by creating a longer diffusion path [138]. Moreover, they significantly improve the mechanical, thermal, and physicochemical properties of organic coating, e.g., UV resistance and wear resistance [157,158]. SiO_2 improves organic coatings' mechanical strength, hydrophobicity, and thermal and chemical stability [159]. Nano-sized TiO_2 possess unique photocatalytic activity and ability to absorb UV light. Therefore, titania has excellent potential for developing anti-UV, anti-bacterial, self-cleaning coating [160]. Al_2O_3 is a hard material and is mainly used to enhance the abrasion resistance of polymeric coatings [161]. ZnO_2 is commonly used in the polymeric matrix to achieve higher hardness, lower refractive index, and improved hydrophobic coating properties [162]. ZrO_2 adds to the polymeric matrix to improve the fracture toughness, wear resistance, and hardness [163].

CeO_2 is a rare earth metal oxide with unique properties, including electrical and optical performance, low water solubility, and high corrosion resistance. Due to the particular importance of this specific rare earth metal oxide in the structure of this PhD work, an intensive review of state of the art will be presented later in the subsection 1.3.7.2.3.

In general, addition of nano-sized oxides to organic coatings improves the corrosion protection properties due to an enhancement of the coatings' barrier performance, increasing water contact angle, increasing adhesion strength at the coating/metal interface, sacrificial protection, and passive layer formation [138,159–163]. Although adding nano-sized inorganic spices (metals and metal oxides) seems to be an interesting approach for improving the protection properties of organic coatings, homogenous dispersion of these particles into the polymeric matrix is a challenging task, and aggregation of NPs is inevitable [138]. Functionalizing the NPs with surfactants, amines, silane, etc., on the one hand considered to be a good solution to have a better dispersion of NPs inside the organic coatings [138,164], and on the other hand, can create a synergistic effect [165], as some of these chemicals by themselves, known as organic corrosion inhibitor [72,150,166]. Moreover, the same approach can be used to create a smart inhibitor system by loading the organic corrosion inhibitor inside or around the nanocarriers, avoiding the leaching of organic corrosion inhibitors and the possible reactions between polymeric coating and inhibitors. In such a smarter system, the inhibitor can be released in response to a specific stimulus where and when corrosion starts, creating a smarter, more controllable and more sustainable anti-corrosion solution [167]. Several approaches can be tackled to design a stimuli-activated system: pH-

response, temperature-response, light-response, pressure-response, and ion-exchange-response, among others. Each system has its advantages and drawbacks, and its application determines the appropriate approach for creating a stimuli-activated system for corrosion protection. The main mechanisms to consider when designing a stimuli-response system for inhibitor activation/release are pressure-response, ion-exchange-response, and pH-response systems, which are discussed below.

1.3.7.2.1 Pressure-response system

Encapsulation of self-healing agents inside e polymeric or hybrid shell capsules was already discussed in subsection 1.4.4.1. The same approach was reported to encapsulate corrosion inhibitor, most commonly into the UF containers [168,169]. When a defect occurs in the coating, the capsule breaks and releases the inhibitors at the defect site. Also, the system's internal pressure may increase by swelling of the polymeric matrix due to the diffusion of corrosive ions [167], breaking the capsules. Marathe and Gite [168], reported that encapsulation of 8-HQ in phenol-formaldehyde (PF) and UF containers, improved the corrosion protection properties of PU. They reported a more sustainable release of inhibitor and better performance of PF-MCs due to smoothest MC´s shell compared to UF-MCs [168]. Farzi et al. [169] reported encapsulation of cerium nitrate in PUF-MCs. Cerium ions (Ce^{+3} and/or Ce^{+4}) were released from PUF-MCs once the damage occurred in the epoxy coating. The healing of the damaged zone was achieved by forming cerium hydroxides and/or cerium oxides in the scratched area. These protective layers can hinder corrosion activity, healing the active areas in the scratch [169]. Although this approach is quite interesting for certain healing species, it is less Interesting for corrosion inhibitors. The reason is that MCs containing inhibitors are homogeneously distributed inside the coating and not preferentially close to coating/substrate interface, where the corrosion is start and where the inhibitor is needed.

1.3.7.2.2 Ion-exchange response system

Layered double hydroxides (LDHs) or hydrotalcite-like structures have recently gained pace in self-healing smart systems, especially since the banning of chromate-based inhibitors [170,171]. LDHs are composed of positively charged mixed metal hydroxide layers, balanced by the presence of both water molecules and anions between the inter-

galleries. High surface area, high thermal stability, homogenous structure, highly tunable structure, and the ion-exchange properties of LDHs make them a good candidate to intercalate corrosion inhibitors and to release them "smartly" in response to the corrosion-related events, i.e., change in pH, diffusion of OH^- ions, and/or presence of aggressive species such as Cl^-. In general, the performance of LDHs involves i) the capture of corrosive ions, ii) release of the inhibition anions, and iii) development of the protective metal hydroxide layer at the cathodic sites, as shown in Figure 1.9 [170,171]. Wang et al. [172] assembled an organic-inorganic composite containing Zn-Al LDHs and benzoate anions as an inhibitor. They reported a significant reduction in the corrosion rate of Q235 carbon steel when benzoate anion intercalated Zn-Al LDHs were added to the corrosive medium, revealed by the EIS and polarization curve. Authors claimed that the leaching of benzoate anions occurred by an exchange mechanism (release of inhibitor and entrapment of Cl^-), demonstrated by X-ray Diffraction (XRD), and Fourier Transform Infrared Spectroscopy (FTIR) analysis of samples recovered from release medium [172]. Deip et al. [173] used the same approach to load BTA into the Zn-Al-LDHs. The inhibitor delivery from LDH-NPs was confirmed by UV-Visible spectroscopy (UV–Vis spectroscopy).

Moreover, Electrochemical Impedance Spectroscopy (EIS) measurements showed 4.5 times increase in polarization resistance, for the carbon steel immersed in a saline solution when 5 wt% of LDH-BTA particles were added directly to 3.5 wt% NaCl solution. EIS also confirmed the enhanced corrosion protection properties of epoxy primer, when modified with 5 wt% of LDH-BTA [173]. Two major shortages were reported by Liu et al. [174] for ion-exchange response systems: i) the small interlayer spacing, and ii) a strong interaction between hydrotalcite layers and interlayer anions. These drawbacks can restrict the use of macromolecular chemicals to be loaded and released in the ion-exchange approach [174]. Therefore, the authors suggested a combination of delamination and self-assembly of LDHs´structure to increase their loading capacity. As a result, they successfully loaded -5-Methyl-1,3,4-thiadiazole-2-thiol into the LDH. The effective inhibition of corrosion of mild steel was confirmed by electrochemical techniques (EIS, Open Circuit Potential (OCP), and polarization curve) [174]. Likewise, LDHs, Javidparvar et al. [175] reported the ability of graphene oxide sheets doped with cerium nitrate to release the cerium cations by ion exchange. The authors stated that the cerium species, which were physically and chemically adsorbed on the nanosheets, could

not easily leave the host, and the ion exchange mechanism led to the liberation of cerium cations in the NaCl saline solution [175].

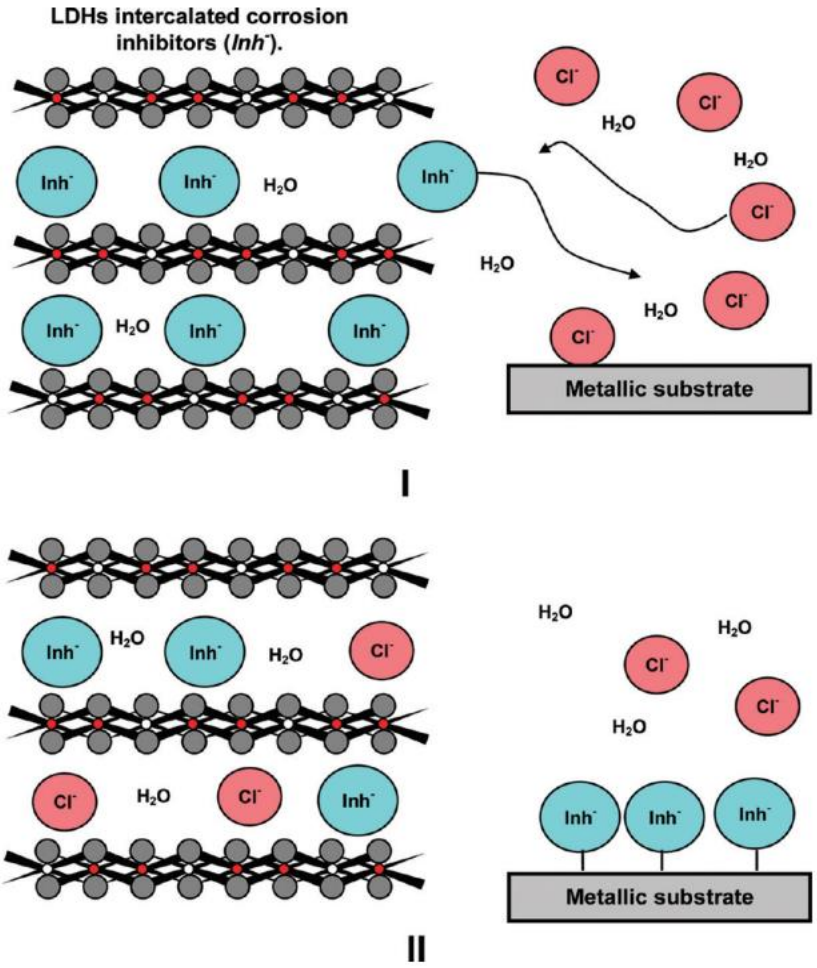

Figure 1.9 Schematic representation of self-healing performance of LDHs, (I) the release of inhibitors (Inh^-) is triggered by the presence of anions in solution (Cl^-). (II) LDHs play a double role, providing inhibitors to protect the metallic substrates and entrapping aggressive species from the environment. Image adapted from [172] with permission.

Despite being an interesting approach, LDHs loaded with inhibitors have been mainly used for corrosion protection of steel reinforced concretes, as LDHs, besides their ability to carry corrosion inhibitors, can also improve the mechanical properties of concrete [176–179].

1.3.7.2.3 pH-response system

Generally, corrosion of steel is accompanied by local pH fluctuations. The oxygen reduction at the cathodic sites (Eq.1.3) leads to local alkalization, while the iron

dissolution (Eqs1.1, and 1.2) at the anodic sites leads to local acidification. Therefore, fluctuation of pH values at the corroded micro-zones can be considered a typical feature of corrosion and it can be used as a stimulus to design a control-release smart self-healing system. Numerous approaches have been reported for the successful design of pH-response system. Polymers with pH-sensitivity, like UF [180], polyaniline nanofibers [181], chitosan [182,183], and Eudragit® [184] can be used to encapsulate the corrosion inhibitors.

For some pH-sensitive MCs, incorporating a specific group into the MCs´ shell can provide the pH sensitivity into MCs. For instance, the ester group can be hydrolyzed in acid and alkaline environments. The prior hydrolysis of this group opens the MCs´ shell and releases the encapsulated inhibitor [185].

The pH-dependent performance of the chitosan biopolymer can be explained by electrostatic repulsion between its chains, caused by protonation in acidic environments, which results in a more open conformation of the polymer layer and release of the inhibitor. However, at pH higher than 6.5, the presence of more hydroxyls causes deprotonation of chitosan's amine groups, so the chains contract and bend, preventing the release of inhibitor [186].

Polyelectrolyte molecules are sensitive to pH changes, with ‘‘open’’ or ‘‘close’’ state by ‘‘swelling’’ to break the shell layer or ‘‘shrinking’’ to recover to the original state, respectively. In fact, the increase/decrease in the local pH can deprotonate/protonate the polymer molecules for improved swelling or accelerate their hydrolytic degradation [187], which both result in enhanced inhibitor release. Nano-sized fillers like hybrid halloysite tubes (HHNs) [188,189], SiO_2 [187], Zeolitic imidazolate frameworks (ZIFs) [142,190], graphene sheets [142,191,192], carbon nanotubes (CNT) [183,193] and natural materials like Attapulgite [194] can be used as reservoirs to design smarter pH-sensitive systems.

The work of Wang et al. [195], which reported the fabrication of hollow mesoporous zirconia nanospheres (HMZSs) by sol-gel, loaded by L-Carnosine (L-CAR) as corrosion inhibitor, probably is the most interesting and is a pioneer work of the kind. The smart nanocontainers, loaded with L-CAR, exhibit acid/alkaline responsive, controlled release property, and the maximum release occurs at pH = 11 [195]. The smart nanocontainers were incorporated into water-borne epoxy coating to protect carbon steel. EIS, Scanning Vibrating Electrode Technique (SVET), and salt spray tests, confirmed the enhanced corrosion protection properties and self-healing ability of the modified coatings.

Haddadi et al. [196] employed the same approach to synthesize carbon hollow spheres (CHSs) using the silica templating method, to be loaded with 2- mercaptobenzimidazole (MBI) inhibitor. The pH-responsive release of MBI from CHSs was observed at pH =11. Electrochemical techniques confirmed a high potential of MBI-doped CHSs for corrosion inhibition of mild steel [196].

Using a facile one-pot method, Yang et al. [197] designed a pH-responsive hydrophilic controlled-release system (BTA@ZIF-8@TA (ZBT)) based on ZIF-8. The ZIF-8 particles were loaded with both BTA and TA as corrosion inhibitor, and loaded particles were further introduced to waterborne epoxy for corrosion protection of carbon steel [197]. When corrosion occurred, both inhibitors were released from ZBT in response to pH gradian. The absorption of BTA at the metallic surface and the formation of a stable ferric tannate layer protect the steel from an aggressive environment. Another research group used the same approach to successfully load Benzimidazole (BI) as a corrosion inhibitor into ZIF-7 NPs [198]. Besides the improved corrosion protection properties of coating modified with BI loaded ZIF-7, authors claimed a higher loading capacity of ZIF-7 in comparison with other similar systems fabricated by halloysite clay nanotubes or silica NPs [198].

Li et al. [142] also fabricated MBI loaded ZIF-8 on graphene oxide (GO) nanosheets as pH-responsive particles to impart the self-healing performance into the epoxy coating. UV–vis spectroscopy and SEM analysis of residual products of MBI-ZIF-8/GO in pH = 4, 7, and 10 after 24 h immersion, confirmed fast and easy decomposition of ZIF-8 particles in acidic condition at (pH = 4) (Figure 1.10a, and b). Therefore, a quick and maximum release of MBI in acidic condition was confirmed. Authors reported the slow-release rates of MBI in neutral and basic condition, due to the good stability of M-ZIF-8/GO in neutral and basic pH (Figure 1.10a, c, and d). Authors also reported higher physical barrier properties of coating modified with GO nanosheets and claimed that GO nanosheets can slow down the penetration of corrosive ions to the steel surface [142].

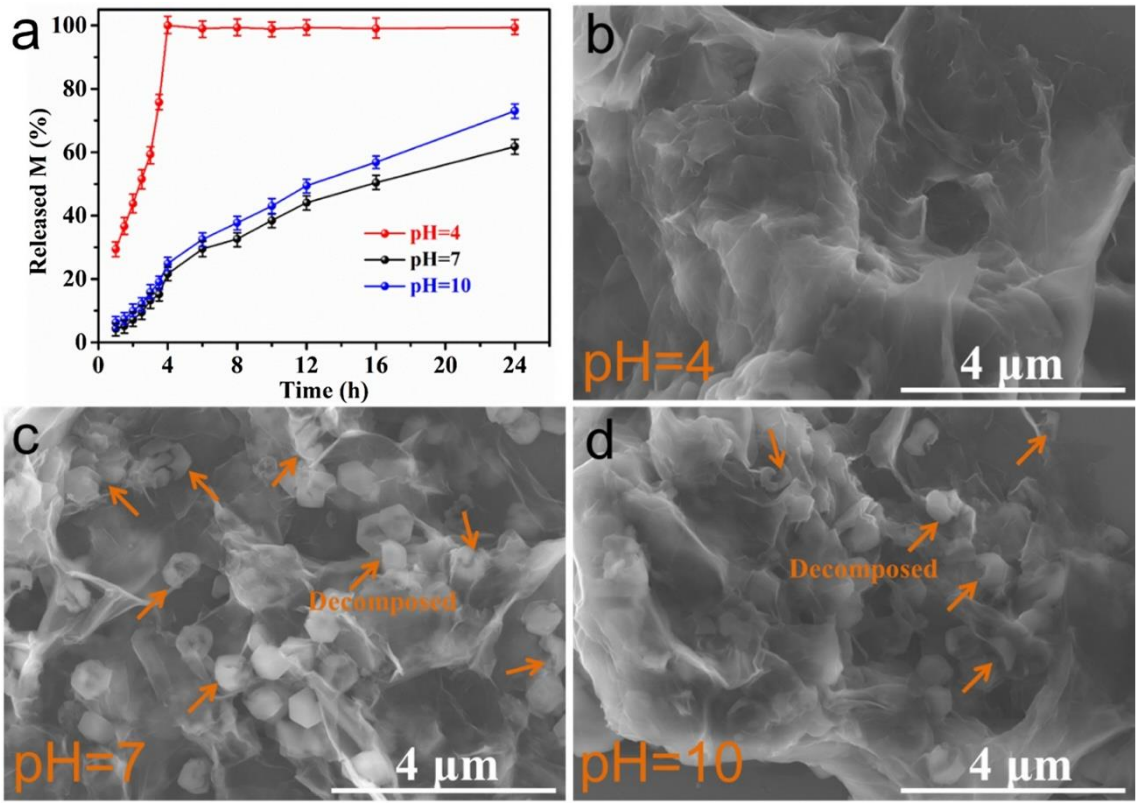

Figure 1.10 a) The release curves of MBI in M-ZIF-8/GO under different pH environments; Residual products of M-ZIF-8/GO in (b) pH = 4, (c) pH = 7, (d) pH = 10 after 24 h release. Image reprinted from [142] with permission.

Mesoporous silica nanoparticles (MSNs) have also been suggested as candidates for fabricating pH-sensitive self-healable coatings. Wen et al. [199] reported carboxyl-functionalized MSNs, loaded by BTA molecules, wrapped by the highly branched PEI to obtain nanocontainers composed of BTA@MSNs-COOH-PEI. These NPs were incorporated into an epoxy coating. UV–vis spectroscopy confirmed the pH-response release property of BTA@MSNs-COOH-PEI, which showed the accelerated release of BTA in alkaline conditions. Finally, the active anti-corrosion performance of the coating modified by 4, 8, and 12 wt% of BTA@MSNs-COOH-PEI was confirmed by EIS measurements and salt spray tests [199]. The same research group also developed a hybrid hydrogel of poly (hydroxypropyl acrylate – vinyl-triethoxysilane – acetic acid)/ polyethyleneimine (PHVA/PEI) pre-loaded with BTA (BTA@PHVA/PEI), through one pot free radical polymerization [200]. The authors demonstrated the pH dependence of the BTA-releasing behavior, with a maximum (91.02 wt%) release at pH = 11. The enhanced corrosion protection and self-healing ability of composite coatings, prepared by incorporation of 5, 10, and 15 wt% of BTA@PHVA/PEI into the alkyd resin, was also

confirmed by EIS and salt spry tests [200]. Feng et al. [187,201] also reported a pH-response SiO_2-based multi-layer self-healing system fabricated via layer-by-layer deposition of poly-(styrene sulfonate) (PSS), and poly-(diallyldimethylammonium chloride) (PDDAC), loaded with BTA. Authors reported the self-release of BTA from the nanocontainers in response to changes in solution pH, specifically in acidic and alkaline pH values (pH = 2 and 11). They claimed that nanocontainers remain ‘‘closed” at near-neutral pH and the inhibitors would not release [187,201].

A similar approach was also reported to develop the pH-response systems using HHNs loaded with imidazole (IM) and dodecylamine (DDA) [188], and natural 1D attapulgite reservoirs loaded with BTA [194],

$CaCO_3$ particles have been reported to be pH-sensitive, which can only decompose under acidic conditions [202]. Wu et al. [203] designed a pH response system by loading BTA within $CaCO_3$ microspheres (BTA-CaCO3) using a co-precipitation method. The BTA-$CaCO_3$ particles then were modified by TA via rapid blending to obtain BTA-CaCO3@TA. A maximum release of 90.53 % was observed at pH = 4.5 by partial decomposition of $CaCO_3$, while at pH = 6.5, only 1.02 % of BTA was released from the BTA-CaCO3@TA microspheres [203]. Raj et al. also reported the ability of $CaCO_3$ loaded with PEI [66], and (PEI + triethanolamine) [69] to suppress the corrosion propagation of carbon steel. The authors incorporated $CaCO_3$-amine-loaded particles into an epoxy coating. The enhanced protection properties of the modified coatings was confirmed by EIS, while SVET, and LEIS proved the self-healing ability of the modified coatings.

As mentioned earlier, CeO_2 is an inorganic filler that can physically hinder the diffusion of aggressive ions into organic coatings. Calado et al. [204] reported on the corrosion inhibition properties of CeO_2. A ceria modified hybrid siloxane-based coating was applied on magnesium alloys, and it was found to be more protective compared to the un-modified coating. The authors reported the enhanced protection properties driven by the fact that CeO_2 can stabilize the corrosion products by formation of a Ce-rich oxide layer [204,205]. Only very few works have investigated the role of CeO_2 NPs as corrosion inhibitors or as carriers of corrosion inhibitors for corrosion protection of steel.

Montemor et al. [61] incorporated CeO_2 NPs loaded with cerium ions into silane coatings applied on galvanized steel to improve the barrier properties of the coatings. The authors studied the combined effect of ceria and cerium ions. They demonstrated that this combination creates a synergistic effect that significantly enhances the corrosion

inhibition capability of thin hybrid silane films. This was evidenced by the decreasing trend in the current density detected by the SVET probe, from 60 µA/cm^2 to 10 µA/cm^2, following the addition of blank CeO_2 NPs to the reference coating. Furthermore, the reduction was even more evidenced for the coating modified with CeO_2 NPs treated with cerium ions, and the current density approached values close to zero [61,206]. Ramezanzadeh et al. [207] studied the role of CeO_2 NPs on the corrosion protection properties of a melamine-cured polyester resin to protect steel. They concluded that the addition of CeO_2 NPs led to high adhesion, better corrosion protection performance, and lower cathodic delamination rate under dry and wet situations [207]. The same group proposed using graphene oxide (GO) nanosheets functionalized with polyaniline (PANI) nanofibers and CeO_2 NPs to modify epoxy coatings for corrosion protection of carbon steel [192]. The results revealed that both barrier and corrosion inhibition properties of GO nanosheets were enhanced by the deposition of PANI and CeO_2 [192]. Harb et al. [208] synthesized organic-inorganic hybrid coatings consisting of poly(methyl methacrylate) covalently bonded to CeO_2/Ce_2O_3 NPs by the sol-gel process. They reported the high anticorrosive efficiency and durability of the ceria modified coatings that was confirmed by impedance modulus up to 8 orders of magnitude higher than the bare carbon steel [208]. Recently, Nawaz et al. [72] reported an improvement of the corrosion protection properties of an epoxy coating modified with CeO_2 NPs loaded with gum Arabic (GA) as an eco-friendly corrosion inhibitor. The overall protective properties of the modified coatings were reported to be in the order of 10^9 Ω cm^2 after 15 days of immersion in NaCl solution, being four orders of magnitude higher compared to the reference epoxy coating [72].

Cerium-containing compounds, i.e., cerium salts, also have been reported as effective inorganic inhibitors [61,192,207–213]. When added to organic coatings, they typically provide cathodic corrosion inhibition by the formation of insoluble cerium oxides and hydroxides due to the reactions of Ce(III) and Ce(IV) ions with OH^- ions formed due to oxygen reduction at the cathodic sites [192,206,214]. The formation of insoluble oxide/hydroxides blocks the cathodic sites and hinders the progress of corrosion. In fact, stable Ce-containing corrosion products form in alkaline conditions [61,205], therefore the protection performance of cerium salts can consider to be pH dependent. More recently, cerium tri(bis(2-ethylhexyl)phosphate ($Ce(DEHP)_3$) as corrosion inhibitor was proposed for corrosion protection of magnesium alloys [215,216], and mild steel [217]. The new developed cerium organophosphate corrosion inhibitor was shown to be pH-

sensitive, with the ability to respond in acidic and alkaline pH conditions, releasing Ce^{3+} cations and bis(2-ethylhexyl)phosphate (DEHP) anions. While Ce^{3+} ions combine with OH^- at the cathodic sites, forming stable $Ce(OH)_3$, and supressing the local cathodic activity, DEHP anions may react with the metallic cations (Mg^{2+} or Fe^{2+}) at the anodic sites, forming protective complexes [215–217]. The phosphate group may also precipitate at the metallic surface to form a protective insoluble bis(2-ethylhexyl)phosphoric acid [217]. The authors stated that a threshold local pH value is necessary to activate $Ce(DEHP)_3$ [204,216].

The most important examples of pH controlled self-healing systems reported for steel are summarized in Table 1.5. The pH stimulus is considered the most reliable one for corrosion protection of steel, as local pH variations are intrinsically associated to local anodic and cathodic activity. It worth mentioning that some authors employed two or more approaches or encapsulated both healing agents and corrosion inhibitors to enhance the self-healing ability of carriers disperse in the coatings [182,183,186,188,218].

In fact, the aim of various self-healing strategies can differ and thus the approaches to reach the goal varies. Each approach may have advantages (such as fast healing, autonomous healing, triggered healing, etc.) and shortages (such as complex scale-up, etc.) [219] and therefore there are still many open questions to enable these systems and to upscale them.

Table 1.5 Summary of most relevant work regarding the application of pH response carriers for smarter, self-healing coatings on steel.

No.	Carrier	Corrosion Inhibitor	Coating	pH for maximum release	Reference
S1	HMZS	L-CAR	epoxy	10	[195]
S2	ZIF-8	BTA/TA[b]	epoxy	5, 10	[197]
S3	ZIF-8/GO[a]	MBI	epoxy	4, 10	[142]
S4	ZIF-7	BI	epoxy	decrease in pH due to corrosion	[198]
S5	UF/Chitosan/Alginate[a]	BTA/Linseed oil[b]	epoxy	3	[186]
S6	UF/PEI/PSS[a]	BTA/Linseed oil[b]	epoxy	5.7	[218]
S7	PHVA/PEI[a]	BTA	epoxy	11	[200]
S8	$CaCO_3$	BTA/TA[b]	epoxy	4.5, 5.5	[203]
S9	$CaCO_3$	PEI PEI/TEA[b]	epoxy	change in pH due to corrosion	[66,69]
S10	HAP	Ce-ions	polyolefin	change in pH due to corrosion	[220]
S11	Mesopores cerium oxide/Eudragit[a]	MBI	epoxy	3	[184]
S12	MSN-COOH	BTA/PEI[b]	epoxy	11	[199]
S13	SiO_2	BTA	epoxy	2, 11	[187,201]
S14	SiO_2/Chitosan[a]	BTA	na	LBL@3 MC@7	[182]
S15	Multiwall CNT/Chitosan[a]	DPA/Chitosan Zn cations[b]	epoxy	3, 11 3	[183]
S16	CHS	MBI	na	11	[196]
S17	HHNT	IM/DDA[b]	epoxy	2	[188]
S18	HHNT	BTA MBT	epoxy	decrease in pH due to corrosion	[189]
S19	Graphene sheet	BTA	epoxy	10	[221]
S20	Graphene sheet	BTA	epoxy	decrease in pH due to corrosion	[222]
S21	Graphene sheet/PANI[a]	CeO_2	epoxy	decrease in pH due to corrosion	[192]
S22	CeO_2[c] SiO_2	cerium nitrate	Sol-gel	alkaline pH	[61]
S23	CeO_2	GA	epoxy	decrease in pH due to corrosion	[41]
S24	CeO_2/Ce_2O_3	na	PMMA	decrease in pH due to corrosion	[223]
S25	na	$Ce(DEHP)_3$	epoxy	change in pH due to corrosion	[217]

a) authors combined several approaches to make an effective carrier
b) authors used mixed inhibitor or combination of various approaches to load the carriers
c) formation of stable oxide/hydroxide and reduction of Cl^- ions were stated by authors

1.4 Methodology to meet the goals

Along chapter 1 the most recent efforts to develop self-healing coatings for corrosion protection of steel, specifically carbon steel, were overviewed. It has started from pioneer works and discussed most effective approaches in the kind. A critical review of the most relevant works regarding self-healing of polymeric matrices, show that lack of global protection properties of organic coating, and creation of new defects due to addition of relatively large MCs, are knowledge gaps in this field. Therefore, the first part of this PhD work is dedicated to find a solution for these issues. In particular, development of small size, highly efficient, thermally, and chemically stable MCs, with long shelf-life, suitable for developing smart self-healing coatings, to overcome the gaps addressed in subsection 1.4.4.1. Reducing the quantity of solvent used in the encapsulation process or employing green solvents would be considered. As decreasing the MCs´ size is not a straightforward process, considerable efforts are necessary to find the proper shell former, proper active H source, and to tune the synthesis parameters, namely, emulsification rate, temperature, synthesis duration, etc. which will be addressed in more detail in Chapter 3.

Those systems which smartly targeted the corrosion propagation in steel, by blocking active corroding zones, were intensively studied. BTA, MBI, and MBT loaded in specific micro or nano sized carriers, introduced into the epoxy coating found to be most effective systems reported. Although, cerium-based inhibitors have been investigated and reported as successful solutions to achieve smarter corrosion protection of metallic structures, investigation of these group of inhibitors has been mostly focused on aluminum alloys, more recently on magnesium alloys and just a few works studied cerium-based carriers and inhibitors for corrosion protection of carbon steel. A need for further study and characterization of such a system for steel and in particular, carbon steel also clearly can be addressed as a gap of knowledge to be investigated. Therefore, for further improvement of the developed coatings (in chapter 3) and to go beyond the state of the art, combination of various self-healing approaches will be investigated. To do so, in first approach two key issues will be targeted: a) the healing of the polymeric matrix resulting in the recovery of the barrier properties of matrix (epoxy); together with b) the incorporation of a pH response corrosion inhibitor into the self-healing coating (epoxy) to target the corrosion events at the coating/substrate interface. The results regarding this approach will be covered in chapter 4.

Further, far beyond the state of the art, a triple action system will be developed. Taking advantage of self-healing ability of polyolefin, the possibility of reinforcing corrosion protection properties of this coating will be investigated. To this end CeO_2 NPs as both corrosion inhibitor and carriers for an organic inhibitor will be tested. The results regarding this approach will be covered in chapter 5.

Therefore, the scientific outcomes of this work can be summarized as development of smarter self-healing epoxy coatings, and development of smarter, and highly protective polyolefin coatings, both compatible with industrial application of carbon steel, e.g., oil and gas industries, as I used simplified versions of commercial products supplied by coating producers and simple synthesis procedures. The latest developed polyolefin coating reported in this Thesis, can be considered the first report of an efficient, relatively thin polyolefin protective coating containing both cerium-based and an organic inhibitor.

1.5 References

[1] L.M. Muresan, Self-Healing Coatings for Corrosion Protection of Steel, in: M.A.S.H. Hosseini M. (Ed.), Industerial Appl. Intell. Polym. Coatings, Springer, Cham, 2016: pp. 479–492. https://doi.org/10.1007/978-3-319-26893-4_22.

[2] E. Basson, 2021 World Steel in Figures, 2021. http://www.worldsteel.org/wsif.php.

[3] K.E. Heusler, D. Landolt, S. Trasatti, Electrochemical corrosion nomenclature, Pure Appl. Chem. 61 (1989) 19–22.

[4] G. Koch, Cost of corrosion, A. M. El Sherik (Ed), Trends Oil Gas Corros. Res. Technol. Prod. Transm. Elsevier Ltd,(2017) 3–30, https://doi.org/10.1016/B978-0-08-101105-8.00001-2.

[5] S.A. Umoren, M.M. Solomon, Protective polymeric films for industrial substrates: A critical review on past and recent applications with conducting polymers and polymer composites/nanocomposites, Prog. Mater. Sci. 104 (2019) 380–450. https://doi.org/10.1016/j.pmatsci.2019.04.002.

[6] V. Sauvant-moynot, S. Gonzalez, J. Kittel, Self healing coatings : an alternative route for anticorrosion protection, in: Eurrocorr 2007, HAL open science, Freiburg, Germany, 2007.

[7] D. Gandy, Carbon Steel Handbook, pp. 4-1, Electric Power Research Institute, California, 2007.

[8] K.M. Usher, A.H. Kaksonen, I. Cole, D. Marney, Critical review: Microbially influenced corrosion of buried carbon steel pipes, Int. Biodeterior. Biodegrad. 93 (2014) 84–106. https://doi.org/10.1016/j.ibiod.2014.05.007.

[9] T. Misawa, K. Hashimoto, S. Shimodaira, The mechanism of formation of iron oxide and oxyhydroxides in aqueous solutions at room, Corrosion. 14 (1974) 131–149.

[10] X. Kui, D. Chao-fang, L. Xiao gang, W. Fu ming, Corrosion Products and Formation Mechanism During Initial Stage of Atmospheric Corrosion of Carbon Steel, J. Iron Steel Res. Int. 15 (2008) 42–48. https://doi.org/10.1016/S1006-706X(08)60247-2.

[11] T. Islam, H.M. Rashed, Classification and Application of Plain Carbon Steels, in: Ref. Modul. Mater. Sci. Mater. Eng., Elsevier Inc., 2019. https://doi.org/10.1016/B978-0-12-803581-8.10268-1.

[12] S.M. Sherif, A comparative study on the inhibition of iron corrosion in aerated stagnant 3 . 5 wt .% sodium chloride solutions by 5-phenyl-1H-tetrazole and 3-amino-1 , 2 , 4-triazole, Ind. Eng. Chem. Res. 26 (2013). 14507–14513 https://doi.org/10.1021/ie400725z.

[13] S. Musić, I. Nowik, M. Ristić, Z. Orehovec, S. Popović, The effect of bicarbonate/carbonate ions on the formation of iron rust, Croat. Chem. Acta. 77 (2004) 141–151.

[14] J.G. Castaño, C.A. Botero, A.H. Restrepo, E.A. Agudelo, E. Correa, F. Echeverría, Atmospheric corrosion of carbon steel in Colombia, Corros. Sci. 52 (2010) 216–223. https://doi.org/10.1016/j.corsci.2009.09.006.

[15] J. Alcántara, B. Chico, I. Díaz, D. de la Fuente, M. Morcillo, Airborne chloride deposit and its effect on marine atmospheric corrosion of mild steel, Corros. Sci. 97 (2015) 74–88. https://doi.org/10.1016/j.corsci.2015.04.015.

[16] K. Matsunami, T. Kato, I. Kosan, Corrosion of Carbon Steel and its Estimation in Aqueous Solution Used in Petroleum Refineries Ecorr, Int. J. Press. Vessel. Pip. 45 (1991) 179–197.

[17] J. Alcántara, D. de la Fuente, B. Chico, J. Simancas, I. Díaz, M. Morcillo, Marine atmospheric corrosion of carbon steel: A review, Materials (Basel). 10 (2017).406. https://doi.org/10.3390/ma10040406.

[18] Y. Fan, W. Liu, S. Li, T. Chowwanonthapunya, B. Wongpat, Y. Zhao, B. Dong, T. Zhang, X. Li, Evolution of rust layers on carbon steel and weathering steel in high humidity and heat marine atmospheric corrosion, J. Mater. Sci. Technol. 39 (2020) 190–199. https://doi.org/10.1016/j.jmst.2019.07.054.

[19] F. Wu, Z. Hu, X. Liu, C. Su, L. Hao, Understanding in compositional phases of carbon steel rust layer with a long-term atmospheric exposure, Mater. Lett. 315 (2022) 131968. https://doi.org/10.1016/j.matlet.2022.131968.

[20] E.K. Ioakeimidis, V.N. Kytopoulos, E. Hristoforou, Investigation of magnetic, mechanical and microfailure behavior of ARMCO-type low carbon steel corroded in 3.5% NaCl-aqueous solution, Mater. Sci. Eng. A. 583 (2013) 254–260. https://doi.org/10.1016/j.msea.2013.06.072.

[21] S.A. Umoren, M.M. Solomon, Recent developments on the use of polymers as corrosion inhibitors- A review, Open Mater. Sci. J. 8 (2014) 39–54. https://doi.org/10.2174/1874088X01408010039.

[22] P. Maab, Corrosion and corrosion protection, in: P. Maab, P. Peibker (Eds.),

Handb. Hot-Dip Galvaniz., WILEY-VCH, 2011: pp. 1–19.

[23] Z. Ahmad, Selection of materials for Corrosive Environmental (Ch-8) in Princ. Corros. Eng. Corros. Control, Elsevier Inc (2006) pp. 479. ISBN: 0750659246.

[24] S. Papavinasam, Materials, in: Corros. Control Oil Gas Ind., Elsevier Inc., 2014: pp. 133–177. https://doi.org/10.1016/B978-0-12-397022-0.00003-0.

[25] K. Hasmmoto, K. Asami, M. Naka, T. Masumoro, The Role of A lloying Elements in Improving the Corrosion Resistance of Amorphous Iron Base Alloys, Corros. Sci. 19 (1979) 857–867.

[26] Y. Choi, S. Nesic, H. Jung, Effect of Alloying Elements on the Corrosion Behavior of Carbon Steel in CO_2 Environments, in: NACE Corros. Conf. Expo, NACE Internacional, 2018: pp. 1–14.

[27] M.F. Ashby, D.R.H. Jones, Steels 2–- Alloy Steels, Eng. Mater. 2 An Introd. to Microstruct. Procesing. (2013) 221–236. https://doi.org/10.1016/B978-0-08-096668-7.00013-9.

[28] Z. Ling yun, W. Di, L. Zhuang, Influence of Alloying Elements on Mechanical Properties and Corrosion Resistance of Cold Rolled C-Mn-Si TRIP Steels, J. Iron Steel Res. Int. 19 (2012) 42–47. https://doi.org/10.1016/S1006-706X(13)60030-8.

[29] M. Ormellese, A. Brenna, Cathodic Protection and Prevention: Principles, Applications and Monitoring, Ref. Modul. Chem. Mol. Sci. Chem. Eng. (2017) 1–11. https://doi.org/10.1016/b978-0-12-409547-2.14281-7.

[30] A. Wiryawan, P.T. Iswanto, Design of impressed current cathodic protection of offshore platform in East Borneo Sea, in: AIP Conf. Proc., 2021. https://doi.org/10.1063/5.0068078.

[31] Z. Ahmad, Cathodic protection (Ch-5), in: Princ. Corros. Eng. Corros. Control, Elsevier Ltd, 2006: pp. 271–351. ISBN: 0750659246.

[32] N. Perez, ed., Anodic Protection, in: Electrochem. Corros. Sci., Springer, 2004: p. 295/300. https://doi.org/10.1007/1-4020-7860-9_9.

[33] T.A. Soylev, M.G. Richardson, Corrosion inhibitor for steel in concrete: State-of-the-art report, Constr. Build. Mater. 22 (2008) 609–622. https://doi.org/10.1016/j.conbuildmat.2006.10.013.

[34] V.S. Sastri, Green corrosion inhibitors (Theory and practice), Wiley Series in Corrosion, Winston Revie, Series Editor, WILEY, 2011.

[35] S.Z. Salleh, A.H. Yusoff, S.K. Zakaria, M.A.A. Taib, A. Abu Seman, M.N.

Masri, M. Mohamad, S. Mamat, S. Ahmad Sobri, A. Ali, P. Ter Teo, Plant extracts as green corrosion inhibitor for ferrous metal alloys: A review, J. Clean. Prod. 304 (2021) 127030. https://doi.org/10.1016/j.jclepro.2021.127030.

[36] M.F. Montemor, Fostering green inhibitors for corrosion prevention, A. E. Hughes et al. (Eds), Active Protecting Coatings, Springer Series in Material Science, (2016).233. https://doi.org/10.1007/978-94-017-7540-3_6.

[37] C.G. Dariva, A.F. Galio, corrosion inhibitors–- Principles, Mechanisms and Applications, in: Dev. Corros. Prot., 2014: pp. 365–379. https://doi.org/10.5772/57255.

[38] F.S.Z.S. Al Shibli, S. Bose, P.S. Kumar, M. Rajasimman, N. Rajamohan, D.V.N. Vo, Green technology for sustainable surface protection of steel from corrosion: a review, Environ. Chem. Lett. (2021). https://doi.org/10.1007/s10311-021-01332-6.

[39] C. Verma, S.H. Alrefaee, K.Y. Rhee, M.A. Quraishi, E.E. Ebenso, Thiol (-SH) substituent as functional motif for effective corrosion protection: A review on current advancements and future directions, J. Mol. Liq. (2021) 115111. https://doi.org/10.1016/j.molliq.2020.115111.

[40] N.A. Negm, A.M.A. Sabagh, M.A. Migahed, H.M.A. Bary, H.M.E. Din, Effectiveness of some diquaternary ammonium surfactants as corrosion inhibitors for carbon steel in 0.5 M HCl solution, Corros. Sci. 52 (2010) 2122–2132. https://doi.org/10.1016/j.corsci.2010.02.044.

[41] S. Habib, E. Fayyad, M. Nawaz, A. Khan, R.A. Shakoor, R. Kahraman, A. Abdullah, Cerium Dioxide Nanoparticles as Smart Carriers for Self-Healing Coatings, Nanomaterials. 10 (2020) 791. https://doi.org/10.3390/nano10040791.

[42] A.A. Farag, M.A. Migahed, E.A. Badr, Thiazole Ionic Liquid as Corrosion Inhibitor of Steel in 1 M HCl Solution: Gravimetrical, Electrochemical, and Theoretical Studies, J. Bio- Tribo-Corrosion. 5 (2019) 53. https://doi.org/10.1007/s40735-019-0246-4.

[43] M.F. Montemor, Functional and smart coatings for corrosion protection: A review of recent advances, Surf. Coatings Technol. 258 (2014) 17–37. https://doi.org/10.1016/j.surfcoat.2014.06.031.

[44] S. Habib, R. A. Shakoor, R. Kahraman, A ficused review on smart carriers taillored for corrosion protection: Developments, application, and chllenges, Prog. Org. Coatings. 154 (2021)106218,

https://doi.org/10.1016/j.progcoat.2021.106218.

[45] M. Doerre, L. Hibbitts, G. Patrick, N.K. Akafuah, Advances in automotive conversion coatings during pretreatment of the body structure: A review, Coatings. 8 (2018) 405. https://doi.org/10.3390/COATINGS8110405.

[46] M.H. Shahini, N. Taheri, H.E. Mohammadloo, B. Ramezanzadeh, A comprehensive overview of nano and micro carriers aiming at curtailing corrosion progression, J. Taiwan Inst. Chem. Eng. 126 (2021) 252–269. https://doi.org/10.1016/j.jtice.2021.06.053.

[47] M.W. Kendig, A.J. Davenport, H.S. Isaacs, The mechanism of corrosion inhibition by chromate conversion coatings from x-ray absorption near edge spectroscopy (Xanes), Corros. Sci. 34 (1993) 41–49. https://doi.org/10.1016/0010-938X(93)90257-H.

[48] M. Zheludkevich, Self-healing Anticorrosin Coatings, in: S.K. Ghosh (Ed.), Self-Healing Mater., WILEY-VCH, 2008. pp 101-135.

[49] M.H. Shahini, H. Eivaz Mohammadloo, B. Ramezanzadeh, Recent advances in steel surface treatment via novel/green conversion coatings for anti-corrosion applications: a review study, J. Coatings Technol. Res. 19 (2022) 159–199. https://doi.org/10.1007/s11998-021-00466-0.

[50] P.S. Sidky, M.G. Hocking, Review of inorganic coatings and coating processes for reducing wear and corrosion, Br. Corros. J. 34 (1999) 171–183. https://doi.org/10.1179/000705999101500815.

[51] The Australasian Corrosion Association, Metallic and Inorganic Coatings, Corros. Technol. (2013) 1–23.

[52] A.A. Olajire, Recent advances on organic coating system technologies for corrosion protection of offshore metallic structures, J. Mol. Liq. 269 (2018) 572–606. https://doi.org/10.1016/j.molliq.2018.08.053.

[53] H. Pulikkalparambil, S. Siengchin, J. Parameswaranpilliai, Corrosion protecvtive self-healing epoxy resin coatings based on inhibitor and polymeric healing agents encapsulated in organic and inorganic micro and nanocontainers, Nano-Strctures & Nano-Objects. 16 (2020) 381–395. https://doi.org/10.1016/j.nanoso.2018.09.010.

[54] A. Noreen, K.M. Zia, M. Zuber, S. Tabasum, A.F. Zahoor, Bio-based polyurethane: An efficient and environment friendly coating systems: A review, Prog. Org. Coatings. 91 (2016) 25–32.

https://doi.org/10.1016/j.porgcoat.2015.11.018.

[55] J. Zhang, Y. Huang, H. Wu, S. Geng, F. Wang, Corrosion protection properties of an environmentally friendly polyvinyl alcohol coating reinforced by a heating treatment and lignin nanocellulose, Prog. Org. Coatings. 155 (2021) 106224. https://doi.org/10.1016/j.porgcoat.2021.106224.

[56] X. Wang, L. Xu, H. Wang, X. Li, Q. Zhang, Y. Gu, Core-shell Fluorine-silicon Modified Polyacrylic Coating for Corrosion Protection of 304 Stainless Steel Substrate, Int. J. Electrochem. Sci. 16 (2021) 1–16. https://doi.org/10.20964/2021.01.75.

[57] M.J. Hollamby, D. Fix, I. Dönch, D. Borisova, H. Möhwald, D. Shchukin, Hybrid polyester coating incorporating functionalized mesoporous carriers for the holistic protection of steel surfaces, Adv. Mater. 23 (2011) 1361–1365. https://doi.org/10.1002/adma.201003035.

[58] I. Thompson, J.R. Saithala, Review of pipeline coating systems from an operator's perspective, Corros. Eng. Sci. Technol. 51 (2016) 118–135. https://doi.org/10.1179/1743278215Y.0000000038.

[59] S. Rio, O. D´Albuquerque, In-Service Pipeline Rehabilitation, in: Prot. Maint. Transm. Pipline, Technology Publishing Company, 2012: pp. 50–56. http://www.eia.gov/pub/oil-gas/natural-gas/analysis-publications/ngpipeline/transsys-design.html.

[60] J. Li, L. Ecco, M. Fedel, V. Ermini, G. Delmas, J. Pan, In-situ AFM and EIS study of a solventborne alkyd coating with nanoclay for corrosion protection of carbon steel, Prog. Org. Coatings. 87 (2015) 179–188. https://doi.org/10.1016/j.porgcoat.2015.06.003.

[61] M.F. Montemor, M.G.S. Ferreira, Analytical characterization of silane films modified with cerium activated nanoparticles and its relation with the corrosion protection of galvanised steel substrates, Prog. Org. Coatings. 63 (2008) 330–337. https://doi.org/10.1016/j.porgcoat.2007.11.008.

[62] M.A. Petrunin, N.A. Gladkikh, M.A. Maleeva, L.B. Maksaeva, T.A. Yurasova, The use of organosilanes to inhibit metal corrosion. A review, Int. J. Corros. Scale Inhib. 8 (2019) 882–907. https://doi.org/10.17675/2305-6894-2019-8-4-6.

[63] J.L. Moeckel, R.S. Bauer, Epoxy resins, in: D.C. Craver, C.E. Carraher (Eds.), Appl. Polym. Sci. 2^{1s}t Century, Elsevier B.V, 2000: pp. 393–424. https://doi.org/10.1016/b978-0-408-15960-9.50032-2.

[64] L.T. Popoola, A.S. Grema, G.K. Latinwo, B. Gutti, A.S. Balogun, Corrosion problems during oil and gas production and its mitigation, Int. J. Ind. Chem. 4 (2013) 1–15. https://doi.org/10.1186/2228-5547-4-35.

[65] N. Hoang, T.A. Khoa, L.T. Nhung, P.M. Phuong, T.T.X. Hang, N. Van Chi, T.D. Nguyen, Corrosion protection of carbon steel using a combination of Zr conversion coating and subsequent zinc-rich silicate coating with a flake ZnAl alloy, Arab. J. Chem. 15 (2022) 103815. https://doi.org/10.1016/j.arabjc.2022.103815.

[66] R. Raj, Y. Morozov, L.M. Calado, M.G. Taryba, R. Kahraman, A. Shakoor, M.F. Montemor, Inhibitor loaded calcium carbonate microparticles for corrosion protection of epoxy-coated carbon steel, Electrochim. Acta. 319 (2019) 801–812. https://doi.org/10.1016/j.electacta.2019.07.059.

[67] K.T. Kim, H.W. Kim, H.Y. Chang, B.T. Lim, H.B. Park, Y.S. Kim, Corrosion inhibiting mechanism of nitrite ion on the passivation of carbon steel and ductile cast iron for nuclear power plants, Adv. Mater. Sci. Eng. 2015 (2015) 408138. https://doi.org/10.1155/2015/408138.

[68] F. Cotting, I.V. Aoki, Smart protection provided by epoxy clear coating doped with polystyrene microcapsules containing silanol and Ce (III) ions as corrosion inhibitors, Surf. Coatings Technol. 303 (2016) 310–318. https://doi.org/10.1016/j.surfcoat.2015.11.035.

[69] R. Raj, Y. Morozov, L.M. Calado, M.G. Taryba, R. Kahraman, R.A. Shakoor, M.F. Montemor, Calcium carbonate particles loaded with triethanolamine and polyethylenimine for enhanced corrosion protection of epoxy coated steel, Corros. Sci. 167 (2020) 108548. https://doi.org/10.1016/j.corsci.2020.108548.

[70] A.S. Fouda, H.S. El-Desoky, M.M. Abdel-Galeil, D. Mansour, Amide Compounds as Corrosion Inhibitors for Carbon Steel in Acidic Environment, Prot. Met. Phys. Chem. Surfaces. 58 (2022) 151–167. https://doi.org/10.1134/S2070205122010105.

[71] T. Szabó, J. Telegdi, L. Nyikos, Linseed oil-filled microcapsules containing drier and corrosion inhibitor–- Their effects on self-healing capability of paints, Prog. Org. Coatings. 84 (2015) 136–142. https://doi.org/10.1016/j.porgcoat.2015.02.020.

[72] M. Nawaz, R.A. Shakoor, R. Kahraman, M.F. Montemor, Cerium oxide loaded with Gum Arabic as environmentally friendly anti-corrosion additive for

protection of coated steel, Mater. Des. 198 (2021) 109361. https://doi.org/10.1016/j.matdes.2020.109361.

[73] B. El Ibrahimi, A. Jmiai, L. Bazzi, S. El Issami, Amino acids and their derivatives as corrosion inhibitors for metals and alloys, Arab. J. Chem. 13 (2020) 740–771. https://doi.org/10.1016/j.arabjc.2017.07.013.

[74] T. Markley, M Forsyth, B. Hinton, Multifunctional rare earth organic corrosion inhibitors, M. Forsyth, B. Hinton (Eds)., Rare Earth-based Corrosion Inhibitors, Woodhead Publishing Limited, (2014) 117-142. https://doi.org/10.1533/9780857093585.117.

[75] R. A. t. M van Benthem, W. Ming, G de With, self-healing Polymer Coating, in S.V.D. Zwaag (Ed), Self Healing Materials an Alternative Approach to 20 Centuries of Materials Science, Springer, Dordrecht, Netherlands, 2007 (139).

[76] S.M. Mirabedini, F. Alizadegan, Self-healing polymeric coatings containing microcapsules filled with active materials, in: S. Thomas, A. Suredran (Eds.), Self-Healing Polym. Syst., 2020: pp. 235–258. https://doi.org/10.1016/b978-0-12-818450-9.00009-x.

[77] E.B. Murphy, F. Wudl, The world of smart healable materials, Prog. Polym. Sci. 35 (2010) 223–251. https://doi.org/10.1016/j.progpolymsci.2009.10.006.

[78] R.S. Trask, G.J. Williams, I.P. Bond, Bioinspired self-healing of advanced composite structures using hollow glass fibres, J. R. Soc. Interface. 4 (2007) 363–371. https://doi.org/10.1098/rsif.2006.0194.

[79] T.C. Mauldin, M.R. Kessler, Self-healing polymers and composites, Int. Mater. Rev. 55 (2010) 317–346. https://doi.org/10.1179/095066010X12646898728408.

[80] X. Liu, X. Sheng, J.K. Lee, M.R. Kessler, Synthesis and characterization of melamine- urea-formaldehyde microcapsules containing ENB-based self-healing agents, Macromol. Mater. Eng. 294 (2009) 389–395. https://doi.org/10.1002/mame.200900015.

[81] S.R. White, N.Scottos, P. Geubelle, J.S. Moore, M.R. Kessler, S.Sriram, E.N. Brown, S. Viswanathan, Autonomic healing of polymer composites, Lett. to Nat. 409 (2001) 794-797.

[82] D.G. Shchukin, D. Borisova, H. Mohwald, Self-Healing Coatings, in: Wolfgang H. Binder (Ed.), Self-Healing Polym. From Princ. to Appl., First, 2013: pp. 381–399. https://doi.org/10.1002/9783527670185.ch6.

[83] D.G. Shchukin, Container-based multifunctional self-healing polymer coatings,

R. Soc. Chem. Chem. 4 (2013) 4871–4877. https://doi.org/10.1039/c3py00082f.

[84] E.N. Brown, N.R. Sottos, S.R. White, Fracture testing of a self-healing polymer composite, Exp. Mech. 42 (2002) 372–379. https://doi.org/10.1177/001448502321548193.

[85] S.H. Cho, H.M. Andersson, S.R. White, N.R. Sottos, P. V. Braun, Polydiniethylsiloxane-based self-healing materials, Adv. Mater. 18 (2006) 997–1000. https://doi.org/10.1002/adma.200501814.

[86] S.H. Cho, S.R. White, P. V. Braun, Self-healing polymer coatings, Adv. Mater. 21 (2009) 645–649. https://doi.org/10.1002/adma.200802008.

[87] H. Jin, C.L. Mangun, A.S. Griffin, J.S. Moore, N.R. Sottos, S.R. White, Thermally stable autonomic healing in epoxy using a dual-microcapsule system, Adv. Mater. 26 (2014) 282–287. https://doi.org/10.1002/adma.201303179.

[88] H. Jin, C.L. Mangun, D.S. Stradley, J.S. Moore, N.R. Sottos, S.R. White, Self-healing thermoset using encapsulated epoxy-amine healing chemistry, Polymer (Guildf). 53 (2012) 581–587. https://doi.org/10.1016/j.polymer.2011.12.005.

[89] H. Zhang, J. Yang, Etched glass bubbles as robust micro-containers for self-healing materials, J. Mater. Chem. A. 1 (2013) 12715–12720. https://doi.org/10.1039/c3ta13227g.

[90] H. Zhang, P. Wang, J. Yang, Self-healing epoxy via epoxy-amine chemistry in dual hollow glass bubbles, Compos. Sci. Technol. 94 (2014) 23–29. https://doi.org/10.1016/j.compscitech.2014.01.009.

[91] D.A. McIlroy, J.S. Moore, N.R. Sottos, B.J. Blaiszik, M.M. Caruso, S.R. White, Microencapsulation of a reactive liquid-phase amine for self-healing Epoxy composites, Macromolecules. 43 (2010) 1855–1859. https://doi.org/10.1021/ma902251n.

[92] H. Choi, K.Y. Kim, J.M. Park, Encapsulation of aliphatic amines into nanoparticles for self-healing corrosion protection of steel sheets, Prog. Org. Coatings. 76 (2013) 1316–1324. https://doi.org/10.1016/j.porgcoat.2013.04.005.

[93] J. Li, A.D. Hughes, T.H. Kalantar, I.J. Drake, C.J. Tucker, J.S. Moore, Pickering-emulsion-templated encapsulation of a hydrophilic amine and its enhanced stability using poly(allyl amine), ACS Macro Lett. 3 (2014) 976–980. https://doi.org/10.1021/mz500455j.

[94] H. Yi, Y. Deng, C. Wang, Pickering emulsion-based fabrication of epoxy and amine microcapsules for dual core self-healing coating, Compos. Sci. Technol.

133 (2016) 51–59. https://doi.org/10.1016/j.compscitech.2016.07.022.

[95] B.J. Blaiszik, M.M. Caruso, D.A. McIlroy, J.S. Moore, S.R. White, N.R. Sottos, Microcapsules filled with reactive solutions for self-healing materials, Polymer (Guildf). 50 (2009) 990–997. https://doi.org/10.1016/j.polymer.2008.12.040.

[96] M.M. Caruso, D.A. Delafuente, V. Ho, N.R. Sottos, J.S. Moore, S.R. White, Solvent-promoted self-healing epoxy materials, Macromolecules. 40 (2007) 8830–8832. https://doi.org/10.1021/ma701992z.

[97] D. Snihirova, S.V. Lamaka, M.F. Montemor, Smart composite coatings for corrosion protection of aluminum alloy in aerospace applications, in: M.F. Montemor (Ed.), Smart Compos. Coatings Membr., Elsevier Ltd, 2016: pp. 83–122. https://doi.org/10.1016/B978-1-78242-283-9.00004-X.

[98] G. Kurt Çömlekçi, S. Ulutan, Acquired self-healing ability of an epoxy coating through microcapsules having linseed oil and its alkyd, Prog. Org. Coatings. 129 (2019) 292–299. https://doi.org/10.1016/j.porgcoat.2019.01.022.

[99] M. Behzadnasab, S.M. Mirabedini, M. Esfandeh, R.R. Farnood, Evaluation of corrosion performance of a self-healing epoxy-based coating containing linseed oil-filled microcapsules via electrochemical impedance spectroscopy, Prog. Org. Coatings. 105 (2017) 212–224. https://doi.org/10.1016/j.porgcoat.2017.01.006.

[100] K. Thanawala, N. Mutneja, A.S. Khanna, R.K. Singh Raman, Development of self-healing coatings based on linseed oil as autonomous repairing agent for corrosion resistance, Materials (Basel). 7 (2014) 7324–7338. https://doi.org/10.3390/ma7117324.

[101] C. Suryanarayana, K.C. Rao, D. Kumar, Preparation and characterization of microcapsules containing linseed oil and its use in self-healing coatings, Prog. Org. Coatings. 63 (2008) 72–78. https://doi.org/10.1016/j.porgcoat.2008.04.008.

[102] S. Hatami Boura, M. Peikari, A. Ashrafi, M. Samadzadeh, Self-healing ability and adhesion strength of capsule embedded coatings - Micro and nano sized capsules containing linseed oil, Prog. Org. Coatings. 75 (2012) 292–300. https://doi.org/10.1016/j.porgcoat.2012.08.006.

[103] P.D. Tatiya, R.K. Hedaoo, P.P. Mahulikar, V. V. Gite, Novel polyurea microcapsules using dendritic functional monomer: Synthesis, characterization, and its use in self-healing and anticorrosive polyurethane coatings, Ind. Eng. Chem. Res. 52 (2013) 1562–1570. https://doi.org/10.1021/ie301813a.

[104] K. Thanawala, A.S. Khanna, R.K.S. Raman, Tung Oil-Urea Formaldehyde

Microcapsules for Anti-Corrosive Self-Healing Epoxy Coatings, J. Mater. Sci. Surf. Eng. 2 (2015) 151–156. http://www.jmsse.org/.

[105] H. Li, Y. Cui, H. Wang, Y. Zhu, B. Wang, Preparation and application of polysulfone microcapsules containing tung oil in self-healing and self-lubricating epoxy coating, Colloids Surfaces A Physicochem. Eng. Asp. 518 (2017) 181–187. https://doi.org/10.1016/j.colsurfa.2017.01.046.

[106] J. Li, H. Shi, F. Liu, E.H. Han, Self-healing epoxy coating based on tung oil-containing microcapsules for corrosion protection, Prog. Org. Coatings. 156 (2021) 106236. https://doi.org/10.1016/j.porgcoat.2021.106236.

[107] M. Behzadnasab, M. Esfandeh, S.M. Mirabedini, M.J. Zohuriaan-Mehr, R.R. Farnood, Preparation and characterization of linseed oil-filled urea-formaldehyde microcapsules and their effect on mechanical properties of an epoxy-based coating, Colloids Surfaces A Physicochem. Eng. Asp. 457 (2014) 16–26. https://doi.org/10.1016/j.colsurfa.2014.05.033.

[108] H. Es-haghi, S.M. Mirabedini, M. Imani, R.R. Farnood, Preparation and characterization of pre-silane modified ethyl cellulose-based microcapsules containing linseed oil, Colloids Surfaces A Physicochem. Eng. Asp. 447 (2014) 71–80. https://doi.org/10.1016/j.colsurfa.2014.01.021.

[109] S.M. Mirabedini, M. Esfandeh, R.R. Farnood, P. Rajabi, Amino-silane surface modification of urea-formaldehyde microcapsules containing linseed oil for improved epoxy matrix compatibility. Part I: Optimizing silane treatment conditions, Prog. Org. Coatings. 136 (2019) 1–10. https://doi.org/10.1016/j.porgcoat.2019.105242.

[110] J. Yang, M.W. Keller, J.S. Moore, N.R. Sottos, S.R. White, Microencapsulation of Isocyanates for Self-Healing Polymers, Macromolecules. 41 (2008) 9650–9655. https://doi.org/10.1021/ma801718v.

[111] M. Haghayegh, S.M. Mirabedini, H. Yeganeh, Microcapsules containing multi-functional reactive isocyanate-terminated polyurethane prepolymer as a healing agent. Part 1: synthesis and optimization of reaction conditions, J. Mater. Sci. 51 (2016) 3056–3068. https://doi.org/10.1007/s10853-015-9616-6.

[112] A. Beglarigale, D. Eyice, Y. Seki, Ç. Yalçinkaya, O. Çopuroglu, H. Yazici, Sodium silicate/polyurethane microcapsules synthesized for enhancing self-healing ability of cementitious materials: Optimization of stirring speeds and evaluation of self-healing efficiency, J. Build. Eng. 39 (2021) 102279.

https://doi.org/10.1016/j.jobe.2021.102279.

[113] N.P.B. Tan, L.H. Keung, W.H. Choi, W.C. Lam, H.N. Leung, Silica-based self-healing microcapsules for self-repair in concrete, J. Appl. Polym. Sci. 133 (2016) 1–12. https://doi.org/10.1002/app.43090.

[114] M. Huang, J. Yang, Facile microencapsulation of HDI for self-healing anticorrosion coatings, J. Mater. Chem. 21 (2011) 11123–11130. https://doi.org/10.1039/c1jm10794a.

[115] D. Sun, J. An, G. Wu, J. Yang, Double-layered reactive microcapsules with excellent thermal and non-polar solvent resistance for self-healing coatings, J. Mater. Chem. A. 3 (2015) 4435–4444. https://doi.org/10.1039/c4ta05339g.

[116] S. Chen, T. Han, Y. Zhao, W. Luo, Z. Zhang, H. Su, B.Z. Tang, J. Yang, A Facile Strategy to Prepare Smart Coatings with Autonomous Self-Healing and Self-Reporting Functions, ACS Appl. Mater. Interfaces. 12 (2020) 4870–4877. https://doi.org/10.1021/acsami.9b18919.

[117] M. Huang, J. Yang, Salt spray and EIS studies on HDI microcapsule-based self-healing anticorrosive coatings, Prog. Org. Coatings. 77 (2014) 168–175. https://doi.org/10.1016/j.porgcoat.2013.09.002.

[118] D. Sondari, A.A. Septevani, A. Randy, E. Triwulandari, Polyurethane microcapsule with glycerol as the polyol component for encapsulated self healing agent, Int. J. Eng. Technol. 2 (2010) 466–471.

[119] P. Kardar, Preparation of polyurethane microcapsules with different polyols component for encapsulation of isophorone diisocyanate healing agent, Prog. Org. Coatings. 89 (2015) 271–276. https://doi.org/10.1016/j.porgcoat.2015.09.009.

[120] Y. Ming, J. Hu, J. Xing, M. Wu, J. Qu, Preparation of polyurea/melamine formaldehyde double-layered self-healing microcapsules and investigation on core fraction, J. Microencapsul. 33 (2016) 307–314. https://doi.org/10.1080/02652048.2016.1178352.

[121] D. Sun, J. An, G. Wu, J. Yang, Double-layered reactive microcapsules with excellent thermal and non-polar solvent resistance for self-healing coatings, J. Mater. Chem. A. 3 (2015) 4435–4444. https://doi.org/10.1039/c4ta05339g.

[122] G. Wu, J. An, D. Sun, X. Tang, Y. Xiang, J. Yang, Robust microcapsules with polyurea/silica hybrid shell for one-part self-healing anticorrosion coatings, J. Mater. Chem. A. 2 (2014) 11614–11620. https://doi.org/10.1039/c4ta01312c.

[123] R. Najjar, M. Akbari, A. Mirmohseni, M. Hosseini, Preparation and corrosion performance of healable waterborne polyurethane coatings containing isophoronediisocyanate loaded silica capsules, J Taiwan Inst Chem Eng. 93 (2018) 1-10. https://doi.org/10.1016/j.jtice.2018.05.021.

[124] B. Di Credico, M. Levi, S. Turri, An efficient method for the output of new self-repairing materials through a reactive isocyanate encapsulation, Eur. Polym. J. 49 (2013) 2467–2476. https://doi.org/10.1016/j.eurpolymj.2013.02.006.

[125] S. Liu, X., Zhang, H., Wang, J., Wang, Z., & Wang, Preparation of epoxy microcapsules based self-healing coatings and their behavior, Surf. Coatings Technol. 206 (2012) 4976–4980. https://doi.org/10.1016/j.surfcoat.2012.05.133.

[126] H. Yi, Y. Yang, X. Gu, J. Huang, C. Wang, Multilayer composite microcapsules synthesized by Pickering emulsion templates and their application in self-healing coating, J. Mater. Chem. A. 3 (2012) 13749–13757. https://doi.org/10.1039/c5ta02288f.

[127] M. Haghayegh, S.M. Mirabedini, H. Yeganeh, Preparation of Microcapsules Containing Multi-functional Reactive Isocyanate-terminated-polyurethane prepolymer as Healing Agent, Part ll: Corrosion Performance and Mechanical properties of a Self Healing Coatings, R. Soc. Chem. Adv. 6 (2016) 50784–50886. https://doi.org/10.1039/c6ra07574f.

[128] M. Attaei, Microencapsulation of isocyanate compounds for autoreactive , monocomponent adhesive, Instituto Superior Technico Lisboa, Lisbon University, MSc Thesis, 2017.

[129] M. Samadzadeh, S.H. Boura, M. Peikari, S.M. Kasiriha, A. Ashrafi, A review on self-healing coatings based on micro/nanocapsules, Prog. Org. Coatings. 68 (2010) 159–164. https://doi.org/10.1016/j.porgcoat.2010.01.006.

[130] Xu. Li, Xi., Li, Y. Zho, Q. Li, J. Wang, M. Kang, Controllable preparation of isophorone diisocyanate microcapsules with silica/polyurea hybrid shell and application in self-healing epoxy coating, Prog. Org. Coatings. 163 (2022)106638. https://doi.org/10.1016/j.porgcoat.2021.106638.

[131] R. Dubey, T.C. Shami, K.U. Bhasker Rao, Microencapsulation technology and applications, Def. Sci. J. 59 (2009) 81–95.

[132] M. V. Loureiro, M. Vale, R. Galhano, S. Matos, J.C. Bordado, I. Pinho, A.C. Marques, Microencapsulation of Isocyanate in Biodegradable Poly(ϵ-caprolactone) Capsules and Application in Monocomponent Green Adhesives,

ACS Appl. Polym. Mater. 2 (2020) 4425–4438. https://doi.org/10.1021/acsapm.0c00535.

[133] M. Haghayegh, S.M. Mirabedini, H. Yeganeh, Preparation of microcapsules containing multi-functional reactive isocyanate-terminated-polyurethane-prepolymer as healing agent, part II: Corrosion performance and mechanical properties of a self healing coating, RSC Adv. 6 (2016) 50874–50886. https://doi.org/10.1039/c6ra07574f.

[134] L. Ma, C. Ren, J. Wang, T. Liu, H. Yang, Y. Wang, Y. Huang, D. Zhang, Self-reporting coatings for autonomous detection of coating damage and metal corrosion: A review, Chem. Eng. J. 421 (2021) 127854. https://doi.org/10.1016/j.cej.2020.127854.

[135] M. Attaei, M. V. Loureiro, M. Vale, J.A.D. Condeço, I. Pinho, J.C. Bordado, A.C. Marques, Isophorone diisocyanate (IPDI) microencapsulation for mono-component adhesives: Effect of the active H and NCO sources, Polymers (Basel). 10 (2018) 825. https://doi.org/10.3390/polym10080825.

[136] M.V. Loureiro, M. Attaei, S. Rocha, M. Vale, J.C. Bordado, R. Simões, I. Pinho, A.C. Marques, The role played by different active hydrogen sources in the microencapsulation of a commercial oligomeric diisocyanate, J. Mater. Sci. 55 (2020). https://doi.org/10.1007/s10853-019-04301-1.

[137] A.A. Olajire, Corrosion inhibition of offshore oil and gas production facilities using organic compound inhibitors - A review, J. Mol. Liq. 248 (2017) 775–808. https://doi.org/10.1016/j.molliq.2017.10.097.

[138] S. Pourhashem, F. Saba, J. Duan, A. Rashidi, F. Guan, E.G. Nezhad, B. Hou, Polymer/Inorganic nanocomposite coatings with superior corrosion protection performance: A review, J. Ind. Eng. Chem. 88 (2020) 29–57. https://doi.org/10.1016/j.jiec.2020.04.029.

[139] M. Rbaa, H. Lgaz, Y.E. Kacimi, B. Lakhrissi, F. Bentiss, A. Zarrouk, Synthesis, characterization and corrosion inhibition studies of polyunsaturated fatty acid derivatives on the acidic corrosion of mild steel: Experimental and computational studies, J. Mol. Liq. 319 (2020) 43–54. https://doi.org/10.1016/j.molliq.2020.114162.

[140] M. Galai, M. Rbaa, M. Ouakki, A.S. Abousalem, E. Ech-chihbi, K. Dahmani, N. Dkhireche, B. Lakhrissi, M. EbnTouhami, Chemically functionalized of 8-hydroxyquinoline derivatives as efficient corrosion inhibition for steel in 1.0 M

HCl solution: Experimental and theoretical studies, Surfaces and Interfaces. 21 (2020) 100695. https://doi.org/10.1016/j.surfin.2020.100695.

[141] H. Cen, J. Cao, Z. Chen, X. Guo, 2-Mercaptobenzothiazole as a corrosion inhibitor for carbon steel in supercritical CO_2 -H_2O condition, Appl. Surf. Sci. 476 (2019) 422–434. https://doi.org/10.1016/j.apsusc.2019.01.113.

[142] H. Li, Y. Qiang, W. Zhao, S. Zhang, 2-Mercaptobenzimidazole-inbuilt metal-organic-frameworks modified graphene oxide towards intelligent and excellent anti-corrosion coating, Corros. Sci. 191 (2021) 109715. https://doi.org/10.1016/j.corsci.2021.109715.

[143] M. Yadav, R.R. Sinha, S. Kumar, T.K. Sarkar, Experimental and theoritical studies on corrosion inhibition effect of synthesized Benzothiazole derivates on mild steel in 15% HCl solution, Int. J. Electrochem. Sci. 10 (2015) 602–624.

[144] Z. Hu, Y. Meng, X. Ma, H. Zhu, J. Li, C. Li, D. Cao, Experimental and theoretical studies of benzothiazole derivatives as corrosion inhibitors for carbon steel in 1 M HCl, Corros. Sci. 112 (2016) 563–575. https://doi.org/10.1016/j.corsci.2016.08.012.

[145] B. Qian, B. Hou, M. Zheng, The inhibition effect of tannic acid on mild steel corrosion in seawater wet/dry cyclic conditions, Corros. Sci. 72 (2013) 1–9. https://doi.org/10.1016/j.corsci.2013.01.040.

[146] Y. Hao, L.A. Sani, T. Ge, Q. Fang, The synergistic inhibition behaviour of tannic acid and iodide ions on mild steel in H_2SO_4 solutions, Corros. Sci. 123 (2017) 158–169. https://doi.org/10.1016/j.corsci.2017.05.001.

[147] A. Keyvani, M. Yeganeh, H. Rezaeyan, Application of mesoporous silica nanocontainers as an intelligent host of molybdate corrosion inhibitor embedded in the epoxy coated steel, Prog. Nat. Sci. Mater. Int. 27 (2017) 261–267. https://doi.org/10.1016/j.pnsc.2017.02.005.

[148] M. Saremi, C. Dehghanian, M.M. Sabet, The effect of molybdate concentration and hydrodynamic effect on mild steel corrosion inhibition in simulated cooling water, Corros. Sci. 48 (2006) 1404–1412. https://doi.org/10.1016/j.corsci.2005.06.009.

[149] J.M. Falcón, F.F. Batista, I. V. Aoki, Encapsulation of dodecylamine corrosion inhibitor on silica nanoparticles, Electrochim. Acta. 124 (2014) 109–118. https://doi.org/10.1016/j.electacta.2013.06.114.

[150] J.M. Falcón, L.M. Otubo, I. V. Aoki, Highly ordered mesoporous silica loaded

with dodecylamine for smart anticorrosion coatings, Surf. Coatings Technol. 303 (2016) 319–329. https://doi.org/10.1016/j.surfcoat.2015.11.029.

[151] E. Shchukina, D.G. Shchukin, Nanocontainer-Based Active Systems: From Self-Healing Coatings to Thermal Energy Storage, Langmuir. 35 (2019) 8603–8611. https://doi.org/10.1021/acs.langmuir.9b00151.

[152] A. Joshi, E. Abdullayev, A. Vasiliev, O. Volkova, Y. Lvov, Interfacial modification of clay nanotubes for the sustained release of corrosion inhibitors, Langmuir. 29 (2013) 7439–7448. https://doi.org/10.1021/la3044973.

[153] K. Schaefer, A. Miszczyk, Improvement of electrochemical action of zinc-rich paints by addition of nanoparticulate zinc, Corros. Sci. 66 (2013) 380–391. https://doi.org/10.1016/j.corsci.2012.10.004.

[154] X. Zhang, F. Wang, Y. Du, Effect of nano-sized titanium powder addition on corrosion performance of epoxy coatings, Surf. Coatings Technol. 201 (2007) 7241–7245. https://doi.org/10.1016/j.surfcoat.2007.01.042.

[155] L. Jian-hua, Z. Zhong-wei, L. Song-mei, Y. Mei, Corrosion resistance of waterborne epoxy coating pigmented by nano-sized aluminium powder on steel, J. Cent. South Univ. 19 (2012) 46–54. https://doi.org/10.1007/s11771-012-0971-z.

[156] Y. Liang, F. Liu, M. Nie, S. Zhao, J. Lin, E. Han, Influence of nano-Al concentrates on corrosion resistance of the epoxy coatings, J. Mater. Sci. Technol. 29 (2013) 353–358.

[157] B. Wetzel, F. Haupert, M.Q. Zhang, Epoxy nanocomposites with high mechanical and tribological performance, Compos. Sci. Technol. 63 (2003) 2055–2067. https://doi.org/10.1016/S0266-3538(03)00115-5.

[158] A.A. Azeez, K.Y. Rhee, S.J. Park, D. Hui, Epoxy clay nanocomposites - Processing, properties and applications: A review, Compos. Part B Eng. 45 (2013) 308–320. https://doi.org/10.1016/j.compositesb.2012.04.012.

[159] S. Ammar, K. Ramesh, I.A.W. Ma, Z. Farah, B. Vengadaesvaran, S. Ramesh, A.K. Arof, Studies on SiO2-hybrid polymeric nanocomposite coatings with superior corrosion protection and hydrophobicity, Surf. Coatings Technol. 324 (2017) 536–545. https://doi.org/10.1016/j.surfcoat.2017.06.014.

[160] C. Mendoza, A. Valle, M. Castellote, A. Bahamonde, M. Faraldos, TiO2 and TiO_2-SiO_2 coated cement: Comparison of mechanic and photocatalytic properties, Appl. Catal. B Environ. 178 (2015) 155–164.

https://doi.org/10.1016/j.apcatb.2014.09.079.

[161] S.K. Dhoke, N. Rajgopalan, A.S. Khanna, Effect of Nanoalumina on the Electrochemical and Mechanical Properties of Waterborne Polyurethane Composite Coatings, J. Nanoparticles. 2013 (2013) 1–11. https://doi.org/10.1155/2013/527432.

[162] S. Ammar, K. Ramesh, B. Vengadaesvaran, S. Ramesh, A.K. Arof, Amelioration of anticorrosion and hydrophobic properties of epoxy/PDMS composite coatings containing nano ZnO particles, Prog. Org. Coatings. 92 (2016) 54–65. https://doi.org/10.1016/j.porgcoat.2015.12.007.

[163] M. Behzadnasab, S.M. Mirabedini, K. Kabiri, S. Jamali, Corrosion performance of epoxy coatings containing silane treated ZrO_2 nanoparticles on mild steel in 3.5% NaCl solution, Corros. Sci. 53 (2011) 89–98. https://doi.org/10.1016/j.corsci.2010.09.026.

[164] B. Willocq, J. Odent, P. Dubois, J.M. Raquez, Advances in intrinsic self-healing polyurethanes and related composites, RSC Adv. 10 (2020) 13766–13782. https://doi.org/10.1039/d0ra01394c.

[165] M. Forsyth, M. Seter, B. Hinton, G. Deacon, P. Junk, New ´Green`Corrosion Inhibitors Based on Rare Earth Compounds, Aust.J.Chem. 64 (2011) 812–819. https://doi.org/10.1071/CH11092.

[166] H. Choi, K.Y. Kim, J.M. Park, Encapsulation of aliphatic amines into nanoparticles for self-healing corrosion protection of steel sheets, Prog. Org. Coatings. 76 (2013) 1316–1324. https://doi.org/10.1016/j.porgcoat.2013.04.005.

[167] X. Fu, L. Tian, Y. Fan, W. Ye, Z.-A. Qiao, J. Zhao, L. Ren, W. Ming, Stimuli-responsive self-healing anticorrosion coatings: from single triggering behavior to synergetic multiple protections, Mater. Today Chem. 22 (2021) 100575. https://doi.org/10.1016/j.mtchem.2021.100575.

[168] R.J. Marathe, V. V. Gite, Encapsulation of 8-HQ as a corrosion inhibitor in PF and UF shells for enhanced anticorrosive properties of renewable source based smart PU coatings, RSC Adv. 6 (2016) 114436–114446. https://doi.org/10.1039/C6RA21684F.

[169] G. Farzi, A. Davoodi, A. Ahmadi, R.E. Neisiany, M.K. Anwer, M.A. Aboudzadeh, Encapsulation of Cerium Nitrate within Poly(urea-formaldehyde) Microcapsules for the Development of Self-Healing Epoxy-Based Coating, ACS Omega. 6 (2021) 31147–31153. https://doi.org/10.1021/acsomega.1c04597.

[170] A.C. Bouali, M. Serdechnova, C. Blawert, J. Tedim, M.G.S. Ferreira, M.L. Zheludkevich, Layered double hydroxides (LDHs) as functional materials for the corrosion protection of aluminum alloys: A review, Appl. Mater. Today. 21 (2020) 100857. https://doi.org/10.1016/j.apmt.2020.100857.

[171] J. Tedim, S.K. Poznyak, A. Kuznetsova, D. Raps, T. Hack, M.L. Zheludkevich, M.G.S. Ferreira, Enhancement of active corrosion protection via combination of inhibitor-loaded nanocontainers, ACS Appl. Mater. Interfaces. 2 (2010) 1528–1535. https://doi.org/10.1021/am100174t.

[172] Y. Wang, D. Zhang, Synthesis, characterization, and controlled release anticorrosion behavior of benzoate intercalated Zn-Al layered double hydroxides, Mater. Res. Bull. 46 (2011) 1963–1968. https://doi.org/10.1016/j.materresbull.2011.07.021.

[173] A.R. Deip, D.A. Leal, G.H. Sakae, F. Maia, M.A.C. Berton, M.G.S. Ferreira, C.E.B. Marino, Performance of commercial LDH traps for chloride ion in a commercial corrosion protection primer for petrochemical industry, Corros. Eng. Sci. Technol. 55 (2020) 66–74. https://doi.org/10.1080/1478422X.2019.1671644.

[174] A. Liu, H. Tian, W. Li, W. Wang, X. Gao, P. Han, R. Ding, Delamination and self-assembly of layered double hydroxides for enhanced loading capacity and corrosion protection performance, Appl. Surf. Sci. 462 (2018) 175–186. https://doi.org/10.1016/j.apsusc.2018.08.109.

[175] A. Javidparvar, R. Naderi, B. Ramezanzadeh, Epoxy-polyamide nanocomposite coating with graphene oxide as cerium nanocontainer generating effective dual active/barrier corrosion protection, Compos. Part B. 172 (2019) 363–375. https://doi.org/10.1016/j.compositesb.2019.05055.

[176] Y. Cao, D. Zheng, J. Luo, F. Zhang, S. Dong, J. Pan, C. Lin, Insight into the Fabrication of ZnAl Layered Double Hydroxides Intercalated with Organic Anions and Their Corrosion Protection of Steel Reinforced Concrete, J. Electrochem. Soc. 166 (2019) C617–C623. https://doi.org/10.1149/2.0361916jes.

[177] Y. Cao, S. Dong, D. Zheng, J. Wang, X. Zhang, R. Du, G. Song, C. Lin, Multifunctional inhibition based on layered double hydroxides to comprehensively control corrosion of carbon steel in concrete, Corros. Sci. 126 (2017) 166–179. https://doi.org/10.1016/j.corsci.2017.06.026.

[178] Z.M. Mir, A. Bastos, D. Höche, M.L. Zheludkevich, Recent advances on the application of layered double hydroxides in concrete-A review, Materials (Basel).

13 (2020) 1–23. https://doi.org/10.3390/ma13061426.

[179] J. Xu, Q. Tan, Y. Mei, Corrosion protection of steel by Mg-Al layered double hydroxides in simulated concrete pore solution: Effect of SO42-, Corros. Sci. 163 (2020) 108223. https://doi.org/10.1016/j.corsci.2019.108223.

[180] T. Siva, S. Sathiyanarayanan, Self healing coatings containing dual active agent loaded urea formaldehyde (UF) microcapsules, Prog. Org. Coatings. 82 (2015) 57–67. https://doi.org/10.1016/j.porgcoat.2015.01.010.

[181] M. Sababi, J. Pan, P.E. Augustsson, P.E. Sundell, P.M. Claesson, Influence of polyaniline and ceria nanoparticle additives on corrosion protection of a UV-cure coating on carbon steel, Corros. Sci. 84 (2014) 189–197. https://doi.org/10.1016/j.corsci.2014.03.031.

[182] L.R.L. Santos, C.E.B. Marino, I.C. Riegel-Vidotti, Silica/chitosan hybrid particles for smart release of the corrosion inhibitor benzotriazole, Eur. Polym. J. 115 (2019) 86–98. https://doi.org/10.1016/j.eurpolymj.2019.03.008.

[183] P. Ghahremani, A.H. Mostafatabar, G. Bahlakeh, B. Ramezanzadeh, Rational design of a novel multi-functional carbon-based nano-carrier based on multi-walled-CNT-oxide/polydopamine/chitosan for epoxy composite with robust pH-sensitive active anti-corrosion properties, Carbon N. Y. 189 (2022) 113–141. https://doi.org/10.1016/j.carbon.2021.11.067.

[184] S. Gu, H. Shi, C. Zhang, W. Wang, F. Liu, E.H. Han, Mesoporous CeO2 containers in water-borne epoxy coatings for dual active corrosion protection of mild steel, Prog. Org. Coatings. 158 (2021) 106376. https://doi.org/10.1016/j.porgcoat.2021.106376.

[185] T. Matsuda, N. Jadhav, K.B. Kashi, M. Jensen, V.J. Gelling, Release behavior of pH sensitive microcapsules containing corrosion inhibitor, Prog. Org. Coatings. 132 (2019) 9–14. https://doi.org/10.1016/j.porgcoat.2019.03.032.

[186] A.B. Cunha, D.A. Leal, L.R. Santos, I.C. Riegel-Vidotti, C.E. Marino, pH-sensitive microcapsules based on biopolymers for active corrosion protection of carbon steel at different pH, Surf. Coatings Technol. 402 (2020) 126338. https://doi.org/10.1016/j.surfcoat.2020.126338.

[187] Y. Feng, S. Chen, F. Cheng, Fabrication of SiO2 nanoparticle–polyelectrolyte nanocontainers with preloaded benzotriazole inhibitors and their self-releasing mechanism and kinetics, J. Mater. Sci. 52 (2017) 8576–8590. https://doi.org/10.1007/s10853-017-1074-x.

[188] A. Khan, A. Hassanein, S. Habib, M. Nawaz, R.A. Shakoor, R. Kahraman, Hybrid Halloysite Nanotubes as Smart Carriers for Corrosion Protection, ACS Appl. Mater. Interfaces. 12 (2020) 37571–37584. https://doi.org/10.1021/acsami.0c08953.

[189] D.I. Njoku, C. Miaomiao, X. Haigang, S. Bailui, L. Ying, Understanding the anticorrosive protective mechanisms of modified epoxy coatings with improved barrier, active and self-healing functiolities: EIS and spectroscopic techniques, Sientific Reports. 7 (2017) 15597. https://doi.org/10.1038/s41598-017-15845-0.

[190] S. Yang, R. Sun, K. Chen, Self-healing performance and corrosion resistance of phytic acid/cerium composite coating on microarc-oxidized magnesium alloy, Chem. Eng. J. 428 (2022) 131198. https://doi.org/10.1016/j.cej.2021.131198.

[191] Y. Ma, J. Song, Y. Jiang, Y. Zhang, J. Gu, Preparation of isocyanate microcapsules by interfacial polymerization/in-situ polymerization and their application in wood adhesives, J. Adhes. (2021) 1988939. https://doi.org/10.1080/00218464.2021.1988939.

[192] B. Ramezanzadeh, G. Bahlakeh, M. Ramezanzadeh, Polyaniline-cerium oxide (PAni-CeO2) coated graphene oxide for enhancement of epoxy coating corrosion protection performance on mild steel, Corros. Sci. 137 (2018) 111–126. https://doi.org/10.1016/j.corsci.2018.03.038.

[193] H. Wei, D. Ding, S. Wei, Z. Guo, Anticorrosive conductive polyurethane multiwalled carbon nanotube nanocomposites, J. Mater. Chem. A. 1 (2013) 10805–10813. https://doi.org/10.1039/c3ta11966a.

[194] X. Liu, Y. Cheng, W. Wang, F. Liu, B. Hou, Application of 1D attapulgite as reservoir with benzotriazole for corrosion protection of carbon steel, Mater. Chem. Phys. 205 (2018) 292–302. https://doi.org/10.1016/j.matchemphys.2017.11.038.

[195] M.D. Wang, M.Y. Liu, J.J. Fu, An intelligent anticorrosion coating based on pH-responsive smart nanocontainers fabricated via a facil method for protection of carbon steel, J. Mater. Chem. A. (2015) 6423–6431. https://doi.org/10.1039/C5TA00417A.

[196] S.A. Haddadi, S.A.A. Ramazani, M. Mahdavian, P. Taheri, J.M.C. Mol, Fabrication and characterization of graphene-based carbon hollow spheres for encapsulation of organic corrosion inhibitors, Chem. Eng. J. 352 (2018) 909–922. https://doi.org/10.1016/j.cej.2018.06.063.

[197] C. Yang, W. Xu, X. Meng, X. Shi, L. Shao, X. Zeng, Z. Yang, S. Li, Y. Liu, X. Xia, A pH-responsive hydrophilic controlled release system based on ZIF-8 for self-healing anticorrosion application, Chem. Eng. J. 415 (2021) 128985. https://doi.org/10.1016/j.cej.2021.128985.

[198] S. Yang, J. Wang, W. Mao, D. Zhang, Y. Guo, Y. Song, J.P. Wang, T. Qi, G.L. Li, pH-Responsive zeolitic imidazole framework nanoparticles with high active inhibitor content for self-healing anticorrosion coatings, Colloids Surfaces A Physicochem. Eng. Asp. 555 (2018) 18–26. https://doi.org/10.1016/j.colsurfa.2018.06.035.

[199] J. Wen, J. Lei, J. Chen, L. Liu, X. Zhang, L. Li, Polyethylenimine wrapped mesoporous silica loaded benzotriazole with high pH-sensitivity for assembling self-healing anti-corrosive coatings, Mater. Chem. Phys. 253 (2020) 123425. https://doi.org/10.1016/j.matchemphys.2020.123425.

[200] J. Wen, J. Lei, J. Chen, J. Gou, Y. Li, L. Li, An intelligent coating based on pH-sensitive hybrid hydrogel for corrosion protection of mild steel, Chem. Eng. J. 392 (2020) 123742. https://doi.org/10.1016/j.cej.2019.123742.

[201] Y. Feng, Y.F. Cheng, An intelligent coating doped with inhibitor-encapsulated nanocontainers for corrosion protection of pipeline steel, Chem. Eng. J. 315 (2017) 537–551. https://doi.org/10.1016/j.cej.2017.01.064.

[202] S. Maleki Dizaj, M. Barzegar-Jalali, M.H. Zarrintan, K. Adibkia, F. Lotfipour, Calcium carbonate nanoparticles as cancer drug delivery system, Expert Opin. Drug Deliv. 12 (2015) 1649–1660. https://doi.org/10.1517/17425247.2015.1049530.

[203] Y. Wu, Y. Duan, J. Qiu, X. Gao, H. Ma, A pH-responsive intelligent coating based on composite CaCO3 microspheres for long-term corrosion protection of Q235 carbon steel, Appl. Surf. Sci. 578 (2022) 151980. https://doi.org/10.1016/j.apsusc.2021.151980.

[204] L.M. Calado, M.G. Taryba, M.J. Carmezim, M.F. Montemor, Self-healing ceria-modified coating for corrosion protection of AZ31 magnesium alloy, Corros. Sci. 142 (2018) 12–21. https://doi.org/10.1016/j.corsci.2018.06.013.

[205] Y. Zhao, Z. Zhang, L. Shi, F. Zhang, S. Li, R. Zeng, Corrosion resistance of a self-healing multilayer film based on SiO_2 and CeO_2 nanoparticles layer-by-layer assembly on Mg alloys, Mater. Lett. 237 (2019) 14–18. https://doi.org/10.1016/j.matlet.2018.11.069.

[206] M.F. Montemor, R. Pinto, M.G.S. Ferreira, Chemical composition and corrosion protection of silane films modified with CeO_2 nanoparticles, Electrochim. Acta. 54 (2009) 5179–5189. https://doi.org/10.1016/j.electacta.2009.01.053.

[207] G. Bahlakeh, B. Ramezanzadeh, M. Ramezanzadeh, Cerium oxide nanoparticles influences on the binding and corrosion protection characteristics of a melamine-cured polyester resin on mild steel: An experimental, density functional theory and molecular dynamics simulation study, Corros. Sci. 118 (2017) 69–83. https://doi.org/10.1016/j.corsci.2017.01.021.

[208] S.V. Harb, A. Trentin, T.A.C. de Souza, M. Magnani, S.H. Pulcinelli, C.V. Santilli, P. Hammer, Effective corrosion protection by eco-friendly self-healing PMMA-cerium oxide coatings, Chem. Eng. J. 383 (2020) 123219. https://doi.org/10.1016/j.cej.2019.123219.

[209] J. Mosa, N.C. Rosero-Navarro, M. Aparicio, Active corrosion inhibition of mild steel by environmentally-friendly Ce-doped organic-inorganic sol-gel coatings, RSC Adv. 6 (2016) 39577–39586. https://doi.org/10.1039/c5ra26094a.

[210] M.F. Montemor, M.G.S. Ferreira, Cerium salt activated nanoparticles as fillers for silane films: Evaluation of the corrosion inhibition performance on galvanised steel substrates, Electrochim. Acta. 52 (2007) 6976–6987. https://doi.org/10.1016/j.electacta.2007.05.022.

[211] R. V. Lakshim, S.T. Aruna, S. Sampath, Ceria nanoparticles vis-á-vis cerium nitrate as corrosion inhibitors for silica-alumina hybrid sol-gel coating, Appl. Surf. Sci. 393 (2017) 397–404. https://doi.org/10.1016/J.APSUSC.2016.10.035.

[212] M. Schem, T. Schmidt, J. Gerwann, M. Wittmar, M. Veith, G.E. Thompson, I.S. Molchan, T. Hashimoto, P. Skeldon, A.R. Phani, S. Santucci, M.L. Zheludkevich, CeO_2-filled sol-gel coatings for corrosion protection of AA2024-T3 aluminium alloy, Corros. Sci. 51 (2009) 2304–2315. https://doi.org/10.1016/j.corsci.2009.06.007.

[213] P. Ghahremani, A.A. Sarabi, S. Roshan, Cerium containing pH-responsive microcapsule for smart coating application: Characterization and corrosion study, Surf. Coatings Technol. 427 (2021) 127820. https://doi.org/10.1016/j.surfcoat.2021.127820.

[214] M. Gobara, A. Baraka, R. Akid, M. Zorainy, Corrosion protection mechanism of Ce4+/organic inhibitor for AA2024 in 3.5% NaCl, RSC Adv. 10 (2020) 2227–2240. https://doi.org/10.1039/c9ra09552g.

[215] L.M. Calado, M.G. Taryba, Morozovo, Y., M.J. Carmezim, M.F. Montemor, Novel smart and self-healing cerium phosphate-based corrosion inhibitor for AZ31 magnesium alloy, Corros. Sci. 170 (2020) 108648. https://doi.org/10.1016/j.corsci.2020.108648.

[216] L.M. Calado, M.G. Taryba, Y. Morozov, M.J. Carmezim, M.F. Montemor, Cerium phosphate-based inhibitor for smart corrosion protection of WE43 magnesium alloy, Electrochim. Acta. 365 (2021) 137368. https://doi.org/10.1016/j.electacta.2020.137368.

[217] Y. Morozov, L.M. Calado, R.A. Shakoor, R. Raj, R. Kahraman, M.G. Taryba, epoxy coatings modified with a new cerium phosphate inhibitor for smart corrosion protection of steel, (2019) 108–128. https://doi.org/10.1016/j.corsci.2019.108128.

[218] D.A. Leal, I.C. Riegel-Vidotti, M.G.S. Ferreira, C.E.B. Marino, Smart coating based on double stimuli-responsive microcapsules containing linseed oil and benzotriazole for active corrosion protection, Corros. Sci. 130 (2018) 56–63. https://doi.org/10.1016/j.corsci.2017.10.009.

[219] S.J. García, H.R. Fischer, S. Van Der Zwaag, A critical appraisal of the potential of self healing polymeric coatings, Prog. Org. Coatings. 72 (2011) 211–221. https://doi.org/10.1016/j.porgcoat.2011.06.016.

[220] R. Raj, M.G. Taryba, Y. Morozov, R. Kahraman, R.A. Shakoor, M.F. Montemor, On the synergistic corrosion inhibition and polymer healing effect of polyolefin coatings modified with Ce-loaded hydroxyapatite particles on steel, Electrochim. Acta. 388 (2021) 138648. https://doi.org/10.1016/j.electacta.2021.138648.

[221] C. Liu, H. Zhao, P. Hou, B. Qian, X. Wang, C. Guo, L. Wang, Efficient Graphene/Cyclodextrin-Based Nanocontainer: Synthesis and Host-Guest Inclusion for Self-Healing Anticorrosion Application, ACS Appl. Mater. Interfaces. 10 (2018) 36229–36239. https://doi.org/10.1021/acsami.8b11108.

[222] Y. Ye, H. Chen, Y. Zou, Y. Ye, H. Zhao, Corrosion protective mechanism of smart graphene-based self-healing coating on carbon steel, Corros. Sci. 174 (2020) 108825. https://doi.org/10.1016/j.corsci.2020.108825.

[223] S. V. Harb, M.S. Rodrigues, T.A.C. de Souza, A. Trentin, M.C. Uvida, D.J. Pochapski, S.H. Pulcinelli, C. V. Santilli, P. Hammer, Smart PMMA-cerium oxide anticorrosive coatings: Effect of ceria content on structure and electrochemical properties, Prog. Org. Coatings. 161 (2021) 106548.

https://doi.org/10.1016/j.porgcoat.2021.106548.

Chapter 2

Electrochemical Techniques

Electrochemical techniques are essential analytical tools in the field of corrosion research. They provide a series of vital information to understand the different corrosion mechanisms, the reaction kinetics, and the interpretation of complex ongoing events during the corrosion of metals or degradation of coatings [1]. One can classify the electrochemical techniques into two main groups: averaged and localized ones. While the averaged or global techniques show the average response of the whole system, the localized techniques can analyze a small area of the sample with high spatial resolution. In this work, Electrochemical Impedance Spectroscopy was used to evaluate the global corrosion protection properties of the coatings. Moreover, three localized techniques, namely, Localized Electrochemical Impedance Spectroscopy, Scanning Vibrating Electrode Technique, and Scanning Ion-Selective Electrode Technique, were employed to evaluate the corrosion and corrosion inhibition processes in coated metal systems locally. Therefore, in this chapter, the basic theory behind these electrochemical techniques is discussed in brief.

2.1 Electrochemical Impedance Spectroscopy (EIS)

Resistance (R) as the ability of material to prevent the flow of electric current is a well-known term, and its relationship with voltage (V) and current (I) explains by Ohm´s law ($R = \frac{V}{I}$) [2], however, the relationship is valid just for DC signals. Using a.c. signals, the relationship will be more complex, but a frequency-dependent analysis of the system provides valuable information which could not be obtained by DC techniques [3]. EIS as a powerful technique for evaluating an electrochemical system is based on the application of a very small (mV) sinusoidal potential perturbation at various frequencies on a stationary electrochemical system, described by equation 2.1 [4]:

$$V_t = V_0 \sin(\omega t) \qquad \text{Eq. 2.1}$$

where V_t is the potential of perturbation, V_0 is the amplitude of the signal, and ω is the angular frequency, which can be converted to the frequency (f) according to equation 2.2:

$$\omega = 2\pi f \qquad \text{Eq. 2.2}$$

For such a small perturbation, the resulting current response (I_t), described by equation 2.3, is approximately linear, suffers a phase shift (φ) in relation to an applied potential (Figure 2.1), and has a different amplitude (I_0).

$$I_t = I_0 \sin(\omega t + \varphi) \qquad \text{Eq. 2.3}$$

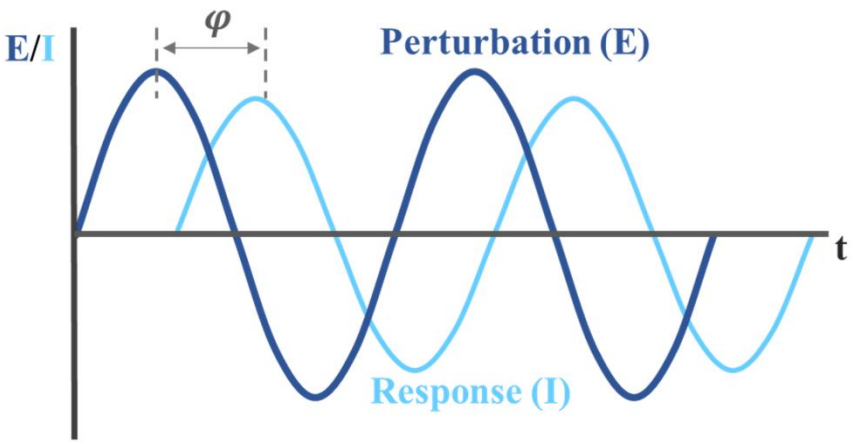

Figure 2.1 A sinusoidal perturbation signal (potential) applied during EIS and a sinusoidal current response signal with a phase shift (φ) between two signals.

According to Ohm´s law, the impedance (Z) in analogous to R can be described as the ratio of the potential (V) to the I, as shown in equation 2.4:

$$Z = \frac{V}{I} = \frac{V_0 \sin(\omega t)}{I_0 \sin(\omega t + \varphi)} = Z_0 \frac{\sin(\omega t)}{\sin(\omega t + \varphi)} \qquad \text{Eq. 2.4}$$

In other words, the modulus of the complex impedance is the ratio between the modulus of the potential and the modulus of the current. At the same time, its phase is the phase difference between voltage and current. Thus, impedance can be written as a complex quantity with a real and an imaginary part according to equation 2.5:

$$Z_\omega = Z_0(\cos\varphi + j\,(\sin\varphi)) = Z_{Re} + j\,Z_{Im} \qquad \text{Eq. 2.5}$$

where Z_{Re}, and $j\,Z_{Im}$ account for the real, and the imaginary components of the complex impedance respectively [2,5].

Bode and Nyquist plots are often used to represent the EIS data (Figure 2.2). Bode plot (Figure 2.2b) is usually a combination of a Bode magnitude plot, expressing the magnitude of the frequency response (the commonly used unit isOhm.cm^2 (Ω cm^2)), and a Bode phase plot, expressing the phase shift (φ) both on the Y-axis, versus log frequency in Hertz on the X-axis [6].

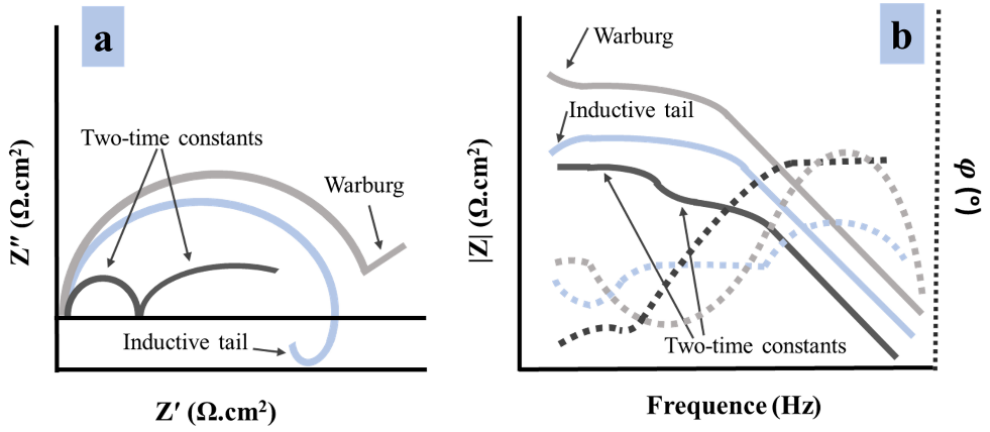

Figure 2.2 Schematic representation of a) Nyquist b) Bode plots, evidencing a spectrum with two-time constants, one with a low frequency inductive loop, and one with a Warburg element.

Nyquist plot is a linear graph of the negative imaginary part of the impedance (Z″) on the Y-axis versus the real part of the impedance (Z′) on the X-axis. Practically, the Nyquist plot describes the impedance in relation to the area, the unit for both Z″ and Z′ is Ω cm^2. In Nyquist plot |Z| represents as a vector and the angle (φ) between this vector and the X-axis, known as "phase angle". While both Bode and Nyquist plots have their advantages in offering the information regarding the deterioration of an electrochemical system, showing the frequency of each measured point makes the Bode plot more attractive to represent the EIS data. The Nyquist plot, in turn, clearly indicates the time constants (Figure 2.2a) [6].

A series of valuable information like the number of time constants, capacitive, resistive, or inductive behavior of a system, can be extracted by looking into the Nyquist and Bode plots. Moreover, the low-frequency impedance modulus ($|Z|_{LF}$) is often used to evaluate organic coatings´ overall corrosion protection performance [7]. Figure 2.3 shows a set of $|Z|_{LF}$ data collected by Gray et al. They summarised a large quantity data extracted from literature on EIS laboratory and fieldwork in a simple graph [8]. This graph gives a general insight into the global protection property of an organic coating.

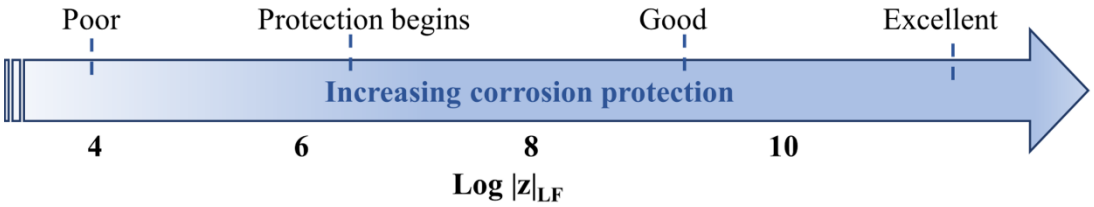

Figure 2.3 Low frequency impedance moduli, as a global protection property of an organic coating. Image adapted from [8] with permission.

The EIS data is valid if only: i) the system stays stable and returns to its original state when the perturbation stops, ii) the response of the system should be only due to the applied perturbation, and iii) the impedance of the system should be independent of the magnitude of the perturbation [4,9]. In these conditions, EIS allows to differentiate electrochemical events ongoing in a system, as each process manifests at different rate and at different frequency [6].

Moreover, different electrochemical phenomena depend on different variables. For instance, the resistive response is frequency independent, but inductive and capacitive responses are frequency dependent. Therefore, they can be distinguished from each other in an electrochemical system by EIS.

It is common to fit the impedance data with electrical equivalent models to separate the contribution of all elements of the system, to identify possible reactions, and to explain the physical processes ongoing in the system under analysis. [5]. These models consist of different electrical components such as resistors, capacitors, and conductors to simulate the electrochemical events within an equivalent electrical circuit (EEC). Additionally, Warburg elements can be introduced to the EEC, to account for mass transport. The essential components in a corroding system are:

The resistor is used to simulate the conductivity of the solution (R_s) or the charge transfer resistance of the dissolving metal (R_{ct}). Being frequency-independent, resistor contributes only to the real part of the impedance (equation 2.6).

$$Z = R \qquad \text{Eq. 2.6}$$

The capacitor (C) simulates double layers at metal surfaces or dielectric oxide barrier layers such as the one of aluminum, which describes according to equation 2.7, where $j = \sqrt{-1}$

$$Z = \frac{1}{j\omega C} \qquad \text{Eq. 2.7}$$

A constant phase element (CPE) is often used instead of a capacitor to include the non-ideal nature of real electrochemical systems that shows a capacitive behavior. CPE can be written according to equation 2.8. It is equal to a C if $n = 1$ and comparable to a pure resistor if $n = 0$.

$$Z = \frac{1}{(j\omega)^n . Y_0} \qquad \text{Eq. 2.8}$$

An electrochemical system containing a coated metal, in most cases, can be simulated with one of the electrical circuits shown in Figure 2.4.

An undamaged coating usually has a very high impedance. Such a high impedance can be simulated with a model comprising a resistor in series with a capacitor (Figure 2.4a) in respect of solution resistance (R_s), and coating capacitance CPE_c respectively. The Bode plot and the Nyquist correlated to such a system shows in Figure 2.4a. Both Bode and Nyquist plots indicate a fully capacitive response of the coated metal evidenced by a capacitive slope (≈ -1) in the impedance modulus plot and phase angle values of approximately -90° in the phase plot [10].

An EEC showed in Figure 2.4b includes a one resistor for solution resistance (R_s), and a set of capacitor/resistor for coating capacitance (CPE_c), and the pore resistance of the coatings (R_p) respectively The Nyquist plot, in this case, shows the typical semicircle, and the impedance modulus at low frequency shows a small plateau, which is associated with a decrease in phase angle.

An EEC showed in Figure 2.4c is also used to fit the EIS experimental data of a coated system. In this EEC, an extra set of capacitor/resistor was added in respect of double layer capacitance (CPE_{dl}) and the Faradic resistance (R_{ct}), respectively. In fact, this extra capacitor/resistor, represents the corrosion process at the interface of metal/coating [10]. The Nyquist plot, in this case, shows two semicircles, and the impedance modulus shows a plateau at low/middle frequency, which is associated with a decrease in phase angle.

After selecting the proper EEC for a system, the fitting of experimental data should be carried on by computer software. However, validation and interpretation of obtained values is a time-consuming task.

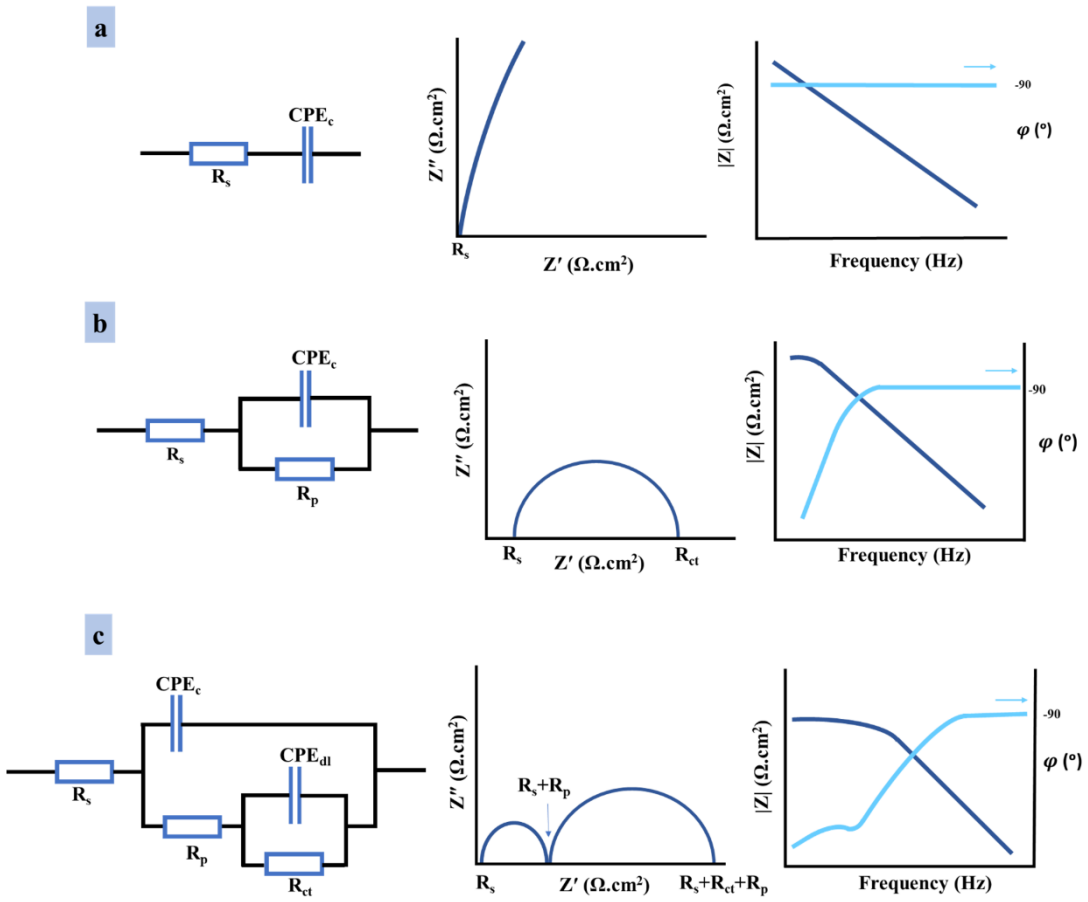

Figure 2.4 EEC, Nyquist, and Bode plots of a coated metal a) un-damaged coating, b) coating showing both capacitive and resistive behavior, and c) a set of resistor-capacitor was added, representing the corrosion process.

A review of the literature reveals the successful application of EIS to study the protective properties of polymeric coatings [11–14], their degradation trend [15], their self-healing properties [13], and the change of the corrosion mechanism due to characteristic changes in EIS spectra [16], during exposure to a corrosive media. The technique was also successfully used to evaluate and to study the effectiveness of corrosion inhibitors [17]. Falcón et al. [18], studied the release of DDA as corrosion inhibitor for carbon steel from SiO_2 nano containers. Inhibitor loaded nanocontainers was added into 0.1 mol/L NaCl solution at various pH (pH = 2, 6.2, and 9). From an increase in the capacitive arc diameter in Nyquist plots and an increasing trend in $|Z|_{LF}$, they conclude the efficient and time dependent release of inhibitor at pH values under 3 (Figure 2.5) [18]. Morozov et al. [19], also used EIS to study the effectiveness of cerium organophosphate as corrosion inhibitor for corrosion protection of bare carbon steel. Evolution of $|Z|_{LF}$ showed the ability of cerium organophosphate for corrosion suppression of carbon steel, when 4 wt% of

inhibitor was added to 0.05 M NaCl solution. Authors also studied the corrosion protection properties of epoxy coatings containing various quantity of this inhibitor using EIS. Evolution of $|Z|_{LF}$ also demonstrated that epoxy coatings modified with addition of 1 wt% of this corrosion inhibitor, showed higher global protection properties compared to the reference epoxy and those coatings modified with 0.1 and 0.5 wt% of inhibitor [19].

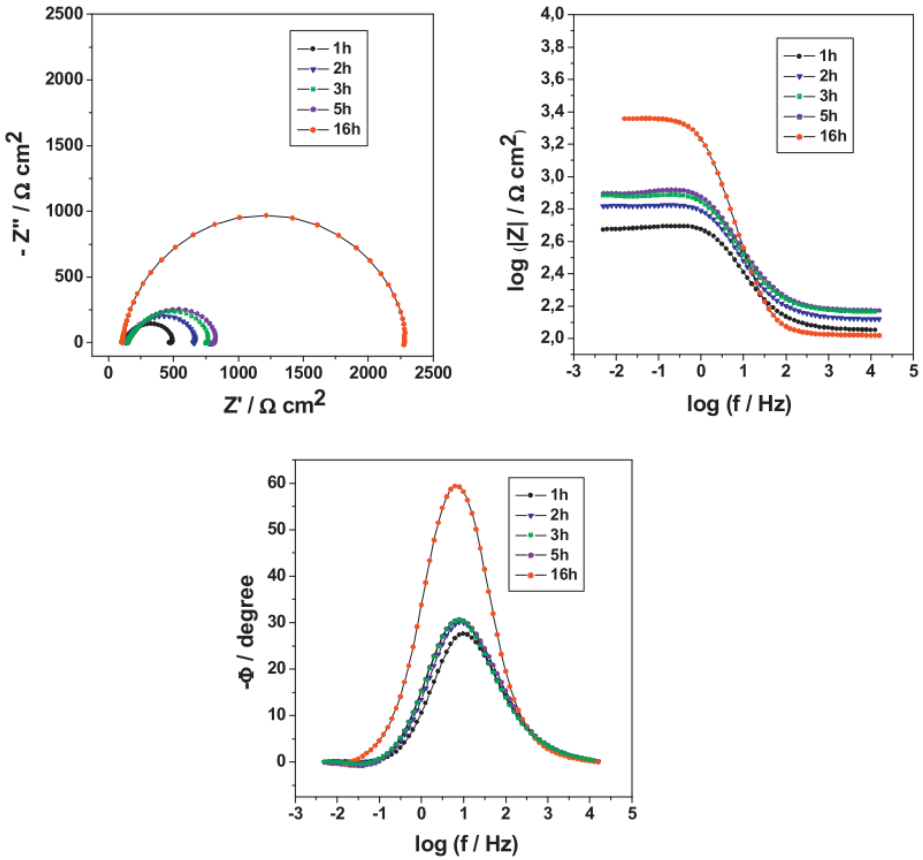

Figure 2.5 a) Nyquist, b, c) Bode plots of carbon steel after different immersion times in 0.1 mol/L NaCl solution at pH = 2 containing 1 wt.% of nanocontainers with encapsulated DDA. Image reprinted from [18] with permission.

The set up for an EIS experiment is relatively simple: the well-known area of the sample (working electrode) to be studied, is immersed in an electrolyte, together with appropriate reference and counter electrodes (Figure 2.6).

EIS is usually not very time consuming. However, as mentioned before, overall data interpretation can be a complex, and time-consuming task.

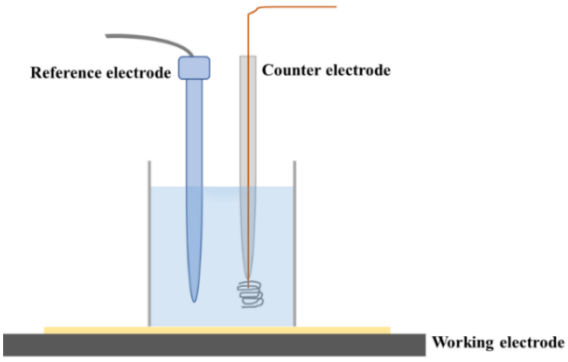

Figure 2.6 Typical sample setup of EIS experiment.

Although EIS is frequently used to evaluate intact coatings, many authors also employed this technique to study coatings containing artificial defects to expose the underlying substrate [13,20,21]. While in such a case still EIS can provide useful information regarding the self- healing ability of coatings, but detected signals provide a surface averaged response included those signals from artificial defect [20] and is not possible to accurately study the phenomena over the scratches. Therefore, localized techniques have been employed to further study of coated materials.

2.2 Localized Electrochemical Impedance Spectroscopy (LEIS)

LEIS with the identical basic principles of EIS, was designed to measure the local impedance of an electrode. It can be performed at a single frequency to map the local impedance of a sample, or a stationary probe can measure the full EIS spectrum by varying the a.c. frequency.

The technique is based on the premise that, in a conventional three-electrode a.c. impedance measurement, the a.c. current densities in a close vicinity to the working electrode is proportional to the local impedance properties of that electrode [22]. A schematic representation of equipotential and current lines formed over an active corrosion site of a working electrode shows in Figure 2.7.

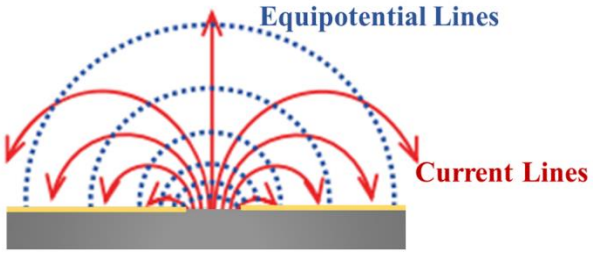

Figure 2.7 Equipotential surfaces and current flux lines generated in a local corrosion cell. Scheme adapted from [40] with permission.

To collect the LEIS data, the a.c. potential drop between planes parallel to the electrode should be measured on a relatively small scale. To do so, a bi-electrode microprobe, shown in Figure 2.8a-set, should be employed.

A sinusoidal voltage perturbation is applied between the working electrode (sample) and the reference electrode, and local impedance data are derived by determination of the ratio between the applied a.c. voltage perturbation and the component of local a.c. current density in the solution normal to the substrate surface, as a function of frequency [23]. The a.c. potential difference between the two probe electrodes is measured and converted into current density values according to equation 2.9:

$$i(\omega)_{local} = \frac{\Delta V(\omega)_{prob} \times \sigma}{l} \qquad \text{Eq. 2.9}$$

where $i_{(\omega)local}$ is the local a.c. current density in solution at the probe tip, $\Delta V_{(\omega)probe}$ is the a.c. potential difference between the two probe electrodes, σ is the electrolyte conductivity of aqueous medium, and *l* is the distance separating the two probe electrodes. Furthermore, from the local a.c. current density, the magnitude of local impedance (area normalized) can be determined according to equation 2.10:

$$|z(\omega)|_{local} = \frac{V(\omega)_{applied}}{i(\omega)_{local}} = \frac{V(\omega)_{applied}}{\Delta V(\omega)_{prob}} \times \frac{l}{\sigma} \qquad \text{Eq. 2.10}$$

where $V(\omega)_{applied}$ is the applied a.c. voltage perturbation. It should be noted that, for this derivation to be valid, it is assumed that the local a.c. current density in solution at the probe tip is equal to the current density at the sample surface, i.e., all the a.c. current at the probe tip is travelling normal to the sample surface. A typical setup for a LEIS experiment (Figure 2.8), includes a five-electrode system: a conventional three-electrode arrangement (calomel electrode as a reference, platinum mesh or carbon rod as counter, and sample as a working electrode), and an additional LEIS bi-electrode probe. The bi-electrode probe (Figure 2.8a-set) is fixed on a scanning head, above the working electrode (sample under study). Stepper motors ensure a precise X, Y, Z positioning of this prob with the accuracy of 1 μm, allowing for accurate scanning of the probe over the sample surface in three dimensions. The LEIS bi-electrode probe as a most important element of this set up designed to measure a normal component of current density in the solution by sensing the a.c. potential difference between planes parallel to the electrode (Figure 2.7). The prob can be designed as needed, however in most of the cases it is consisted of two metallic wires (mostly platinum wires).

The probe used for the work presented in this Thesis was supplied by Uniscan Instruments, Inc. and is composed of a platinum ring as upper electrode and a platinum tip as lower electrode (Figure 2.7a-set). To improve spatial resolution, the probe tip can be cut and modified as a disk. Further improvement may be done by deposition of platinum black on the tip of prob to increase surface area and capacitance. This can improve the signal to noise ratio by increasing the prob sensibility.

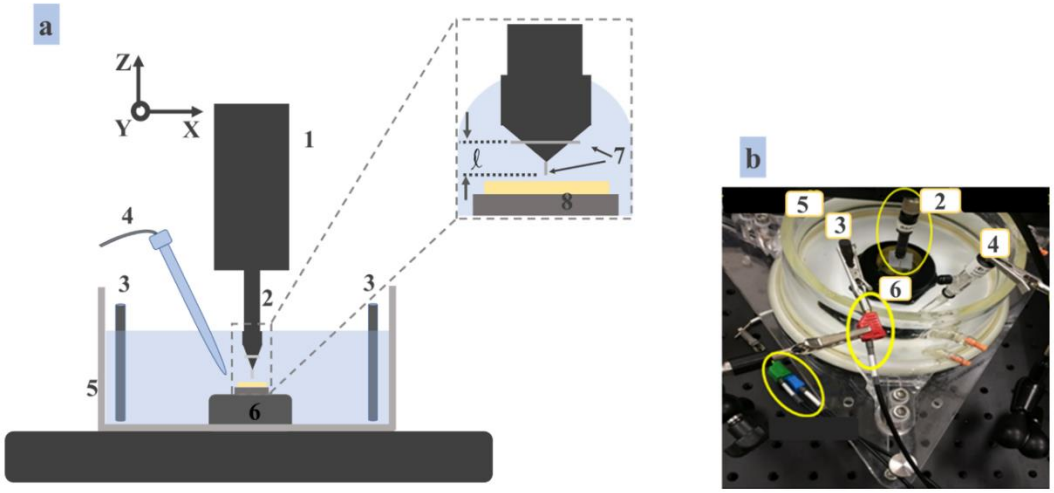

Figure 2.8 a) Schematic representation of typical LEIS setup, b) a top view of the experimental setup (some connections also marked on the image). 1 – Scanning head, attached to stepper motors for accurate X, Y, Z probe placement; 2 – bi-electrode probe; 3 – counter electrodes (graphic rods); 4 – Reference electrode 5 – Electrochemical cell containing a Plexiglas container, the electrolyte, and the sample inserted into the sample holder (6); 7 – two platinum wires allocated with the distance (l); 8 – working electrode (coated sample).

Being a sensitive measuring equipment, several precautions should be taken in account to obtain reliable result. The system should be isolated from any small mechanical vibration, and any airborne electromagnetic interference available around the equipment. The operation temperature should be kept between 10° to 25°C. The system calibration should be performed, to ensure the hardware and software are operating correctly [24].

Both sample preparation, and sample positioning at the center of the Plexiglas container, are not straightforward, and can be quite time consuming. The surface of sample to be studied should be as flat as possible preventing contact between the tip of LEIS probe and the sample surface during measurement [28]. Also, to avoid misleading signals, the samples need to be masked with beeswax and only the area of interest should be exposed for the measurement.

LEIS has provided the opportunity to probe the electrochemical events on the localized level [23,25]. Therefore, the technique is widely used for characterization of corrosion [26,27], degradation of coating [22,23,28], evaluation of protective properties of coatings [29], coating delamination [30], inhibitor performance [31], and self-healing ability of coating [19,32–34]. Being a microscopic technique, it may also be employed to evaluate the electrochemical activity of microscopic inclusions present in metals or alloys (Figure

2.9) [35]. Most recently LEIS found its place to visualization and characterization of solid/liquid [36], and heterogenous [37] interfaces.

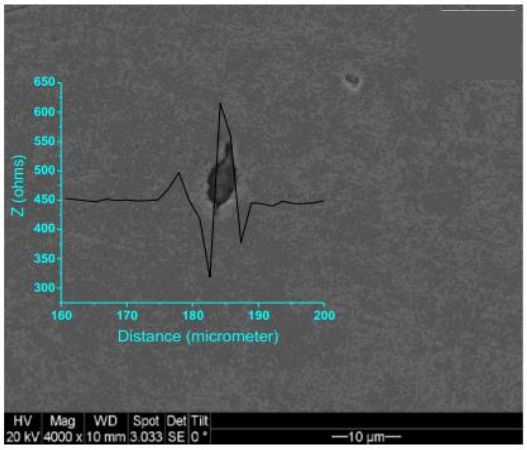

Figure 2.9 LEIS map taken across the micro-inclusion in an X-100 steel. Image adapted from [35] with permission.

Several research groups used LEIS to evaluate self-healing performance of organic coatings for protection of steel substrates [15,19,31,34]. As an example, Ye et al. [15], studied the self-healing performance of an epoxy coating modified with graphene sheets loaded with BTA as a corrosion inhibitor, for corrosion protection of carbon steel. They studied carbon steel samples covered with pure epoxy, epoxy modified with graphene sheets, and epoxy modified with BTA-loaded graphene sheet. Coatings included an artificial point defect were immersed into the 3.5 wt% of NaCl solution to be evaluated by LEIS. The efficient release of BTA, and self-healing ability of coating modified with BTA-loaded graphene sheets were demonstrated by decreasing trend of admittance (inverse of impedance) over the defect [15].

Some authors used LEIS as a complimentary technique to get insight into the corrosion mechanism. For instance, Zhong et al. [26], successfully studied the corrosion mechanism of steel under the defected coating. According to the data collected by LEIS (Figure 2.10), authors concluded that the corrosion mechanism at the defect site is strongly related to the size of defect. They stated that: LEIS allows to characterize microscopically the local electrochemical corrosion reaction of steel under the defected coating.

Indira et al. [38], studied the effect of immersion time and Cl^- ion concentration on the early stage of corrosion, for both carbon steel, and low alloy steel using LEIS. LEIS probe scanned the epoxy coated samples containing an artificial scratch exposed to various concentration of NaCl solutions. They found LEIS a reliable technique to study the

electrochemical reactions around the scratch defect at the early stages of corrosion process [38].

In this PhD work LEIS was used as spatially resolved technique to evaluate the inhibition effectiveness and self-healing performance of the developed coatings. The combination of data obtained by EIS and LEIS give important insights into the self-healing ability of an organic coating. However, other localized technique like SVET, and SIET can offer additional information, which may lead to deeper understanding of the protection mechanism of a specific coating.

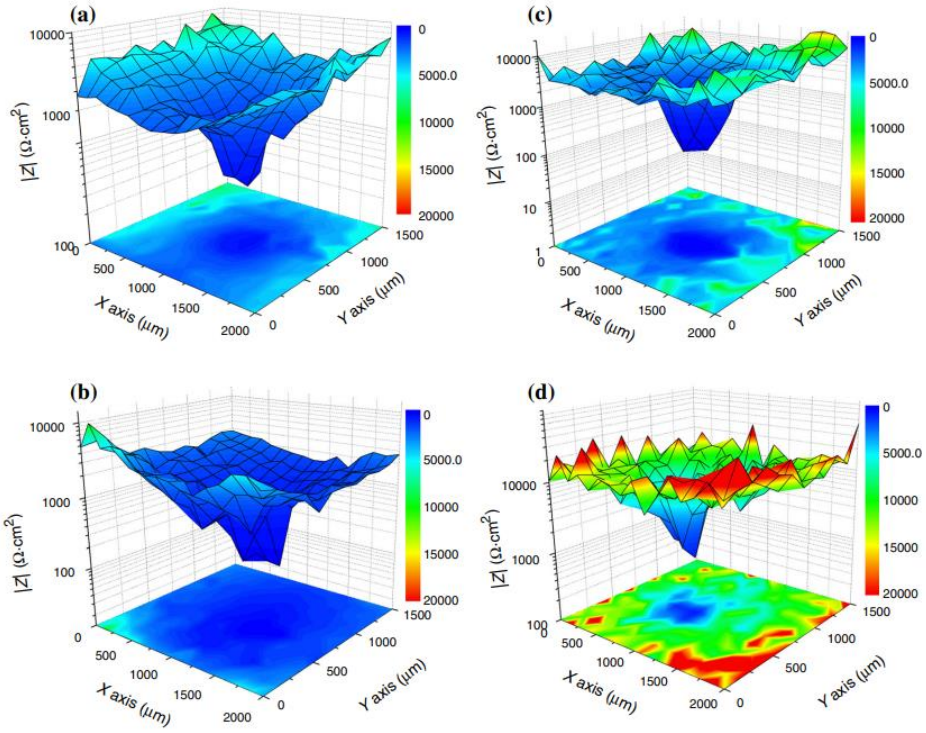

Figure 2.10 LEIS maps around the defective area of the epoxy coating after a) 3 h b) 12 h, c) 32 h, and d) 164 h immersion in NaCl solution. Image re-printed from [29] with permission.

2.3 Scanning Vibrating Electrode Technique (SVET)

Originally SVET was developed for biomedical and physiological applications, e.g. monitoring of ionic gradients around cells [39]. As a nondestructive technique SVET found its place for corrosion study in the eighties. The measurement principle is based on the difference of the electrolyte potentials at two points due to an ionic flux in the solution. This flux originates in the electrolyte solution from the redox reaction at the surface of the metallic substrate due to ongoing anodic and cathodic processes (Figure 2.7).

Therefore, the technique can identify the zones with positive and negative ionic flow above the electroactive surface [39,40]. Current density close to zero may indicate either inactive surface or the frontier between positive and negative ionic flows.

In a SVET measurement, potential difference in solution between the extreme points of the vibration amplitude (equipotential lines), is measured by a vibrating microelectrode (Figure 2.11c), close to the surface (typical distance varies from 50 to 200 μm). Since the amplitude of this vibration is relatively small (usually around 30 μm), the electric field over this distance can be considered constant.

For such a system, Ohm's law can be applied to calculate the local ionic current density (j_{local}), in the direction of probe vibration, from the potential difference (ΔV) (equation 2.11):

$$j_{local} = -\frac{\Delta V}{k \cdot d} \qquad \text{Eq. 2.11}$$

where *k* is the conductivity of the solution and *d* the distance between the two points of measurement.

Most SVET systems measure current density in two directions. Typically, only vertical component of current density, normal to the surface, is analyzed [39].

Figure 2.11b shows a typical electrochemical cell and an example of set up used for SVET measurement. The sample fixed in an epoxy holder and the adhesive tape around it, makes a small solution reservoir on top of the sample. A thin layer of beeswax isolates the sample from the solution and only the area of interest is in contact with electrolyte. Normally, SVET measurements are performed in a conductive aqueous solution.

The vibrating electrode (Figure 2.11c) is platinum/iridium (80/20 %) electrode, 1.5 cm long, coated with a polymer (parylene C) except at the tip. The tip with an approximate diameter of 10 μm is platinized, to increase the surface area of the tip and therefore the signal-to-noise ratio is strongly increased [41].

The SVET microelectrode is connected to a linkage with two piezoelectric oscillators (Figure 2.11a), with each responsible for the X, and Z direction vibrations. The vibration creates a signal modulation (sinusoidal signal) that after passing through a lock-in amplifier, substantially reduces the influence of noise, i.e. the signal-to-noise ratio is increased [42].

The vibration frequency is usually in a range between 55 - 400 Hz, and the amplitude of vibration varies between 20-30 μm (peak-to-peak). A three stepper motors, with resolution of less than 1 μm, are used for positioning and movement of the probe over the

sample surface in the X, Y, and Z directions. The measurement is performed with the probe vibrating at the fixed frequencies at which the system was calibrated. Two Pt black electrodes are employed to provide the necessary reference and ground during the measurements. By signal amplification, SVET can measure current densities as low as nA/cm². To avoid interference of stray currents and mechanical disturbances, the measurements is performed in a Faraday cage and equipment is installed on an antivibration table (highly recommended).

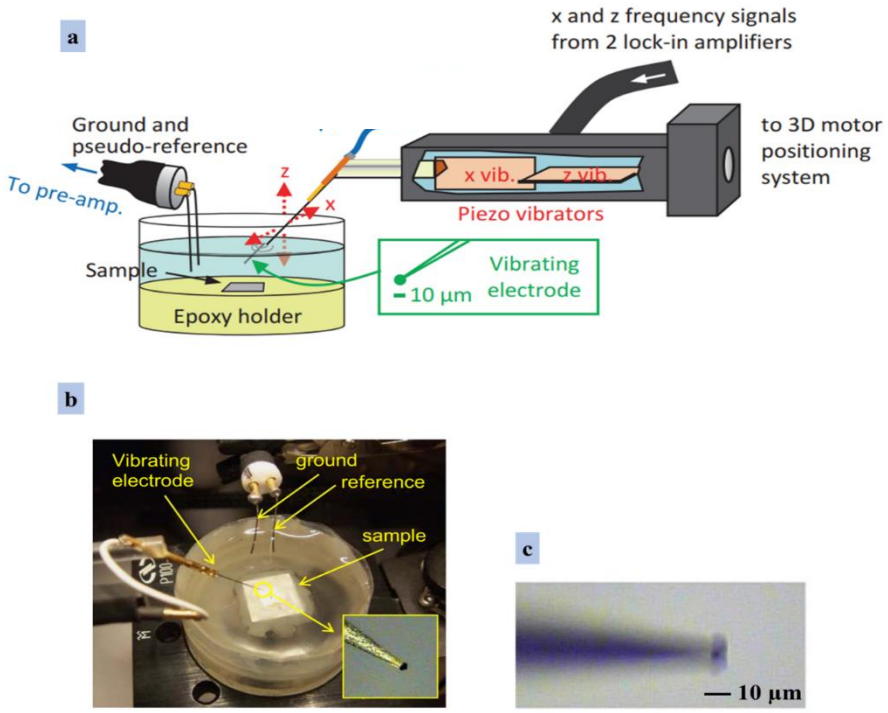

Figure 2.11 a) Typical setup for a SVET measurement. (Scheme adapted from [40] with permission, b) electrochemical cell for SVET experiments and set SVET electrode with platinum black deposited at the tip (Image adapted from [42] with permission), c) vibrating SVET electrode (Image adapted from [39] with permission).

In practice, the relation between the potential measured by SVET and the current density associated to it is obtained by calibration. Calibration can be performed in different ways that depend on the equipment and detailed information regarding the calibration process can be found elsewhere [42].

In practice, the relation between the potential measured by SVET and the current density associated to it is obtained by calibration. Calibration can be performed in different ways that depend on the equipment and detailed information regarding the calibration process can be found elsewhere [42].

The SVET results can be presented in different ways, 2D maps, 3D maps, and simple plots of current density versus distance among others. The technique is extensively used to study corrosion and corrosion mechanisms of metallic substrates, to evaluate coating quality and identification of defects, and to study the self-healing properties of a coating [43–45]. The technique also has its place to study interfaces [46,47] (e.g., metal/weld interface), and inhibition effect of corrosion inhibitors for specific metals [18,46,48–50]. Schmitzhaus et al. [50], used SVET to study anticorrosive performance and the inhibition mechanism of ionic liquid (N-methyl-2-hydroxyethylammonium oleate,[m- 2HEA][Ol]) as corrosion inhibitor for steel (Figure 2.12). They also studied the effect of concentration of sodium chloride in the corrosive medium by SVET. Authors could successfully support the results obtained by SVET measurements, using surface characterization and global electrochemical techniques [50].

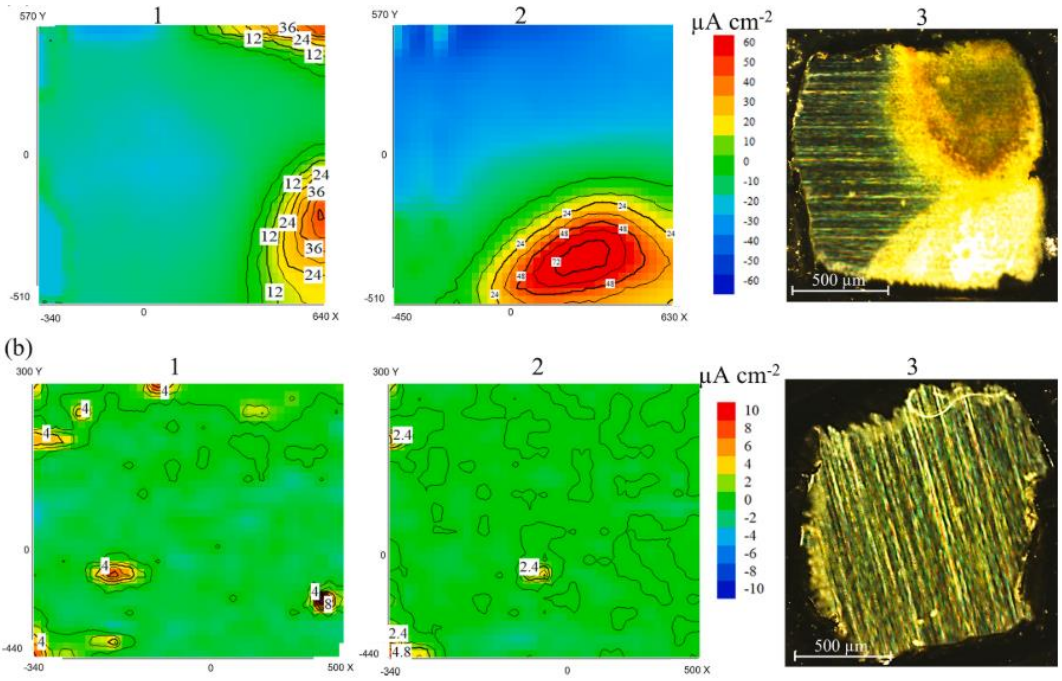

Figure 2.12 Current density mapping of pure iron exposed to a) control sample in 0.03 mol/L NaCl solution, b) 0.03 mol/L NaCl + 1 µmol/L [m-2HEA][Ol]. Image re-printed from [50] with permission.

Hao et al. [45], used SVET to investigate the self-healing properties of epoxy coating modified by 0.5wt % of graphene@PANI@BTA. The successful release of BTA, and the self-healing ability of modified coating was confirmed by SVET measurements. Authors compared two carbon steel substrates coated with reference epoxy, and modified epoxy by SVET, when artificial defects were produced in both coatings, to expose steel substrate to NaCl solution. The self-healing ability of modified coating was confirmed by reduction

of maximum cathodic and anodic current density over the defects, revealed by SVET maps after 24h of immersion in 3.5 wt% NaCl solution (Figure 2.13) [45].

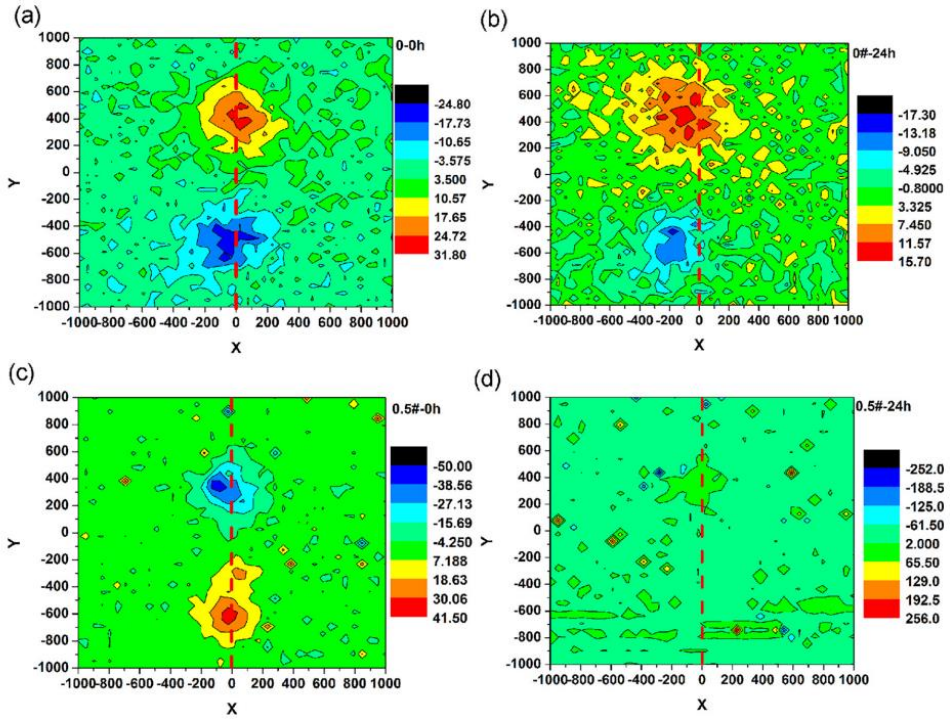

Figure 2.13 SVET current density maps of steel coated with epoxy coatings contain defects immersed in 3.5 wt% NaCl solution a,b) for reference epoxy; c,d) for epoxy coating modified with 0.5 wt% of graphene@PANI@BTA, after 0 h, and 24 h of immersion. Image re-printed from [45] with permission.

Samiee et al. [51], also studied the smart corrosion protection properties of a water-based hybrid organo-silane film modified with non-toxic organic/inorganic eco-friendly corrosion inhibitors on mild steel, by SVET. A reference water-base hybrid organo-silane was modified with addition of praseodymium cations (Pr3+) and BI inhibitors. Authors studied both reference and modified coatings by immersion of coatings contain artificially made defects into the 3.5 wt% NaCl solution. Authors observed the decreasing trend of both anodic and cathodic current density recorded around the defect sites of modified coating. They concluded that the release of inhibitors in the scratch is responsible for decreased corrosion activities around the scratch. i.e., effective release of both inhibitor and as a consequence self-healing ability of modified coating was confirmed by evolution of current density over the defects recorded by SVET [51]. Cotting et al. [52], incorporated various quantity of poly (urea-formaldehyde-melamine) (PUFM) MCs containing a commercial epoxy ester resin into a three-layer epoxy coating to develop self-healing multilayer coatings. Authors studied the self-healing ability of developed

systems by SVET. SVET was performed over one artificial scratch in coatings without MCs, with 10 wt %, and 15 wt % of MCs. Samples were immersed into a 0.01 M NaCl solution during the 24 h of SVET measurements. Authors concluded that the highest concentration (15 wt. %) of MCs in the coating system led to a more effective self-healing effect, proved by SVET[1][52].

Although SVET is considered a powerful technique to evaluate the corrosion events, the technique suffers some limitations which is important to be considered when analyzing the data: i) the current density is a 3D vector and SVET measures only one (Z) or two (X and Z) components, this may lead to underestimate the ongoing corrosion events in the system under the study; ii) for small defects (several micrometer) available in the coating, the current density flow may not reach to the probe level (located about 100 µm over the ample surface) and therefore these small defects cannot be detected by SVET prob; iii) delamination, blistering and in general underneath events cannot be detected; iv) SVET is not recommended for relatively fast or too slow systems [40].

2.4 Scanning Ion-Selective Electrode Technique (SIET)

Like SVET, at first SIET was introduced by biomedical scientists [53]. SIET as a complement technique to SVET, is a micro-potentiometric tool, used to identify and detect some of the ions involved in the corrosion process, e.g., OH^-, and H^+. While these ions are mainly responsible for localise alkalization or acidification at anodic and cathodic sites respectively, several other ions also may identified by this technique [40].

The technique is based on potentiometric measurement between two electrodes: a reference electrode, usually an Ag/AgCl electrode, and an ion-selective microelectrode (ISME). The latest which is also an Ag/AgCl, contains an electrolyte with a constant concentration of the ion of interest, and a selective ionophore-based oil-like membrane at the tip. In the case of commercial SIET electrode, both reference and ISME combined, and the total cell can be represented as follow [40]:

Reference electrode		ISME electrode
Ag | AgCl | KCl	|| test solution ||	Membrane | internal solution | AgCl | Ag

1 In point of view of author, this was only possible, as a layer of blank epoxy without microcapsules was applied as a topcoat.

Therefore, in a SIET measurement, the potential difference between reference electrode and ISME electrode (E_{cell}) is given by equation 2.12:

$$E_{cell} = (E_{int} - E_{ref}) + E_m + E_{lj} \qquad \text{Eq. 2.12}$$

where $E_{int} - E_{ref}$ is the potential difference between the ISME internal reference and the reference electrode, E_m is the potential of the ISME membrane, and E_{lj} is the liquid junction potential at the reference electrode/electrolyte interface [25]. In equation 2.12 E_m is the only variable which is sensitive on concentration gradients of the target ion through the membrane.

The cell potential can be written according to equation 2.13:

$$E_{cell} = E_{const} + \frac{RT}{zF} Ln(\frac{a_{ext}}{a_{int}}) \qquad \text{Eq. 2.13}$$

Where, E_{const} is the sum of all constants of equation 2.12, R is the gas constant, T is the temperature, z is the target ion charge number, F is the Faraday constant, and a_{ext} and a_{int} are the activity of the target ion in the external and internal solution of the ISME membrane, respectively.

To obtain the concentration of the target ion, the cell potential is first determined for a various number of solutions with known activity to plot a calibration curve (E_{cell} versus $Ln(a_{ext})$), which is then used for the determination of the activity of the target ion [40].

Activity of the target ion (a_i) can be written according to equation 2.14 and has a direct relation with both ion concentration (C_i), and the activity coefficient (f_i)

$$a_i = f_i . C_i \qquad \text{Eq. 2.14}$$

The activity coefficient can be calculated with the Debye-Hückel equation (equation 2.15):

$$-Log\ (f_i) = \frac{z_i^2 A\sqrt{I_s}}{1+B\alpha_i\sqrt{I_s}} \qquad \text{Eq. 2.15}$$

where A is the Debye-Hückel constant (A = 0.5085 for aqueous solutions at 298K), B is a solvent characteristic constant, which depends on temperature and dielectric properties (B = 0.3281 for aqueous solutions at 298K), I_s is the ionic strength of the electrolyte, and α_i is the effective ionic radius of the target ion.

The SIET results can be presented in different ways, most commonly 2D maps.

A device set up with similarity to SVET contains a 3D computerized stepper motors used for positioning the ISME over the working electrode, an amplifier, a signal digitizer to boost the potential difference measured in the potentiometric cell, and a video camera [53]. The sample preparation process is also quite similar to those for SVET measurement.

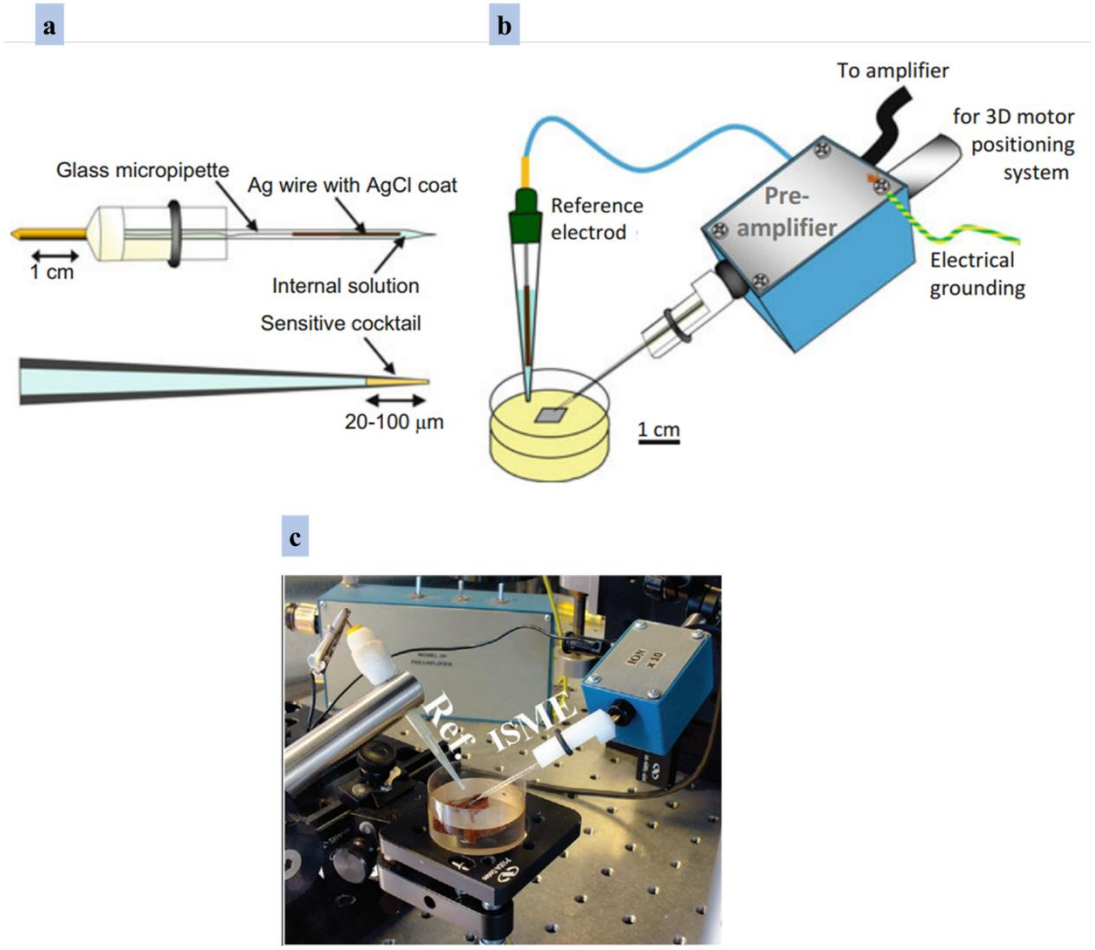

Figure 2.14 a) Liquid membrane ion-selective microelectrode, b) schematic and c) real representation of typical measuring cell and SIET set up. Image adapted from [39,40]

As mentioned before SIET measurements often are used as complementary to SVET. However, considering the pH variations at both cathodic and anodic sites during the corrosion progress, the technique can offer important information regarding the ongoing processes, and therefore corrosion or healing mechanism. For that, H^+-selective electrodes are the most used in the field of corrosion and coating [54]. Marques et al. [55], studied the corrosion mechanism and the possibility of employing SVET, and SIET as complementary techniques to study corrosion at the microscale. Authors used a model cut edge consisting of a zinc anode and an iron cathode (Figure 2.15 a). Figure 2.15b shows evolution of pH and current density recorded by SIET, and SVET probs respectively, after 1 h and 10 h immersion of sample into the 0.01 M NaCl solution (pH neutral). Authors reported alkalization and a substantial pH gradient around steel components of the model sample detected by the SIET probe [55].

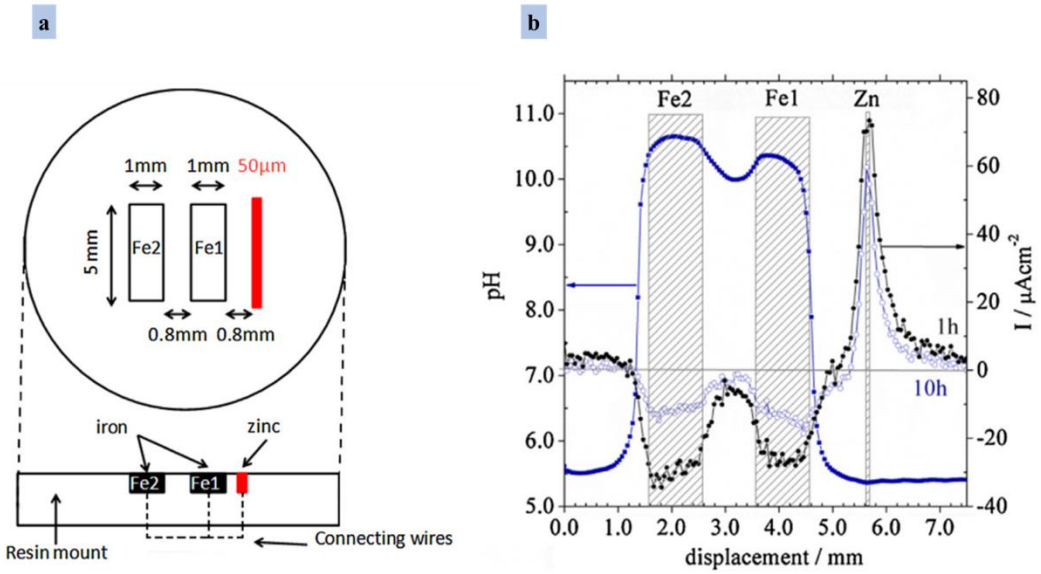

Figure 2.15 a) Schematic diagram of the model cut edge, b) SVET/SIET line scans measured as the tip travelled over the model. The SVET curves are for 1 h and 10 h exposure and SIET for 10 h. Image adapted from [55] with permission.

Alvarez-Pampliega et al. [56], also reported the successful application of SIET to map the pH gradient (alkalization) over the steel part (Figure 2.16), provoked by cut-edge corrosion in various environment for both aluminum-rich metallic coated steel and un-coated steel. Raj et al. [57], also reported the alkalization detected by SIET probe, over the artificial defects created in the blank epoxy coating, and an epoxy coating modified with inhibitor loaded calcium carbonate.

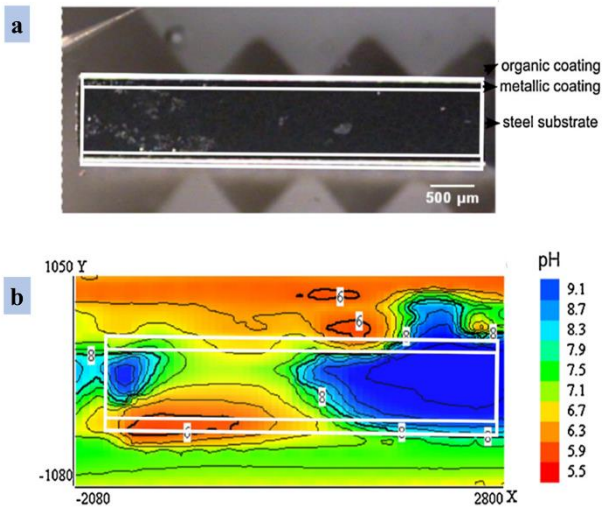

Figure 2.16 a) optical micrograph, b) corresponding SIET mapping above coated steel. Image adapted from [56] with permission.

To summarize, among localized techniques used to characterize corroding systems SIET with ability to identify specific ion can provide very important information. This information can help to identify corrosion mechanism, as well as healing mechanism associated with addition of inhibitor into a under studied system. However, the technique suffers from various drawbacks mostly related to the short lifetime, and fragility of glass capillary microelectrodes. The technique also suffers some difficulties associated to set up of the prob at the close vicinity of sample due to its transparency [25,40].

2.5 Summary

In this chapter the conventional EIS technique, and localized electrochemical techniques mostly used in this PhD work were discussed in brief. This chapter covered the basic theory behind each technique, advantages, and shortages of each technique also discussed. Several related examples also given to clarify better each technique.

In this work, EIS was used to evaluate the global protective performance and barrier properties epoxy-based and polyolefin-based coatings before and after modification with MCs and /or NPs, used for corrosion protection of carbon steel. The technique also was used to evaluate the effectiveness of corrosion inhibitor for protection of carbon steel used in this work. Localized techniques namely, LEIS, SVET, SIET also were employed to study the coatings performance in the presence of defects, to evaluate the self-healing ability of developed coatings and to identify those mechanisms involved in the protective performance of the coatings. The compilation of all results obtained from evaluation of coatings by both EIS and localized techniques also can provide series of crucial important information leading to identify the protection mechanism offers by addition of healing agents or specific corrosion inhibitor. However, most of the time several others phsysico-chemical characterization techniques e.g., Raman Spectroscopy, optical and electronic microscopies, EDX, and micro-FTIR, also used to further characterize and to understand the protective mechanisms involved.

2.6 References

[1] J.M. McIntyre, H.Q. Pham, Electrochemical impedance spectroscopy; a tool for organic coatings optimizations, Prog. Org. Coatings. 27 (1996) 201–207. https://doi.org/10.1016/0300-9440(95)00532-3.

[2] V.F. Lvovich, Impedance spectroscopy Applications to Electrochemical and Dielectric Phenomena, John Wiley & Sons, 2012, pp 1-19.

[3] A. Lasis, Electrochemical Impedance Spectroscopy and its applications.pdf, in: B.E. Conway (Ed.), Mod. Asp. Electrochem., Plenum, 1999: pp. 143–248.

[4] Gamry Instruments, Basics of electrochemical impedance spectroscopy, Appl. Note. (2018) 1–28.

[5] U. Rammelt, G. Reinhard, Application of electrochemical impedance spectroscopy (EIS) for characterizing the corrosion-protective performance of organic coatings on metals, Prog. Org. Coatings. 21 (1992) 205–226. https://doi.org/10.1016/0033-0655(92)87005-U.

[6] B.J. Merten, S. Prochaska, C. Henderson, A. Skaja, D. Tordonato, Electrochemical Impedance Methods to Assess Coatings for Corrosion Protection, Reclamation Managing Water in the West, Technical Publication No. 8540-2019-03, Colorado, 2019.

[7] D.I. Njoku, M. Cui, H. Xiao, B. Shang, Y. Li, Understanding the anticorrosive protective mechanisms of modified epoxy coatings with improved barrier, active and self-healing functionalities: EIS and spectroscopic techniques, Sci. Rep. 7 (2017) 15597. https://doi.org/10.1038/s41598-017-15845-0.

[8] L.G.S. Gray, B.R. Appleman, EIS: Electrochemical Impedance Spectroscopy - A tool to predict remaining coating life?, J. Prot. Coatings Linings. 20 (2003) 66–74.

[9] J.S. Fernandes, Short Course on EIS, 2008.

[10] ISO, Paints and varnishes — Electrochemical impedance spectroscopy (EIS) on high-impedance coated specimens — Part 4: Examples of spectra of polymer-coated specimensInternational Standard ISO 16773-4, ISO. (2009) 13.

[11] S. Gu, H. Shi, C. Zhang, W. Wang, F. Liu, E.H. Han, Mesoporous CeO_2 containers in water-borne epoxy coatings for dual active corrosion protection of mild steel, Prog. Org. Coatings. 158 (2021) 106376. https://doi.org/10.1016/j.porgcoat.2021.106376.

[12] T. Siva, A. Ramadoss, S. Sathiyanarayanan, Emerging action of corrosion prevention based on sustained self-healing coatings, Surfaces and Interfaces. 26 (2021) 101440. https://doi.org/10.1016/j.surfin.2021.101440.

[13] C. Liu, H. Wu, Y. Qiang, H. Zhao, L. Wang, Design of smart protective coatings with autonomous self-healing and early corrosion reporting properties, Corros. Sci. 184 (2021) 109355. https://doi.org/10.1016/j.corsci.2021.109355.

[14] N. Jayakumar, K. Karattu Veedu, N.K. Gopalan, Durable Hydrophobic Coating Based on Cerium Phosphate Nanorod-Siliconized Epoxy for Corrosion Protection, ACS Appl. Nano Mater. 2 (2019) 2689–2696. https://doi.org/10.1021/acsanm.9b00172.

[15] Y. Ye, H. Chen, Y. Zou, Y. Ye, H. Zhao, Corrosion protective mechanism of smart graphene-based self-healing coating on carbon steel, Corros. Sci. 174 (2020) 108825. https://doi.org/10.1016/j.corsci.2020.108825.

[16] F. Mansfeld, M.W. Kendig, S. Tsai, Evaluation of Corrosion behavior of Coated Metals with AC Impedance Measurments, Corrosion-NACE. 38 (1982) 478–485.

[17] Y. Lin, R. Chen, Y. Zhang, Z. Lin, Q. Liu, J. Liu, Y. Wang, L. Gao, J. Wang, Sandwich-like polyvinyl alcohol (PVA) grafted graphene: A solid-inhibitors container for long term self-healing coatings, Chem. Eng. J. 383 (2020) 123203. https://doi.org/10.1016/j.cej.2019.123203.

[18] J.M. Falcón, F.F. Batista, I. V. Aoki, Encapsulation of dodecylamine corrosion inhibitor on silica nanoparticles, Electrochim. Acta. 124 (2014) 109–118. https://doi.org/10.1016/j.electacta.2013.06.114.

[19] Y. Morozov, L.M. Calado, R.A. Shakoor, R. Raj, R. Kahraman, M.G. Taryba, epoxy coatings modified with a new cerium phosphate inhibitor for smart corrosion protection of steel, (2019) 108–128. https://doi.org/10.1016/j.corsci.2019.108128.

[20] G. Bahlakeh, B. Ramezanzadeh, M. Ramezanzadeh, Cerium oxide nanoparticles influences on the binding and corrosion protection characteristics of a melamine-cured polyester resin on mild steel: An experimental, density functional theory and molecular dynamics simulation study, Corros. Sci. 118 (2017) 69–83. https://doi.org/10.1016/j.corsci.2017.01.021.

[21] T. Matsuda, N. Jadhav, K.B. Kashi, M. Jensen, A. Suryawanshi, V.J. Gelling, Self-healing ability and particle size effect of encapsulated cerium nitrate into pH sensitive microcapsules, Prog. Org. Coatings. 90 (2016) 425–430.

https://doi.org/10.1016/j.porgcoat.2015.10.021.

[22] M.P.J. Lillard R. S, Kruger J, Tait W. S., Using Local Electrochemical Impedance Spectroscopy to Examine Coating Failure, Corros. Sci. 51 (1995) 251–259. https://doi.org/10.5006/1.3293590.

[23] L.V.S. Philippe, G.W. Walter, S.B. Lyon, Investigating Localized Degradation of Organic Coatings- Comparison of Electrochemical Impedance Spectroscopy with Local Electrochemical Impedance Spectroscopy, J. Electrochem. Soc. 150 (2003) 1554913. B111–B119. https://doi.org/10.1149/1.1554913.

[24] BioLogic, Operating Manual-LEIS370 Localised Electrochemical Impedance Spectroscopy System, (n.d.) 1–78.

[25] N. Jadhav, V.J. Gelling, Review—The Use of Localized Electrochemical Techniques for Corrosion Studies, J. Electrochem. Soc. 166 (2019) C3461–C3476. https://doi.org/10.1149/2.0541911jes.

[26] C. Zhong, X. Tang, Y.F. Cheng, Corrosion of steel under the defected coating studied by localized electrochemical impedance spectroscopy, Electrochim. Acta. 53 (2008) 4740–4747. https://doi.org/10.1016/j.electacta.2008.02.014.

[27] M.C. Li, Y.F. Cheng, Corrosion of the stressed pipe steel in carbonate-bicarbonate solution studied by scanning localized electrochemical impedance spectroscopy, Electrochim. Acta. 53 (2008) 2831–2836. https://doi.org/10.1016/j.electacta.2007.10.077.

[28] M. Mouanga, M. Puiggali, O. Devos, EIS and LEIS investigation of aging low carbon steel with Zn-Ni coating, Electrochim. Acta. 106 (2013) 82–90. https://doi.org/10.1016/j.electacta.2013.05.021.

[29] Y. Zhang, Y. Shao, G. Meng, T. Zhang, P. Li, F. Wang, Evaluation of the corrosion protection of defective polyaniline/epoxy coating by localized electrochemical impedance spectroscopy, J. Coatings Technol. Res. 12 (2015) 777–785. https://doi.org/10.1007/s11998-015-9679-y.

[30] J.-B. Jorcin, E. Aragon, C. Merlatti, N. Pébère, Delaminated area beneath organic coating: A local electrochemical impedance approach, Corros. Sci. 48 (2006) 1779–1790. https://doi.org/10.1016/j.corsci.2005.05.031.

[31] R. Raj, Y. Morozov, L.M. Calado, M.G. Taryba, R. Kahraman, A. Shakoor, M.F. Montemor, Inhibitor loaded calcium carbonate microparticles for corrosion protection of epoxy-coated carbon steel, Electrochim. Acta. 319 (2019) 801–812. https://doi.org/10.1016/j.electacta.2019.07.059.

[32] C. Liu, H. Zhao, P. Hou, B. Qian, X. Wang, C. Guo, L. Wang, Efficient Graphene/Cyclodextrin-Based Nanocontainer: Synthesis and Host-Guest Inclusion for Self-Healing Anticorrosion Application, ACS Appl. Mater. Interfaces. 10 (2018) 36229–36239. https://doi.org/10.1021/acsami.8b11108.

[33] L. Cheng, C. Liu, H. Wu, H. Zhao, F. Mao, L. Wang, A mussel-inspired delivery system for enhancing self-healing property of epoxy coatings, J. Mater. Sci. Technol. 80 (2021) 36–49. https://doi.org/10.1016/j.jmst.2020.10.075.

[34] Y. Lei, Z. Qiu, N. Tan, H. Du, D. Li, J. Liu, T. Liu, W. Zhang, X. Chang, Polyaniline/CeO_2 nanocomposites as corrosion inhibitors for improving the corrosive performance of epoxy coating on carbon steel in 3.5% NaCl solution, Prog. Org. Coatings. 139 (2020) 105430. https://doi.org/10.1016/j.porgcoat.2019.105430.

[35] T.Y. Jin, Y.F. Cheng, In situ characterization by localized electrochemical impedance spectroscopy of the electrochemical activity of microscopic inclusions in an X100 steel, Corros. Sci. 53 (2011) 850–853. https://doi.org/10.1016/j.corsci.2010.11.026.

[36] A.S. Bandarenka, K. Eckhard, A. Maljusch, W. Schuhmann, Localized electrochemical impedance spectroscopy: Visualization of spatial distributions of the key parameters describing solid/liquid interfaces, Anal. Chem. 85 (2013) 2443–2448. https://doi.org/10.1021/ac303490t.

[37] O. Gharbi, K. Ngo, M. Turmine, V. Vivier, Local electrochemical impedance spectroscopy: A window into heterogeneous interfaces, Curr. Opin. Electrochem. 20 (2020) 1–7. https://doi.org/10.1016/j.coelec.2020.01.012.

[38] K. Indira, T. Nishimura, In-Situ Electrochemical Monitoring and Ex-Situ Chemical Analysis of Epoxy Coated Steels in Sodium Chloride Environment Using Various Spectroscopic Techniques, Trans. Indian Inst. Met. 70 (2017) 2347–2360. https://doi.org/10.1007/s12666-017-1096-8.

[39] A.C. Bastos, M.G.. Ferreira, Application of the scanning vibrating electrode technique to the characteon of modern coatings, in: M. Aliofkhazrai, N. Ali, M. Chipra, N.B. Ladani, J.M.D. Hosson (Eds.), Handb. Mod. Coat. Technol., Elsevier B.V, 2021: pp. 1–34. https://doi.org/10.1016/c2012-0-06251-5.

[40] A. Bastos, Application of SVET / SIET Techniques to Study Healing Processes in Coated Metal Substrates, in: L. Klein, M. Aparicio, A. Jitianu (Eds.), Hand B. Sol/Gel Sci. Technol., 2017. Pp. 1-57. Springer International Publishing AG

https://doi.org/10.1007/978-3-319-19454-7.

[41] G. Grundmeier, W. Schmidt, M. Stratmann, Corrosion protection by organic coatings: Electrochemical mechanism and novel methods of investigation, Electrochim. Acta. 45 (2000) 2515–2533. https://doi.org/10.1016/S0013-4686(00)00348-0.

[42] A.C. Bastos, M.C. Quevedo, O. V. Karavai, M.G.S. Ferreira, Review—On the Application of the Scanning Vibrating Electrode Technique (SVET) to Corrosion Research, J. Electrochem. Soc. 164 (2017) C973–C990. https://doi.org/10.1149/2.0431714jes.

[43] S. Neema, M. Selvaraj, J. Raguraman, S. Ramu, Investigating the self healing process on coated steel by SVET and EIS techniques, J. Appl. Polym. Sci. 127 (2013) 740–747. https://doi.org/10.1002/app.37791.

[44] W. Trabelsi, P. Cecilio, M.G.S. Ferreira, M.F. Montemor, Electrochemical assessment of the self-healing properties of Ce-doped silane solutions for the pre-treatment of galvanised steel substrates, Prog. Org. Coatings. 54 (2005) 276–284. https://doi.org/10.1016/j.porgcoat.2005.07.006.

[45] Y. Hao, Y. Zhao, B. Li, L. Song, Z. Guo, Self-healing effect of graphene@PANI loaded with benzotriazole for carbon steel, Corros. Sci. 163 (2020) 108246. https://doi.org/10.1016/j.corsci.2019.108246.

[46] F. Thébault, B. Vuillemin, R. Oltra, K. Ogle, C. Allely, Investigation of self-healing mechanism on galvanized steels cut edges by coupling SVET and numerical modeling, Electrochim. Acta. 53 (2008) 5226–5234. https://doi.org/10.1016/j.electacta.2008.02.066.

[47] S. Wang, J. Ding, H. Ming, Z. Zhang, J. Wang, Characterization of low alloy ferritic steel-Ni base alloy dissimilar metal weld interface by SPM techniques, SEM/EDS, TEM/EDS and SVET, Mater. Charact. 100 (2015) 50–60. https://doi.org/10.1016/j.matchar.2014.12.007.

[48] H. Choi, K.Y. Kim, J.M. Park, Encapsulation of aliphatic amines into nanoparticles for self-healing corrosion protection of steel sheets, Prog. Org. Coatings. 76 (2013) 1316–1324. https://doi.org/10.1016/j.porgcoat.2013.04.005.

[49] A.M. Simões, J.C.S. Fernandes, Studying phosphate corrosion inhibition at the cut edge of coil coated galvanized steel using the SVET and EIS, Prog. Org. Coatings. 69 (2010) 219–224. https://doi.org/10.1016/j.porgcoat.2010.04.022.

[50] E.T. Schmitzhaus, R.M.O. Vega, R. Schroeder, J.G. Salvador, I.L. Muller, S.

Mattedi, M. Taryba, C.F. Malfatti, Localized corrosion behavior studies by SVET of 1010 steel in different concentrations of sodium chloride containing [m-2HEA][Ol] ionic liquid as corrosion inhibitor, Electrochim. Acta. 419 (2022) 140385. https://doi.org/10.1016/j.electacta.2022.140385.

[51] R. Samiee, B. Ramezanzadeh, M. Mahdavian, E. Alibakhshi, Assessment of the smart self-healing corrosion protection properties of a water-base hybrid organo-silane film combined with non-toxic organic/inorganic environmentally friendly corrosion inhibitors on mild steel, J. Clean. Prod. 220 (2019) 340–356. https://doi.org/10.1016/j.jclepro.2019.02.149.

[52] F. Cotting, A. Koebsch, I.V. Aoki, Epoxy Self-Healing Coating by Encapsulated Epoxy Ester Resin in Poly (Urea-Formaldehyde-Melamine) Microcapsules, Front. Mater. 6 (2019), Article 314. https://doi.org/10.3389/fmats.2019.00314.

[53] S. Lamaka, R.M. Souto, M.G.S. Ferreira, In-situ visualization of local corrosion by Scanning Ion-selective Electrode Technique (SIET), Microsc. Sci. Technol. Appl. Educ. (2010) 2162–2173.

[54] A.. Zdrachek, A.. Karotkaya, V.A. Nazarov, K.A. Andronchyk, L.S. Stanishevskii, V.V. Egorov, M.G. Taryba, D. Sinhirova, M. Kopylovich, S.V. Lamaka, H+-selective microelectrodes with optimized measuring range for corrosion studies, Sensors Actuators B Chem. 207 (2015) 967–975. https://doi.org/10.1016/j.snb.2014.07.106.

[55] A.G. Marques, M.G. Taryba, A.S. Panão, S.V. Lamaka, A.M. Simões, Application of scaning electrod techniques for the evaluation of iron-zinc corrosion in nearly neutral chloride solutions, Corros. Sci. 104 (2016) 123–131. https://doi.org/10.1016/j.corsci.2015.12.002.

[56] A. Alvarez-Pampliega, S. V. Lamaka, M.G. Taryba, M. Madani, J. De Strycker, E. Tourwé, M.G.S. Ferreira, H. Terryn, Cut-edge corrosion study on painted aluminum rich metallic coated steel by scanning vibrating electrode and micro-potentiometric techniques, Electrochim. Acta. 61 (2012) 107–117. https://doi.org/10.1016/j.electacta.2011.11.110.

[57] R. Raj, Y. Morozov, L.M. Calado, M.G. Taryba, R. Kahraman, R.A. Shakoor, M.F. Montemor, Calcium carbonate particles loaded with triethanolamine and polyethylenimine for enhanced corrosion protection of epoxy coated steel, Corros. Sci. 167 (2020) 108548. https://doi.org/10.1016/j.corsci.2020.108548.

Chapter 3

Isocyanate-based microcapsules for autonomous self-healing of epoxy coatings for corrosion protection of carbon steel

This chapter contributes to the development of epoxy coating modified with microcapsules containing isophorone diisocyanate as self-healing agent. The first part of this chapter dedicates to synthesis and characterization of microcapsules. This part was published in "M. Attaei, M. Vale, A. Shakoor, R. Kahraman, M.F. Montemor, and A. C. Marques, *Hybrid shell Microcapsules Containing Isophorone Diisocyanate (IPDI) With High Thermal and Chemical Stability for Autonomous Self-Healing of Epoxy Coatings*, Journal of Applied Polymer Science, 2019, 137, 48751. The second part of the chapter is dedicated to the characterization of epoxy coatings modified with microcapsules. This part was published in "M. Attaei, L. Calado, M. Taryba, Y. Morozov, A. Shakoor, R. Kahraman, A.C. Marques, and M. F. Montemor, *Autonomous self-healing in epoxy coatings provided by high efficiency isophorone diisocyanate (IPDI) microcapsules for protection of carbon steel*, Progress in Organic Coatings, 2020, 139, 105445".

3.1 Introduction

Steel and its alloys are common materials used in different industries, for a variety of applications. It combines good mechanical properties with adequate durability and competitive cost. However, steel components are sensitive to corrosion, particularly when exposed to aggressive environments. During the last decades, intensive works have been devoted to the development of more effective organic coatings for corrosion protection of steel. One important research stream has been dedicated to self-healing coating, based on use of encapsulated self-healing agents. Encapsulation of polymerizable species inside MCs can be considered one the most flexible routes for introducing certain functionalities, like ability to heal a polymeric matrix [1]. Among different possible healing agents, application of one-component materials, which do not require addition of catalyst for their reactions have attracted considerable interest. These materials can be easily transformed into a polymeric protective layer via activation and reaction with moisture without needing any other chemicals [2]. Encapsulation of isocyanates as healing agent, gives the possibility to prepare autonomous self-healing systems in water/moisture-containing environments, due to the extreme reactivity of the isocyanate chemical group (NCO), which can form chemical bonds with any chemical group containing an active hydrogen (H) atom. The capsules filled with isocyanates as healing agent must be sensitive to external stimuli such as temperature, or pressure. This is critical to ensure the release of the encapsulated species and to ensure its healing effectiveness in the working condition [3]. In Chapter 1 the state of the art in microencapsulation of self-healing agents was explored in detail. Particular attention was paid into the encapsulation of isocyanate as one of the most efficient chemicals for self-healing, with special focus on IPDI. Although successful encapsulation of isocyanate has been already reported [4,5], the short shelf life of MCs due to shell permeability and low encapsulation efficiency are challenges that still require further investigation. Moreover, for a successful design of self-healing coatings, by addition of MCs, the size of container should be reduced at least to one third of coating thickness, otherwise addition of large containers introduces defects into the coating and, in general, drastically decreases the global protection properties of the coatings. In such a condition, applying the topcoat to cover those defects and porosities would be necessary [6].

The present doctoral work aims at developing self-healing coatings of thickness up to 100 µm, therefore, it is necessary to keep the size of MCs under 30 µm. However, decreasing

the MCs´ size neither is a straightforward, nor an easy task. Therefore, a proper MCs´ design, previous to the synthesis, with a careful selection of all chemicals and reaction parameters involved, would be required.

In this work, emulsion formation followed by interfacial polymerization was the selected technique for encapsulation of IPDI. Since, interfacial polymerization occurs at the surface of droplets, smaller droplet means more reactive sites due to higher surface area to volume (S⁄V) compared to the larger ones. Therefore, huge effort would be necessary to find the proper shell former, proper active H source, and to tune the synthesis parameters, namely emulsification rate, temperature, synthesis duration, etc. Thus, fabrication of small (< 30 µm), high efficiency, long shelf-life, and robust IPDI-MCs was defined as the first step toward the development of self-healing coating. As in most of the cases extra solvent needs to be added to make IPDI and shell former miscible or to achieve a stable emulsion, reducing the quantity of solvent or using an eco-friendly solvent also was pursued during this work.

In recent years, an intensive effort has been done and is still on going in the framework of the "Technology Platform on Microencapsulation and Immobilization"[2] to encapsulate IPDI. Successful encapsulation of IPDI was reported using a commercially available oligomeric MDI source, Ongronat® 2500, with higher reactivity than IPDI as a shell former [7][3]. In this work, four different active H sources were tested, namely aminosilane in combination with TEOS, DETA and IPES, to achieve faster polymerization reactions and as a result, an increased encapsulation yield. A pure IPDI encapsulation at 60 wt % was reported in MCs with an average diameter of 82 ± 7 µm [7], which was an acceptable mean diameter for the envisaged application, namely crosslinking agents in adhesive formulations. However, as mentioned before, the shift to a new application, consisting of autonomous healing of epoxy coatings for corrosion protection, raised the need to reduce the size of MCs. Although it was possible to reduce the size of MCs by increasing the emulsification rate and emulsifier concentration and using IPES as an active H source (the best performing active H source in previous work), the resultant MCs evidenced a high tendency for aggregation, when added to the epoxy coating formulation.

2 Author of this PhD work is a member of "The Technology Platform on Microencapsulation and Immobilization" *(TECHNOLOGY PLATFORM ON MICROENCAPSULATION AND IMMOBILIZATION (ulisboa.pt)).*

3 Author of this PhD work is the first author of this scientific article, published at the framework of her Master Thesis.

To overcome such agglomeration issue and achieve high efficiency MCs, the use of other active H sources, the replacement of Ongronat®2500 by a lower viscosity and higher reactivity polyisocyanate, and the optimization of the synthesis' parameters, were carried out.

Additionally, the work of Loureiro et al[4]. confirmed the role played by active H sources in terms of encapsulation efficiency, shelf life, shell's chemical structure, and thermal stability. Authors concluded that the NH-based active H sources, EDA and PEI, were the ones that led to a higher encapsulation efficiency. However, it was reported that the best overall performance was achieved for the combination of the high NH functionality PEI and the silane n-OTES, as active H sources [8]. Therefore, in this PhD work, to obtain desired MCs in terms of encapsulation efficiency, chemical resistance, and shelf life, firstly, a highly reactive, and low viscosity polyisocyanate Desmodur RFE (DRFE) was employed as shell former (replacing the highly viscous Ongronat®2500), and then various active H sources, namely DETA, Butanediol, PEI, and the silanes (n-OTES, and hexadecyltrimethoxysilane (HDMS)) were tested, to ensure faster formation of polymeric and hybrid shells and an improvement in terms of MCs´ shelf life and chemical resistance. Additionally, several combinations of these active H sources were tested. It is worth to note that different active hydrogen sources may have different chain lengths and different chemical structures and, therefore, different steric hindrance and reactivity, which strongly influences the MCs' shell thickness and morphology [9]. Among various successful attempts to obtain desire MCs, three MCs with longer shelf life and higher efficiency were selected for incorporation in the epoxy formulation. Thus, the following pages are dedicated to the synthesis and characterization of these three types of MCs, tailored to have longer shelf life and higher efficiency. Table A 1.1 in Appendix 1 – page 217 shows some other attempts, namely the successful encapsulation of IPDI, but in shorter shelf-life MCs and/or MCs with less stability inside the solvents. FTIR spectra collected 3 days after synthesis of these MCs are shown in Figure A. 1.1, Appendix 1 page 217. The list of materials used to synthesize these MCs can be found in Table A 1.2 (Appendix 1 – page 218).

4 The corresponding research work was co-authored by the author of this PhDThesis.

3.2 Experimental

3.2.1 Preparation of microcapsules

O/W emulsion formation followed by interfacial polymerization was the method selected to encapsulate IPDI. The key feature in interfacial polymerization is the diffusion of two different reactive monomers to the interface [10]. Both phases (water-based and oil-based) contain reactive monomers, which come into contact at the interface of droplets and react there to create a membrane that at early stages forms an impermeable shell around the oil droplets.

In more detail, firstly, an aqueous solution of GA (7 wt% of total emulsion (W+O)) was prepared at room temperature (RT). This solution was vigorously mixed with the oil phase at 8000 rpm with an emulsifier for 5 min to obtain a stable emulsion. The oil phase (8 wt% of total emulsion) was composed by two isocyanates, being IPDI and DRFE, present at 70 wt% and 30 wt% in the oil phase, respectively. The DRFE is more reactive than IPDI, which allowed encapsulation of IPDI due to the faster reaction of DRFE with OH or NH groups from the aqueous phase. The active H sources, DETA, HDMS and n-OTES were added to the emulsion system, dropwise, under mechanical stirring (400 rpm), using a mechanical stirrer. The temperature increased gradually from RT to 60°C and the reaction was stopped after 60 min. The polymeric shell forms by reaction of the NCO group in the isocyanate compound with the NH groups of amines, while the hybrid shell forms by reaction of NCO group of isocyanate compound with silanol groups, by poly condensation reactions, to form siloxane moieties. The resulting shell, in this case, is a hybrid material based on PUa/PU and silica [3,11]. The solution was left to reach the RT and the MCs were then separated from the solution and washed several times with ethanol and/or deionized water, using a centrifuge, at 4000 rpm. The final product was dried at atmospheric pressure and RT for 24 h. A summary of the syntheses parameters and material concentrations is listed in Table 1.

Table 3.1 Syntheses' parameters

MCs	Water phase (wt %)[a]	Oil phase (wt %)[a]	Active H source (wt %)[b]	Maximum Temperature. (º C)
D MC	W + GA 85 + 7	IPDI + DRFE 5.5 + 2.5	DETA 5	55-60
H MC			HDMS 4	
N MC			n-OTES 4	

[a] wt% of total emulsion
[b] wt% of total W solution

3.2.1.1 Characterization of microcapsules

The morphology of MCs was studied by Scanning electron microscopy (SEM). The structural characterization of the MCs was carried out using Fourier transformed infrared spectroscopy - Attenuated Total Reflectance (FTIR-ATR). The collected FTIR spectra also was used to estimate the relative encapsulation yield (Y), which represents an indirect measure of the isocyanate encapsulation using equation 3.1. For this purpose, the area of the peak regarding the isocyanate NCO group at 2260 cm^{-1} and the peak at 1306 cm^{-1}, which correlated to C–O stretching, were considered. This latter peak is typically related to the PUa/PU shell material and does not tend to suffer significant changes over time after synthesis of the MCs.

$$Y = \frac{\text{Area}_{2260\text{cm}-1}}{\text{Area}_{1306\ \text{cm}-1}} \qquad \text{Eq. 3.1}$$

The latest equation also was used to estimate the shelf-life of MCs. To this end, FTIR spectra were collected at certain time intervals from the synthesis of MCs. The first Y value was considered 100 %, while the following values were compared with the first one; the time at which the Y value was reduced to 50 % of the first value, was considered as shelf-life of MCs. All the MCs were stored at RT and atmospheric pressure during the experiment.

Using equation 3.1, the chemical stability of MCs in working conditions also was assessed by analyzing the FTIR spectra of the MCs after immersion tests in relevant media during the 200 h at RT. For this purpose, 0.1 g of MCs were immersed into 5 ml of ethanol,

acetone, and hardener part of epoxy. MCs then were separated from the media, washed, and dried before further analysis.

The presence of MCs might affect the curing process and curing time of the epoxy coatings and such phenomenon was also evaluated by FTIR spectroscopy. Two coatings (reference and modified with addition of 5 wt% MCs) were applied on degreased glass lamella (both with 30 µm thickness). The first analysis was performed close to time zero (immediately after mixing of epoxy and hardener in the case of the blank coating and after mixing of epoxy, hardener, and MCs in the case of the modified one). The coated lamellas were kept inside the oven at 40°C during the test. Detached coating samples were analyzed by FTIR-ATR spectroscopy at selected time intervals. The typical epoxy band, (antisymmetric epoxy ring breathing) centered at 916 cm^{-1}, was used to monitor the effect on the curing time [12,13]. The area under this peak within the range of ca. 930-890 cm^{-1}, was measured by the OriginPro 2016 software. The reduction of this area can be assigned to epoxy groups consumption. The time at which the peak disappears gives an indication of the curing time.

Finally, the Thermogravimetric Analysis (TGA) was used to evaluate the thermal stability of the MCs and to calculate their core fraction (loading efficiency). (Detailed information regarding equipment used to characterize the particles, and method of characterization can be found in Appendix 2.)

3.2.1.2 Results and Discussion (Microcapsules)

3.2.1.2.1 Size and morphology of microcapsules

The size and morphology of the MCs were assessed by SEM (Figure 3.1). All the MCs display nearly spherical shapes (Figures 3.1a, b, d, e, g, and h) and present a core-shell morphology (Figures 3.1c, f, and i) with smooth outer and inner surfaces with an average diameter of 10 ± 1 µm and an average shell thickness of 1.5 ± 0.5 µm.

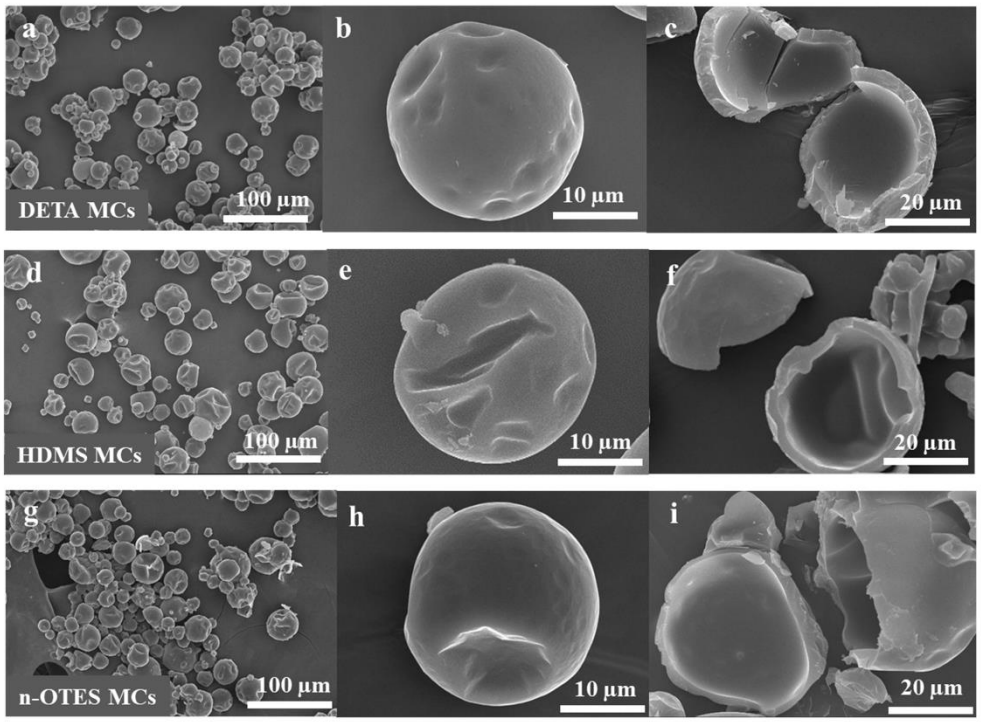

Figure 3.1 SEM images of a,b) DETA MCs, d,e) HDMS MCs, g,h) n-OTES MCs, and c, f, and i) a purposefully broken MC, demonstrating a core−shell morphology, for DETA MCs, HDMS MCs, and n-OTES MCs respectively.

Through the analysis of the size distribution of the MCs, using the Fiji software, it was possible to conclude that the MCs have an average diameter of 10 ± 1 µm in all cases (Figure 3.2). Since emulsification rate, stirring rate and emulsifier concentration, as key parameters that determine the size of MCs, were kept constant in all the syntheses, obtaining the same size of MCs in all the syntheses was expected. [7,14,15].

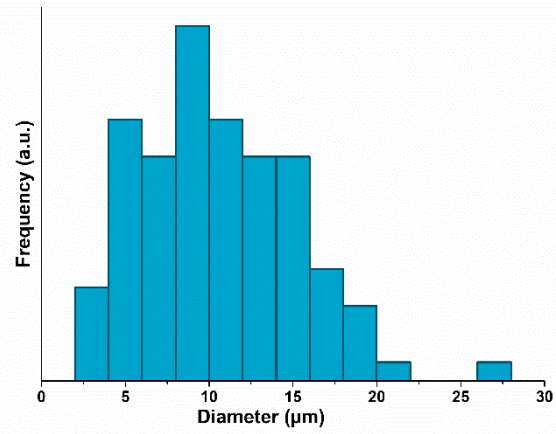

Figure 3.2 MCs' size distribution.

3.2.1.2.2 Chemical structure of microcapsules

The chemical structure of both MCs and pure IPDI were investigated by FTIR-ATR. As shown in Figure 3.3a, an intense band appeared at ca. 2260 cm^{-1}, related to the N=C=O stretching vibration bond in both IPDI and MCs spectra, indicating the presence of unreacted NCO groups in the MCs and the successful encapsulation of IPDI [16].

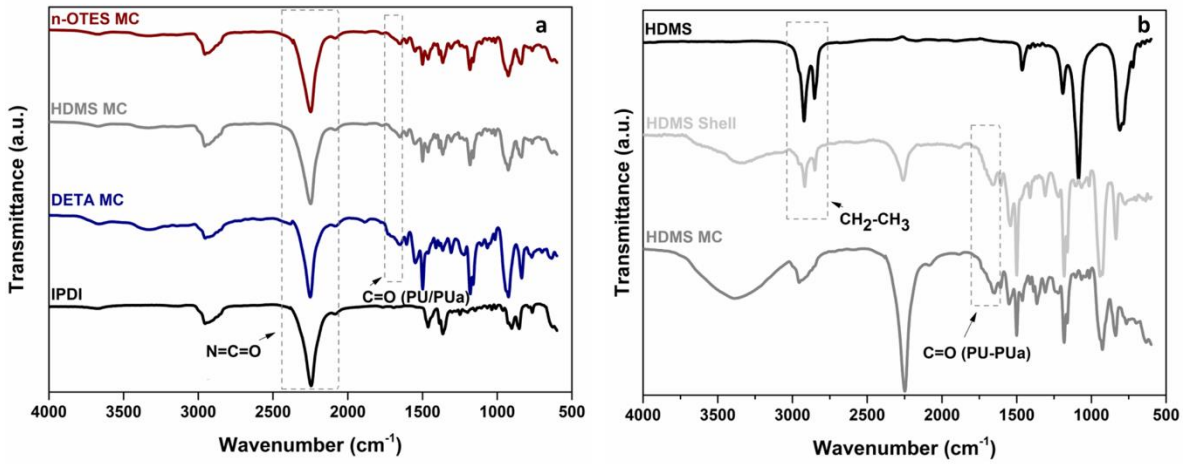

Figure 3.3 a) FTIR spectra of IPDI and MCs, b) FTIR spectra of HDMS MCs, HDMS MC's shell and HDMS.

The peaks ascribed to the N-H stretching of the amine bonds at ca. 3400-3200 cm^{-1}, N-H bending at ca. 1510 cm^{-1}, carbonyl groups at ca. 1730-1715 cm^{-1} (C=O from urethane) and at ca. 1700-1680 cm^{-1} (C=O from urea), C=C at ca. 1522 cm^{-1} and C-O-C at ca. 1214 cm^{-1} confirmed the presence of urethane and urea linkages, providing an evidence that the shell was composed by PUa/PU [14,17].

Regarding the synthesis of DETA MCs, at which DETA was added as active H source, the successful encapsulation of IPDI can be explained by the reaction of the amine groups of DETA with NCO groups of the DRFE, leading to fast formation of the PUa shell due to high reactivity of DRFE.

In the case of HDMS MCs, as shown in Figure 3.3b, in the high frequency region there were two strong absorption peaks at ca. 2924 cm^{-1} (C-H asymmetric stretching vibration) and at ca. 2852 cm^{-1} (C-H symmetric stretching vibration) in both spectra of HDMS and HDMS MCs' shell, confirming the presence of the long CH chain from HDMS in the HDMS MCs 's shell [18]. Furthermore, the presence of the carbonyl groups observed at ca. 1730–1715 cm^{-1} (C=O from urethane) and in 1700–1680 cm^{-1} (C=O from urea) [19], in the spectrum of HDMS MCs' shell, suggested the formation of PUa/PU shell. The tendency of HDMS to hydrolyse when added to the aqueous phase leads to the formation of silanol groups, which by polycondensation reaction can form siloxane moieties. These silanol groups, on the other hand, can react with the NCO groups of DRFE, forming urethane moieties. So, it can be argued that the HDMS MCs' shell was a silica-PUa/PU hybrid material, including hexadecyl siloxanes.

Although it was not possible to identify a clear fingerprint for n-OTES in n-OTES MCs, as it will be discussed below, the behaviour of n-OTES MCs was quite identical to HDMS MCs, in terms of thermal and chemical stability, suggesting the formation of hybrid shells for this case as well.

3.2.1.2.3 Thermal and chemical stability of microcapsules

For practical application, the MCs should be robust enough to tolerate various harsh environments, such as solvents, humidity, and mechanical pressure, that exist in the materials processing cycles. Furthermore, when present in the final material (in the intended case an epoxy coating) the MCs should be able to release their core content in response to certain stimuli, in this case, mechanical pressure. The ability is critical to render self-healing properties to the coating [3,20].

TGA thermograms of DETA MCs and IPDI, as well as their first derivative curves are shown in Figure 3.4a. According to these thermograms, DETA MCs exhibit a high thermal stability and start loosing mass at a temperature increased by 120°C, when compared to pure IPDI. The sharp drop-off for IPDI started at 110°C, while for DETA

MCs it started at 230°C. From the same thermograms, as the main drop-off in TGA curve was finished at 24 wt% for DETA MCs, the core fraction can be calculated as:

$$Core\ fraction\ (\%) = \frac{1-0.24}{1-0} \times 100 = 76\%$$

Figure 3.4b shows the FTIR spectra of DETA MCs, after 200 h immersion inside the solvents and hardener. Remarkably, DETA MCs showed excellent environment resistance while immersed inside the acetone, ethanol, and hardener as the NCO peaks in all spectra are still intense.

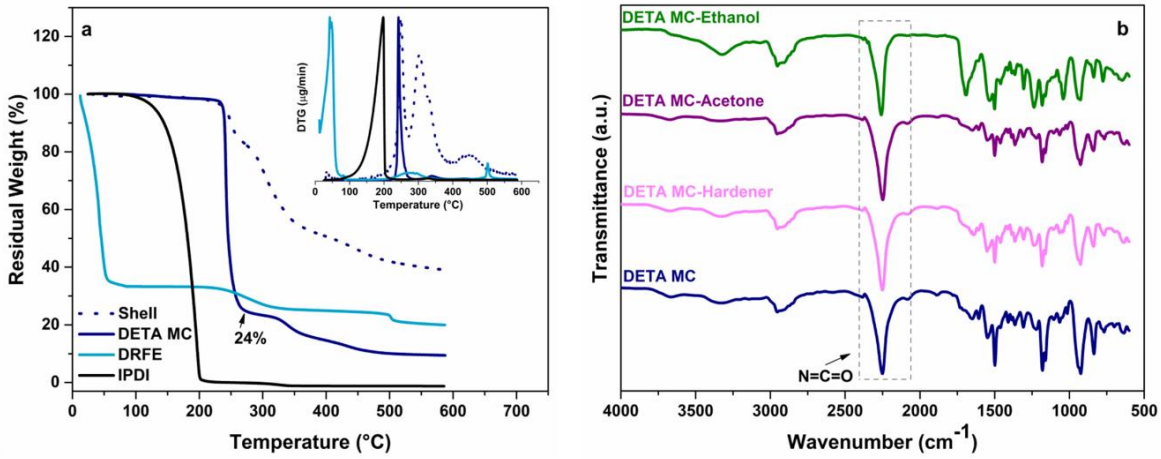

Figure 3.4 a) TGA of DETA MCs, IPDI and DRFE. The inset shows the corresponding first derivative curves, b) FTIR spectra of DETA MCs before and after immersion inside the solvents and hardener component of coating formulation.

In the case of HDMS MCs, at which HDMS was added for the formation of hybrid shell MCs, the initial mass loss of the MCs was found to be increased by 66-69°C compared to pure IPDI. The decomposition of HDMS MCs started at 180°C (Figure 3.5a). As it can be observed from TGA thermograms and their first derivative curves, the main drop-off in HDMS MC's TGA curve started at 93 wt% and ended at 24 wt%, so the core fraction could be calculated as:

$$Core\ fraction\ (\%) = \frac{0.93-0.24}{1-0} \times 100 = 69\ \%$$

It should be noted that the mass loss occurring from 100 wt% to 93 wt% might come from the decomposition of the organic part belonging to the HDMS (Figure A 1.2 - Appendix 1-page 218), which further corroborates the presence of a hybrid shell.

Figure 3.5b depicts the FTIR spectra of HDMS MCs after 200 hr immersion inside solvents and hardener. Although HDMS MCs showed excellent resistance against

hardener and acetone, due to intense NCO peaks still available in related spectra, they showed quite poor stability, when immersed in ethanol. Probably, the polycondensation reactions to form a silica network were not completed and there is still some gel material derived from the silane employed in the synthesis, which tends to dissolve in the presence of ethanol.

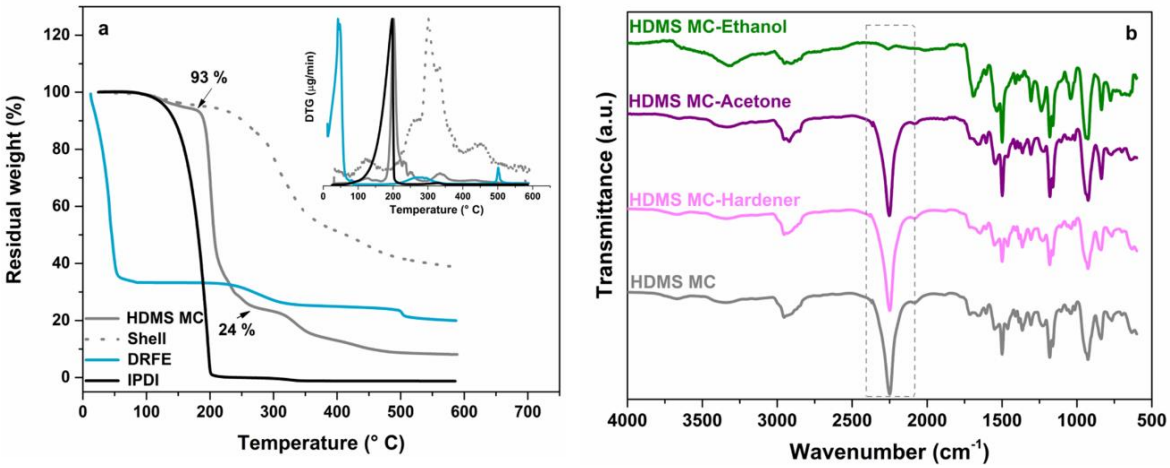

Figure 3.5 a) TGA of HDMS MCs, IPDI and DRFE. The inset shows the corresponding first derivative curves, b) FTIR spectra of HDMS MCs before and after immersion inside the solvents and hardener component of coating formulation.

Concerning n-OTES MCs, the thermal and chemical stabilities of these MCs were quite identical to those observed for the HDMS MCs. Indeed, the thermal stability of n-OTES MCs increased by ca. 65°C when compared to pure IPDI, with a corresponding decomposition starting at 175°C (Figure 3.6a). From the same TGA thermograms, decomposition of n-OTES MCs' core started at 94 wt% and ended at 29 wt% and the core fraction can be calculated as:

$$Core\ fraction\ (\%) = \frac{0.94-0.29}{1-0} \times 100 = 65\ \%$$

In this case, the mass loss occurring from 100 to 94 wt% comes probably from the decomposition of the organic part belonging to the n-OTES, which confirms, as well, the presence of a hybrid shell (Figure A 1.2 - Appendix 1- page 218). From the FTIR spectra of n-OTES MCs (Figure 3.6b), it can be concluded that n-OTES MCs show excellent stability inside the acetone and hardener, while they are not stable when immersed in ethanol. Although it was not possible to detect clear fingerprints of n-OTES in the FTIR spectra of n-OTES MCs and respective shell (Figure 3.6b), thermal and chemical stability

behavior of these MCs was found to be quite similar to that of HDMS MCs and it can be argued that the n-OTES MCs shell is composed of hybrid material, as well.

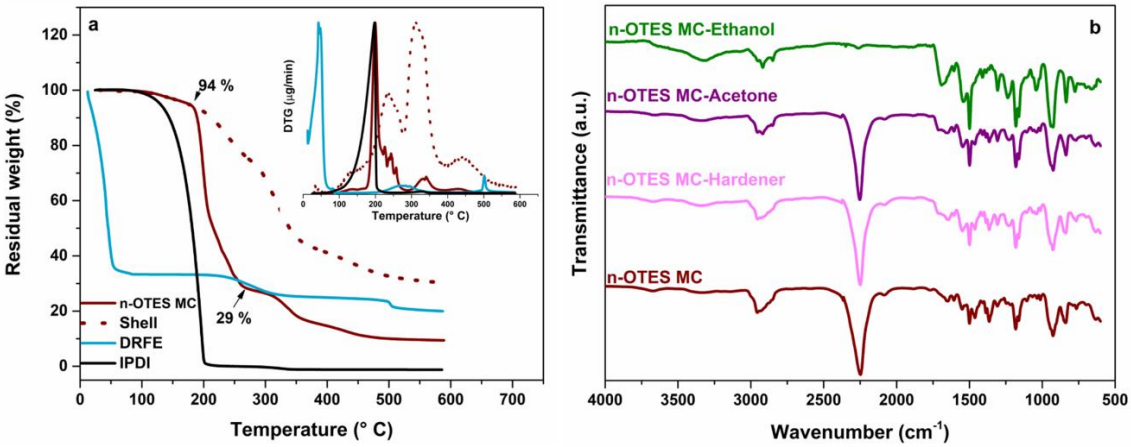

Figure 3.6 TGA of n-OTES MCs, IPDI and DRFE. The inset shows the corresponding first derivative curves, b) FTIR spectra of n-OTES MCs before and after immersion inside the solvents and hardener component of coating formulation.

3.2.1.2.4 Microcapsules' shelf life

As explained before, shelf-life of MCs can be estimated from FTIR spectra through the calculation of Y value. Figure 3.7b shows the evolution of the Y with the storage time after synthesis, for the three MCs´ of this study (the corresponding FTIR spectra of all three MCs are presented in Figures A 1.3a, b, and c - Appendix 1- page 219).

In the case of DETA MCs there was a gradual drop of the Y values during the first 60 days of storage, reducing to 70 % of initial value after 60 days. It is worth mentioning that an intense NCO peak was observed in FTIR spectrum at this time (Figure A 1.3a - Appendix 1 – page 219). The Y values of DETA MC then attain a steady state condition until 150 days, evidenced by merely 1% decrease of Y value at 150 days when compared to Y value at 60 days. DETA MCs attain a Y of 50 % after 160 days, which is considered as shelf-life of these MCs. Interestingly, the NCO peak at 160 days was still quite intense (Figure 3.7a- blue dashed line).

The n-OTES MCs on the other hand, demonstrated the same behavior, but the first drop in Y value has a sharper slope when compared with DETA MCs. The steady state condition lasted for a shorter time, starting at 30 days and ended at 80 days, when, the NCO peak still was intense at this time (80days). The Y value attained 50 % of its initial value after 110 days of storage, therefore, 110 days was considered as shelf-life of n-

OTES MCs. The intense NCO peak is still available after 110 days (Figure 3.7a-dark red dashed line). In the case of HDMS MCs, the Y value decreased continuously, and attained the 50 % of initial value at the 55th day, the time which was considered as shelf-life of these MCs. It is worth mentioning that, at this time an intense NCO peak, still can be observed (Figure 3.7a-gray dashed line). In general, the defined value (Y) for shelf-life seems to be safe enough, to ensure sufficient encapsulated IPDI is available even by the end of shelf-life. For instance, NCO peak was still quite intense after 80 days of storage of HDMS MCs (Figure A 1.3c-Appendix 1 – page 219), while the shelf-life was considered to be 55 days.

To summarize, the shelf-life of DETA MCs, n-OTES MCs and HDMS MCs was estimated to be more than 5, 3.5 and 2 months respectively.

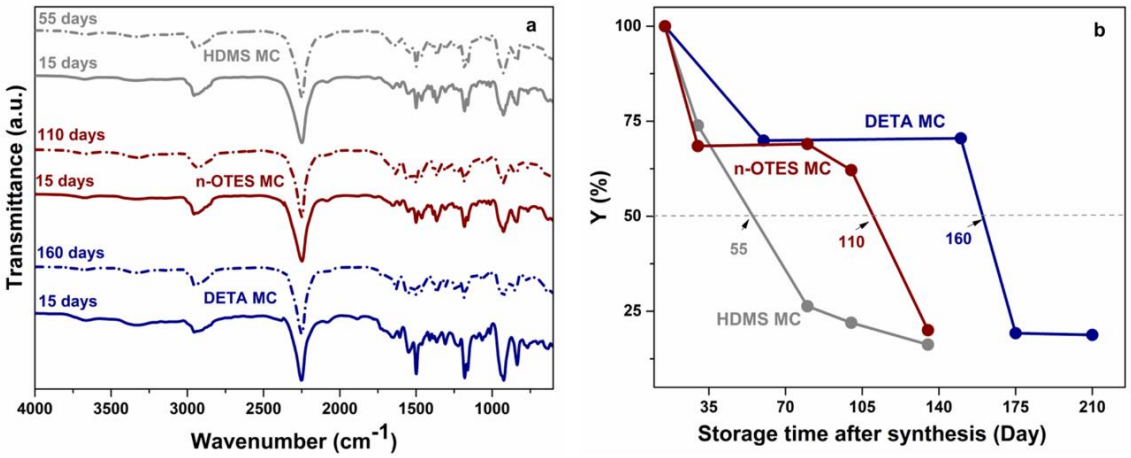

Figure 3.7 a) FTIR spectra of DETA, n-OTES, and HDMS MCs, after 15 days and at shelf-life time, b) Evolution of Y with the storage time after synthesis, giving an idea about their corresponding shelf-life.

A compilation of the main results regarding the MCs characterization is shown in Table 3.2. To summarize, although HDMS MCs and n-OTES MCs show excellent thermal and chemical stability inside acetone and hardener component of coating, they were found to loose the stability when immersed in ethanol. Moreover, the shelf-life of these MCs was found to be considerably shorter than that of DETA MCs. These results indicate that highly efficient, and long shelf-life MCs can be achieved by addition of DETA as an active H source to the aqueous phase of the emulsion. Moreover, thin, but chemically and thermally stable PUa/PU shell, was formed around the IPDI droplets via fast reaction of the NH groups from DETA with the NCO groups from DRFE. These outstanding shell's properties enabled the MCs to tolerate working conditions, and storage conditions

for longer time. These MCs were selected to be added to epoxy coating formulation to improve the healing properties of the coating.

Table 3.2 Summary of the results

MC Type	Shelf life (months)	Core fraction (wt%)	Thermal stability °C	Chemical stability		
				Acetone	Hardener	Ethanol
DETA MC	≈ 5	76	230	stable	stable	stable
HDMS MC	≈ 3.5	69	180	stable	stable	unstable
n-OTES MC	≈ 2	65	175	stable	stable	unstable

3.2.1.2.5 Effect of microcapsules on the coating curing time

Addition of MC contains IPDI into the epoxy coatings may affect the curing time of coating and this effect was studied by FTIR. As discussed before, fully consumption of epoxy band centred at ca. 916 cm^{-1}, is a good indicator for fully cured epoxy-based coating. Figure A 1.4a, and b (Appendix 1 – page 220) show FTIR spectra of modified and reference coatings respectively, collected during the 100 h experiment. For both modified and reference coatings (Figure A 1.4) an absorbance band at ca. 916 cm^{-1} decreases rapidly upon curing. This change suggests fast consumption of epoxy groups at very early stages (until 5 h) of curing, when coatings are exposed to 40°C. The linear change of the area vs. time at 40°C (Figure 3.8) can be justified by the uniform thickness of the applied coatings in both cases [12]. For the modified coating, the peak at 916 cm^{-1} almost disappeared after the sharp drop observed until 5 h (Figure A 1.4a), suffering only a slight change after 27 h. There was no relevant conversion neither in the area value nor in the shape of the peak after this time. Thus, 27 h was considered as curing time of the modified coating.

For the reference coating, although the peak disappeared after 97 h (Figure A 1.4b - Appendix 1 – page 220), the area under the peak, depicted at 916 cm^{-1}, was still reducing after 100 h (Figure 3.8), indicating an important delay in the curing time, when compared to the MCs containing coating.

The short curing time for the modified coating can be explained by a possible reaction between the epoxy groups and the unreacted secondary amine in MCs' shell, which

consequently fastens the consumption of epoxy groups. This fact can lead to a faster coating preparation step.

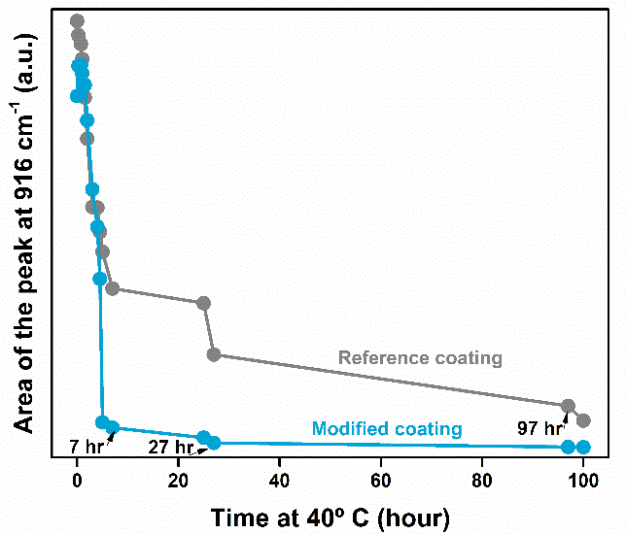

Figure 3.8 Evolution of the FTIR spectra of reference and modified coatings when exposed to 40°C.

To wrap up, the first part of this chapter regarding the synthesis and characterization of MCs, shows that spherical and long shelf-life PUa/PU and silica-PUa/PU MCs containing IPDI in their core were successfully obtained by a combined strategy of emulsion formation and interfacial polymerization within an O/W emulsion. The diameter and shell thickness of MCs were adjusted to be in the range of 5-20 µm and 1-2 µm, respectively, by adjusting the emulsification speed, emulsifier concentration, as well as synthesis duration. Addition of DRFE as a highly reactive isocyanate source to IPDI, allowed fast formation of a thin shell around the IPDI droplets, increasing the loading efficiency of MCs by avoiding NCO groups of IPDI reacting with active H source and participating in the shell formation process. Moreover, the addition of DETA, as active H source, resulted in a good combination of shelf-life (> 5 months), thermal and chemical stability, as well as high encapsulation yield, which qualify DETA MCs to be added to epoxy coating formulations, aiming at autonomous self-healing properties.

3.2.2 Preparation and application of coatings

Two groups of coatings were prepared and applied on carbon steel[5] coupons:

The reference coating (commercial epoxy coating[6]) was prepared by mixing the epoxy part of coating with the hardener (70/30(wt%)). These two components were mixed gently together and left at RT during the 24h before applying on steel coupons.

Modified coating containing MCs[7] was prepared by adding small quantity of ethanol (1.5 - 2 wt%) to the MCs (2, 3 wt.%) to help a better dispersion of MCs before adding into the hardener part of coating (30 wt%). The mixture was stirred manually until a homogenous dispersion of MC inside the hardener was obtained. Finally, the mixture was added into the epoxy part (70 wt%) and mixed slowly. Like the reference coating, the modified ones were also left for 24 h at RT before applying on steel coupons.

The steel coupons were degreased in acetone followed by drying with hot air before applying the coating. The coatings were applied on steel coupons by dip-coating, using a dip coater machine (detailed information can be find in Appendix 2)

The coated samples were dried and cured in the oven at 40°C for 5 days to allow stable dry film thickness.

3.2.2.1 Characterization of coatings

The coating thickness was determined with a digital gauge. Cross-cut tests (using standard procedure ASTM D3359-09) [21] were performed to evaluate the adhesion of both reference and modified coatings to the steel substrate. EIS experiments were carried out to investigate the barrier properties of the reference and modified coatings applied on carbon steel coupons, immersed in 0.05 M NaCl solution.

LEIS was performed to assess the local changes in admittance at an artificial defect made in the reference and modified coatings, while the sample was immersed in 0.005 M of NaCl solution.

SVET and SIET measurements were performed over coated samples containing point defects to evaluate the localized corrosion activity, during immersion of sample in 0.05 M NaCl solution. (detailed information regarding the equipment used to characterize the coatings, and method of characterization can be found in Appendix 2).

5 Carbon steel plates (DC01) were kindly provided by Voestalpine. The chemical composition of DC01 was reported Chapter 1.

6 A model epoxy coating, based on a commercial formulation, was kindly provided by Sherwin-Williams.

7 Several modified coatings were prepared with addition of different concentrations of DETA, n-OTES, and HDMS MCs. Results presented throughout this chapter comprise the most representative data obtained for modified coating containing DETA MCs.

3.2.2.2 Results and Discussion (Coatings)

3.2.2.2.1 EIS Experiments

The average thicknesses of reference, modified coating with 2 wt% of MC, and modified coating with 3 wt% of MC, were 68 ± 5.3, 78 ± 5.3, 76 ± 7.8 respectively. EIS was performed to investigate the barrier properties of the reference coating and coatings modified with 2 and 3 wt% of DETA MCs, applied on carbon steel coupons, immersed in 0.05 M NaCl solution during 180 days for modified coating, and 120 days for reference coating. A representative set of Bode plots obtained on both reference and coating modified with 2 wt% of MCs are depicted in Figure 3.9[8]. For reference coating impedance results displayed a capacitive behavior in the high frequency domain that slightly attenuated during immersion (Figure 3.9a), suggesting that the coating barrier properties suffered only minor changes. In the low frequency domain, the magnitude plot showed a resistive trend and the total impedance decreased from $1.6 \times 10^9\ \Omega\ cm^2$ to values close to $5 \times 10^8\ \Omega\ cm^2$ at the end of the immersion test. This descending trend was accompanied by formation of a time constant in the low frequency domain (Figure 3.9b), confirming the onset of corrosion activity at the steel-coating interface. A set of representatives Bode plots obtained for the modified coatings containing 2 wt% of MCs are depicted in Figure 3.9c, and d. At early stages the total impedance was around $1 \times 10^9\ \Omega\ cm^2$ and remained quite stable for more than one month of immersion. After 35 days of immersion the Bode plots reveal an increase of the low frequency impedance (Figure 3.9c) and a broadening of the phase angle (Figure 3.9 d) that reflect recovery of the coating barrier properties.

8 The response of both modified coatings (containing 2, and 3 wt% of MCs) was completely identical, therefore, only Bode plots of coatings modified with 2 wt% of MCs are reported in this chapter. However, in Figure 3.10 low frequency impedance moduli (light blue line) of coating modified with 3 wt% of MCs were reported, to show the identical behavior of both modified coatings. EIS plots regarding the modified coating containing 3 wt% of MCs will be reported in Chapter 4.

This recovery continues over time, as evidenced by the increase for more than one order of magnitude of the impedance modulus until end of experiment (180 days). Concomitantly, the phase angle decay shifted to lower frequencies and the onset of the low frequency time constant (related to steel activity) observed at early stages vanished. The low frequency impedance modulus ($|Z|_{LF}$) is often taken as a parameter to evaluate the overall corrosion protection performance of organic coatings [22,23]. Figure 3.10 compares this parameter for the reference, and for both modified coatings. The $|Z|_{0.005\ Hz}$ values for the reference coating show a decreasing trend over the entire immersion time and fluctuated in the range 1.5 to 0.5 × 10^9 Ω cm^2, evidencing continuous electrolyte uptake, formation of conductive paths, and deterioration of the coating barrier properties.

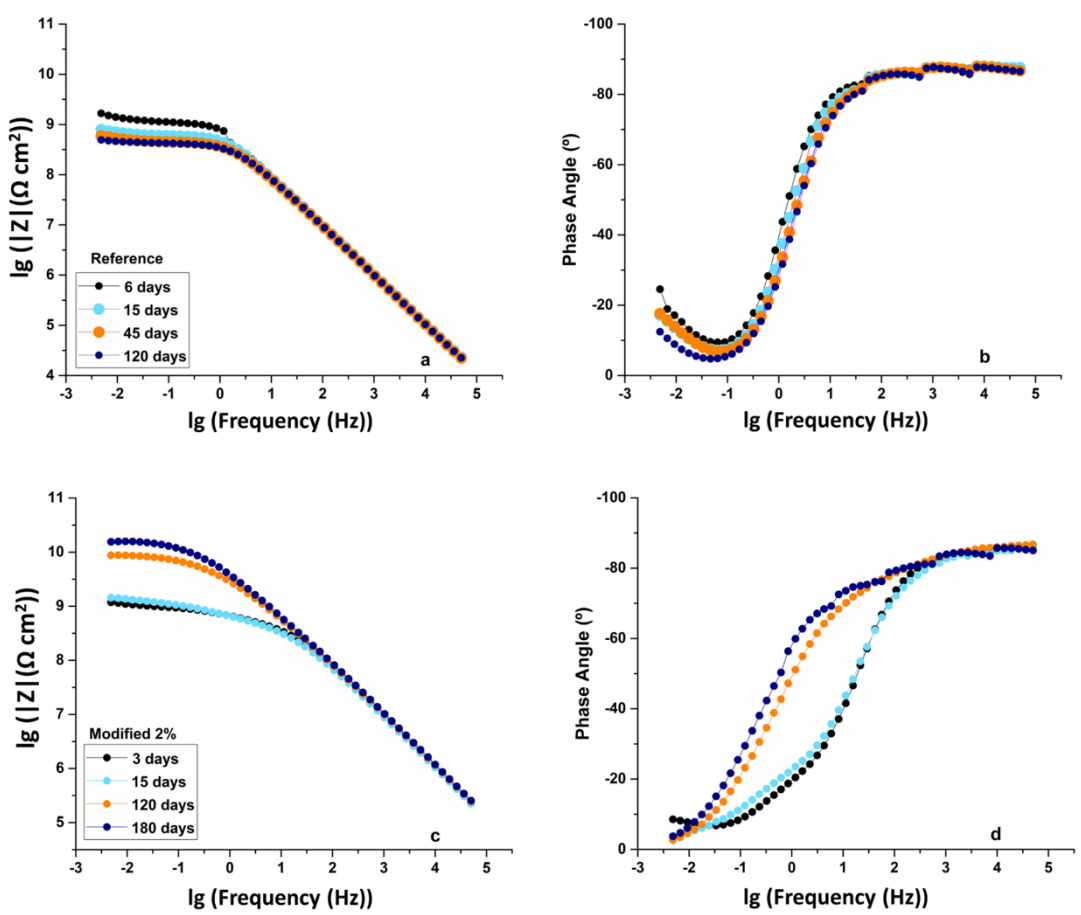

Figure 3.9 Bode plots for the reference coating (a, b); and coating modified with 2 wt% of DETA MCs (c, d).

Contrarily, $|Z|_{0.005\ Hz}$ obtained for the modified coatings show an increasing trend after 35 days of immersion, from 1 × 10^9 Ω cm^2 towards values close to 1 × 10^{10} Ω cm^2, evidencing an important recovery of the barrier properties of the modified coatings.

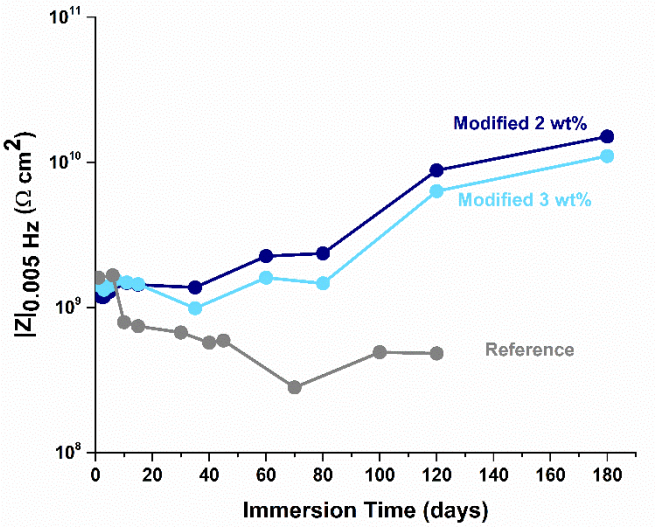

Figure 3.10 Comparison of the low frequency impedance values (measured at 0.005 Hz) on steel plates coated with reference and modified coatings.

At early stages, the decrease of $|Z|_{0.005\ Hz}$ for both reference and modified coatings (for modified coating a slight decrease was observed until 40 days of immersion) can be due to corrosion onset. Indeed, the formation of a time constant in the low frequency range in the coating modified with MCs (Figure 3. 9d) supports this assumption. While this effect becomes more pronounced for the reference coating, it vanished for the modified coating. As it shown in Figure 3.10, the coating contains 2 wt% of MCs revealed the highest $|Z|_{0.005\ Hz}$ values over time, i.e., the most notorious self-healing effect when compared to coating modified with 3 wt% of MCs. Thus, this coating was chosen for further evaluation using the localized electrochemical techniques to assess the self-healing ability.

As it discussed in chapter 2, experimental EIS data can be simulated with an equivalent circuit, providing information regarding the various ongoing processes when coated metals are exposed to a corrosive environment [24]. For both reference and modified coatings, the shape of the obtained spectra (Figure 3.9) suggested the presence of two-time constants, one at high/middle frequency range, and one at low frequencies throughout the immersion period. The time constant at higher frequencies can be attributed to the barrier properties of the coating, and the low frequency time constant can be assigned to interfacial processes between the coating and the substrate [25].

An equivalent circuit shown in Figure 3.11 was used to fit the EIS data obtained for reference and modified coatings during immersion in 0.05 M NaCl for the entire immersion period. In this circuit, at high frequency, R_p was assigned to the pore resistance

of the coatings and its variation is expected to reflect the formation of conductive paths due to electrolyte uptake, while CPE_{Coat} was assigned to coating capacitance. At low frequency, R_{ct}, and CPE_{dl} were assigned to the Faradic resistance and the capacitance of the double layer, respectively. The constant phase elements were used instead of capacitors due to deviations from the ideal condition. In this circuit, R_s represents the resistance of electrolyte.

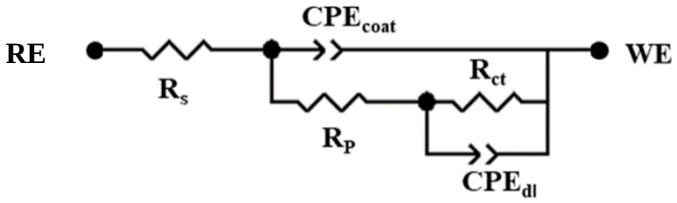

Figure 3.11 EEC used to simulate the experimental EIS data obtained for the reference and modified coatings during immersion in 0.05 M NaCl.

Figure 3.12a shows the pore resistance of reference, and modified coating containing 2 wt% of MCs. The pore resistance of the reference coating showed a decreasing trend during the immersion in saline solution, displaying initial values close to $8 \times 10^8\ \Omega\ cm^2$ at the early stages which reduced for more than one order of magnitude, reaching $3 \times 10^7\ \Omega\ cm^2$ by end of the test (100 days). This trend evidenced a notorious degradation of the barrier properties of the coating as consequence of solution uptake. For the modified coating the pore resistance initial value was $1.9 \times 10^8\ \Omega\ cm^2$ and it decreased slightly during the first 5 days of immersion, probably because of solution uptake. From this time forward the values showed a continuous increasing trend tile 80 days, reaching a value close to $5.2 \times 10^8\ \Omega\ cm^2$ at 80 days, being more than an order of magnitude higher than the same value for reference coating ($3.4 \times 10^7\ \Omega\ cm^2$) at the identical immersion time, suggesting a recovery of the barrier properties of the modified coating due to release of IPDI from the MCs and mending of pores and/or defects formed in the polymeric matrix.

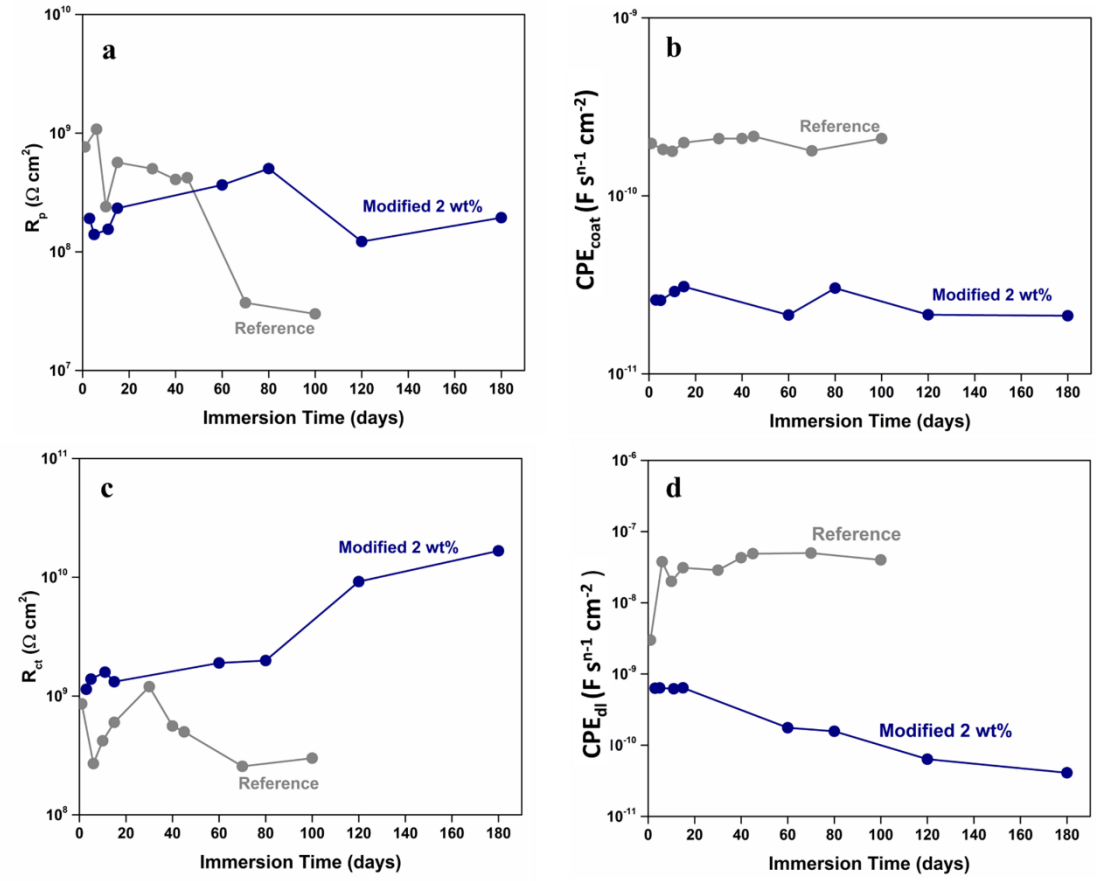

Figure 3.12 Evolution of a) coating pore resistance, b) admittance of the coating; c) Faradic resistance, d) admittance of the double layer (Data are available in Tables A 1.3, and A 1.4 -Appendix 1).

The CPE_{coat} admittance value of modified coating was significantly lower than those value for reference coating during the entire immersion time (Figure 3.12b), and a slight fluctuation was observed in admittance values of both coatings.

Figure 3.12c shows the R_{ct} values for both reference and modified coatings which are assigned to the faradic resistance at the interface of coating-steel. For the reference coating these values showed some fluctuations during the immersion time and suffered an overall decrease at the end of the test. The R_{ct} value was 1×10^9 Ω cm^2 at the beginning of immersion and reduced about one order of magnitude by the end of the test, reaching values of 2.8×10^8 Ω cm^2. The fluctuations of R_{ct} and the respective admittance values, CPE_{dl}, evidence corrosion activity at the steel-coating interface which leads to accumulation of corrosion products that can partially block the coating pores. For the modified coating the faradic resistance value initially was 1.06×10^9 Ω cm^2, quite identical to the reference coating. By that time, the values showed an increasing trend,

and were in the range 1.6×10^{10} Ω cm^2 at the end of test (180 days), meaning that the modified coating displayed the highest Faradic resistance (almost two orders of magnitude) compared to the reference coating. In other words, the interfacial activity of modified coatings was suppressed continuously, confirming the formation of highly protective polymeric layer at the interface of steel-coating due to reaction of released IPDI from MCs with OH groups or water. The continuous reduction of CPE_{dl} for the modified coatings (Figure 3.12d) also confirms an important healing effect due to the presence of MCs (All EEC parameters used to fit the EIS plots of reference and modified coatings can be found in Table A. 1.3, and A 1.4, Appendix 1 – page 220).

3.2.2.2.2 Localized Electrochemical Techniques

As discussed in Chapter 2, EIS is an effective tool for the evaluation of the corrosion protection performance of coatings, however it is a surface-averaged technique, and the response of the system under study includes the responses of defects in the coating and of intact coating around the defect. Thus, localized electrochemical techniques with ability to collect the signal from the specific point, or area of interest, help to evaluate locally the corrosion processes, protection mechanisms, and healing ability of a system. Therefore, the healing ability of the modified coating containing 2 wt.% MCs was studied by LEIS and the results were compared to those obtained for reference coating. For that, an artificial pin-hole defect was created with a sharp needle on the surface of the coated samples. Figure 3.13 shows LEIS maps that evidence the evolution of the admittance over time. As expected, the maximum admittance values were found over the defect made in the coating where the bare steel was exposed. This maximum values over the defect showed a continuous increase in the reference coating (Figure 3.13a, b, and c), confirming the presence and progress of corrosion activities. In contrast, the admittance values over the defect formed in the modified coating showed an increase during the first 48 h of immersion and reached a maximum value at this time of immersion (Figure 3.13d, and e). From this time forward, the corrosion activity showed a descending trend (Figure 3.13g) and later became negligible (Figure 3.13f). The results reveal that the corrosion activity in the artificial defect could be effectively suppressed.

It is worth to mention that the overall admittance values for the modified coating were approximately one order of magnitude lower compared to the reference coating.

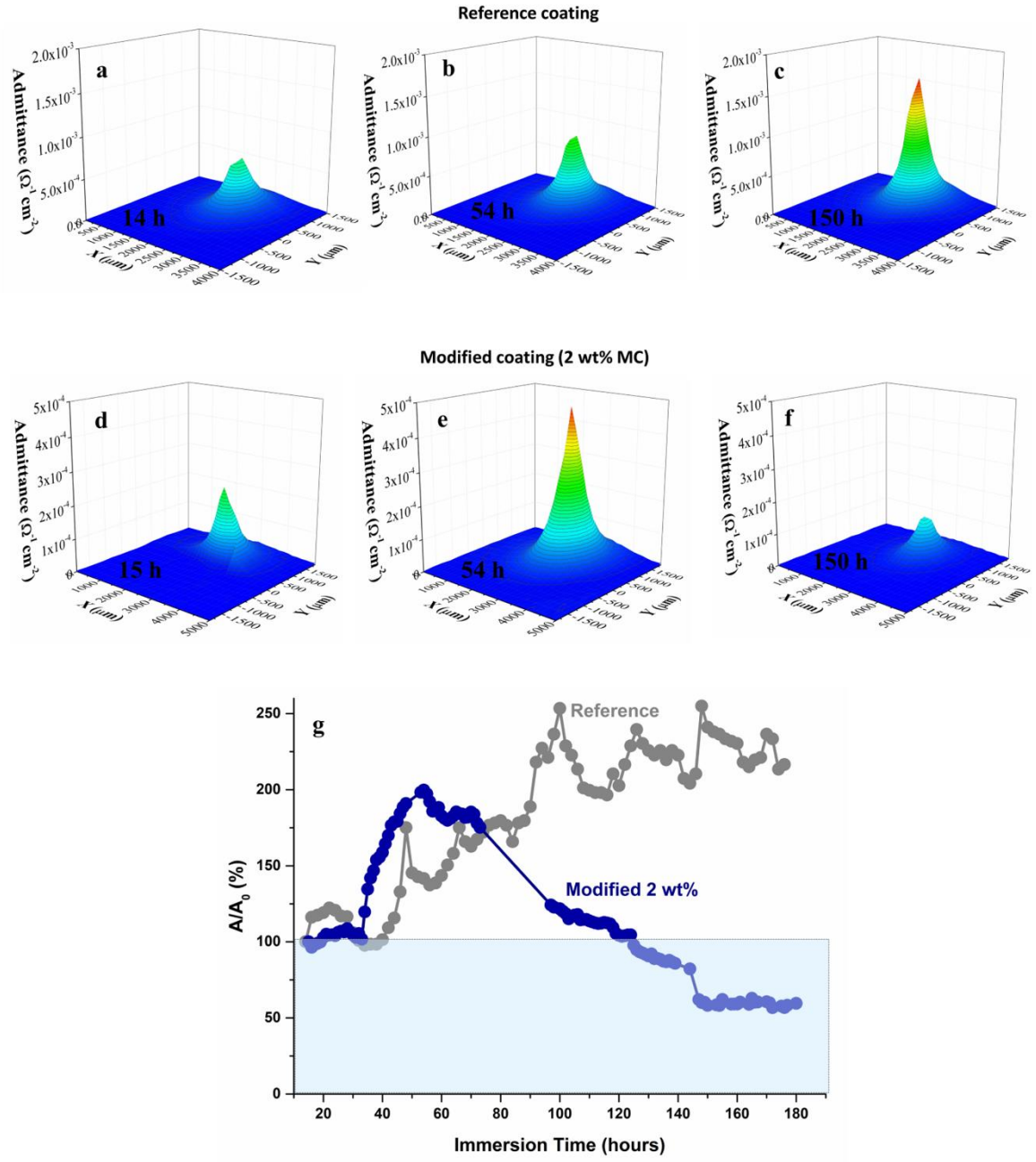

Figure 3.13 LEIS admittance maps obtained after 14 h, 54 h, and 150 h, immersion of the reference coating (a, b, and c); after 15 h, 54 h, and 150 h, immersion of modified coating (2 wt% MC) (d, e, and f) in 0.005 M NaCl solution; Evolution of the admittance ratio for the reference and modified coatings during immersion in 0.005 M NaCl solution (g).

The overall evolution of admittance at the artificial defects in coatings evaluated by LEIS is shown in Figure 3.13g. This figure represents the ratio between maximum admittance values determined over the defect at a specific time (A) and the maximum value

measured at the beginning of immersion (A_0). Therefore, an increase of this ratio can be assigned to increased admittance, and therefore higher corrosion activity over the defect, while a decrease of the ratio is evidence of inhibition of the corrosion activity, or healing of the material.

For the reference coating, despite some fluctuations, A/A_0 values over the defect increased over time, evidencing continuous corrosion activities over the defect. The fluctuations observed are probably related to formation and dissolution of corrosion products that can partially block some active areas of the steel exposed to the electrolyte. Modified coatings also evidenced a trend close to the reference sample during the first 48 h of immersion, showing that corrosion could progress over time. However, from this time forward an inversion was noticed and the A/A_0 values for the modified coating started to decrease, evidencing inhibition of the corrosion activity. After approximatly120 h, the A/A_0 values reached the ones measured at the initial stages and continued to decrease, becoming even lower that the initial ones, suggesting the formation of a protective film on steel that further prevents corrosion activity. The continuous decline over time until 147 h of immersion clearly evidences the healing effect of the modified coating. The A/A_0 values then were kept nearly constant, being around 50-60 % of the initial value until end of the experiment. The LEIS response shows that activation of the healing effect requires a certain time delay, time after which the corrosion activity became effectively suppressed. Overall, the results show the healing ability of the coating modified with MCs over defects due to the formation of a protective barrier layer, in good agreement with results obtained from EIS.

SVET and SIET were employed as complementary techniques to gain insight on the performance of the MC-modified coating on local defects. While SVET gives information about the total ionic fluxes resulting from local corrosion activity, SIET provides important data on the chemical nature of the species involved in the corrosion process [26]. In this work, SIET was employed to determine local pH gradients.

SVET was carried out over an area containing the artificial defect created in the coatings, while coated samples were immersed into the 0.05 M of NaCl solution during the 13 h. Figure 3.14 shows the most representative distributions of current density along the immersion time recorded for the reference and modified coated samples, while the corresponding SIET maps were illustrated in Figure 3.15. In the reference coating, both cathodic and anodic activities were observed from the early stages of immersion and showed a slow increase from 2 h until 13 h of immersion (Figure 3.14c, and i). This

gradual increase in current density was accompanied by localized alkalinization (Figure 3.15a and b) over the defect due to the release of hydroxyl anions produced by reduction of oxygen at the cathodic sites. A small decrease of the current density was noticed after 6 h of immersion, probably due to accumulation of corrosion products at the defect (Figure 3.14d, and i) which can hinder the flux of ionic species from the active areas. In fact, corrosion products were clearly observed at the end of the test (Figure 3.14b). The accumulation of iron corrosion products also limits the access of oxygen towards the cathodic sites and attenuates the alkalinization effects.

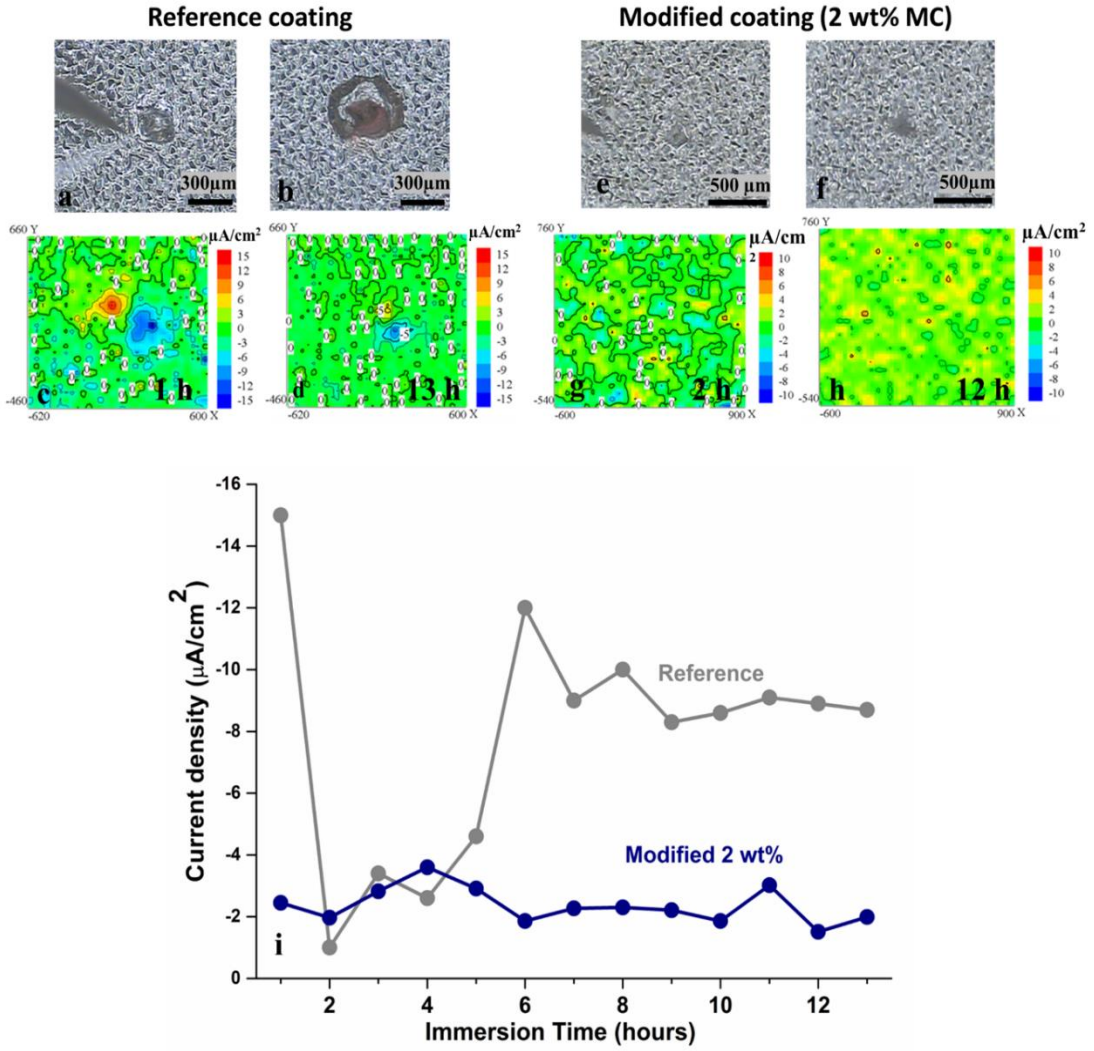

Figure 3.14 Optical micrographs (a, b, e, f) and SVET maps obtained for the reference coating after 1 h (c) and 13 h (d), and for the modified coating after 2 h (e) and 12 h (f) of immersion in 0.05 M NaCl. The optical micrographs (a, b: reference coating at the beginning and at the end of immersion time, respectively; e, f: modified coating at the beginning and at the end of immersion time, respectively.

The results obtained for the modified coating revealed a radically different behavior compared to the reference coating. Neither anodic, nor cathodic activities could be detected by SVET during the immersion (Figure 3.14g, h, and i). Complementary pH mapping also did not show relevant changes over the defect during the immersion test (Figure 3.15 c, and d). Compared to the reference coating, such a behavior confirmed the self-healing ability of the modified coating. In this specific test, no early activity could be detected, probably because the area to be healed was smaller compared to the one studied by LEIS.

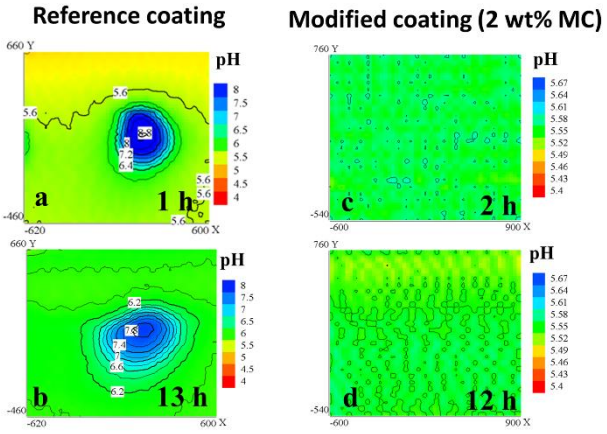

Figure 3.15 SIET maps obtained for reference coating after 1 h (a) and 13 h (b), and for the modified coating after 2 h (c) and 12 h (d) of immersion in 0.05 M NaCl.

Figure 3.14i shows the maximum cathodic current density registered at the defect, during the immersion time, which gives quantitative evidence of the corrosion activity over the artificial defect. For the sample coated with reference coating, the cathodic current density over the defect at the early stage of immersion (1h) in electrolyte was noticeable. From 2 h to 4 h current density was reduced, probably due to formation of corrosion products at the defect surface, which could difficult the access of oxygen to the cathodic sites temporarily. From this time ahead, the current density started to increase and kept stable from 7 h until the end of the test. The small fluctuations in current density can be justified by random formation and dissolution of corrosion products over and around the defect. For the modified coating the maximum cathodic current density over the defect was negligible for the entire immersion period, confirming the successful corrosion healing due to the IPDI released from the broken MCs.

3.3 Self-healing process of IPDI MCs

The self-healing ability of the modified coating was proved by various techniques. Based on the results it is possible to postulate that the self-healing mechanism associated with the use of IPDI MCs involves several steps as schematically depicted in Figure 3.16: i) MCs, which are uniformly dispersed throughout the coating, can be broken under mechanical damage; ii) the IPDI is released from the broken MCs under the generated stress (Figure 3.16a); iii) the healing agent (IPDI), in the presence of water/OH, reacts and polymerizes at defects, healing the coating locally (Figure 3.16a, and c). Under these circumstances, the epoxy matrix is repaired, the barrier properties are recovered (Figure 3.16b) and the corrosion activity of steel vanishes [27–29].

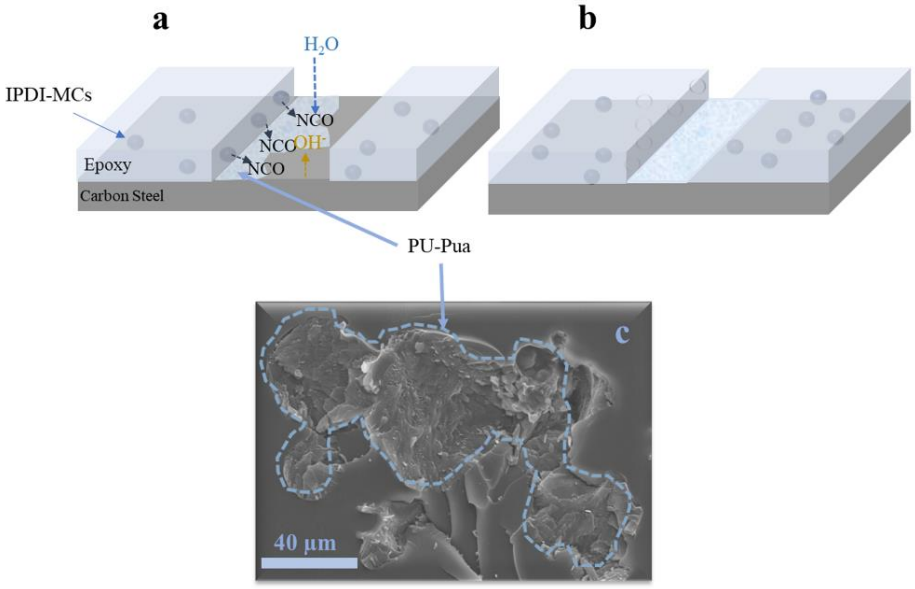

Figure 3.16 Proposed mechanism of function of IPID-MCs to heal an artificial defect made in the epoxy coating: a) release of IPDI from broken MCs following by its reaction with OH^-/water; b) PU/PUa protective layer totally covers the defect; c) SEM photo of artificially damaged epoxy coating after 7 days of immersion in 0.005 M NaCl (dashed line shows the polymeric phases formed due to the release and reaction of IPDI).

In fact, the isocyanate chemical group is extremely reactive and can form chemical bonds with any chemical group that contains an active H atom, such as NH groups or OH groups [7,30]. The reaction between –NCO groups and different active H sources can lead to different compounds: i) in the presence of water it leads to the formation of an amine; ii) reaction with –OH groups leads to the formation of urethane linkages; iii) and reaction with amino groups promotes urea leakages (Figure 3.17) [7,31]. These reactions are involved in formation of the polymeric protective layer that heals defects formed in the coating.

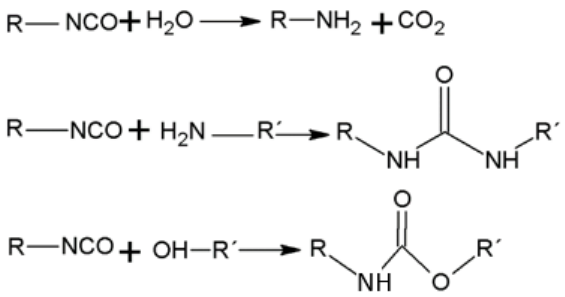

Figure 3.17 Reaction of NCO group of isocyanates with water, amine, and hydroxyl groups.

Based on the experimental observations, for the intact coating, the impedance modulus showed an increasing trend that proves the continuous improvement of the barrier properties. The process is likely to involve a gradual diffusion of electrolyte through pores and defects that exist around the MCs and consequent reaction of the –NCO groups of the isocyanate compound with water leading to the formation of amines. Then these amines react with further –NCO groups and finally lead to the formation of a polymeric phase according to the scheme depicted in Figure 3.17. Moreover, MCs may swell in contact with the electrolyte [23] and this process may stimulate initiation of new microcracks that generate interfacial stress at the MCs' shell, followed by slow release and diffusion of IPDI into the epoxy matrix. Since coating defects and porosity are in the vicinity of MCs the released IPDI can fill those sites and its further reaction will form a polymeric phase that heals the defects, as evidenced by the continuous recovery of impedance over 180 days of immersion.

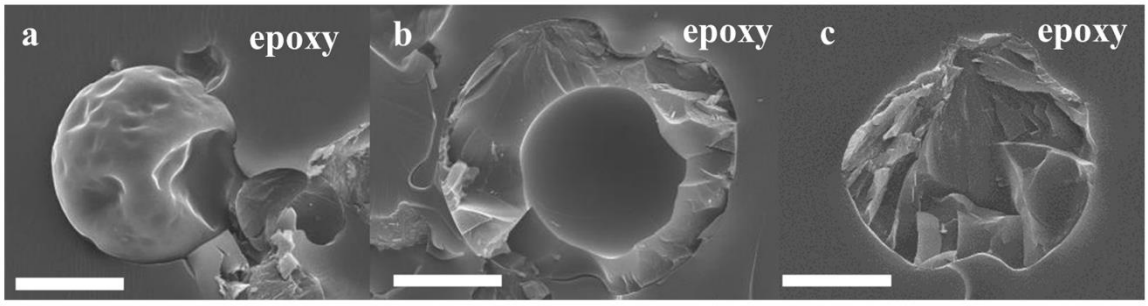

Figure 3.18 SEM micrograph of cross-section of coating a) with intact MCs, b) with broken MCs, c) SEM photomicrograph of epoxy cross-section containing fully polymerized MCs (Scalebar = 20 µm for all three micrographs).

Figure 3.18 shows the cross section of an epoxy coating containing 2 wt.% MCs. The gradual formation of the polymeric phase due to diffusion of moisture to the MCs ´shell,

results in the thickening of the shell ≈10 μm (Figure 3.18b) compared to the original MCs' shell thickness ≈ 2 μm (Figure 1c, f, and i), before addition to the epoxy formulation. The process will progress, and some MCs turn into a fully polymerized structure (Figure 3.18c). This polymeric phase can hinder further the diffusion of electrolyte, recovering the barrier properties of the coating as confirmed by EIS [23]. However, this process is slow since the MCs' shell are designed to be impermeable and, very likely, this is the reason why the impedance recovery only became noticeable after 35 days of immersion. When the coating was artificially damaged, the pressure exerted in the process is expected to disrupt some MCs that immediately release their content. Thus, the artificial defect allows the fast and direct contact of IPDI with active hydrogen sources, leading to a much faster activation of the healing process. In small defects, as the ones studied by SVET, there is no significant time delay as the amount of released IPDI is high and sufficient to form a stable and protective polymeric layer. This is most probably a polyurethane-based layer, due to availability of oxygen at the cathodic sites, over steel, some early oxygen reduction occurs (in fact SVET detected weak cathodic currents), and the OH^- released, easily react with the –NCO group of the isocyanate compound leading to the formation of a protective polymeric layer that forms over the cathodic sites, inhibiting further access of oxygen and therefore suppress the cathodic reaction. Consequently, the corrosion process is hindered, and the healing effect becomes noticeable.

However, in larger defects, as the ones studied by LEIS the corrosion process occurs in a larger area and the early release of IPDI from the broken capsules may not be sufficient and the corrosion activity could continue until the electrolyte uptake and accumulation of water activates more MCs at the vicinity of the defect. Therefore, after some time, additional supply of IPDI is achieved and efficient healing could be observed, justified by the formation of a polymeric layer. Moreover, the presence of more OH^- ions, released in the cathodic sites also may trigger the reaction with the –NCO groups forming a polyurethane protective layer.

It is worth mentioning that, the presence of tertiary amines in the coating epoxy matrix can catalyze the reaction between free hydroxyl groups of the epoxy with IPDI, which helps healing the damaged zone [32]. Generally, formation of hydrogen bonds between the functional groups of the epoxy (hydroxyls and tertiary amines) and IPDI´s functional groups can be considered as a side healing process [33].

3.4 Conclusion

The work presented in this Chapter addresses the synthesis and characterization of IPDI-MCs and further modification of the epoxy coating with addition of those MCs to confer self-healing ability to the epoxy reference coating.

Core-shell, spherical and robust MCs of PUa/PU, and silica-PUa/PU shell, containing IPDI in their core were synthesized by a combined strategy of emulsion formation and interfacial polymerization within the O/W emulsion. The diameter and shell thickness of MCs were optimized by adjusting the emulsification speed, emulsifier concentration, as well as synthesis duration. Besides that, optimized isocyanate-based shell forming agent and active H source were selected to achieve MCs that are eligible to be employed as self-healing agents for epoxy coatings. Addition of DRFE as a highly reactive polyisocyanate source to IPDI, allowed the fast formation of a thin shell around the IPDI droplets, increasing the loading efficiency of MCs by limiting the reaction of –NCO groups of IPDI with OH groups.

DETA MCs, i.e., IPDI MCs prepared with DETA as active H source, with high thermal and chemical resistance and a high (76%) encapsulation efficiency, were added to an epoxy coating formulation to impart self-healing ability. EIS confirmed an important healing ability of the modified coating applied on carbon steel as evidenced by the one order of magnitude increase of the low frequency impedance modulus for 6 months immersion in 0.05 M NaCl.

The healing ability of modified coating was confirmed by LEIS, as the relative admittance values decreased significantly after a certain time of immersion.
SVET confirmed that the presence of IPDI filled MCs in artificially damaged epoxy coating can suppress the corrosion activity in a large extent. SIET also confirmed the absence of corrosion activity since neither acidification, nor alkalization have been detected over the steel surface exposed at the defects, contrarily to the behavior observed in the reference coating where, important alkalization of the steel was noticed. Overall, the healing process involves a sequence of steps and reactions involving water, amine and hydroxyl groups as follow: i) partial conversion of isocyanate groups in contact with water to corresponding amine groups; ii) reaction of generated amines with remaining isocyanate groups to form polyurea; iii) reaction of isocyanate groups with hydroxyl

groups and formation of PU, that all together result in the formation of a stable and protective polymeric layer.

3.5 References

[1] M.F. Montemor, Functional and smart coatings for corrosion protection: A review of recent advances, Surf. Coatings Technol. 258 (2014) 17–37. https://doi.org/10.1016/j.surfcoat.2014.06.031.

[2] W. Wang, L. Xu, X. Li, Y. Yang, E. An, Self-healing properties of protective coatings containing isophorone diisocyanate microcapsules on carbon steel surfaces, Corros. Sci. 80 (2014) 528–535. https://doi.org/10.1016/j.corsci.2013.11.050.

[3] M. Attaei, Microencapsulation of isocyanate compounds for autoreactive, monocomponent adhesive, MSc Thesis, Instituto Superior Técnico Lisboa, 2017.

[4] P. Kardar, Preparation of polyurethane microcapsules with different polyols component for encapsulation of isophorone diisocyanate healing agent, Prog. Org. Coatings. 89 (2015) 271–276. https://doi.org/10.1016/j.porgcoat.2015.09.009.

[5] L.T.T. Nguyen, X.K.D. Hillewaere, R.F.A. Teixeira, O. Van Den Berg, F.E. Du Prez, Efficient microencapsulation of a liquid isocyanate with in situ shell functionalization, Polym. Chem. 6 (2015) 1159–1170. https://doi.org/10.1039/c4py01448k.

[6] F. Cotting, A. Koebsch, I.V. Aoki, Epoxy Self-Healing Coating by Encapsulated Epoxy Ester Resin in Poly (Urea-Formaldehyde-Melamine) Microcapsules, Front. Mater. 6 (2019), Article 314. https://doi.org/10.3389/fmats.2019.00314.

[7] M. Attaei, M. V. Loureiro, M. Vale, J.A.D. Condeço, I. Pinho, J.C. Bordado, A.C. Marques, Isophorone diisocyanate (IPDI) microencapsulation for mono-component adhesives: Effect of the active H and NCO sources, Polymers (Basel). 10 (2018) 825. https://doi.org/10.3390/polym10080825.

[8] M.V. Loureiro, M. Attaei, S. Rocha, M. Vale, J.C. Bordado, R. Simões, I. Pinho, A.C. Marques, The role played by different active hydrogen sources in the microencapsulation of a commercial oligomeric diisocyanate, J. Mater. Sci. 55 (2020). https://doi.org/10.1007/s10853-019-04301-1.

[9] I. Polenz, S.S. Datta, D.A. Weitz, Controlling the morphology of polyurea microcapsules using microfluidics, Langmuir. 30 (2014) 13405–13410. https://doi.org/10.1021/la503234z.

[10] M. Hu, J. Guo, Y. Yu, L. Cao, Y. Xu, Research advances of microencapsulation

and its prospects in the petroleum industry, Materials (Basel). 10 (2017) 1–19. https://doi.org/10.3390/ma10040369.

[11] B. Duan, Handbook of Encapsulation and Controlled Release, Handb. Encapsulation Control. Release. (2015) 297–305. https://doi.org/10.1201/b19038.

[12] L. Li, Q. Wu, S. Li, P. Wu, Study of the infrared spectral features of an epoxy curing mechanism, Appl. Spectrosc. 62 (2008) 1129–1136. https://doi.org/10.1366/000370208786049204.

[13] J. Mijović, S. Andjelić, A Study of Reaction Kinetics by Near-Infrared Spectroscopy. 1. Comprehensive Analysis of a Model Epoxy/Amine System, Macromolecules. 28 (1995) 2787–2796. https://doi.org/10.1021/ma00112a026.

[14] M. Huang, J. Yang, Facile microencapsulation of HDI for self-healing anticorrosion coatings, J. Mater. Chem. 21 (2011) 11123–11130. https://doi.org/10.1039/c1jm10794a.

[15] P.D. Tatiya, R.K. Hedaoo, P.P. Mahulikar, V. V. Gite, Novel polyurea microcapsules using dendritic functional monomer: Synthesis, characterization, and its use in self-healing and anticorrosive polyurethane coatings, Ind. Eng. Chem. Res. 52 (2013) 1562–1570. https://doi.org/10.1021/ie301813a.

[16] H. Han, S. Li, X. Zhu, X. Jiang, X.Z. Kong, One step preparation of porous polyurea by reaction of toluene diisocyanate with water and its characterization, RSC Adv. 4 (2014) 33520–33529. https://doi.org/10.1039/c4ra06383j.

[17] J. Xu, H. Han, L. Zhang, X. Zhu, X. Jiang, X.Z. Kong, Preparation of highy uniform and crosslinked polyurea microspheres through percipitation copolymerization and their property and structure characterization, RSC Adv. 4 (2014) 32134–32141. https://doi.org/10.1039/C4RA04206A.

[18] S. Yu, X. Wang, D. Wu, Microencapsulation of n-octadecane phase change material with calcium carbonate shell for enhancement of thermal conductivity and serving durability: Synthesis, microstructure, and performance evaluation, Appl. Energy. 114 (2014) 632–643. https://doi.org/10.1016/j.apenergy.2013.10.029.

[19] A.S. Khan, Z. Ahmad, M.J. Edirisinghe, F.S.L. Wong, I.U. Rehman, Preparation and characterization of a novel bioactive restorative composite based on covalently coupled polyurethane-nanohydroxyapatite fibres, Acta Biomater. 4 (2008) 1275–1287. https://doi.org/10.1016/j.actbio.2008.04.016.

[20] G. Wu, J. An, D. Sun, X. Tang, Y. Xiang, J. Yang, Robust microcapsules with

polyurea/silica hybrid shell for one-part self-healing anticorrosion coatings, J. Mater. Chem. A. 2 (2014) 11614–11620. https://doi.org/10.1039/c4ta01312c.

[21] ASTM, Standard Test Methods for Measuring Adhesion by Tape Test D3359-09, (2009) 1–8. https://doi.org/10.1520/D3359-09E02.2.

[22] D.I. Njoku, M. Cui, H. Xiao, B. Shang, Y. Li, Understanding the anticorrosive protective mechanisms of modified epoxy coatings with improved barrier, active and self-healing functionalities: EIS and spectroscopic techniques, Sci. Rep. 7 (2017) 15597. https://doi.org/10.1038/s41598-017-15845-0.

[23] W. Wang, L. Xu, X. Li, Z. Lin, Y. YAng, E. An, Self-healing mechanisms of water triggered smart coating in seawater, (2014) 1914–1921. https://doi.org/10.1039/c3ta13389c.

[24] E. Cavalcanti, O. Ferraz, A.R. Di Sarli, The use of electrochemical impedance measurements to assess the performance of organic coating systems on naval steel, Prog. Org. Coatings. 23 (1993) 185–200. https://doi.org/10.1016/0033-0655(93)80010-8.

[25] Y. Morozov, L.M. Calado, R.A. Shakoor, R. Raj, R. Kahraman, M.G. Taryba, epoxy coatings modified with a new cerium phosphate inhibitor for smart corrosion protection of steel, (2019) 108–128. https://doi.org/10.1016/j.corsci.2019.108128.

[26] S. V. Lamaka, M. Taryba, M.F. Montemor, H.S. Isaacs, M.G.S. Ferreira, Quasi-simultaneous measurements of ionic currents by vibrating probe and pH distribution by ion-selective microelectrode, Electrochem. Commun. 13 (2011) 20–23. https://doi.org/10.1016/j.elecom.2010.11.002.

[27] M.F. Montemor, Hybrid nanocontainer-based smart self-healing composite coatings for the protection of metallic assets, in: Smart Compos. Coatings Membr., Elsevier Ltd, 2016: pp. 183–210. https://doi.org/10.1016/B978-1-78242-283-9.00007-5.

[28] Z. He, S. Jiang, N. An, X. Li, Q. Li, J. Wang, Y. Zhao, M. Kang, Self-healing isocyanate microcapsules for efficient restoration of fracture damage of polyurethane and epoxy resins, J. Mater. Sci. 54 (2019) 8262–8275. https://doi.org/10.1007/s10853-018-03236-3.

[29] A.K. Padhan, D. Mandal, Types of chemistries involved in self-healing polymeric systems, in: Self-Healing Polym. Syst., Elsevier Inc., 2020: pp. 17–74. https://doi.org/10.1016/B978-0-12-818450-9.00002-7.

[30] D.Y. Zhu, M.Z. Rong, M.Q. Zhang, Self-healing polymeric materials based on microencapsulated healing agents: From design to preparation, NceProgress Polym. Scie. 49–50 (2015) 175–220. https://doi.org/10.1016/j.progpolymsci.2015.07.002.

[31] F. Zhang, P. Ju, M. Pan, D. Zhang, Y. Huang, G. Li, X. Li, Self-healing mechanism in smart protective coatings: A review, Corros. Sci. 144 (2018) 74–88. https://doi.org/10.1016/j.corsci.2018.08.005.

[32] Tomasz Szmechtyk, N. Sienkiewicz, K. Strzelec, Polythiourethane microcapsules as novel self-healing system for epoxy coatings, Polym. Bull. 75 (2018) 149–165. https://doi.org/10.1007/s00289-017-2021-3.

[33] L.M. Meng, Y.C. Yuan, M.Z. Rong, M.Q. Zhang, A dual mechanism single-component self-healing strategy for polymers, J. Mater. Chem. 20 (2010) 5969–6196. https://doi.org/10.1039/c0jm00268b.

Chapter 4

Multilevel corrosion protection of epoxy coated carbon steel using isophorone diisocyanate microcapsules and cerium-based inhibitor

This chapter contributes to the development of epoxy coatings modified by simultaneous addition of microcapsules containing isophorone diisocyanate as self-healing agent, and cerium organophosphate as pH sensitive corrosion inhibitor. This chapter was published in "M. Attaei, L. Calado, M. Taryba, Y. Morozov, A. Shakoor, R. Kahraman, A.C. Marques, and M.F. Montemor, *Smart epoxy coating modified with isophorone diisocyanate microcapsules and cerium organophosphate for multilevel corrosion protection of carbon steel*, Progress in Organic Coatings, 2020, 147, 105864".

4.1 Introduction

As mentioned in previous chapters smart coatings, with healing ability, may repair the polymeric network due to the presence of polymerizable agents, and/or may passivate/inhibit the areas attacked by corrosion by controlled delivery of corrosion inhibitors [1,2]. Revision of recent bibliography revealed that isocyanate compounds and in particular IPDI are efficient self-healing agents [3–8]. High reactivity and low viscosity of IPDI made it an attractive choice as a healing agent to impart self-healing ability in different coating matrices [9–11]. It reacts with water/moisture up taken by the coating to form a polymeric material that fills the surrounding pores and defects, thereby restoring the coating barrier properties [12]. However, through diffusion of the electrolyte, there are still corrosive ions, which can pass through these polymeric protective layers and reach the metallic surface. Thus, the protection ability of organic coatings needs to be further enhanced by addition of corrosion inhibitors. A wide variety of corrosion inhibitors, such as organic compounds [13] and inorganic complexes [14], has been proposed for corrosion protection of steel, and has been intensively reviewed in chapter 1.

Although direct addition of inhibitors has been reported as an effective way to enhance the corrosion protection properties of coatings, several major drawbacks were reported: leaching or fast depletion of corrosion inhibitor [15], possible reactions between coating and inhibitors [16], and poor distribution of corrosion inhibitors within the coating matrix [17]. Therefore, development of a smart inhibitor, with ability to be released in response to certain stimulus, has gained pace recently [1,18]. As corrosion of metals and, is normally accompanied by local pH gradient, pH-triggered systems can be designed to release the inhibitor smartly and efficiently, when and where corrosion is active. Therefore, these systems at least can be an answer to the first drawback, i.e., fast depletion of inhibitor. Recently, a new cerium organophosphate ($Ce(DEHP)_3$) corrosion inhibitor was developed for corrosion protection of magnesium alloys [19,20], and showed a promising result for protection of carbon steel as well [21]. The corrosion inhibition efficiency of $Ce(DEHP)_3$ was ascribed by the synergistic action of cerium cations and phosphate anions, triggered by the local pH gradients due to active corrosion process. This pH sensitive inhibitor in acidic pH, can release the organophosphate ions, and forms an insoluble/protective Fe/Mg-DEHP. While in basic pH conditions can release cerium ions, forms a stable cerium hydroxide species that are able to protect the metal from further dissolution [21].

In previous chapter, highly efficient IPDD MCs, was developed by emulsion formation following by interfacial polymerization. Further addition of MCs into the epoxy coating, provided an important healing ability into the epoxy coating, evidenced by various electrochemical techniques. $Ce(DEHP)_3$ particles, also reported an effective corrosion inhibition for carbon steel, thanks to their smart response to corrosion events at cathodic and anodic sites [21].

Following these two previously reported results, this chapter studies the multilevel (synergistic) effect of IPDI MCs and $Ce(DEHP)_3$ particles, when simultaneously introduced to the epoxy formulation used to coat carbon steel plates. The enhanced corrosion protection effect was investigated by using both global and localised electrochemical techniques.

4.2 Experimental [9]

4.2.1 Preparation of coatings

Three groups of coatings were prepared and applied on carbon steel coupons. Table 4.1 shows detailed information regarding these coatings evaluated and studied in this chapter. The epoxy coating was obtained from the same commercial formulation used to prepare coatings in the previous chapter. Also, coating preparation processes including mixing of the coating components, curing time and temperature, etc., were the same as described before.

The first group of coatings was prepared by addition of DETA MCs (best IPDI-contained MCs, reported in previous chapter), following the same procedure described before.

The second group of coatings was prepared by initially add 1 wt.% $Ce(DEHP)_3$ to the hardener component of the coating formulation, following by further addition of this solution into the epoxy component of the coating.

9 Synthesis and characterization of IPDI MCs were fully described in Chapter 3 of this thesis.

Synthesis of $Ce(DEHP)_3$ particles, are briefly described in Appendix 1- page 222, and the characterization result can be found in " L. M. Calado, M. G. Taryba, Y. Morozov, M. J. Carmezim, and M.F. Montemor, Cerium phosphate-based inhibitor for smart corrosion protection of WE43 magnesium alloy, Electrochimica Acta 365 (2021) 137368.

For preparation of the third group of coatings, firstly 1 wt.% of $Ce(DEHP)_3$ was added into the hardener component of the coating formulation, followed by adding the DETA-MCs, and finally this mixture was added into the epoxy component of the coating.
All coatings were kept at RT for 24h before applying on steel substrate.

Table 4.1 Coatings´ formulation and acronyms.

Group	Acronym	$Ce(DEHP)_3$ (wt%)	DETA-MC (wt%)	Hardener (wt%)	Epoxy (wt%)
1	Modified-MC-2%	0	2	30	70
	Modified-MC-3%	0	3		
2	Modified-Ce-1%	1	0		
3	Modified-MC-2%-Ce-1%	1	2		
	Modified-MC-3%-Ce-1%	1	3		

Steel coupons were degreased following the same procedure described in Chapter 3. Coatings were applied on steel coupons by dip-coating, using a dip coater machine (more detailed information can be found in Appendix 2).

4.2.2 Stability of MCs in presence of $Ce(DEHP)_3$ particles

In previous chapter the chemical stability of MCs in working conditions was assessed by analysing the FTIR spectra of the MCs after immersion tests in relevant media during the 200 h at RT. Addition of $Ce(DEHP)_3$ into the hardener component of the coating formulation rose the necessity to evaluate the chemical stability of MCs inside the hardener in presence of $Ce(DEHP)_3$. Following the same procedure, the stability of MCs was assessed by analyzing the FTIR spectra of the MCs after and before immersion tests in the solution of $Ce(DEHP)_3$ in hardener component of the coating formulation. For this purpose, 0.2 g of MCs were immersed into a solution of hardener containing 1 wt.% $Ce(DEHP)_3$, for 200 h at RT. MCs then were separated from the media by centrifugation, at 2500 rpm, washed and dried before further analysis.
Optical microscopy was employed to observe the MCs´ structure and check if the MCs´ shell was not affected by the hardener solution and confirm the presence of an intact shell (detailed information regarding the equipment employed for these analyses can be found in Appendix 2).

4.3 Preparation of coatings

As reported in previous chapter both coatings modified by addition of 2, and 3 wt% of DETA MCs showed an identical behaviour during the immersion into the 0.05 M NaCl. Among those coatings modified with simultaneous addition of both MC and $Ce(DEHP)_3$, the one modified by addition of 3 wt% of DETA-MCs and 1 wt% of $Ce(DEHP)_3$ (modified-MC-3%-Ce-1%) showed the most promising results. Therefore, in this chapter the following coatings were compared: modified-MC-3%, modified-MC-3%-Ce-1%, and modified-Ce-1% coatings.

The average thicknesses of modified-MC-3%, modified-MC-3%-Ce-1%, and modified-Ce-1% coatings, were 76 ± 7.8, 58 ± 5.3, and 53.5 ± 1.3 respectively. The results did not show significant differences in the thickness of coatings in the same family.

4.4 Characterization of coatings

Coating thickness was determined with a digital gauge. Cross-cut tests (using standard procedure ISO 2409) were performed to evaluate the adhesion of both reference and modified coatings. EIS experiments were carried out to investigate the barrier properties of the reference and modified coatings applied on carbon steel coupons, immersed in 0.05 M NaCl solution.

LEIS was performed to assess the local changes in admittance at an artificial defect made in the reference and modified coatings, while the sample was immersed in 0.005 M of NaCl solution. SVET and SIET measurements were performed over coated samples containing point defects to evaluate the localized corrosion activity, during immersion of sample in 0.05 M of NaCl solution. (detailed information regarding the equipment used to characterize coatings, and method of characterization can be found in Appendix 2).

4.5 Results and Discussion

4.5.1 Stability of MCs in presence of $Ce(DEHP)_3$ particles

The effect of $Ce(DEHP)_3$ particles on the chemical stability of MCs was evaluated from the FTIR spectra and optical microscopy images. Figure 4.1a shows a micrograph of the MCs and they still evidence a round shape, with intact shell, confirming that the MCs´ shells were stable inside the solution of $Ce(DEHP)_3$ in the hardener after 200 h of immersion.

Overall, the FTIR spectra revealed that the MCs possess very good chemical stability when immersed in such solution, since no relevant changes were noticed in the intensity of the NCO peaks after immersion (Figure 4.1b). The slight reduction in the NCO peak intensity after immersion was probably due to the presence of some broken MCs during the washing process (Figure 4.1c).

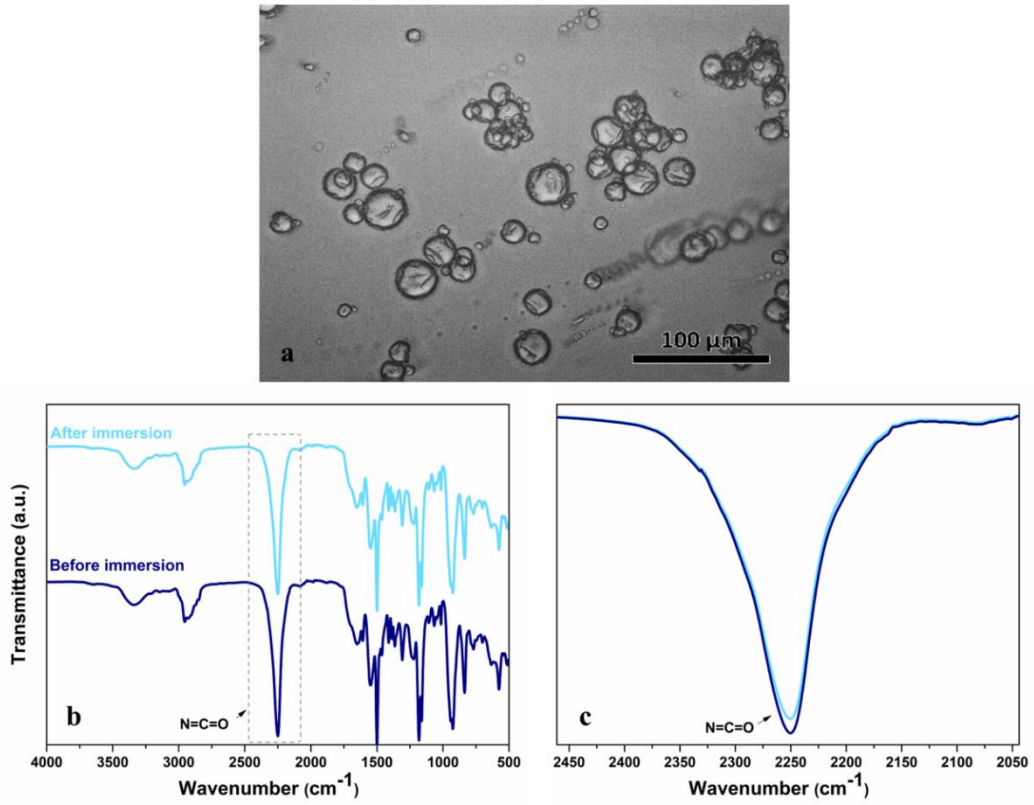

Figure 4.1 a) Optical micrographs of MCs after 200 h immersion in solution of 1 wt% $Ce(DEHP)_3$ in the hardener; b) FTIR spectra obtained on MCs as prepared and after immersion; c) overlapped NCO peaks before (dark blue line), and after (light blue line) immersion.

4.5.2 EIS Experiments

EIS was used to assess the protective properties of the coatings and the evolution of their barrier properties during the immersion of coated samples in 0.5 M NaCl solution. The exposed area was 3.63 cm^2. A set of representatives Bode plots for the modified-MC-3% are depicted in Figure 4.2a, b. Modified-MC-3% coatings showed a capacitive response in the high frequency domain. The global impedance values at the early stages of immersion

were approximately 1.4×10^9 Ω cm^2, which increased about an order of magnitude during the immersion test, reaching values close to 1.1×10^{10} Ω cm^2 (Figure 4.2a). This increasing trend was accompanied by the broadening of the phase angle, and clearly reflects an enhancement of the coating barrier properties over time. It is worth mentioning that the time constant at low frequency, which could be observed until the 15 days of immersion, vanished for longer immersion times (Figure 4.2b). This fact, together with the continuous increase of global impedance, confirmed the beneficial effect of MCs in improving the coating barrier properties. This evolution suggests that the presence of MCs can hinder the diffusion of aggressive ions toward the coating/steel interface and enhance the barrier properties of the coating.

The selected EIS plot for modified-Ce-1% coatings are depicted in Figure 4.2c, d. Although at early stages of immersion the global impedance values were close to 1×10^{11} Ω cm^2, the values showed a descending trend, to approximately 1×10^{10} Ω cm^2, i.e. an order of magnitude lower than the initial value, by the end of immersion. In the high frequency range neither the impedance values (Figure 4.2c) nor the phase angle (Figure 4.2d) showed noticeable changes, confirming the good stability of the coating barrier properties. The absence of the low frequency time constant also indicates the absence of corrosion and, therefore, the better anti-corrosion properties of modified-Ce-1% coatings in comparison to modified-MC-3% coatings.

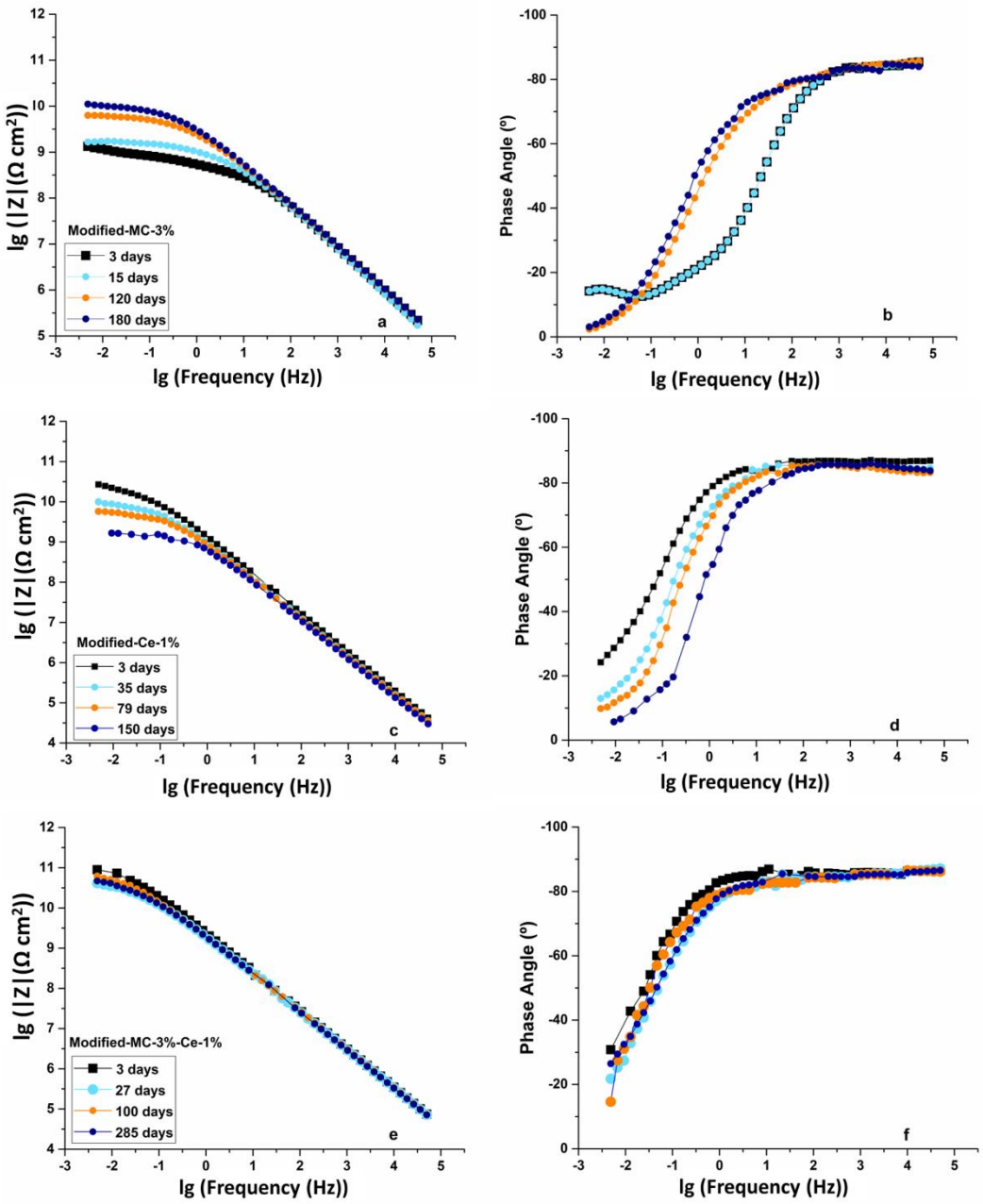

Figure 4.2 Bode plots for modified-MC-3% (a, b); modified-Ce-1% (c, d), and modified-MC-3%-Ce-1% (e, f) coatings.

The selected EIS plots for modified-MC-3%-Ce-1% (Figure 4.2e, f) displayed phase angle values close to -90° over a wide range of frequencies, as well as a very stable impedance modulus (Figure 4.2e) over time. The capacitive responses of coating were expanded over a large frequency domain, evidencing a stable barrier property of this coating. At early stages of immersion, the global impedance values were above 1×10^{11} Ω cm^2. Later, the values oscillated in the range between 1×10^{11} Ω cm^2 and 4×10^{10} Ω cm^2 but were always

above those values observed for other coatings studied in this chapter. At high frequencies both impedance and phase angle values remained stable (Figure 4.2e, f) confirming negligible changes in the coating barrier properties. Moreover, at lower frequencies, no time constant could be detected at any immersion time, confirming the absence of interfacial activity and the enhanced corrosion resistance of modified-MC-3%-Ce-1% coating after 285 days of immersion.

As mentioned before, the impedance modulus at low frequency ($|Z|_{LF}$) has been considered an important parameter to estimate the overall corrosion protection properties of organic coatings. Figure 4.3 compares this parameter for all coatings studied in this chapter. The $|Z|_{0.005\ Hz}$ values for modified-MC-3% coatings, revealed a growing trend, in the range of 1.5-7 × 10^9 Ω cm^2, showing an important improvement of the barrier properties of modified-MC-3% coatings.

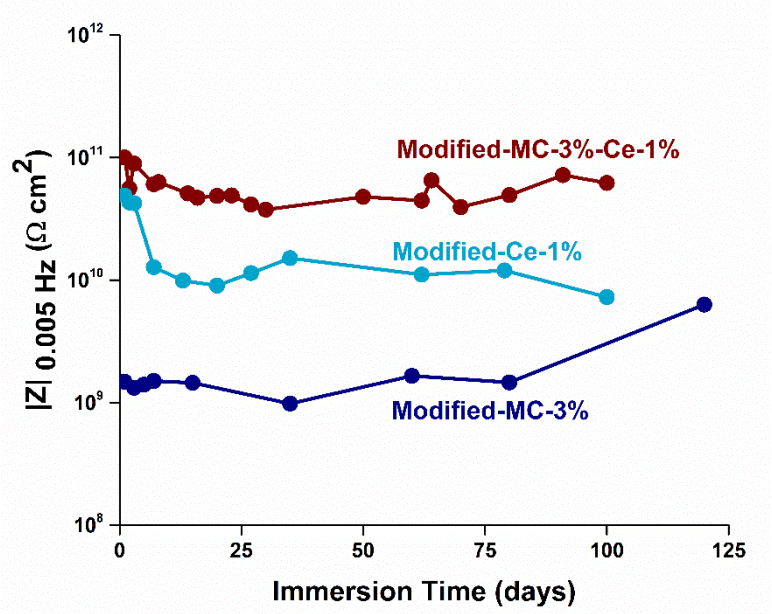

Figure 4.3 Comparison of the low frequency impedance values (measured at 0.005 Hz) on steel plates coated with the three modified coatings reported in this chapter.

The low frequency impedance values of modified-Ce-1% coatings were initially close to 5 × 10^{10} Ω cm^2 and evidenced a decreasing trend, reaching values around 7 × 10^9 Ω cm^2 at the end of the experiment. For the modified-MC-3%-Ce-1%, $|Z|_{0.005\ Hz}$ values showed a slow decay and then a slight increase in the range from 1 × 10^{11} Ω cm^2 to 6.2 × 10^{10} Ω cm^2, being always one order of magnitude higher than the values determined for modified-Ce-1% coatings. The values are also two orders of magnitude above those determined for the

modified-MC-3% coatings, confirming the enhanced corrosion protection obtained by the combination of MCs and $Ce(DEHP)_3$ inhibitor.

An equivalent circuit composed of one time constant (Figure 4.4a) was used to simulate the experimental EIS data of modified-MC-3%-Ce-1% coatings, while an equivalent circuit with two-time constants (Figure 4.4b) was required to simulate the experimental data of modified-Ce-1% and modified-MC-3% coatings. In the equivalent circuits R_P and CPE_{Coat}, at high frequency, were used to fit the pore/coating resistance and the constant phase element describing the coating capacitance, respectively. R_{Ct}, CPE_{dl}, at low frequency, were used to fit the Faradic resistance and the constant phase element associated to the capacitance of the double layer, respectively. The fitting results obtained for all three coatings reported in this chapter are depicted in Figure 4.5a to d.

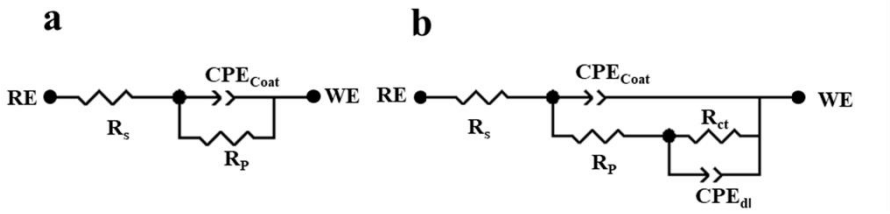

Figure 4.4 EEC used to fit a) modified-MC-3%-Ce-1% coating; b) modified-Ce-1% and modified-MC-3% coatings data.

Figure 4.5a shows the pore/coating resistance of all coatings studied in this chapter. The pore resistance of modified-Ce-1% coating displayed initial values close to 5×10^8 Ω cm^2 that decreased almost one order of magnitude after 3 days. However, after that period the values were kept nearly constant until the end of the test. For modified-MC-3% coatings the pore resistance initial value (2.6×10^8 Ω cm^2) decreased almost one order of magnitude during the first 5 days of immersion and attained the minimum value of 2.5×10^7 Ω cm^2. Later a sudden increase until 10 days of immersion was observed. For longer immersion times there was a slow five times increase of the pore resistance until the end of immersion (1×10^8 Ω cm^2), suggesting a continuous recovery of the barrier properties of the coating due to release of IPDI from the MCs and mending of pores and/or defects formed in the polymeric matrix. The coating resistance values for modified-MC-3%-Ce-1% coatings remained constant over the entire immersion time, and fluctuated between 1-10 $\times 10^{10}$ Ω cm^2, being almost three orders of magnitude higher than those observed for the other families of coatings (Figure 4.5a). This trend accounts for the excellent

coating barrier properties that were achieved in the presence of the two additives. The significant increase of the coating resistance in the modified-MC-3%-Ce-1% coatings accounts for an important synergistic effect when the two additives are combined and evidences the multilevel protection effect.

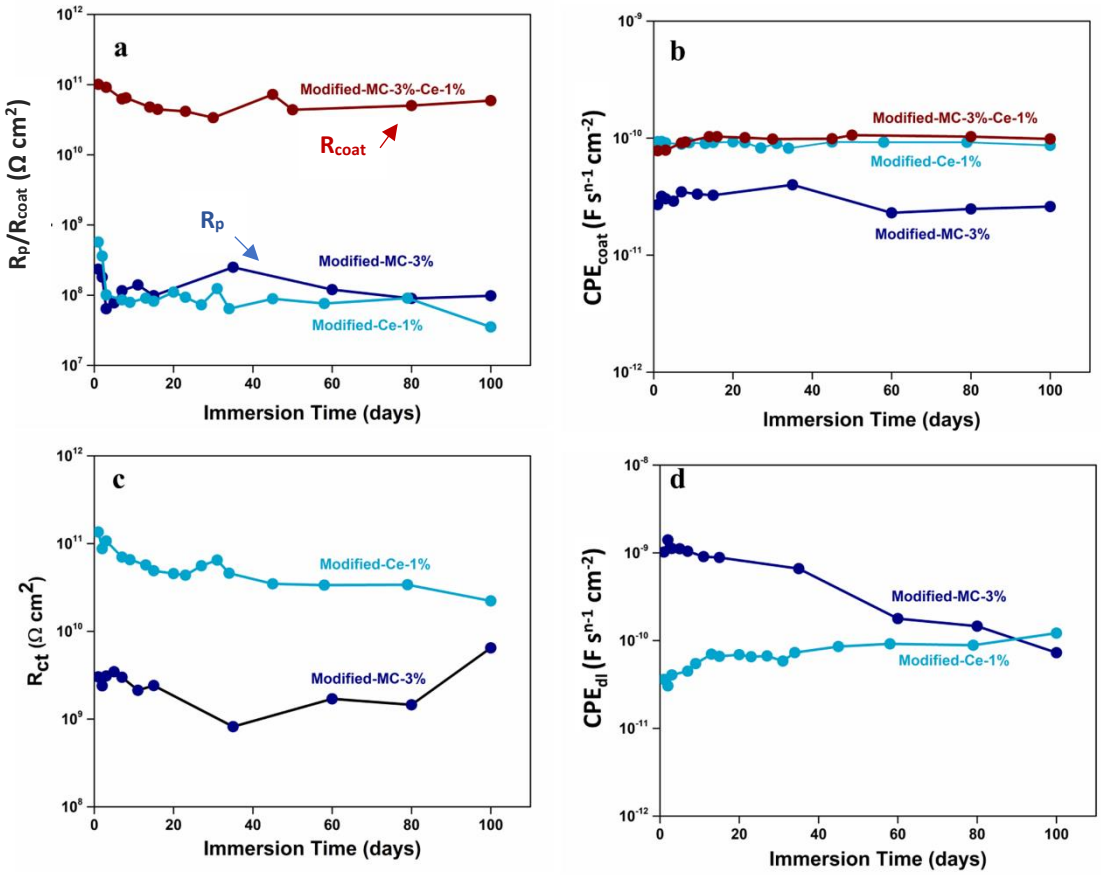

Figure 4.5 Evolution of a) coating pore resistance; b) admittance of the coating; c) Faradic resistance; d) admittance of the double layer (Data are available in Tables A.6, and A 1.7- Appendix 1).

The values of CPE_{coat} admittance for the coatings depicted in Figure 4.5b. These values increased slightly at early stages for all the coatings. The close admittance values observed for modified-MC-3%-Ce-1% and modified-Ce-1% coatings indicate that both MCs and $Ce(DEHP)_3$ have good compatibility with the epoxy coating. The CPE_{coat} admittance for modified-MC-3% coatings displayed values below those values observed for modified-MC-3%-Ce-1% and modified-Ce-1% coatings (probably due to slightly higher thickness of this coating in comparison with others).

As mentioned before, it was not possible to detect the low frequency time constant for the modified-MC-3%-Ce-1% coatings, meaning that no corrosion activity was noticed at the

steel-coating interface. Such result confirms the multilevel effect of MCs and $Ce(DEHP)_3$ to suppress corrosion activity.

In Figure 4.5c the R_{ct} values, assigned to the Faradic resistance at the interface coating-steel, was higher for modified-Ce-1% coatings when compared to modified-MC-3% coatings. For modified-Ce-1% coatings the Faradic resistance values were in the range of 1.4-0.2 × 10^{11} Ω cm^2, meaning that modified-Ce-1% coatings displayed the highest Faradic resistance (almost two orders of magnitude) compared to modified-MC-3% coatings (3-6 × 10^9 Ω cm^2). In other words, the interfacial activities of modified-Ce-1% coatings were negligible compared to modified-MC-3% coatings, confirming the high inhibition effect of $Ce(DEHP)_3$ inhibitor. A significantly lower R_{ct} values for modified-MC-3%, can be justified by the presence of inevitable micro voids and flaws produced in the epoxy coatings due to the presence of MCs. It is worth mentioning that the quantity of defects, increases by increasing the quantity of MCs added to the coating formulation, and this justifies a slightly better quality of modified-MC-2%, when compared with the modified-MC-3%.

Concomitantly, the CPE admittance values depicted in Figure 4.5d, evidence the lowest admittance values of the modified-Ce-1% coatings in comparison with the modified-MC-3% coatings. It is worth mentioning that the continuous reduction of $CPE_{dl\text{-}modified\text{-}MC\text{-}3\%}$ confirms an important healing effect due to the presence of MCs, while the high values of $R_{ct\text{-}modified\text{-}Ce\text{-}1\%}$ reflect the inhibitive role of $Ce(DEHP)_3$ in suppressing corrosion activity at the bare steel. The absence of the low frequency time constant in the modified-MC-3%-Ce-1% coating pinpoints towards an important multilevel effect in what concerns corrosion inhibition, in good agreement with the evolution of the coating barrier properties when the two additives are present.

4.5.3 Localized Electrochemical Techniques

LEIS was used to evaluate the localized corrosion protection resulting from the joint addition of $Ce(DEHP)_3$ and MCs. For this purpose, the LEIS probe was scanned over artificial defects made in the coating, to monitor the local admittance of the steel. LEIS maps were acquired continuously for a period of 100 h. The selected maps that evidence the evolution of the admittance over time for both modified-MC-3%-Ce-1% and modified-MC-3% were illustrated in Figure 4.6. Figure 4.6g shows the ratio between maximum admittance values determined over the defect at a specific time (A) and the maximum

value measured at the beginning of immersion (A_0) to minimize the effect of non-identical distances between the LEIS probe and the coating surface. As discussed in previous chapter, an increase of this ratio can be assigned to an increased admittance, and therefore higher corrosion activity over the defect, while a decrease evidences inhibition or healing of corrosion damage. For the modified-MC-3% coating, an initial increase in admittance was registered during the first 16 hours of immersion which can be explained by early corrosion onset and increase in the local corrosion activity. Then, and until approximately 60 hours of immersion, admittance showed some fluctuations, following a decreasing trend (Figure 4.6a, and b), which are related to the progressive self-healing effect of the IPDI stored in the DETA-MCs. However, after 60 hours of immersion, the protective trend vanished probably due to the consumption of all IPDI released from broken capsules (Figure 4.6c, and g). In fact, when capsules are broken IPDI is released and reacts rapidly with OH groups forming a protective polymeric layer that partially repairs the defects. After 60 hours most probably all IPDI has been consumed and corrosion activity started to increase. It is worth mentioning that the primary role of IPDI is to heal the polymer matrix, and not to heal the bare steel exposed in defects as the one studied here. Nevertheless, the formation of the protective species over steel might be responsible for an important delay in the corrosion activity.

Contrarily, the modified-MC-3%-Ce-1% coating displayed a very stable corrosion inhibition trend. The selected LEIS map at 23, 58, and 100 h of immersion in saline solution for modified-MC-3%-Ce-1% coating show almost the stable and identical values of admittance for this coating (Figure 4.6d, e, and f).

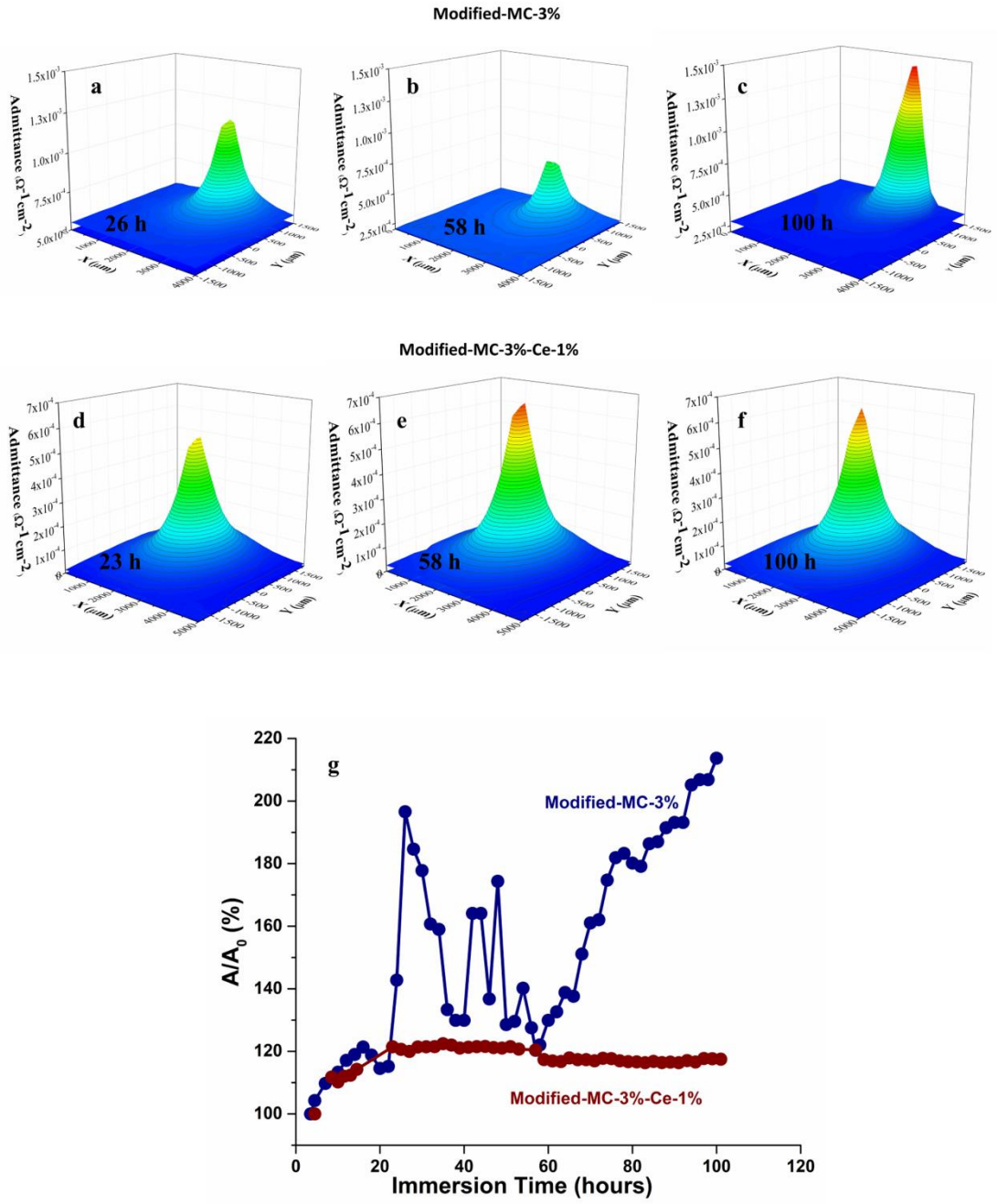

Figure 4.6 LEIS admittance maps obtained after a) 26 h, b) 58 h, and c) 100 h, immersion of the modified-MC-3% coating; after d) 23 h, e) 58 h, and f)100 h, immersion of modified-MC-3%-Ce-1% coating in 0.005 M NaCl solution; g) Evolution of the admittance ratio for modified-MC-3%, and modified-MC-3%-Ce-1% coatings during immersion in 0.005 M NaCl solution.

This sample also showed an initial increase in the local corrosion activity but after 20 hours of immersion, the admittance values stabilized and evidenced a slight decrease after approximately 60 hours of immersion. This stable response after 60 hours can be related to the combined action of the cerium cations and organophosphate anions that are formed due to the acid-basic conversion of the original species and that can effectively protect steel through the formation of cerium hydroxide species and hydrophobic organophosphate layers as previously reported [21].

The initial behaviour of the samples was rather similar, indicating that, during the first hours of immersion in the electrolyte, the released IPDI helps to retard corrosion activity probably by forming a protective layer that decreases the surface of steel exposed to the electrolyte. However, this layer cannot effectively suppress all activity and local pH gradients are likely to occur leading to hydrolysis of $Ce(DEHP)_3$ and activation of the protective species and, as consequence, effective suppression of the corrosion activity that was extended over time. The combination of DETA-MCs, and $Ce(DEHP)_3$ seems responsible for an important synergistic effect, since neither MCs by themselves nor $Ce(DEHP)_3$ used solely [21] could provide such extended inhibition ability. In previous work [21] it was reported that addition of 0.5 wt.% of $Ce(DEHP)_3$ to an epoxy coating could control the corrosion activity only until 12-15 hours of immersion [21], while as discussed in previous chapter, activation of the healing effect of MCs required a certain time delay, due to slow release and time needed for the reaction of IPDI. Thus, a comparison of previous findings and the results depicted in Figure 4.6g allow concluding that the combined addition of MCs and $Ce(DEHP)_3$ provides a continuous and more effective suppression of the corrosion activity at the exposed steel surface. This is explained by the formation of polymeric species (from 25 to 60 h of immersion) due to the reaction between the NCO group of IPDI and OH that reduce the size of the artificial defect, assisting the inhibition of the species released from $Ce(DEHP)_3$.

In previous chapter, the ability of MCs to suppress corrosion in artificial defects created in steel coated samples was confirmed by SVET. The SVET results revealed negligible anodic and cathodic activities when samples were immersed in 0.05 M NaCl solution, and the SIET measurements did not show any significant changes in pH values measured over the defect during the test. The inhibitive role of $Ce(DEHP)_3$ was also confirmed by SVET as well [21].

Thus, in this work the modified-MC-3%-Ce-1% coating was studied by SVET and SIET. The measurements were performed over a defined area with an artificial defect (ca. 200

μm) created in the coating (Figure 4.7a and b), for 24 hours. Figure 4.7 shows the SVET and SIET maps for this sample. The measurements revealed a net surplus of negatively charged species related to the cathodic activity that increased slightly until 12-13 hours of immersion. Simultaneously the pH rose until 8.9 (Figure 4.7f, and g) confirming the predominance of hydroxyl anions and therefore a slight increase of the localized corrosion activity in accordance with the LEIS results. It is worth to mention that the cathodic current density values were much lower (> one order of magnitude) when compared to a non-modified coating (previous chapter). Later, the cathodic current density decreased to much lower values and the pH variations were attenuated (Figure 4.7h).

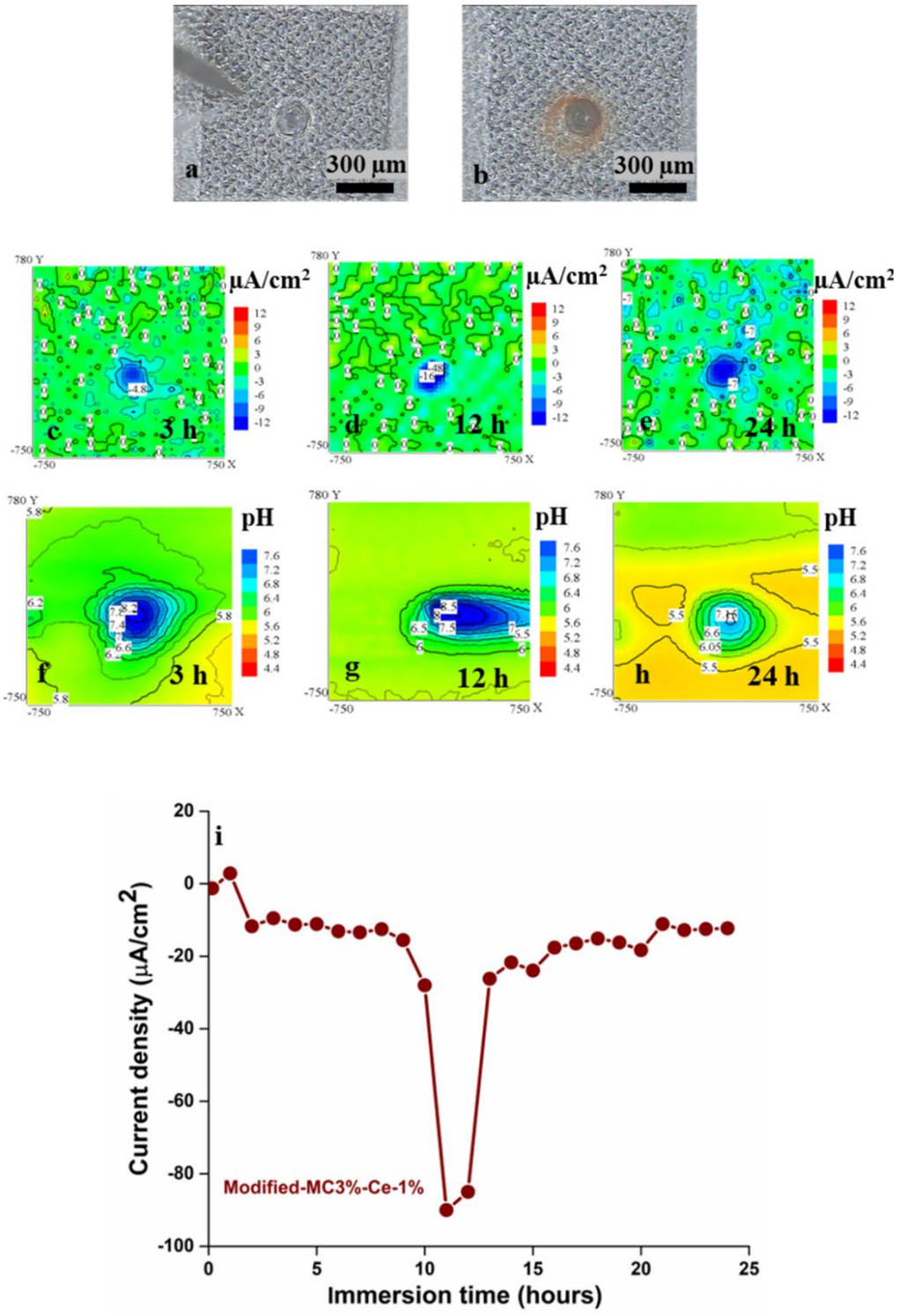

Figure 4.7 Optical micrographs of artificially made defect obtained after a) 1 h and b) 24 h of immersion, SVET maps obtained after c) 3 h, d) 12 h and e) 24 h; SIET maps at f) 3 h, g) 12 h and h) 24 h of immersion of the steel coupons protected with the modified-MC-3%-Ce-1% coating in 0.05 M NaCl solution; i) evolution of the maximum values of the cathodic current densities for the modified-MC-3%-Ce-1% coating during 24 h immersion in 0.05 M NaCl

This trend was observed until the end of immersion. The maximum cathodic current density registered over the defect can serve as an indicator of the corrosion activity and its evolution is depicted in Figure 4.7i. Clearly, it is shown that the cathodic activity over the defect was negligible until 10 hours of immersion. After this period a small increase was noticed but the activity was suppressed, again, after approximately 14h. This effect can be explained by the delayed release of IPDI from the MCs following by the pH assisted release of Ce(III) ions from $Ce(DEHP)_3$ and formation of protective species. As consequence, the activity drops towards negligible values.

4.6 Proposed healing mechanism

The ability of modified-MC-3%-Ce-1% coating to prevent and to heal corrosion activity in defects was proved by several techniques. Accordingly, it is possible to propose that the mechanism of corrosion healing associated to the simultaneous addition of MCs and $Ce(DEHP)_3$ particles involves several steps that combine the individual function of each additive since their prime roles are different and their protective effect is activated by different stimuli.

On the one hand, IPDI is released either by swelling of the shell or by MCs rupture and its main objective is to heal the polymeric matrix. In this case those reactions mentioned in chapter 3 (Figure 3.17) are involved in the formation of the protective polymeric layer. On the other hand, the corrosion inhibition mechanism of $Ce(DEHP)_3$ is pH dependent as previously demonstrated [19–21]. Upon corrosion onset, due to dissolved oxygen reduction there is alkalization of the cathodic zones and $Ce(DEHP)_3$ dissolves and re-precipitates at the steel surface as cerium(III) hydroxide, which may be further oxidized to CeO_2 or $Ce(OH)_4$. The species formed, $Ce(OH)_3$, CeO(OH), $Ce(OH)_4$, and CeO_2, inhibit cathodic activity and therefore the corrosion process slows down [22–25].

In the anodic zones, where dissolution of steel takes place, acidification may occur due to hydrolysis of iron cations. In such acidic conditions, $Ce(DEHP)_3$ dissolves and may form a protective hydrophobic film of bis(2-ethylhexyl) phosphate (DEHP) on the steel surface or a mixture of DEHP and $Fe(DEHP)_2$ may form. The formation of DEHP can also occur in the pores of the coating, making them more hydrophobic and preventing water transport. This mechanism is supported by the experimental findings. In fact, reduced electrolyte uptake was revealed by the evolution of the impedance values for modified-MC-3%-Ce-1% coating and modified-Ce-1% coating that contain $Ce(DEHP)_3$

in good agreement with previous results observed by Morozov et al. [21]. EIS demonstrated that both modified-MC-3%-Ce-1%, and modified-MC-3% coatings revealed improved barrier properties with time (Figures 4.2, 4.3 and 4.5) due to slow polymerization of IPDI in pores and coating defects, which can partially heal these flows. Nevertheless, $Ce(DEHP)_3$ is responsible for stable impedances at low frequencies due to its inhibitive role, while the MCs reinforce the coating barrier effect. This creates a synergy that, at the end, results in much higher corrosion protection, and no corrosion could be noticed for the modified-MC-3%-Ce-1% coating during the testing period. In the presence of defects, IPDI stored in MCs is released and spreads over steel, creating a polymeric film that decreases the steel area exposed to the electrolyte. This effect, as previously reported (Chapter 3), reduces the initial corrosion rate, and may heal the defect completely (when defect is relatively small).

Therefore, the mixture of additives proposed in this chapter creates a multilevel corrosion protection effect summarized in Figure 4.8, that involves i) inhibition of the cathodic reaction by formation of protective layer of Ce-species; ii) inhibition of anodic reaction by formation of stable film of DEHP; iii) reduced water transport through the polymeric coating by hydrophobization of pores; iv) decreased water and oxygen uptake and repair of coating defects via the polyurea-based polymer, formed from reaction of IPDI released from the capsules. These effects significantly improve the coating protective properties.

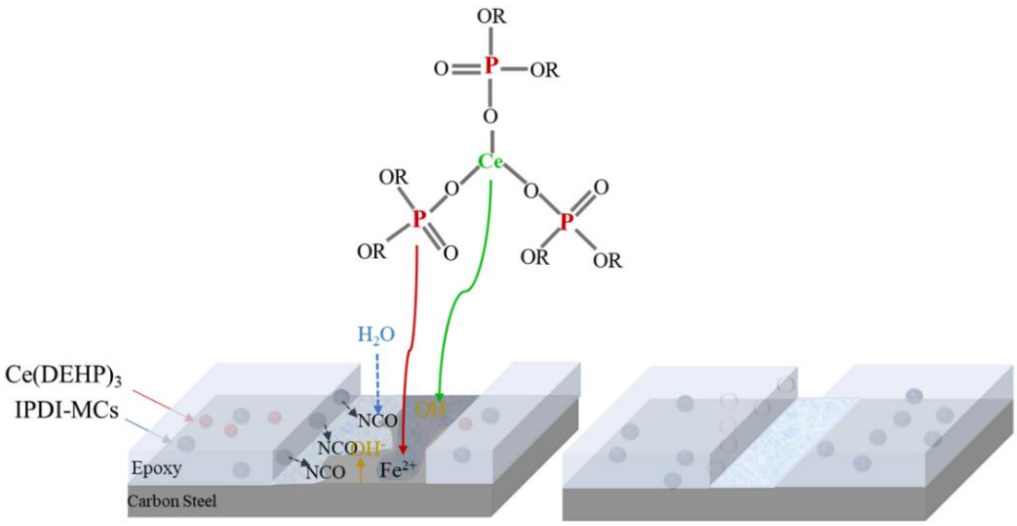

Figure 4.8 Proposed healing mechanism evidencing the synergistic effect of both additives.

4.7 Conclusion

IPDI MCs and $Ce(DEHP)_3$ were successfully introduced in an epoxy coating formulation to improve the coating barrier properties and to introduce multilevel corrosion healing effects.

EIS evidenced a synergistic protective effect when both additives are combined. This resulted in significantly higher and more stable coating barrier properties since the low frequency impedance values were always one order of magnitude above the values determined for modified-Ce-1% coatings and two orders of magnitude above those determined for the modified-MC-3% coatings. Moreover, the pore resistance values for modified-MC-3%-Ce-1% coatings ranged between $1\text{-}10 \times 10^{10}\ \Omega\ cm^2$, being almost three orders of magnitude higher than those observed for the other families of coatings.

The corrosion healing ability over defects formed in the modified-MC-3%-Ce-1% coating was confirmed by LEIS and SVET, and SIET. An important and stable corrosion inhibition effect was noticed over defects formed in the coating containing the mixture of both additives. SVET and SIET evidenced that a stage of increased corrosion activity seems to be required to trigger the action of the inhibitive species. This is probably due to the accumulation of hydroxyl ions (SIET confirmed a nearly 3 units increase of pH). Once activated, the healing species could provide stable corrosion protection over time.

Overall, the healing process involves multilevel protection and a synergistic effect that significantly reinforces the corrosion protection conferred by the modified epoxy coating.

4.8 References

[1] M.F. Montemor, Functional and smart coatings for corrosion protection: A review of recent advances, Surf. Coatings Technol. 258 (2014) 17–37. https://doi.org/10.1016/j.surfcoat.2014.06.031.

[2] M.L. Zheludkevich, J. Tedim, M.G.S. Ferreira, "Smart" coatings for active corrosion protection based on multi-functional micro and nanocontainers, Electrochim. Acta. 82 (2012) 314–323. https://doi.org/10.1016/j.electacta.2012.04.095.

[3] P. Kardar, Preparation of polyurethane microcapsules with different polyols component for encapsulation of isophorone diisocyanate healing agent, Prog. Org. Coatings. 89 (2015) 271–276. https://doi.org/10.1016/j.porgcoat.2015.09.009.

[4] Y. Ming, J. Hu, J. Xing, M. Wu, J. Qu, Preparation of polyurea/melamine formaldehyde double-layered self-healing microcapsules and investigation on core fraction, J. Microencapsul. 33 (2016) 307–314. https://doi.org/10.1080/02652048.2016.1178352.

[5] L.T.T. Nguyen, X.K.D. Hillewaere, R.F.A. Teixeira, O. Van Den Berg, F.E. Du Prez, Efficient microencapsulation of a liquid isocyanate with in situ shell functionalization, Polym. Chem. 6 (2015) 1159–1170. https://doi.org/10.1039/c4py01448k.

[6] A.C. Silva, A. Dorri Moghadam, P. Singh, P.K. Rohatgi, Self-healing composite coatings based on in situ micro–nanoencapsulation process for corrosion protection, J. Coatings Technol. Res. (2017) 1–29. https://doi.org/10.1007/s11998-016-9879-0.

[7] D. Sun, J. An, G. Wu, J. Yang, Double-layered reactive microcapsules with excellent thermal and non-polar solvent resistance for self-healing coatings, J. Mater. Chem. A. 3 (2015) 4435–4444. https://doi.org/10.1039/c4ta05339g.

[8] J. Yang, M.W. Keller, J.S. Moore, N.R. Sottos, S.R. White, Microencapsulation of Isocyanates for Self-Healing Polymers, Macromolecules. 41 (2008) 9650–9655. https://doi.org/10.1021/ma801718v.

[9] W. Wang, L. Xu, X. Li, Y. Yang, E. An, Self-healing properties of protective coatings containing isophorone diisocyanate microcapsules on carbon steel surfaces, Corros. Sci. 80 (2014) 528–535.

https://doi.org/10.1016/j.corsci.2013.11.050.

[10] H. Yi, Y. Yang, X. Gu, J. Huang, C. Wang, Multilayer composite microcapsules synthesized by Pickering emulsion templates and their application in self-healing coating, J. Mater. Chem. A. 3 (2012) 13749–13757. https://doi.org/10.1039/c5ta02288f.

[11] D.Y. Zhu, M.Z. Rong, M.Q. Zhang, Self-healing polymeric materials based on microencapsulated healing agents: From design to preparation, NceProgress Polym. Scie. 49–50 (2015) 175–220. https://doi.org/10.1016/j.progpolymsci.2015.07.002.

[12] M. Attaei, Microencapsulation of isocyanate compounds for autoreactive , monocomponent adhesive, Instituto Superior Technico Lisboa, MSc Thesis, Lisbon University, 2017.

[13] A.A. Olajire, Corrosion inhibition of offshore oil and gas production facilities using organic compound inhibitors - A review, J. Mol. Liq. 248 (2017) 775–808. https://doi.org/10.1016/j.molliq.2017.10.097.

[14] S. Pourhashem, F. Saba, J. Duan, A. Rashidi, F. Guan, E.G. Nezhad, B. Hou, Polymer/Inorganic nanocomposite coatings with superior corrosion protection performance: A review, J. Ind. Eng. Chem. 88 (2020) 29–57. https://doi.org/10.1016/j.jiec.2020.04.029.

[15] D. Snihirova, S.V. Lamaka, M.F. Montemor, Smart composite coatings for corrosion protection of aluminum alloy in aerospace applications, in: M.F. Montemor (Ed.), Smart Compos. Coatings Membr., Elsevier Ltd, 2016: pp. 83–122. https://doi.org/10.1016/B978-1-78242-283-9.00004-X.

[16] E. Shchukina, D.G. Shchukin, Nanocontainer-Based Active Systems: From Self-Healing Coatings to Thermal Energy Storage, Langmuir. 35 (2019) 8603–8611. https://doi.org/10.1021/acs.langmuir.9b00151.

[17] A. Joshi, E. Abdullayev, A. Vasiliev, O. Volkova, Y. Lvov, Interfacial modification of clay nanotubes for the sustained release of corrosion inhibitors, Langmuir. 29 (2013) 7439–7448. https://doi.org/10.1021/la3044973.

[18] G. Cui, Z. Bi, S. Wang, J. Liu, X. Xing, Z. Li, B. Wang, A comprehensive review on smart anti-corrosive coatings, Prog. Org. Coatings. 148 (2020) 105821. https://doi.org/10.1016/j.porgcoat.2020.105821.

[19] L.M. Calado, M.G. Taryba, Y. Morozov, M.J. Carmezim, M.F. Montemor, Cerium phosphate-based inhibitor for smart corrosion protection of WE43

magnesium alloy, Electrochim. Acta. 365 (2021) 137368. https://doi.org/10.1016/j.electacta.2020.137368.

[20] L.M. Calado, M.G. Taryba, Morozovo, Y., M.J. Carmezim, M.F. Montemor, Novel smart and self-healing cerium phosphate-based corrosion inhibitor for AZ31 magnesium alloy, Corros. Sci. 170 (2020) 108648. https://doi.org/10.1016/j.corsci.2020.108648.

[21] Y. Morozov, L.M. Calado, R.A. Shakoor, R. Raj, R. Kahraman, M.G. Taryba, epoxy coatings modified with a new cerium phosphate inhibitor for smart corrosion protection of steel, (2019) 108–128. https://doi.org/10.1016/j.corsci.2019.108128.

[22] M.F. Montemor, M.G.S. Ferreira, Cerium salt activated nanoparticles as fillers for silane films: Evaluation of the corrosion inhibition performance on galvanised steel substrates, Electrochim. Acta. 52 (2007) 6976–6987. https://doi.org/10.1016/j.electacta.2007.05.022.

[23] M. Gobara, A. Baraka, R. Akid, M. Zorainy, Corrosion protection mechanism of Ce4+/organic inhibitor for AA2024 in 3.5% NaCl, RSC Adv. 10 (2020) 2227–2240. https://doi.org/10.1039/c9ra09552g.

[24] L.M. Calado, M.G. Taryba, M.J. Carmezim, M.F. Montemor, Self-healing ceria-modified coating for corrosion protection of AZ31 magnesium alloy, Corros. Sci. 142 (2018) 12–21. https://doi.org/10.1016/j.corsci.2018.06.013.

[25] S.V. Harb, A. Trentin, T.A.C. de Souza, M. Magnani, S.H. Pulcinelli, C.V. Santilli, P. Hammer, Effective corrosion protection by eco-friendly self-healing PMMA-cerium oxide coatings, Chem. Eng. J. 383 (2020) 123219. https://doi.org/10.1016/j.cej.2019.123219.

Chapter 5

Highly protective polyolefin coating modified with ceria nano particles treated with N,N,N',N'-Tetrakis(2-hydroxyethyl)ethylenediamine for corrosion protection of carbon steel

This chapter contributes to the development of smart polyolefin coatings modified with ceria nanoparticles treated with N,N,N',N'-Tetrakis(2-hydroxyethyl)ethylenediamine, as corrosion inhibitor. The first part of this chapter is dedicated to the synthesis and characterization of nanoparticles, while the second part is dedicated to the characterization of developed coatings. This chapter was published in M. Attaei, M. Taryba, A. Shakoor, R. Kahraman, A.C. Marques, and M.F. Montemor, "*Highly protective polyolefin coating modified with ceria nanoparticles treated with N,N,N',N'-Tetrakis(2-hydroxyethyl)ethylenediamine for corrosion protection of carbon steel*" Corrosion Science, 2022, 198, 110162.

5.1 Introduction

Research work regarding the application of "smart coatings" has undergone important advances over recent years [1,2]. In such a smart system, corrosion inhibitors are separated from the polymeric matrix and inhibitor release process occurs at specific time in response to the corrosion related triggers [3]. In the quest for effective corrosion inhibitor, cerium salts have been found to be promising inorganic inhibitors [4–12]. When added to organic coatings, they typically provide cathodic corrosion inhibition by formation of insoluble cerium oxides and hydroxides due to the reactions of Ce (III) and Ce (IV) ions with OH^- ions produced due to oxygen reduction at the cathodic sites [7,13,14]. The formation of insoluble oxide/hydroxides blocks the cathodic sites and hinders the progress of corrosion. Despite intensive studies in what concerns the beneficial effects of cerium salts as corrosion inhibitors [1,10,15–17], only very few have investigated the role of cerium oxide (CeO_2) NPs as corrosion inhibitors or as carriers of corrosion inhibitors for protection of steel.

Literature reports that the combination of rare earth metal ions and organic inhibitor may create synergies in suppressing both cathodic and anodic activities, leading to a substantial improvement of corrosion protection [15].

In this chapter, a very protective composite coating based on polyolefin was developed by adding CeO_2 NPs treated with N,N,N',N'-Tetrakis(2-hydroxyethyl)ethylenediamine (THEEDA). The proposed corrosion inhibition system takes advantage of CeO_2 NPs as effective cathodic inhibitors and THEEDA, an organic inhibitor. This compound contains hydroxyl and amine groups and has been reported to act as anodic inhibitor in high concentrations [15] or as a nucleophile that forms covalent bonds with iron, protecting the steel surface [16]. The polyolefin dispersion used in this work has been reported to be healable by nature [17,18] due to the presence of aldehyde and low-molecular amines which can have some roles in further crosslinking, bridging small defects [19]. Despite the excellent barrier properties of this coating, the corrosion inhibition ability still needs to be improved to extend its lifetime. To the authors' best knowledge, neither CeO_2 NPs, nor THEEDA were previously used to impart corrosion inhibition properties to polyolefin coatings used to protect carbon steel. Therefore, this work unveils a new and very effective corrosion inhibition additive that is highly compatible with polyolefin coatings. The corrosion protection performance was evaluated using EIS during sample immersion in 0.05 M NaCl, and the localized healing of the ceria-containing coatings was studied

using LEIS, and SVET. A possible mechanism for protective action of the ceria NPs is also proposed.

5.2 Experimental

5.2.1 Preparation of cerium oxide nanoparticles

16.8 g of $Ce(NO_3)_3 \cdot 6H_2O$ (detailed information regarding the material used to synthesize these NPs can be find in Table A 1.5, Appendix 1 – page 222) was added to pure ethanol and stirred for half an hour at RT to ensure complete dissolution. The temperature was then increased up to 70 °C, and NH_4OH solution was added dropwise to precipitate cerium(IV) hydroxide. The addition of NH_4OH was continued until the pH attained a value of 10 to ensure all cerium nitrate had been precipitated as cerium hydroxide, while the mixture was continuously stirred (300 rpm). The reaction was stopped after 60 min, and the solution was left to cool down and attained the RT. The precipitate was collected using a centrifuge at 5000 rpm and washed several times with Ethanol. The final product was dried at 50°C overnight and calcinated at 900 °C at the temperature ramp of 5 °C/min for 1 h. The process of formation of CeO_2 from cerium nitrate hexahydrate can be explained as follows: when ammonia was added to the solution of $Ce(NO_3)_3 \cdot 6H_2O$ in ethanol, firstly $Ce(OH)_3$ precipitated due to low solubility constant of Ce(III) hydroxide ($K_{sp}= 6.3\times10^{-24}$ at 25 °C). A high alkaline environment promotes the oxidation of Ce(III) to Ce(IV) hydroxide, and finally, Ce(IV) hydroxide changed to the cerium(IV) oxide [20].

5.2.1.1 Characterization of nanoparticles

The morphology and size of the synthesized particles were studied using a SEM and TEM. Raman Spectroscopy was conducted to evaluate the chemical structure of the particles. The powder crystallinity of ceria NPs was analyzed by XRD. The chemical structure of THEEDA and of the NPs before and after treatment with THEEDA was assessed by FTIR-ATR. TGA was used to determine the quantity of THEEDA in the ceria NPs. (a detailed information regarding equipment used to characterize the particles, and method of characterization can be found in Appendix 2.)

5.2.1.2 Results and Discussion (nanoparticles and inhibitor)

5.2.1.2.1 Size and morphology of nanoparticles

Size and morphology of the CeO_2 NPs were investigated by TEM and FEG-SEM[10] as shown in Figure 5.1. The results evidenced particles displaying a nearly cubic shape with an average size of 45 ± 10 nm. The TEM image of ceria NPs treated with THEEDA (Figure 5.1b), revealed the presence of a layer of corrosion inhibitor on the NPs´ surface (marked by black arrows).

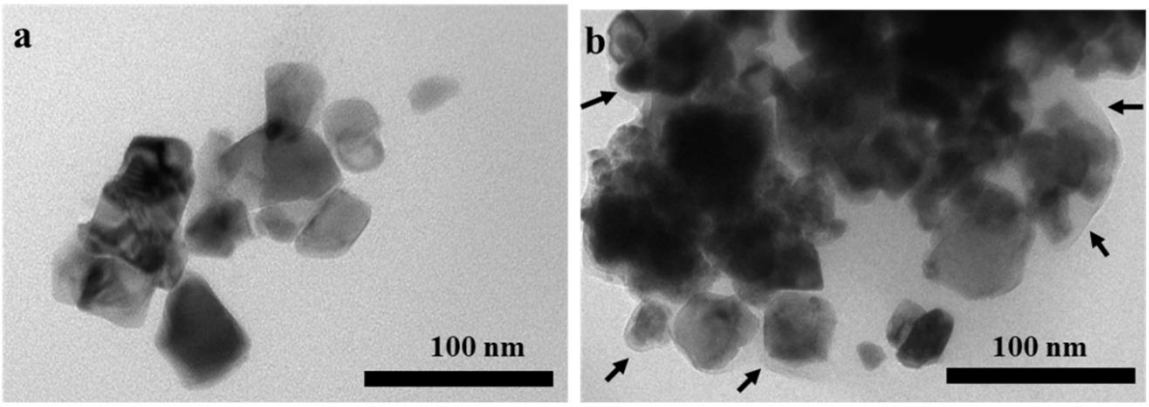

Figure 5.1 TEM micrograph of CeO_2 NPs a) before, and b) after treatment with the corrosion inhibitor.

5.2.1.2.2 Chemical structure of nanoparticles

The chemical structure of the CeO_2 NPs was investigated by Raman spectroscopy (Figure 5.2a). The Raman spectrum displays only an intense peak at ca. 461 cm^{-1} due to F_{2g} Raman active mode of the fluorite structure, often attributed for simplicity to the symmetrical stretching vibration of the Ce–O_8 units. In fact, it involves both Ce-O and O-O force constants, the O-O contribution is more significant than the Ce-O stretching one [21–24]. The absence of any other peaks or features in the CeO_2 spectrum suggests that the NPs are of high purity [24,25].

10 SEM micrograph of ceria NPs can be found in Appendix 1 page 225.

XRD was used to evaluate the crystallinity of ceria NPs. From this XRD pattern (Figure 5.2b), the representative peaks corresponding to (1 1 1), (2 0 0), (2 2 0), (3 1 1), (2 2 2), (4 0 0), (3 3 1) and (4 2 0) planes are positioned at 2θ = 28.6°, 33.2°, 47.6°, 56.4°, 59.2°, 69.5°, 76.8°, 79.2° respectively, consistent with the (ICDD PDF No. 81-0792) for CeO_2 with cubic fluorite structure. The strong and sharp diffraction peaks indicate high degree of crystallization. No additional peaks were observed, confirming the high purity of the prepared ceria NPs, in good agreement with the results obtained by Raman spectroscopy.

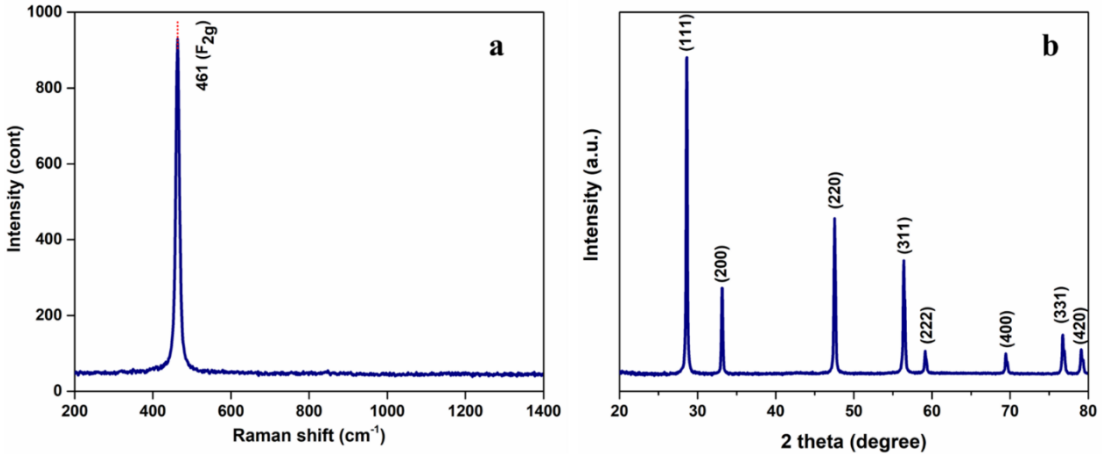

Figure 5.2 a) Raman spectrum, b) diffractogram of the CeO_2 NPs.

The average crystallite size of ceria NPs was calculated using the Scherrer equation (Eq. 5.1):

$$D = \frac{k\lambda}{\beta cos\theta} \qquad \text{Eq. 5.1}$$

where *D* is the average size of the crystals, *K* is the Scherrer constant (0.9 in this work), λ is the wavelength of the incident radiation (1.5418 Å), β is the full width at half maximum (radians) of the (1 1 1) plane diffraction peak, and θ is the Bragg's diffraction angle [26]. The crystallite grain size of the ceria NPs were calculated to be about 54 nm, in good agreement with the average of particles' grain size observed in the TEM images (Figure 5.1a).

The chemical structure of THEEDA and ceria NPs before and after treatment with THEEDA was investigated by FTIR-ATR. According to Figure 5.3a, both spectra of THEEDA and treated NPs showed a broadband in the range 3700-3035 cm^{-1} due to O-H and N-H stretching vibrations, while the O-H and N-H deformation (scissoring) modes occurred at ca. 1632 cm^{-1}. The weak bands at ca. 2969 and 3035 cm^{-1} and an intense peak

at ca. 1022 cm^{-1} were attributed to the characteristic absorption bands of the C-H group of THEEDA [27]. The spectrum of untreated ceria NPs showed an intense peak at ca. 717 cm^{-1} due to the stretching vibration of Ce-O bonds [9,28–30], which was present in both treated and untreated particles; these results confirmed the successful treatment of the CeO_2 NPs with THEEDA.

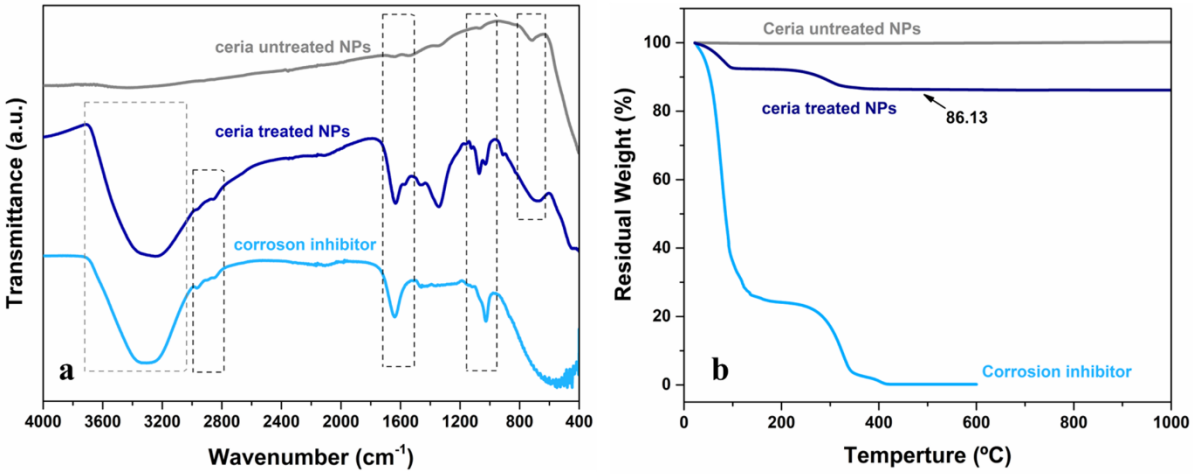

Figure 5.3 a) FTIR-ATR, b) TGA spectra of the THEEDA corrosion inhibitor and ceria NPs before and after treatment with the corrosion inhibitor.

TGA was performed to quantify the wt% of THEEDA present in the treated ceria NPs. Figure 5.3b shows the TGA spectra of THEEDA and both treated and untreated ceria NPs. The residual mass of ceria NPs at 1000 ^oC was the same as the initial mass as expected (NPs were heat treated already at 900^oC), while this value for the treated NPs was approximately 86 wt% of the initial mass. Thus, the quantity of THEEDA present around the NPs is estimated to be about 14 wt%.

5.2.1.2.3 Corrosion inhibition of THEEDA

The corrosion inhibition performance of THEEDA was studied by EIS on bare carbon steel plate immersed in 0.05 M NaCl solution without and with addition of 1 wt% of inhibitor. Figure 5.4 show Bode plots obtained for bare steel immersed in NaCl solution without (Figure 5.4a, and b) and with (Figure 5.4 c, and d) inhibitor.

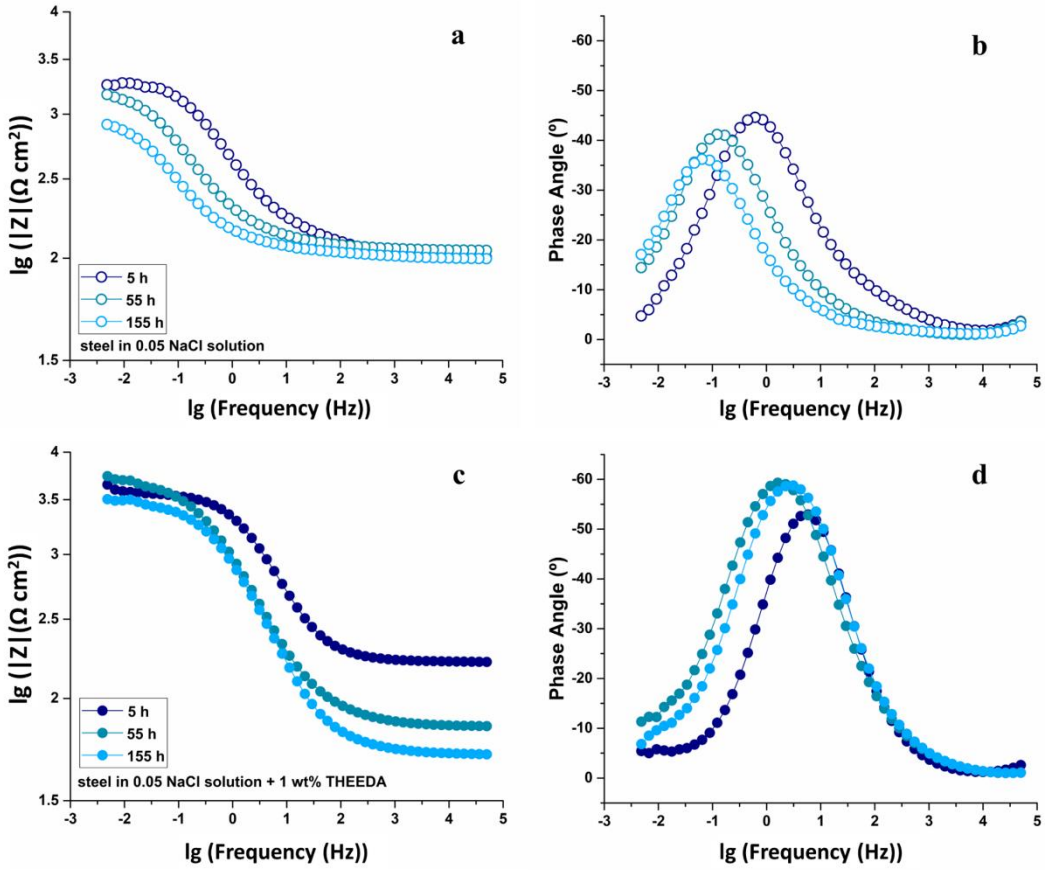

Figure 5.4 Bode plots for bare carbon steel immersed in 0.05 M NaCl solution a,b) without inhibitor; c,d) with 1 wt% of THEEDA as corrosion inhibitor.

For the bare carbon steel exposed to the NaCl solution the overall impedance values decreased during the immersion time, obtained a value of 0.8×10^3 Ω cm^2 at the end of the test (Figure 5.4a). This descending trend was accompanied with the shift of time constant at low frequency toward even lower frequencies probably due to onset of mass transfer-controlled process [31] (Figure 5.4b). In presence of 1 wt% inhibitor, the low frequency impedance values were always higher (Figure 5.4c) compared to the ones observed in sample immersed in NaCl without inhibitor. These values obtaining the maximum of 7×10^3 Ω cm^2 after 25 h of immersion and fluctuating slightly by the end of

the test. This was accompanied by an overall shift of low frequency time constant toward the higher frequencies by the end of immersion time (Figure 5.4d).

Figure 5.5 illustrated the low frequency impedance modulus for both samples, evidenced that during the entire immersion time, the sample exposed to the saline solution contains THEEDA showed the highest impedance values, confirm the effectiveness of THEEDA probably due to formation of protective layer over the bare steel. It is worth to mentioned that at the end of immersion red rust didn't observe neither over the steel surface nor inside the electrochemical cell (Appendix 1, Figure A 1.9, Page 226).

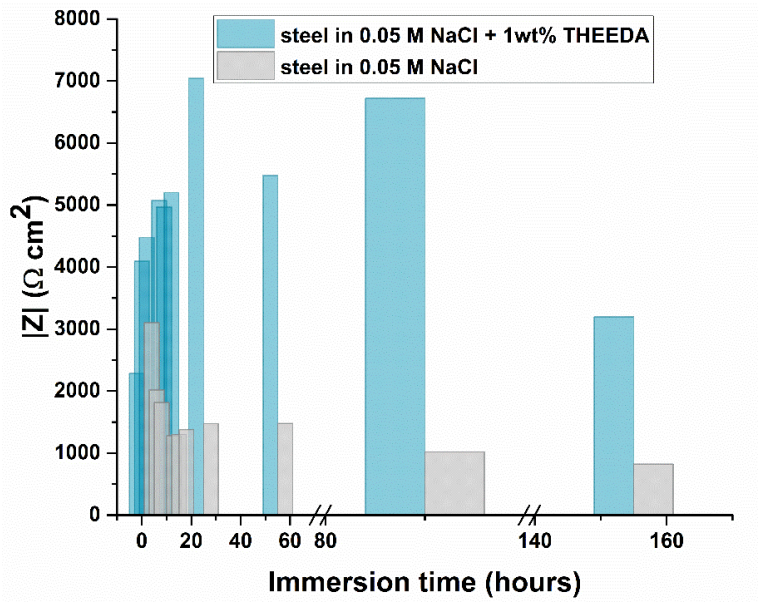

Figure 5.5 Evolution of low frequency impedance modulus for carbon steel inside 0.05 NaCl solution.

5.2.2 Preparation and application of coatings

A commercial polyethylene-based polyolefin coating (CANVERA^{TM} 1110)[11] was selected for this work. It results from an aqueous acid-modified polyolefin dispersion containing 44 ± 2.0 wt% solid polyolefin. Three groups of coatings were prepared and applied on carbon steel coupons. Table 5.1 shows detailed information regarding these coatings evaluated and studied in this chapter. A reference coating was prepared by applying the as received formulation onto the steel plates without further processing. Two different sets of modified coatings were prepared. The first set was prepared by adding the CeO_2 NPs (1 and 5 wt%) to the CANVERA^{TM} 1110 formulation (further abbreviated as "modified untreated" coating).

11 CANVERA^{TM} 1110 was kindly supplied by DOW.

The NPs were first dispersed by adding 1 and 5 wt% of alkaline water (pH ≈ 9) to the particles, followed by sonication for 10 minutes before incorporation in the coating formulation. The second set of modified coatings was prepared by adding the CeO_2 NPs (1 and 5 wt%) treated with THEEDA, directly to the base formulation (further abbreviated as "modified treated" coating).

Table 5.1 coatings' formulation and acronyms

Group	Acronym	CeO_2 NPs (wt%)	Treated CeO_2 NPs (wt%)	Alkaline water (wt%)
1	Reference	0	0	0
2	Modified untreated-1%	1	0	1
	Modified untreated-5%	5	0	5
3	Modified treated-1%	0	1	0
	Modified treated-5%	0	5	0

The ceria NPs were treated by THEEDA using the incipient wetness impregnation method. To this end, THEEDA was added to the ceria NPs dropwise and the mixture was stirred continuously using magnetic stirrer. The prosses continued until complete coverage of NPs by THEEDA evidence by change of NPs´ appearance from powder-like to paste-like material (these particles will be abbreviated as treated ceria NPs).

The steel coupons were degreased following the same procedure in Chapter 3. The coatings were applied on steel coupons by dip-coating, using a dip coater machine (detailed information can be find in Appendix 2) The coated samples were dried and cured in the oven at 175 ^{o}C for 5 minutes.

5.2.2.1 Characterization of coatings

Coating thickness was determined with a digital gauge. Cross-cut tests (using standard procedure ASTM D3359-09) [32] were performed to evaluate the adhesion of both reference and modified coatings. EIS experiments were carried out to investigate the barrier properties of the reference and modified coatings applied on carbon steel coupons, immersed in 0.05 M NaCl solution.

LEIS was performed to assess the local changes in admittance at an artificial defect made in the reference and modified coatings, while the sample was immersed in 0.005 M of NaCl solution.

SVET and scanning fiber-optic dissolved oxygen microsensor measurements were performed over coated samples containing point defects to evaluate the localized corrosion activity. The cross-sections of the modified coatings were observed with SEM and the elemental analysis over the selected area of the coating cross-section was carried out. The surface roughness of the reference and modified coatings was evaluated using SEM.

Micro-FTIR was performed to study the surface of the defects (scratches), artificially made on the surface of the studied coatings after immersion in 0.05 M NaCl. A scratch with an approximate length of 6 mm created with a sharp knife, exposing the bare metal. Furthermore, SEM was used to analyze the corrosion products formed onto the surface of artificial scratches. (detailed information regarding the equipment used to characterize the coatings, and method of characterization can be found in Appendix 2).

5.2.2.2 Results and Discussion (Coatings)

All coatings studied in this work had an average thickness of 35 ± 5 μm. The coating morphology and the distribution of ceria NPs were evaluated by SEM. The corresponding results can be found in Appendix 1, Figure A 1.10, page 226.

5.2.2.2.1 EIS Experiments

EIS was used to evaluate the protective properties of coatings during the immersion of coated samples in 0.05 M NaCl solution. The Bode plots obtained for the reference and modified coatings are shown in Figure 5.6. The reference coating showed a fully capacitive response along all frequency range during the first 15 days of immersion. Further immersion of the coated samples in the NaCl solution led to a monotonous decrease of the coating barrier properties due to continuous electrolyte uptake, evidenced by the loss of the coating capacitive behavior, formation of a time constant at low and medium frequencies, and the shift of these time constants towards slightly higher frequencies. The descending trend of the coating barrier properties was confirmed by a drop in the low-frequency impedance moduli, from 3.6×10^{11} Ω cm^2 at the beginning of immersion to approximately 1×10^{10} Ω cm^2 after 125 days (Figure 5.6a, b). A slight

increase in impedance moduli around the 50^{th} day of immersion, accompanied by an attenuation of the time constant at low-middle frequencies, might be related to the self-healing properties of polyolefin coating as previously reported [17,18]. However, this effect could not be observed for a long time.

A set of representatives Bode plots obtained for the modified coatings containing 5 wt% of untreated NPs, and 5 wt% of NPs treated with THEEDA are depicted in Figure 5.6c, d, e, and f. Contrarily to the reference coating, these modified coatings exhibited a superior capacitive response over the entire frequency range and during the whole immersion time (125 days) in 0.05 M NaCl electrolyte. This capacitive response extended over the entire frequency domain and this trend evidenced the stable barrier properties of the modified coatings. The impedance modulus at low frequency reached the constant values close to 10^{12} Ω cm^2 for both modified coatings, being always two orders of magnitude above the values recorded for the reference coating. These high impedance moduli were always accompanied by phase angle values close to -90 degrees (Figure 5.6d, and f). No time constants could be detected at low frequencies, confirming the absence of interfacial activity and the enhanced corrosion resistance of modified coatings after 125 days of immersion. The coatings modified with 1 wt% of ceria untreated NPs and modified with 1 wt% of treated ceria NPs, were evaluated by EIS. As the response of these coatings was completely identical to the one modified with 5 wt% of NPs, and to evidence such a behavior, the Bode plots of coatings modified with 1 wt% of NPs obtained after 125 days of immersion were added to Figure 5.6c, d, e, and f (orange lines).

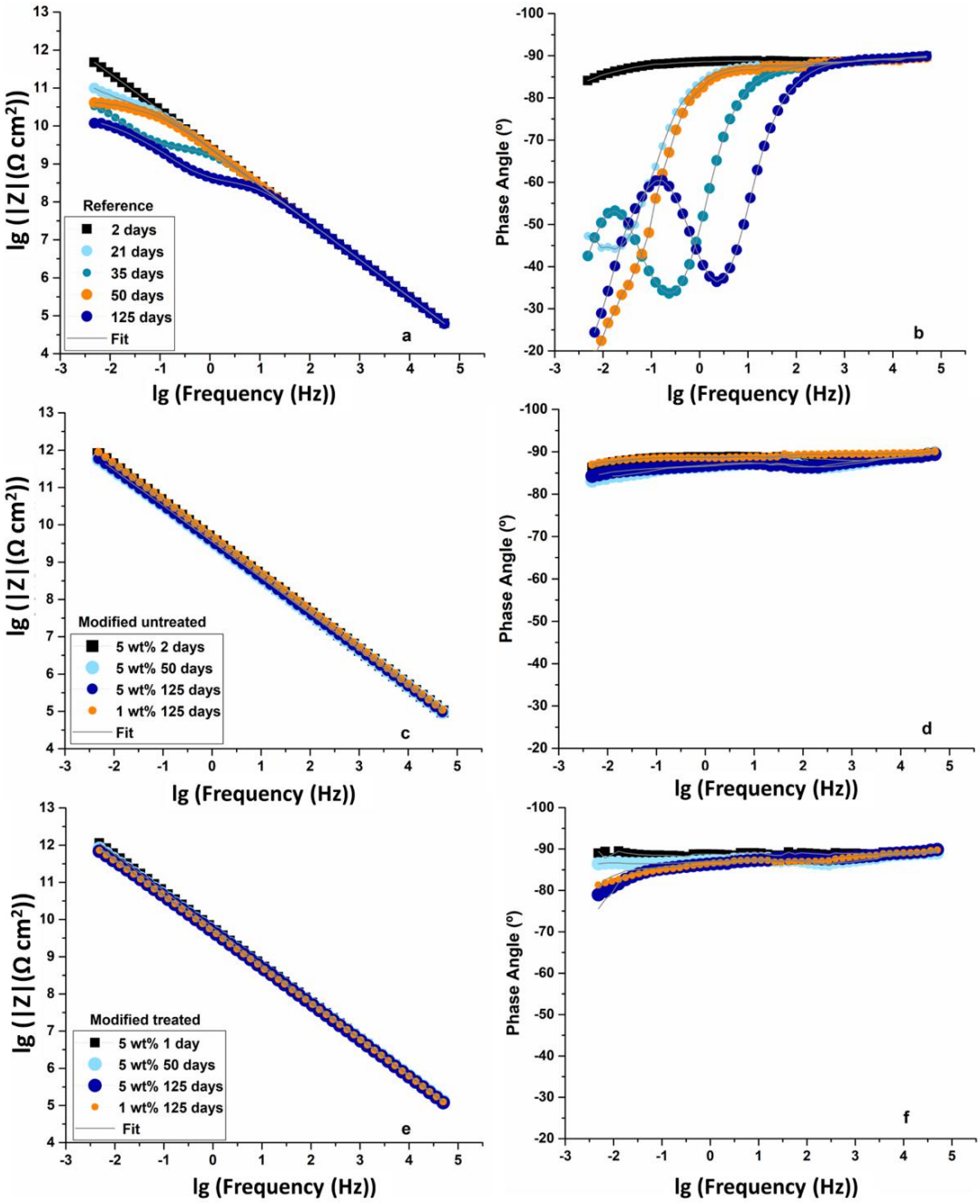

Figure 5.6 Bode plots for Reference (a, b); modified untreated (c, d); modified treated (e, f) coatings.

Low frequency impedance modulus taken at 0.005 Hz for the reference and modified coatings contain 1 and 5 wt% of untreated ceria NPs and coatings modified with 1 and 5 wt% of ceria NPs treated with THEEDA is shown in Figure 5.7. The impedance modulus at low frequency for the reference coating showed an overall decreasing trend over the

entire immersion time and the values showed some fluctuations in the range 4.7×10^{11} Ω cm^2 to 1.1×10^{10} Ω cm^2.

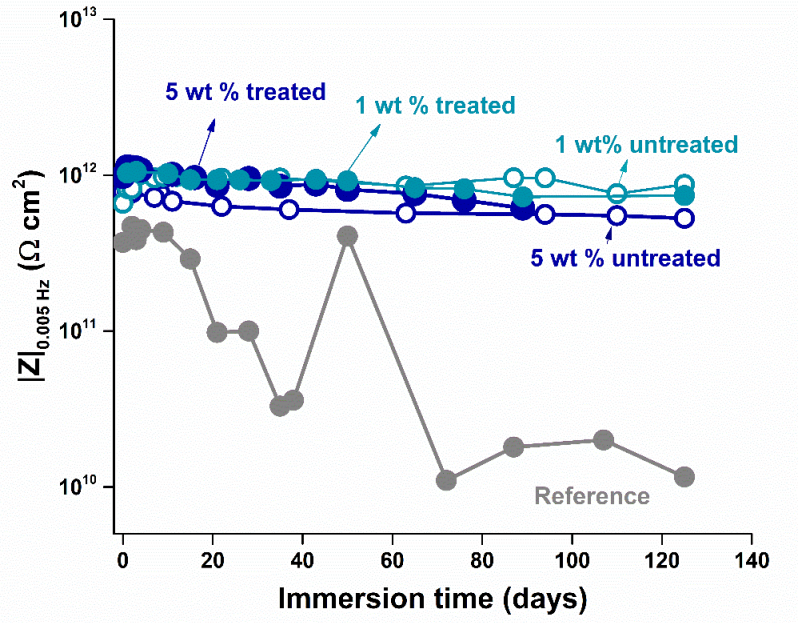

Figure 5.7 Comparison of the low frequency impedance values (measured at 0.005 Hz) on steel plates coated with reference and modified coatings – Image reprinted with permission.

Contrarily, the impedance moduli for all coatings modified with ceria NPs, showed nearly constant values over the entire immersion time. The values measured for the coatings modified with 1 and 5 wt% of untreated ceria NPs fluctuated between 9.8×10^{11} Ω cm^2 to 6.6×10^{11} Ω cm^2, and between 9.5×10^{11} Ω cm^2 to 5.5×10^{11} Ω cm^2, respectively, evidencing the very stable barrier properties of the modified coatings over immersion. For coatings modified with 1 and 5 wt% of treated ceria NPs, very stable impedance moduli at low frequencies were also observed. The values fluctuated between approximately 1×10^{12} Ω cm^2 and 7.2×10^{11} Ω cm^2, and between 1.1×10^{12} Ω cm^2 and 6.1×10^{11} Ω cm^2 for the coatings modified with 1 and 5 wt% of treated particles, respectively. Overall, the low-frequency impedance values for the modified coatings were approximately two orders of magnitude higher than for the reference coating by the end of immersion time. Thus, the EIS results proved the superior protective performance of the ceria NPs-modified coatings. No relevant effects were noticed when the ceria NPs were treated with inhibitor, a result that confirms the excellent compatibility of this inhibitor both with the NPs carriers and the polyolefin matrix.

An equivalent circuit composed of one time constant (Figure 5.8a) was used to fit the experimental EIS data of the reference coating for the first 20 days of immersion and to fit the EIS data obtained for both modified coatings over the entire immersion period. An equivalent circuit with two-time constants (Figure 5.8b) was also used to fit the EIS data obtained for reference coating from 21 days till the end of the immersion period. In these two circuits, at high frequency, R_p was assigned to the pore/coating resistance of the coatings, and CPE_{Coat} was assigned to coating the capacitance. At low frequency, R_{Ct}, and CPE_{dl} were assigned to the Faradic resistance and the capacitance of the double layer, respectively. In both circuits, R_s represents the resistance of the electrolyte and the constant phase elements were used instead of capacitors due to deviation from the ideal condition.

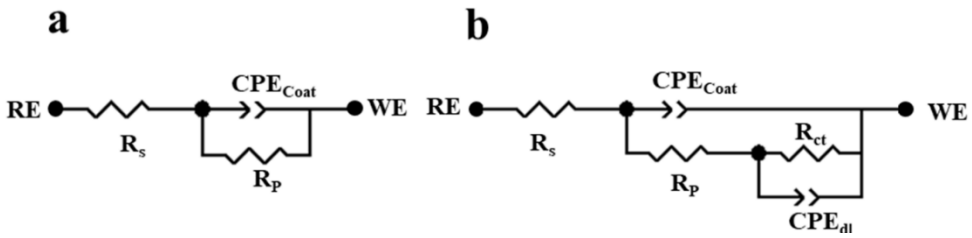

Figure 5.8 EEC used to fit the data obtained for (a) reference coating during the first 20 days and modified coatings throughout the immersion: (b) reference coating after 20 days of immersion.

The fitting results obtained for the reference and modified coatings are depicted in Figure 5.9a, b, and c. Due to the identical results obtained for both modified coatings containing 1, and 5 wt% of particles just one set of results, those obtained for the 5 wt% Ceria NPs modified coatings (untreated and treated with THEEDA) were selected.

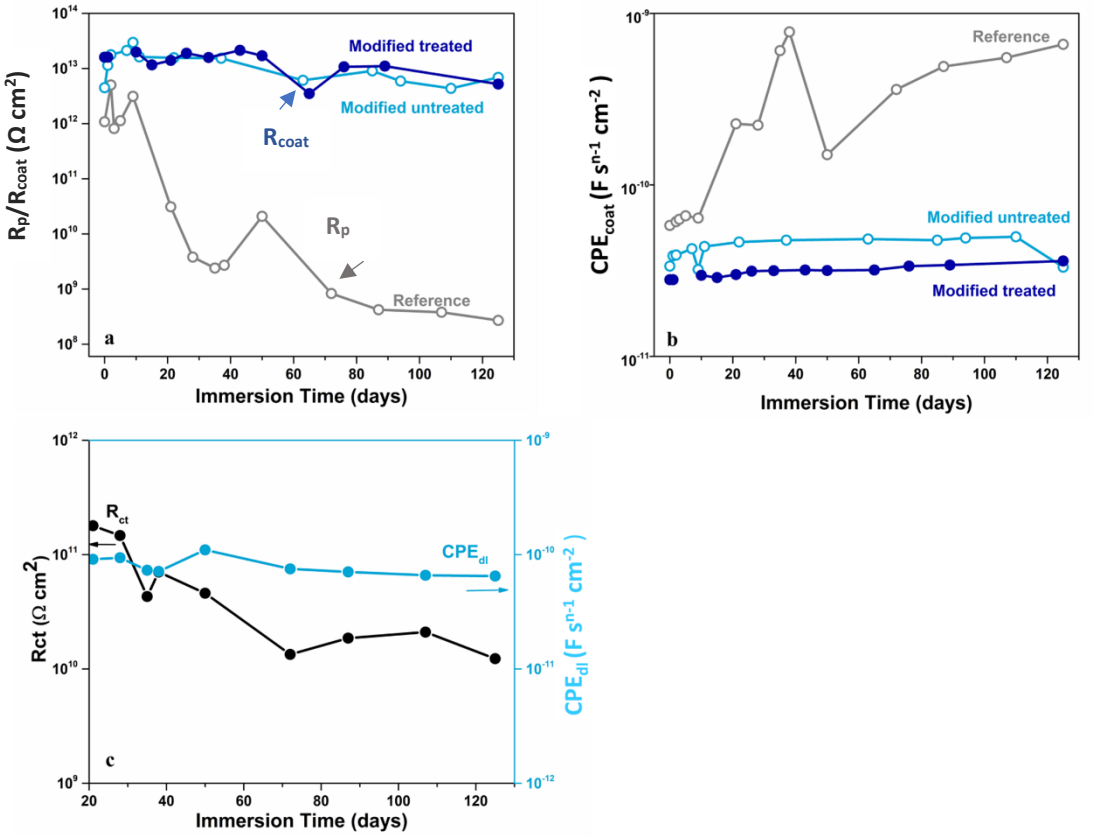

Figure 5.9 Evolution of a) pore resistance of the reference and modified coatings contain 5 wt% of treated and untreated NPs; b) admittance of the reference and modified coatings containing 5 wt% of treated and untreated NPs; c) Faradic resistance and admittance of the double layer for reference coating from 21 days until the end of immersion time (Data are available in Tables A 1.9, A 1.10, and A 1.11 - Appendix 1.)- Image re-printed with permission.

Figure 5.9a shows the pore resistance of reference, and coating resistance (R_{coat}) of coatings modified with 5 wt% of treated ceria and untreated ceria NPs. The pore resistance of the reference coating showed a decreasing trend during immersion, displaying values close to 1×10^{12} Ω cm^2 at the early stages that reduced four orders of magnitude, reaching 2.5×10^{8} Ω cm^2 by the end of the test. This descending trend in the pore resistance of the reference coating was accompanied by a concomitant increase of the respective CPE_{coat}, as expected (Figure 5.9b). These results evidenced a notorious degradation of the coating barrier properties due to electrolyte uptake and the development of conductive paths that accelerate coating degradation.

In turn, the coating resistance of both modified coatings displayed very high and stable values all over the immersion time, being always above 10^{13} Ω cm^2 (Figure 5.9a). This confirms the high and stable corrosion protection properties of the modified coatings

conferred by the addition of ceria NPs (treated and untreated), as expected from the fully capacitive responses of these coatings. R_{coat} values for the modified coatings were more than four orders of magnitude higher compared to R_{pore} of the reference coatings at the end of immersion time. This was accompanied by the lower but stable values of the CPE_{coat} admittance during the immersion time (Figure 5.9b). Overall, this result confirmed the excellent protective properties of the modified coatings. Slight oscillations in R_{coat} can be related to electrolyte uptake and formation of conductive paths, which might be blocked by the formation of stable and insoluble cerium species due to the presence of ceria NPs [14] and/or formation of protective species from the reaction of THEEDA with Fe^{2+} and Fe^{3+} [16]. The possibility of polymer healing cannot be excluded as reported elsewhere [19].

In addition, the Faradic resistance (R_{ct}) for the reference coating, which was obtained from EIS data after 21 days of immersion, using the circuit shown in Figure 5.6b, suffered a decrease over the time. The R_{ct} values were 1.8×10^{11} Ω cm^2 at 21st day of immersion and reduced more than one order of magnitude by the end of the test, reaching values of 1.2×10^{10} Ω cm^2. The fluctuations of R_{ct} and the respective admittance values, CPE_{dl}, evidence corrosion activity at the steel-coating interface which leads to accumulation of corrosion products that can partially block the pores. This effect contributes to reduce fluctuations of R_{ct} values after 70 days (Figure 5.9c). To summarize, EIS results, and the respective fitting parameters evidenced the more stable and superior corrosion protection conferred by polyolefin coatings modified with ceria NPs untreated and treated with THEEDA.

Due to identical EIS results obtained for the coatings modified with 1, and 5 wt% of NPs, just those containing 5 wt% ceria NPs (untreated and treated with THEEDA) together with the reference coating, were selected to be further tested by localized electrochemical techniques.

5.2.2.2.2 Localized Electrochemical Techniques

LEIS was performed to evaluate the healing ability and the local corrosion protection efficiency of the coatings. To this end, an artificial defect was made in the coating, exposing the carbon steel to the 0.005M NaCl solution, while the LEIS probe was scanned over an area (blue rectangles in Figure 5.10c, f, and i) which includes the artificial defect, monitoring the local admittance of the working electrode. Figure 5.10 illustrates a

representative set of LEIS maps that show the evolution of admittance over time. The maximum admittance values were always measured over the defect. The overall evolution of admittance at the artificial defects in coatings is shown in Figure 5.10j. As discussed in the previous chapters, this figure depicts the ratio between maximum admittance values determined over the defect at a specific time (A) and the maximum value measured at the beginning of immersion (A_0) to minimize the effect of non-identical distances between the LEIS prob and the coating surface. Therefore, an increase of this ratio can be assigned to increased admittance, and therefore higher corrosion activity over the defect, while a decrease evidences inhibition or healing of the corrosion activity.

For the reference coating, the first signals of corrosion activity were recorded after 2 h of immersion. The corrosion activity intensified abruptly at the defect until the 11 h of immersion (Figure 5.10a), reaching a value 750 % higher compared to the initial value, confirming the presence of intense corrosion activity over the defect. From this time forward, and until 40 h of immersion, admittance values over the defect showed a slight descending trend (Figure 5.10j), probably due to an inherent self-healing ability of polyolefin as well as accumulation of corrosion products which can partially block the defect, decreasing the active area. However, after 40 h the admittance values showed again an increasing trend, and a plateau was reached by the end of the experiment (70 h). This fluctuation can be explained by the formation and dissolution of poorly stable corrosion products from the exposed surface (Figure 5.10c).

For the coating modified with 5 wt% of untreated ceria NPs, the first signs of corrosion activity were also detected after 2 h of immersion. Overall admittance values over the defect showed a gradual increase during immersion, reaching the maximum of 178 % of the initial value by the end of immersion. This value is significantly lower (four times) compared to the maximum admittance value (750 %) recorded for the reference coating (Figure 5.10j), confirming the inhibition of the corrosion activity in the defect, in the presence of ceria NPs. Also, a descending admittance trend over the defect was observed in a short time (37-45 h) (Figure 5.10e, j).

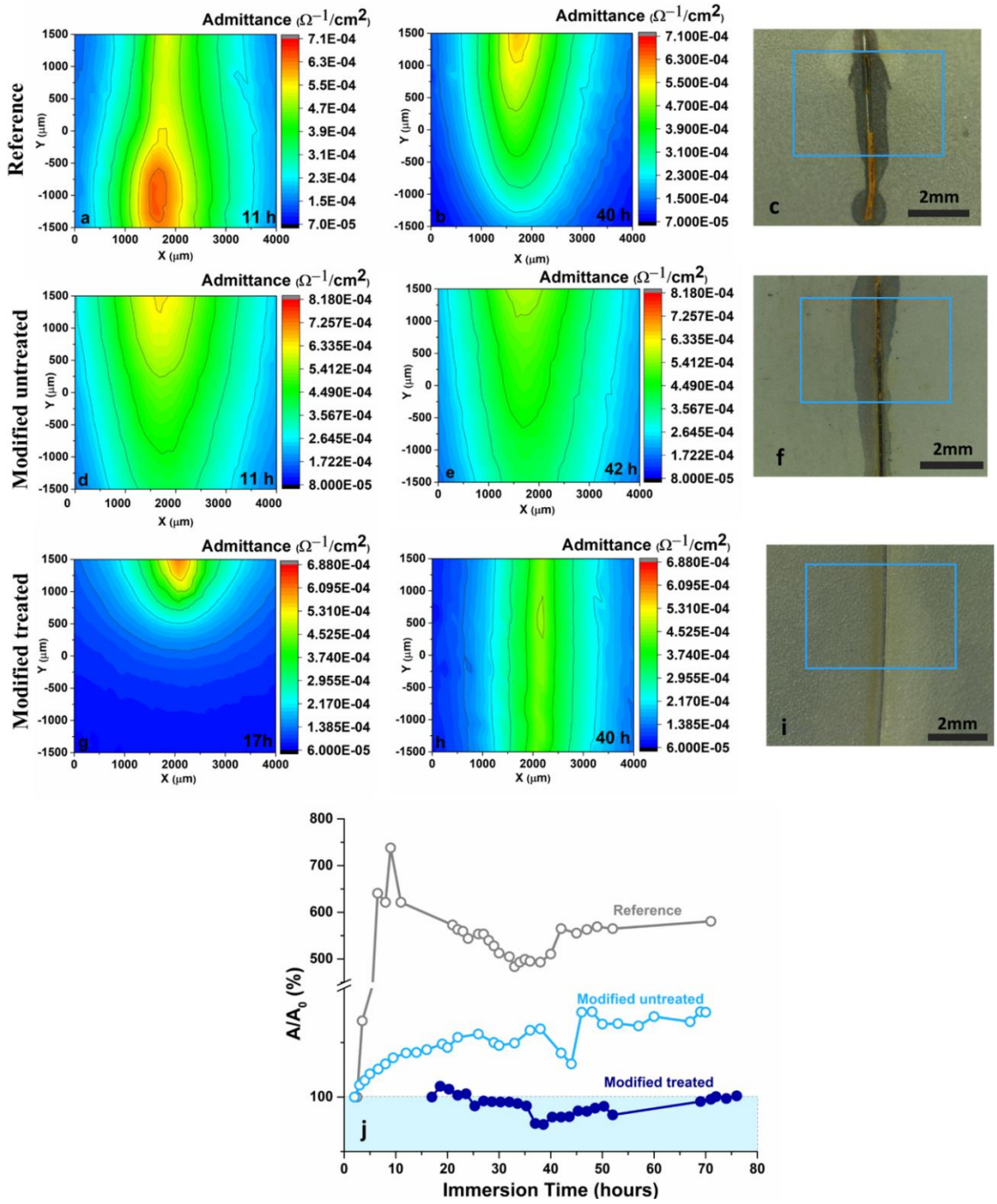

Figure 5.10 LEIS admittance maps obtained after 11 h, and 40 h, immersion of the reference coating (a, b); after 11 h, and 42 h, immersion of modified untreated coating (d, e); after 17 h, and 40 h, immersion of modified treated coating (g, h) in 0.005 M NaCl solution; respective optical microscope images of each sample at the end of immersion time (the approximate scanned areas are highlighted in the yellow rectangles) (c, f, i); Evolution of the admittance ratio for the reference and modified coatings during immersion in 0.005 M NaCl solution (j).

In contrast, for the coating modified with 5 wt% of treated ceria NPs, the first signs of corrosion activity were only detected after 17 h of immersion (Figure 5.10g). This means

that even though the bare carbon steel was exposed to the NaCl solution, the healing mechanism due to the presence of the inhibitor loaded onto the ceria NPs can effectively hinder the propagation of the corrosion activity at the defect. A negligible increase in the admittance values was observed until 19 h, which was immediately suppressed. From this time onwards, the local admittance showed a descending trend (Figure 5.10j) and reached a minimum vale after 40 h of immersion, which was about 50 % of the admittance measured initially (Figure 5.10h); this result evidence a notorious healing effect. The admittance values over the defect remained below the first value recorded until the end of immersion time, revealing the effective and stable corrosion healing effect conferred by the treated ceria NPs. These treated particles on the one hand can form insoluble $Ce(OH)_3$ at the micro-cathodic zone that suppresses the cathodic corrosion activity [14] and, on the other hand, the released THEEDA can form a complex with Fe^{2+} and Fe^{3+} which can protect micro-anodic sites suppressing corrosion activity [16,33]. The micrographs of samples at the end of the experiment also revealed that ceria NPs by themselves can decrease the quantity of corrosion products over the defect compared to the reference coating (Figure 5.10c, and f). However, for the coating modified with treated NPs, neither delamination nor corrosion products were observed at the defect by the end of immersion (Figure 5.10i).

SVET was used to further discriminate the corrosion behavior of all coated samples at the microscale in the presence of a defect. Coated samples were immersed into the 0.05 M of NaCl solution. Figure 5.11 illustrates the most representative distributions of current density along the immersion time recorded for the reference coated sample. This coating showed corrosion activity from the early stages of immersion which was always located over the defect. The detected activity was predominantly cathodic during the first 13 h of the immersion (Figure 5.11d). The values of the current density were from -3 to -15 $\mu A/cm^2$. The predominance of cathodic activity with no visible delamination (Figure 5.11a) (till 13 h) can be explained as follows: cathodic oxygen reduction, consumed the oxygen available in the electrolyte, leading to formation of OH^- that creates a negatively charged ionic flow detectable by the SVET probe. In turn, most of the iron ions produced during anodic dissolution may precipitate over the defect before reaching the plane where SVET measurements were performed (100 µm above the surface). Such precipitation may occur due to hydrolysis when the anodic activity is highly localized. Since the intensity of the anodic process was low, the produced H^+ could not reach the plane of the SVET measurements (100 µm). No reproducible corrosion activity was detected from 13h to

20h of immersion (Figure 5.11e). However, delamination became visible after 13h of immersion (Figure 5.11b), suggesting that the corrosion process propagated underneath the coating and undetectable for the SVET probe, placed above the coating. After 20 h and until the end of immersion, anodic corrosion activity with maximum current density values of 20 µA/cm^2 was clearly detected over the defect (Figure 5.11f). Concomitantly, the cathodic process located underneath the coating promoted coating delamination (Figure 5.11c).

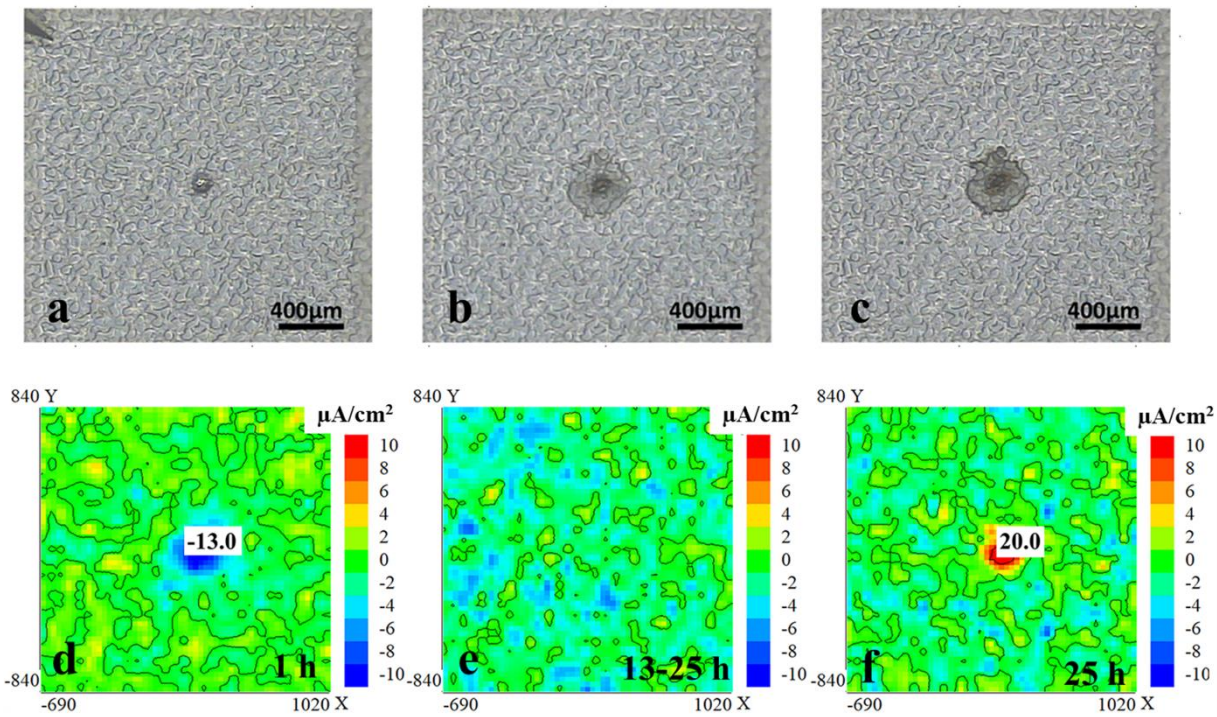

Figure 5.11 Optical micrographs (a, b, and c) and their corresponding current density distribution for the reference coating after 1 h and 25 h of immersion (d, f); representative current density distribution corresponding to time interval 13-20 h (e)- (X and Y correspond to the coordinates of the scan in µm) - Image reprinted with permission.

Both coatings modified with ceria NPs particles (untreated and treated)), demonstrated remarkable improvement in corrosion protection compared to the reference coating. No delamination was observed for both modified coatings at any time of immersion (Figure 5.12a, b, e, and f). The coating containing untreated ceria NPs did not show detectable corrosion activity during the first 24 h of immersion (Figure 5.12c). The subtle (and reproducible) activity was only observed after 24 h of immersion (Figure 5.12d).

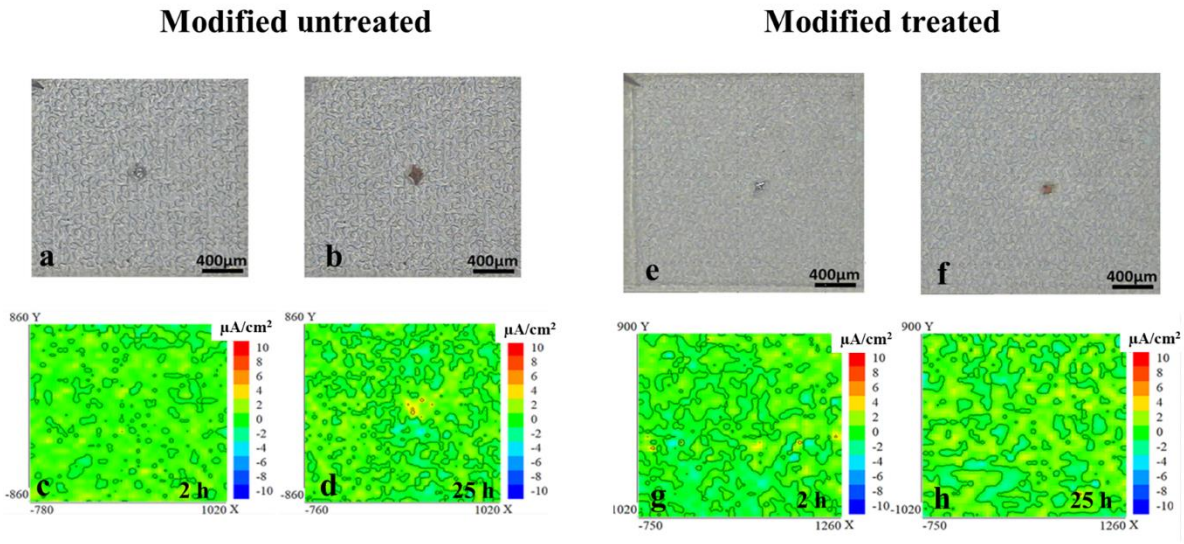

Figure 5.12 Optical micrographs obtained at the beginning and end of immersion time for a, b) modified coating contains 5 wt% of untreated NPs; e, f) for modified coating contains treated ceria NPs; SVET maps for modified coating contains c, d) 5 wt% of untreated NPs; e, f) contains 5 wt% of treated ceria NPs at 2 and 25 h of immersion time.

The coating modified with treated ceria NPs did not show any detectable corrosion activity during the entire immersion time (Figure 5.12g, and h), confirming the formation of protective species over the defect [14,16,33] and, as consequence, effective suppression of corrosion activity extended over time. Thus, the SVET study of reference and modified coatings allowed to rank the protective properties in the following order: Reference coating < Modified untreated coating < Modified treated coating, in good agreement with results obtained by LEIS.

To further discriminate the differences in the electrochemical activity, identical samples were also tested using the fiber-optic dissolved oxygen microsensor. Figure 5.13 shows the distribution of dissolved oxygen (DO) for all samples. The oxygen depletion zone located over the defect for all coated samples (Figure 5.13a, b, and c), confirmed the presence of cathodic activity in the defect. Figure 5.13d illustrates the evolution of the minimum DO concentration over the defect along the time. The more pronounced depletion of DO concentration can be assigned to a more intense cathodic process, and consequently, more intense overall corrosion activity. For the reference coating the DO level decreased drastically during the first 16 h of immersion, confirming the presence of cathodic activities over the defect. A slight, temporary increase observed between 16 - 21 h of immersion results from depletion of available oxygen and therefore the activity

started to be more intense underneath the coating, leading to the onset of cathodic delamination, in agreement with the decrease of corrosion activity observed for similar time intervals in the SVET maps. However, after 21 h of immersion, DO concentration decreased again, indicating the progress of corrosion activity in the defect. In turn, for the coatings modified with 5 wt% of untreated ceria NPs and treated ceria NPs, no significant depletion in DO concentration was observed until 17 h of immersion time, evidencing that cathodic activity has been significantly reduced. A slight decrease in DO concentration was observed between 17-21 h, which recovered immediately.

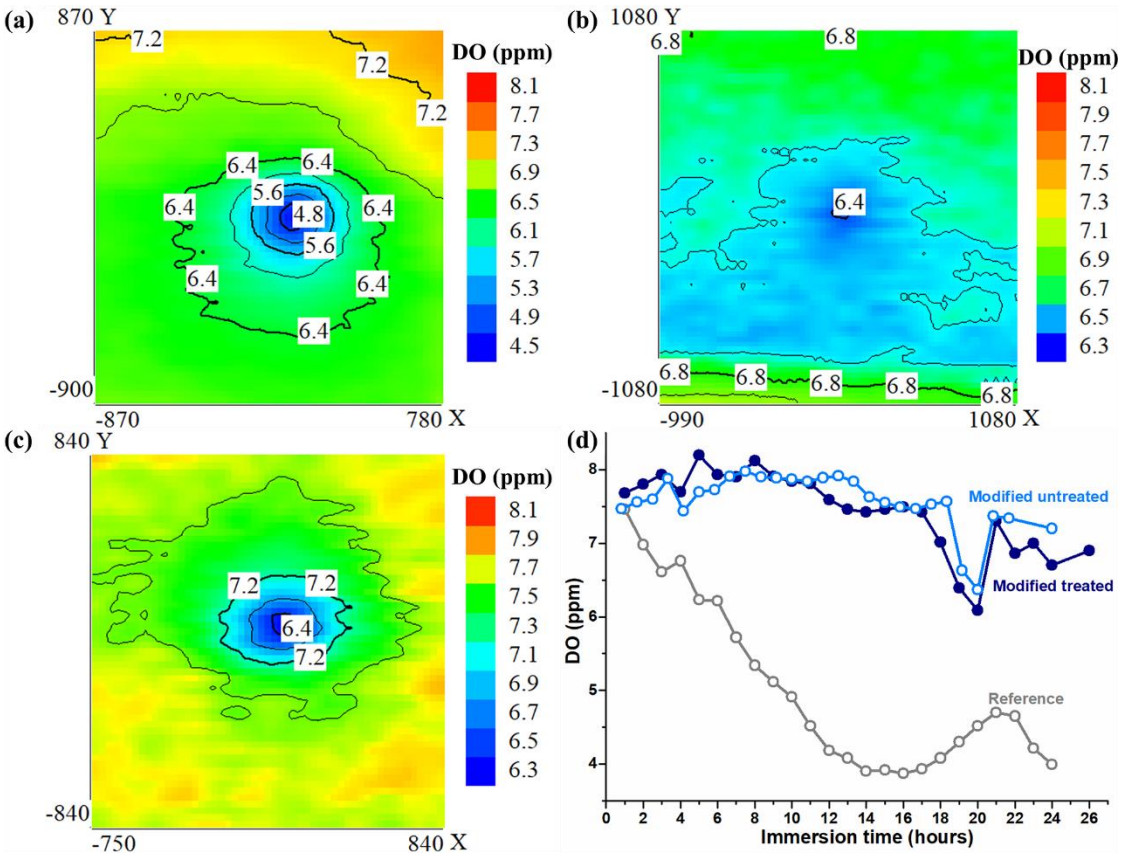

Figure 5.13 DO distributions recorded after 20h of immersion for (a) reference, (b) modified untreated, and (c) modified treated coatings; d) evolution of the minimum DO concentration (i.e., reflecting the maximum cathodic activity achieved) over the defect in the reference and both modified coatings – Image reprinted with permission.

Therefore, the onset of weak corrosion activity was immediately suppressed, probably due to the formation of protective species over the exposed area. It is worth mentioning that the activity observed in a time interval of 17-19 h in the modified treated coating, is in agreement with those observed in LEIS for identical immersion times.

5.2.2.3 Characterization of corrosion products

To better understand the corrosion protection mechanism of polyolefin coatings modified with ceria NPs, the corrosion products formed over the artificial defect in the reference and modified coatings were analyzed by micro-FTIR and EDS. Figure 5.14 shows the defects made in the reference and in the coatings modified with 5 wt% of NPs treated by THEEDA, after 24 and 48 h of immersion in 0.05 M NaCl, and the respective micro-FTIR spectra which were collected over these defects (blue rectangles Figure 5.14). Defects with an approximate length of 6 ± 0.5 mm and a narrow width of 20 ± 5 µm were produced equally for both coatings using a sharp knife (Figure 5.14a, and e). For the reference coating after 24 h of immersion, a considerable quantity of corrosion products was observed over the artificial defect (Figure 5.14a, and b). This was accompanied by a widening of the defect, from 20 µm up to 150 µm (Figure 5.14b). After 48 h of exposure to the electrolyte, corrosion propagation around the defect site was even more pronounced, accompanied by additional defect widening up to 200 µm (Figure 5.14c, and d). Contrarily, for the modified treated coatings, neither corrosion products nor any change in the defect width were observed after 24 h of immersion in 0.05 M NaCl solution (Figure 5.14e, and f).

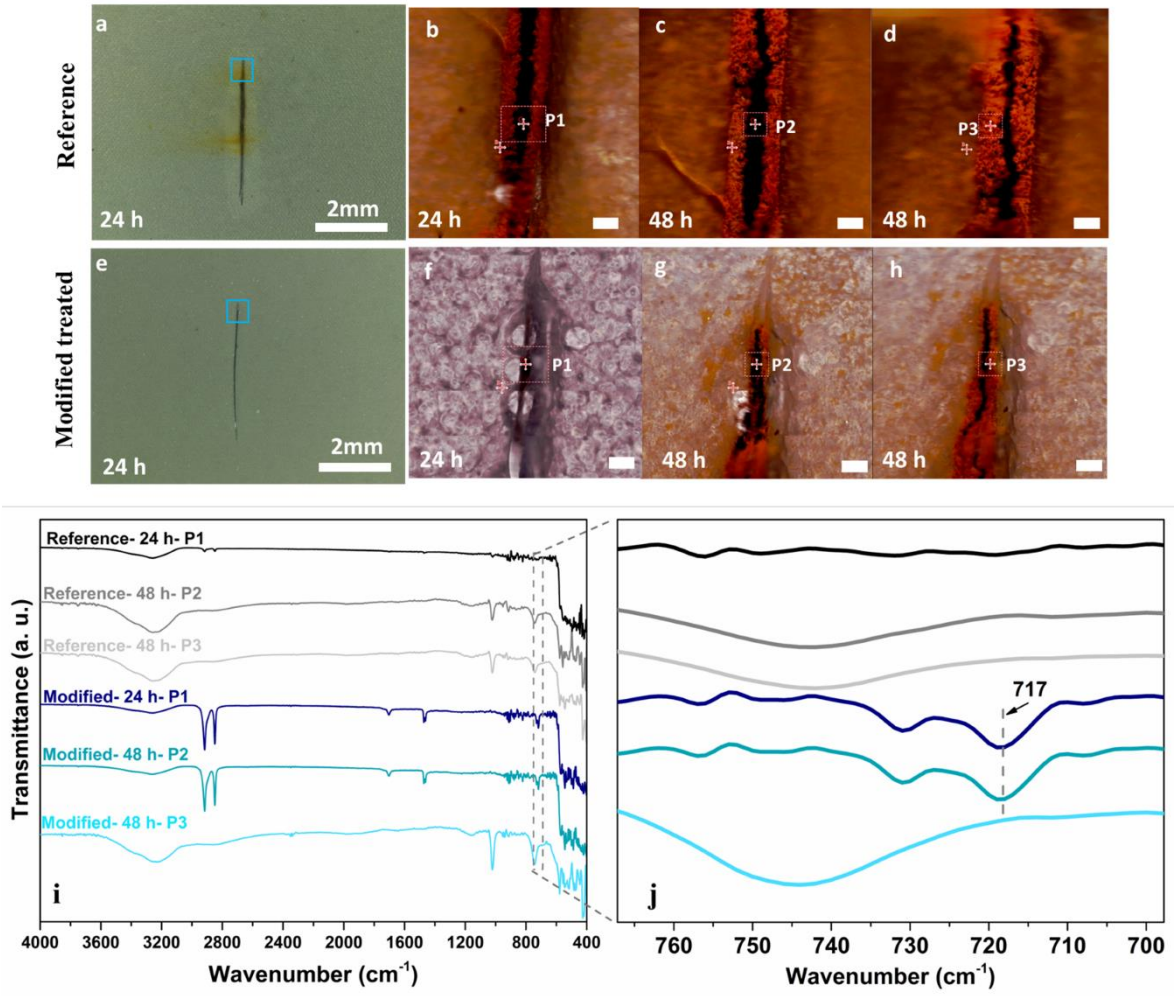

Figure 5.14 Optical micrographs of the defects produced on the reference (a-d) and modified treated (e-h) coatings after 24 h (a, b, e, and f) and after 48 h (c, d, g, and h) of immersion in 0.05 M NaCl aqueous solution (scalebars of b, c, d, f, g, and h = 100 µm); i) Micro-FTIR spectra of corrosion products accumulated at artificial defects made on the reference and modified treated coatings after 24 h and 48 h of immersion in 0.05 M NaCl, j) magnified zone of spectra at 698-760 cm^{-1}.

However, after 48 h of immersion, corrosion products were detected over the defect (Figure 5.14g, and h), which were accompanied by a slight widening of the defect (up to 80 µm), however much smaller than the reference coating (200 µm), confirming the protective effect of treated NPs added to the polyolefin formulation.

Micro-FTIR spectra (Figure 5.14i) were obtained for the reference and modified treated coatings at several spots marked as P1, P2, and P3 in Figure 5.14b-d, and f-h after 24 and 48 h of immersion. After 24 h of immersion, the spectrum obtained at P1 (middle of the scratch) for modified treated coating showed two sharp peaks at ca. 2919 cm^{-1} and ca. 2899 cm^{-1} ascribed to methylene (–CH_2–) of polyolefin, namely C–H bond asymmetric

stretching and symmetric stretching, respectively [34]. Also, two small peaks located at ca. 1468 cm^{-1} and 731 cm^{-1} were assigned to methylene C–H symmetric bending vibration, and methylene $–(CH_2)_n–$ rocking vibration, respectively; all these are characteristic peaks of polyolefin [35]. A small peak at ca. 717 cm^{-1} derived from Ce–O bonds, which was observed before by FTIR-ATR of both treated and untreated NPs (Figure 5.3a) was also detected in spectra of P1 and P2 collected at the middle of the scratch in the modified treated coatings (Figure 5.14j). This shows the tendency of the modified coating to heal the artificial defect, well evidenced by the absence of corrosion product after 24 h, and narrower opening size of the defect compared to that of the reference coating.

In the micro-FTIR spectrum obtained at P1 for the reference coating after 24 h of immersion, those peaks, characteristic of polyolefin, were hardly detectable, as expected. While the spectrum obtained at P2 for the modified treated coating after 48 h of immersion still displays the characteristic peaks of polyolefin. Moreover, several fingerprint peaks, characteristic of iron oxide/hydroxide were found in this spectrum (reference coating) as follow: broadband centered roughly at 3360 cm^{-1}, ascribed to –OH stretching due to the presence of water, a weak peak located at ca. 1247-1108 cm^{-1} was assigned for vibrations of OH_2 coordinated with Fe (Fe-OH_2) [36], two peaks at ca. 1021 cm^{-1}, and 745 cm^{-1} can be assigned to lepidocrocite (γ-FeOOH) [37], and a peak (shoulder) located at ca. 580 cm^{-1} can be assigned as magnetite (Fe_2O_3) [37]. However, in the micro-FTIR spectra obtained at P2 for the reference coating and over P3 for both reference and modified treated coatings, only iron oxide/hydroxide peaks were detected.

EDS was also carried over artificial defects made on both modified coatings to further characterize the corrosion products. Figure 5.15 shows the EDS maps obtained at the defect made on both modified coatings after 48 h of immersion in 0.05M NaCl solution. For both modified untreated and modified treated coatings, cerium, oxygen, and iron were detected over the defect (Figure 5.15), confirming the participation of cerium-containing species in the corrosion products.

Carbon was also found in the corrosion products over the defects for both modified coatings (Figure 5.15a, and b). The presence of carbon supports the presence of THEEDA and/or polyolefin base coating over the defect. The elemental distribution suggests the participation of cerium containing species in the protective layers formed over the defect in the presence of ceria NPs, i.e., the presence of a corrosion healing mechanism conferred by the presence of ceria NPs.

To summarize, the study of the corrosion products over the defects using micro-FTIR and EDS revealed that the corrosion inhibition provided by ceria NPs and THEEDA suppresses corrosion activity over the bare steel in contact with electrolyte. In such a condition, the polyolefin, due to its intrinsic self-healing ability, can help to close the defects [19]. However, this inherent self-healing ability, by itself, under the conditions tested in this work was not able to suppress completely the corrosion activity detected in the defect made in the reference coating exposed to NaCl solution.

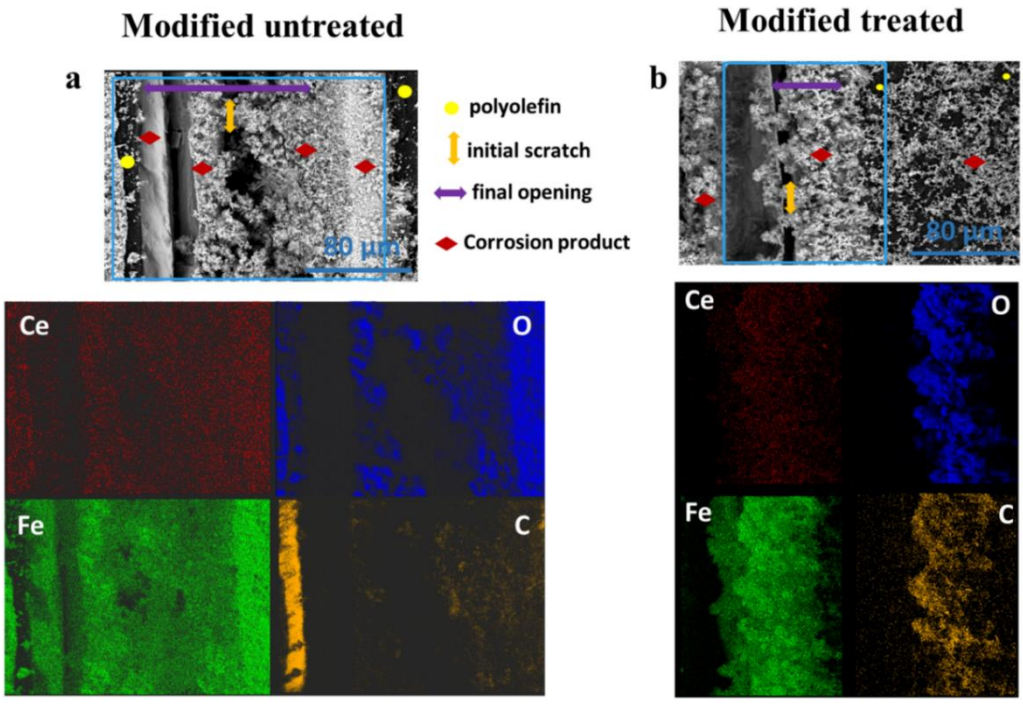

Figure 5.15 EDS maps obtained at the artificial defect made on the a) modified untreated, and b) modified treated coating, after 48 h of immersion in 0.05 M NaCl solution.

5.3 Proposed mechanism

Figure 5.16 shows a schematic representation of the proposed corrosion protection mechanism conferred by the ceria NPs treated by THEEDA. As discussed in chapter 1, the general corrosion mechanism of carbon steel in aqueous NaCl environments can be divided into two separate reactions: iron dissolution (Eq. 1.1) at the anodic sites and oxygen reduction (Eq. 1.3) at the cathodic sites. The electronic structure of cerium facilitates the exchange between the two most common oxidation states (Ce^{4+}, Ce^{3}) [38,39]. According to the work of Ostwald and Freundlich [40], it is assumed that when the particles size reduces to several nanometers, their solubility increases significantly,

enabling the release of cerium cations. Moreover, ceria NPs in acidic medium (pH < 5) become unstable, dissolve, and cerium cations can be formed [41,42]. In the coating modified with untreated ceria NPs, upon corrosion onset at the anodic sites, where iron dissolution takes place (Eq. 1.1) acidification may occur due to hydrolysis of iron cations. Depending on the concentration of Fe cations, the pH may fall down to values below 3. In such acidic conditions cerium cations are easily formed. These cerium cations preferentially formed at the anodic sites combine with OH^- ions produced at the cathodic sites (Eq. 1.3), forming stable and insoluble cerium hydroxides that are a well-known cathodic inhibitor [8,10].

The formation of these insoluble cerium species can protect micro-cathodes, suppressing the corrosion activity [14]. These insoluble species can only form when and where a sufficient concentration of OH^- is available [10,43], which can justify the gradual increase in the admittance values (observed in LEIS experiment) over the defect in the coatings modified with ceria untreated NPs until 27 h, following by fluctuations of these values until 48 h (Figure 5.10j). In fact, an initial stage of corrosion might be necessary to induce sufficient acidification at the anodic sites to activate the corrosion inhibition effect of the ceria NPs. The EDS maps over the defect in the coating modified with ceria untreated NPs, also confirmed the presence of both cerium and oxygen (Figure 5.15a).

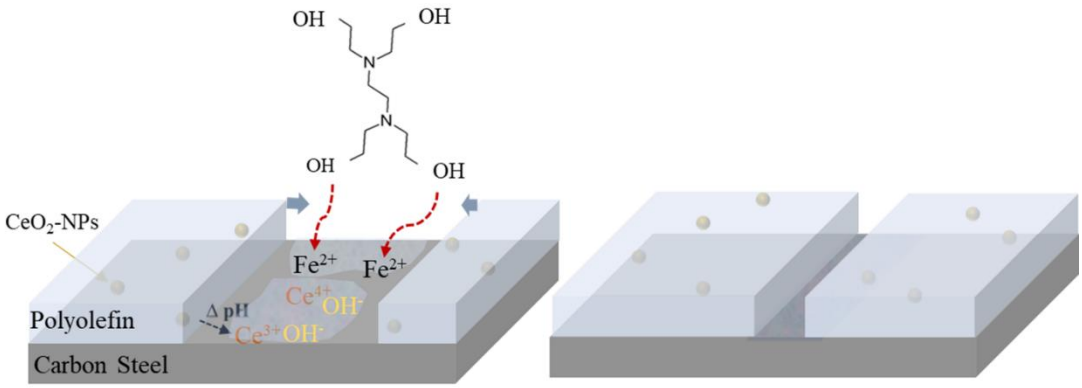

Figure 5.16 Proposed mechanism of protection conferred by ceria NPs treated with THEEDA to carbon steel.

For coatings modified with CeO_2 NPs treated with corrosion inhibitor, two different mechanisms may participate synergistically in corrosion protection. THEEDA contains hydroxyl and amine groups that act as nucleophilic agents and easily react with iron [16]. The lone pair of electrons of hydroxyl and amine groups donate to the vacant d-orbital of

iron atoms and forms coordinated covalent bonds, together with a protective complex layer that hinders the access of aggressive species to the exposed steel surface [16]. Ceria NPs, and in general cerium containing inhibitors typically act with some delay, after a stage of corrosion onset (necessary to produce hydroxyl ions) [44,45] and subsequent formation of protective species at the cathodic sites. Thus, the successful suppression of corrosion activity by treated ceria NPs involves at initial stages the formation of protective layers of inhibitor at the anodic sites. However, this layer is uneven [15] and not fully protective, allowing weak localized corrosion activity and anodic acidification that induces dissolution of the CeO_2 NPs and later precipitation of cerium compounds at the cathodic sites. Simultaneously, the inhibitor released from the NPs reinforces the protective layers and over time this synergistic effect fully inhibits the corrosion activity in defects formed in the coating modified with inhibitor treated NPs.

5.4 Conclusion

In this chapter, CeO_2 NPs treated by THEEDA are proposed as an effective corrosion inhibitor additive to improve the corrosion protection properties of polyolefin coatings applied on carbon steel.

Modified coatings, containing 5 wt% of NPs treated with THEEDA, showed improved barrier properties and increased pore resistances compared to reference coatings in 0.05 M NaCl electrolyte after 125 days of immersion. The pore resistance of the modified coatings was up to four orders of magnitude higher than the reference ones, reaching values in order of 10^{13} Ω cm^2. The self-healing ability of the modified coating was proved using localized electrochemical techniques (LEIS, SVET, and fiber-optic dissolved oxygen monitoring). Results showed that untreated ceria NPs were able to reduce the corrosion activity, while NPs treated with THEEDA suppressed very effectively the corrosion activity, completely preventing the propagation of corrosion from defects. LEIS indicated a local increase of 750% in admittance over an artificial defect made in the reference coating, while the coating modified with treated ceria NPs showed an intense decrease of admittance by the end of 80 h of immersion in 0.005 M NaCl solution.

Similarly, SVET results showed negligible cathodic and/or anodic activities in defects for both modified coatings when compared to the reference coatings. Monitoring of DO also confirms the weaker depletion of DO concentration for both modified coatings,

suggesting weaker corrosion activity compared to the reference coating. The coating developed in this work is therefore highly protective and confers remarkable corrosion protection to carbon steel.

5.5 References

[1] M.F. Montemor, Functional and smart coatings for corrosion protection: A review of recent advances, Surf. Coatings Technol. 258 (2014) 17–37. https://doi.org/10.1016/j.surfcoat.2014.06.031.

[2] C. Haoyuan, W. Peng, Z. Dun, Smart anticorrosion coating based on stimuli-responsive micro/nanocontainer: a review, J. Oceanol. Limnol. 38 (2020) 1045–1063. https://doi.org/10.1007/s00343-020-0058-x.

[3] D.A. Leal, I.C. Riegel-Vidotti, M.G.S. Ferreira, C.E.B. Marino, Smart coating based on double stimuli-responsive microcapsules containing linseed oil and benzotriazole for active corrosion protection, Corros. Sci. 130 (2018) 56–63. https://doi.org/10.1016/j.corsci.2017.10.009.

[4] J. Mosa, N.C. Rosero-Navarro, M. Aparicio, Active corrosion inhibition of mild steel by environmentally-friendly Ce-doped organic-inorganic sol-gel coatings, RSC Adv. 6 (2016) 39577–39586. https://doi.org/10.1039/c5ra26094a.

[5] G. Bahlakeh, B. Ramezanzadeh, M. Ramezanzadeh, Cerium oxide nanoparticles influences on the binding and corrosion protection characteristics of a melamine-cured polyester resin on mild steel: An experimental, density functional theory and molecular dynamics simulation study, Corros. Sci. 118 (2017) 69–83. https://doi.org/10.1016/j.corsci.2017.01.021.

[6] M.F. Montemor, M.G.S. Ferreira, Analytical characterization of silane films modified with cerium activated nanoparticles and its relation with the corrosion protection of galvanised steel substrates, Prog. Org. Coatings. 63 (2008) 330–337. https://doi.org/10.1016/j.porgcoat.2007.11.008.

[7] B. Ramezanzadeh, G. Bahlakeh, M. Ramezanzadeh, Polyaniline-cerium oxide (PAni-CeO2) coated graphene oxide for enhancement of epoxy coating corrosion protection performance on mild steel, Corros. Sci. 137 (2018) 111–126. https://doi.org/10.1016/j.corsci.2018.03.038.

[8] M.F. Montemor, M.G.S. Ferreira, Cerium salt activated nanoparticles as fillers for silane films: Evaluation of the corrosion inhibition performance on galvanised steel substrates, Electrochim. Acta. 52 (2007) 6976–6987. https://doi.org/10.1016/j.electacta.2007.05.022.

[9] R. V. Lakshim, S.T. Aruna, S. Sampath, Ceria nanoparticles vis-á-vis cerium nitrate as corrosion inhibitors for silica-alumina hybrid sol-gel coating, Appl.

Surf. Sci. 393 (2017) 397–404. https://doi.org/10.1016/J.APSUSC.2016.10.035.

[10] S.V. Harb, A. Trentin, T.A.C. de Souza, M. Magnani, S.H. Pulcinelli, C.V. Santilli, P. Hammer, Effective corrosion protection by eco-friendly self-healing PMMA-cerium oxide coatings, Chem. Eng. J. 383 (2020) 123219. https://doi.org/10.1016/j.cej.2019.123219.

[11] M. Schem, T. Schmidt, J. Gerwann, M. Wittmar, M. Veith, G.E. Thompson, I.S. Molchan, T. Hashimoto, P. Skeldon, A.R. Phani, S. Santucci, M.L. Zheludkevich, CeO_2-filled sol-gel coatings for corrosion protection of AA2024-T3 aluminium alloy, Corros. Sci. 51 (2009) 2304–2315. https://doi.org/10.1016/j.corsci.2009.06.007.

[12] P. Ghahremani, A.A. Sarabi, S. Roshan, Cerium containing pH-responsive microcapsule for smart coating application: Characterization and corrosion study, Surf. Coatings Technol. 427 (2021) 127820. https://doi.org/10.1016/j.surfcoat.2021.127820.

[13] M.F. Montemor, R. Pinto, M.G.S. Ferreira, Chemical composition and corrosion protection of silane films modified with CeO_2 nanoparticles, Electrochim. Acta. 54 (2009) 5179–5189. https://doi.org/10.1016/j.electacta.2009.01.053.

[14] M. Gobara, A. Baraka, R. Akid, M. Zorainy, Corrosion protection mechanism of Ce4+/organic inhibitor for AA2024 in 3.5% NaCl, RSC Adv. 10 (2020) 2227–2240. https://doi.org/10.1039/c9ra09552g.

[15] M. Forsyth, M. Seter, B. Hinton, G. Deacon, P. Junk, New “Green” Corrosion Inhibitors Based on Rare Earth Compounds, Aust.J.Chem. 64 (2011) 812–819. https://doi.org/10.1071/CH11092.

[16] H.S. Ryu, J.K. Singh, H.M. Yang, H.S. Lee, M.A. Ismail, Evaluation of corrosion resistance properties of N, N′-Dimethyl ethanolamine corrosion inhibitor in saturated Ca(OH)2 solution with different concentrations of chloride ions by electrochemical experiments, Constr. Build. Mater. 114 (2016) 223–231. https://doi.org/10.1016/j.conbuildmat.2016.03.174.

[17] J.F.F. Doddema, H.H. Vugteveen, New Pipeline Coating Systems - Putting an End to Coating Degradation, 7th Pipeline Technol. Conf. (2012).

[18] G. Zanchin, G. Leone, Polyolefin thermoplastic elastomers from polymerization catalysis: Advantages, pitfalls and future challenges, Prog. Polym. Sci. 113 (2021) 101342. https://doi.org/10.1016/j.progpolymsci.2020.101342.

[19] R. Raj, M.G. Taryba, Y. Morozov, R. Kahraman, R.A. Shakoor, M.F. Montemor,

On the synergistic corrosion inhibition and polymer healing effect of polyolefin coatings modified with Ce-loaded hydroxyapatite particles on steel, Electrochim. Acta. 388 (2021) 138648. https://doi.org/10.1016/j.electacta.2021.138648.

[20] H.I. Chen, H.Y. Chang, Homogeneous precipitation of cerium dioxide nanoparticles in alcohol/water mixed solvents, Colloids Surf. A. 242 (2004) 61–69. https://doi.org/10.1016/j.colsurfa.2004.04.056.

[21] D. Avram, C. Rotaru, B. Cojocaru, M. Sanchez-Dominiguez, M. Florea, C. Tiseanu, Heavily impregnated ceria nanoparticles with europium oxide: Spectroscopic evidences for homogenous solid solutions and intrinsic structure of Eu^{3+}-oxygen environments, J. Mater. Sci. 49 (2014) 2117–2126. https://doi.org/10.1007/s10853-013-7904-6.

[22] J. Cui, G.A. Hope, Raman and Fluroescence Spectroscopy of Ceo2, Er2O3, Nd_2O_3, Tm_2O_3, Yb_2O_3, La_2O_3, and Tb_4O_7, J. Spectrosc. 2015 (2015) 940172. https://doi.org/10.1155/2015/940172.

[23] E. Sartoretti, C. Novara, F. Giorgis, M. Piumetti, S. Bensaid, N. Russo, D. Fino, In situ Raman analyses of the soot oxidation reaction over nanostructured ceria-based catalysts, Sci. Rep. 9 (2019) 9–13. https://doi.org/10.1038/s41598-019-39105-5.

[24] S. Loridant, Raman spectroscopy as a powerful tool to characterize ceria-based catalysts, Catal. Today. 373 (2021) 99-111. https://doi.org/10.1016/j.cattod.2020.03.044.

[25] B. Reddy, M, G. Thrimurthulu, P. Saikia, P. Bharali, Silica supported ceria and ceria -zirconia nanocomposite oxide for selective dehydration of 4-methylpentan-2-ol, J. Mol. Catal. A Chem. 275 (2007) 167–173. https://doi.org/10.1016/j.molecata.2007.05.037.

[26] G. Wang, Q. Mu, T. Chen, Y. Wang, Synthesis, characterization and photoluminescence of CeO2 nanoparticles by a facile method at room temperature, J. Alloys Compd. 493 (2010) 202–207. https://doi.org/10.1016/j.jallcom.2009.12.053.

[27] W. Du, X. Wang, G. Chen, J. Zhang, M. Slaný, Synthesis, property and mechanism analysis of a novel polyhydroxy organic amine shale hydration inhibitor, Minerals. 10 (2020) 1–13. https://doi.org/10.3390/min10020128.

[28] B. Samai, S. Sarkar, S. Chall, S. Rakshit, S.C. Bhattacharya, Polymer-fabricated synthesis of cerium oxide nanoparticles and applications as a green catalyst

towards multicomponent transformation with size-dependent activity studies, CrystEngComm. 18 (2016) 7873–7882. https://doi.org/10.1039/c6ce01104g.

[29] P. Periyat, F. Laffir, S.A.M. Tofail, E. Magner, A facil aqueous sol-gel method for high surface area nanocrystalin CeO_2, RSC Adv. 1 (2011) 1794–1798. https://doi.org/10.1039/c1ra00524c.

[30] Z. Diaconeasa, L. Barbu-tudoran, C. Coman, A. Mesaros, O. Pop, D. Rugina, R. Stefan, F. Tabaran, S. Tripon, C. Socaciu, Cerium Oxide Nanoparticles and Its Cytotoxicity Human Lung Cancer Cells, Rom. Biotechnol. Lett. 20 (2015) 10679–10687.

[31] Y. Morozov, L.M. Calado, R.A. Shakoor, R. Raj, R. Kahraman, M.G. Taryba, epoxy coatings modified with a new cerium phosphate inhibitor for smart corrosion protection of steel, (2019) 108–128. https://doi.org/10.1016/j.corsci.2019.108128.

[32] ASTM, Standard Test Methods for Measuring Adhesion by Tape Test D3359-09, (2009) 1–8. https://doi.org/10.1520/D3359-09E02.2.

[33] M.P. Desimone, G. Grundmeier, G. Gordillo, S.N. Simison, Amphiphilic amido-amine as an effective corrosion inhibitor for mild steel exposed to CO_2 saturated solution: Polarization, EIS and PM-IRRAS studies, Electrochim. Acta. 56 (2011) 2990–2998. https://doi.org/10.1016/j.electacta.2011.01.009.

[34] H. Hajfarajollah, S. Mehvari, M. Habibian, B. Mokhtarani, K.A. Noghabi, Rhamnolipid biosurfactant adsorption on a plasma-treated polypropylene surface to induce antimicrobial and antiadhesive properties, RSC Adv. 5 (2015) 33089–33097. https://doi.org/10.1039/c5ra01233c.

[35] T.A. Nguyen, Ø.W. Gregersen, F. Männle, Thermal oxidation of polyolefins by mild pro-oxidant additives based on iron carboxylates and lipophilic amines: Degradability in the absence of light and effect on the adhesion to paperboard, Polymers (Basel). 7 (2015) 1522–1540. https://doi.org/10.3390/polym7081468.

[36] H. Inan, E. Alaydin, Phosphate and nitrogen removal by iron produced in electrocoagulation reactor, Desalin. Water Treat. 52 (2014) 1396–1403. https://doi.org/10.1080/19443994.2013.787950.

[37] S. Musić, I. Nowik, M. Ristić, Z. Orehovec, S. Popović, The effect of bicarbonate/carbonate ions on the formation of iron rust, Croat. Chem. Acta. 77 (2004) 141–151, https://hrcak.srce.hr/102658.

[38] J. Seo, J. Moon, J.H. Kim, K. Lee, J. Hwang, H. Yoon, D.K. Yi, U. Paik, Role of

the oxidation state of cerium on the ceria surfaces for silicate adsorption, Appl. Surf. Sci. 389 (2016) 311–315. https://doi.org/10.1016/j.apsusc.2016.06.193.

[39] D.R. Mullins, The surface chemistry of cerium oxide, Surf. Sci. Rep. 70 (2015) 42–85. https://doi.org/10.1016/j.surfrep.2014.12.001.

[40] D.R. Ely, R. Edwin García, M. Thommes, Ostwald-Freundlich diffusion-limited dissolution kinetics of nanoparticles, Powder Technol. 257 (2014) 120–123. https://doi.org/10.1016/j.powtec.2014.01.095.

[41] T. V. Plakhova, A.Y. Romanchuk, S.N. Yakunin, T. Dumas, S. Demir, S. Wang, S.G. Minasian, D.K. Shuh, T. Tyliszczak, A.A. Shiryaev, A. V. Egorov, V.K. Ivanov, S.N. Kalmykov, Solubility of nanocrystalline cerium dioxide: Experimental data and thermodynamic modeling, J. Phys. Chem. C. 120 (2016) 22615–22626. https://doi.org/10.1021/acs.jpcc.6b05650.

[42] P. Yu, S.A. Hayes, T.J. O'Keefe, M.J. O'Keefe, J.O. Stoffer, The Phase Stability of Cerium Species in Aqueous Systems, J. Electrochem. Soc. 153 (2006) C74. https://doi.org/10.1149/1.2130572.

[43] Montemor, M. F., Snihirova, D., Taryba, M. G., Lamaka, S.V., Kartsonakis, I.A., A.C. Balaskas, Kordas, G., Tedim, J, A. Kuznetsova, M.L. Zheludkevich, M.G.S. Ferreira, Evaluation of self-healing ability in protective coatings modified with combination of layered double hydroxides and cerium molibdate nanocontainers filled with corrosion inhibitors, Electrochim. Acta. 60 (2012) 31–40. https://doi.org/10.1016/j.electacta.2011.10.078.

[44] T. Markley, M Forsyth, B. Hinton, Multifunctional rare earth organic corrosion inhibitors, M. Forsyth, B. Hinton (Eds)., Rare Earth-based Corrosion Inhibitors, Woodhead Publishing Limited, (2014) 117-142. https://doi.org/10.1533/9780857093585.117.

[45] K.A. Yasakau, M.L. Zheludkevich, S. V. Lamaka, M.G.S. Ferreira, Mechanism of corrosion inhibition of AA2024 by rare-earth compounds, J. Phys. Chem. B. 110 (2006) 5515–5528. https://doi.org/10.1021/jp0560664.

Chapter 6

Summary and Outlook

6.1 Summary

In recent years, the concept of smart, self-healing coatings has attracted increasing interest. As an efficient anticorrosion strategy, self-healing coatings offer active, autonomous self-healing to the organic coatings [1–4]. These coatings can respond to certain stimuli, releasing appropriate healing agents, e.g., self-healing monomers or corrosion inhibitors, only when necessary [3,5–7].

During this PhD Thesis, various combination[12] of self-healing strategies were modeled to develop a highly protective and highly stable self-healing system beyond state of the art. Figure 6.1 shows three strategies that were selected to accomplish the main aims defined for this work.

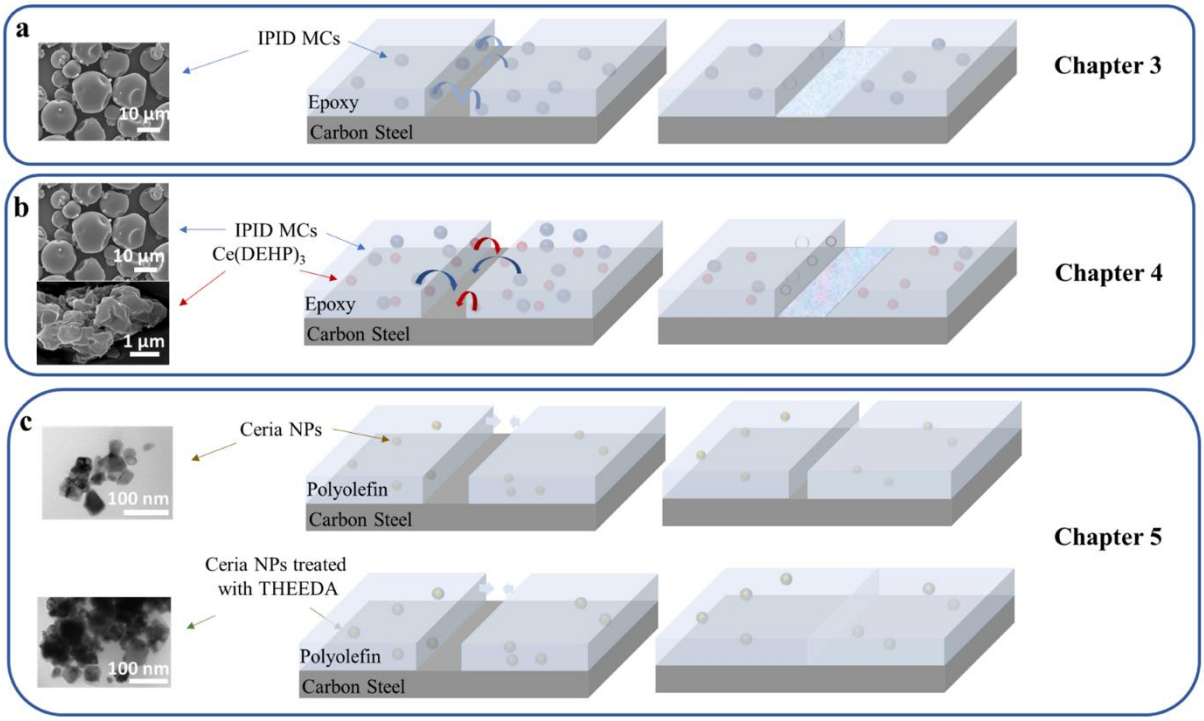

Figure 6.1 Schematic overview of modeled self-healing coatings presented in three chapters of this PhD Thesis.

In chapter 1, the literature was intensively explored and the most important efforts to develop self-healing systems for steel corrosion protection were identified [8–14].

12 In the framework of this Thesis, two more self-healing systems were developed. To keep this Thesis short, and due to lack of time, these works didn't add to the structure of this document. However, some preliminary reports regarding these two systems were reported in Appendix 3.

The literature review was started from pioneer works [8,9] and the most effective approaches were discussed. A critical review of the most relevant works regarding self-healing of polymeric matrices, revealed three main gaps in the state of the art: i) lack of global protection properties of modified organic coatings due to addition of relatively large MCs, or due to ii) addition of a high percentage of MCs into the coating, and iii) creation of new defects due to addition of these large MCs. Probably for these reasons, in most publications, the global protection properties of coatings modified with MCs, have not been reported [8,15–17]. Therefore, the first part of this PhD work was dedicated to find a solution for these issues. Based on the knowledge, was obtained during previous works[13] [18–20], small and highly efficient MCs were successfully produced. The polymeric shell MCs (DETA MCs), with high thermal and chemical resistance and a high (76%) encapsulation efficiency, were added to the epoxy coating formulation to impart self-healing ability. Figure 6.2 compares the properties of the first self-healing system developed during this PhD work, reported in chapter 3, with the most important self-healing systems based on isocyanate MCs. These systems were reported in chapter 1- Table 1.4- page 25, which were denominated as MC1 to MC7.

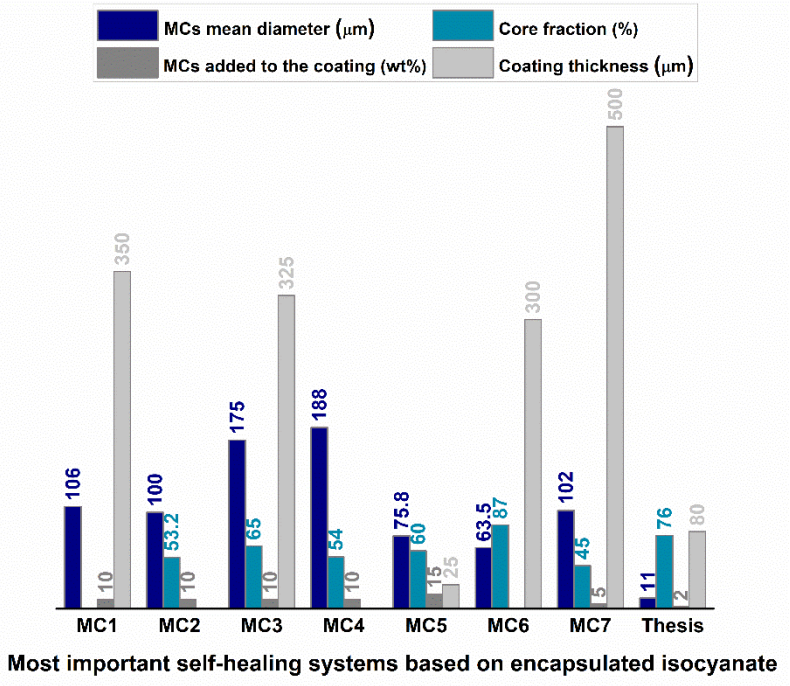

Figure 6.2 Comparison of most important self-healing systems, based on isocyanate MCs with the self-healing system reported in chapter 3.

13 These works were performed in the framework of Eco-bond project, in CERENA group, at Technology Platform on Microencapsulation and Immobilization, and were co-authored by the author of this Thesis.

From this overview it is possible to conclude: i) the core fraction of IPDI-MCs synthesized in the framework of this Thesis is comparable to the system MC3 and MC6, with mean diameter of 175 µm and 63.5 µm respectively, while mean diameter of the MCs synthesized in this work was 11 µm; ii) due to small size of MCs, development of relatively thin coating with high global protection properties (evidenced by EIS), and promising self-healing ability (evidenced by localized techniques) was possible; iii) due to the high efficiency of synthesized MCs; even incorporation of relatively low percentages of MCs (2-3 wt%), provided appropriate quantity of IPDI to impart efficient self-healing into the epoxy coating. As mentioned before, in most of systems reported in Figure 6.2, self-healing properties were evaluated by salt spray tests on artificially scratched coatings, therefore, numerical data was not available to compare quantitatively the newly developed system with those reported systems.

However, the quantitative comparison of systems developed in this PhD work, with those reported in chapter 1- Table 1.5 – page 42 is possible. To do so, first the quantitative comparison of three self-healing coatings developed in this work was conducted. For the system reported in chapter 3, EIS confirmed an important healing ability of the modified coating when applied on carbon steel. The evolution of the ratio between the initial impedance value at low frequency ($|Z|_{LF\ (0)}$) and the same value measured over the immersion time ($|Z|_{LF(t)}$) in percentage ($Z_R = \frac{|Z|_{LF(t)}}{|Z|_{LF(0)}} \times 100$) is considered a reliable parameter to estimate the global protection properties of coating. This ratio, when above 100 %, evidences an improvement of the global protection properties of coating, while below 100 % shows the deterioration of this property. Contrarily to what has been reported in literature so far, results revealed a positive effect in the global protection properties of modified coatings, when MCs are present. As shown in Figure 6.3, for the reference coating the ratio decreases from 100 % to 30 % after 100 days of immersion, but Z_R shows a tremendous increase, from 100 to more than 740 % in the coating modified with 2 wt% of MCs. Therefore, these small, highly efficient, and chemically stable MCs, when added (in small quantity) to the epoxy matrix, not only impart the healing ability (confirmed by LEIS) into the matrix, but also improve the global protection properties of the coating. Therefore, the limitation addressed before (the deterioration of global protection properties of coatings due to addition of MC), was successfully resolved.

Figure 6.3 shows Z_R values for two more coatings: one modified with 1 wt% of $Ce(DEHP)_3$ (modified-Ce-1-wt%), and another modified simultaneously with

$Ce(DEHP)_3$ and DETA-MCs (modified-MC-3-wt%-Ce-1-wt%) (both represented in chapter 4). For modified-Ce-1-wt% Z_R values decrease from 100 % to 14 % after 100 days of immersion. For the modified-MC-3-wt%-Ce-1-wt% Z_R values decreased to 62 % after 100 days of immersion NaCl solution. Although, this decreasing trend is a normal consequence of electrolyte uptake in organic coatings, the positive effect of MCs in stabilizing the global protection properties of the epoxy-based coating, can be well observed (comparing these two modified coatings).

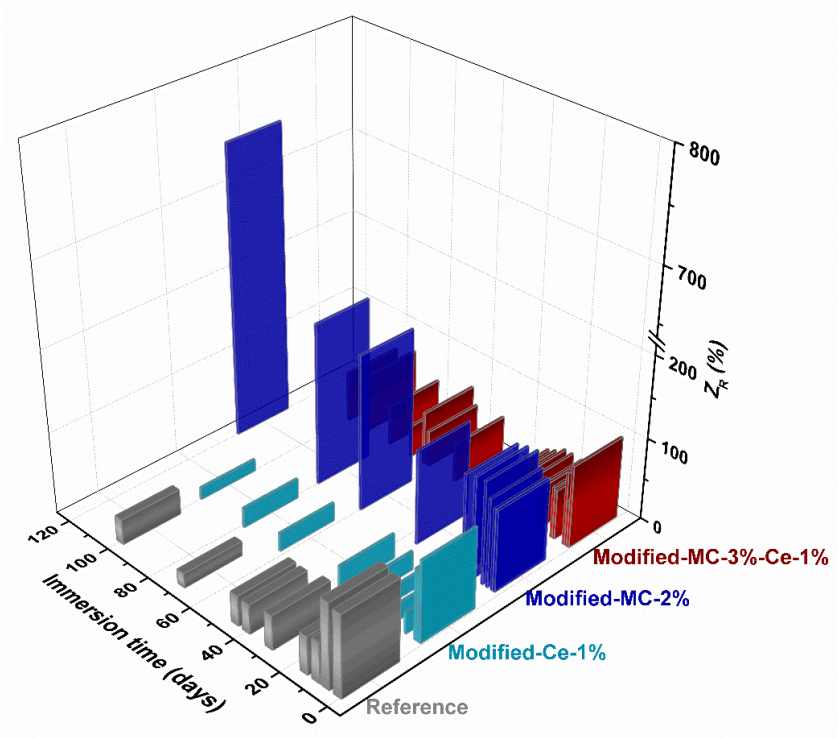

Figure 6.3 Evolution of ratio between initial low frequency impedance and the low frequency impedance measured at the certain time for reference, modified-Ce-1 wt%, modified-MC-2 wt%, and modified MC-3-wt%-Ce-wt% coatings.

As mentioned in Chapter 2, Gray et al. summarised the information extracted from literature on EIS carried out on laboratory and fieldwork in a simple graph (chapter 2-Figure 2.3) [21], which gives a comprehensive insight into the overall protection properties of an organic coating. Therefore, comparison of the systems developed in this Thesis with the pattern provided by Gray et al. clearly evidences the contribution of this Thesis to the state of the art.

To do so, impedance values at low frequency ($|Z|_{LF}$) obtained after approximately four months (100-120 days) of immersion for reference, modified-Ce-1-wt%, modified-MC-2-wt%, and modified-MC-3-wt%-Ce-1-wt% coatings (most promising epoxy-based

coatings developed in this PhD work) were normalized according to the coating thickness. The normalized impedance values were, respectively $4.9 \times 10^8\ \Omega\ cm^2$, $8.7 \times 10^9\ \Omega\ cm^2$, $1.0 \times 10^{10}\ \Omega\ cm^2$, and $7.06 \times 10^{10}\ \Omega\ cm^2$. These values, are illustrated by colored triangles in Figure 6.4 and prove the superior barrier property of all modified coatings, compared to reference ones, even after long time immersion in NaCl solutions.

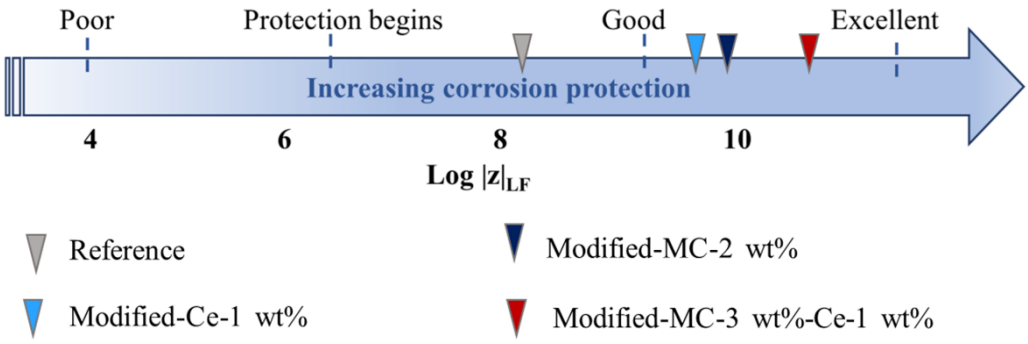

Figure 6.4 Log $|Z|_{LF}$ for epoxy-based coatings, developed in this work, after approximately four months immersion in 0.05 M NaCl solution.

Figure 6.5 shows the evolution of Z_R values for polyolefin-based coatings reported in Chapter 5. For the reference polyolefin coating, Z_R values decreased from 100 % to 3 % after 125 days of immersion. For the coating modified with 5 wt% of blank CeO_2 (modified-untreated-5 %), Z_R values decreased to 68 % of initial value after 125 days of immersion in saline solution. Finally, Z_R for coatings modified with 5 wt% of CeO_2 treated with THEEDA organic inhibitor achieved 73 % of its initial value after 125 days. These results evidence that the incorporation of metal oxides into the polymeric matrix, act as a filler and can physically control the diffusion of corrosive ions by creating a longer diffusion path, as reported elsewhere [22].

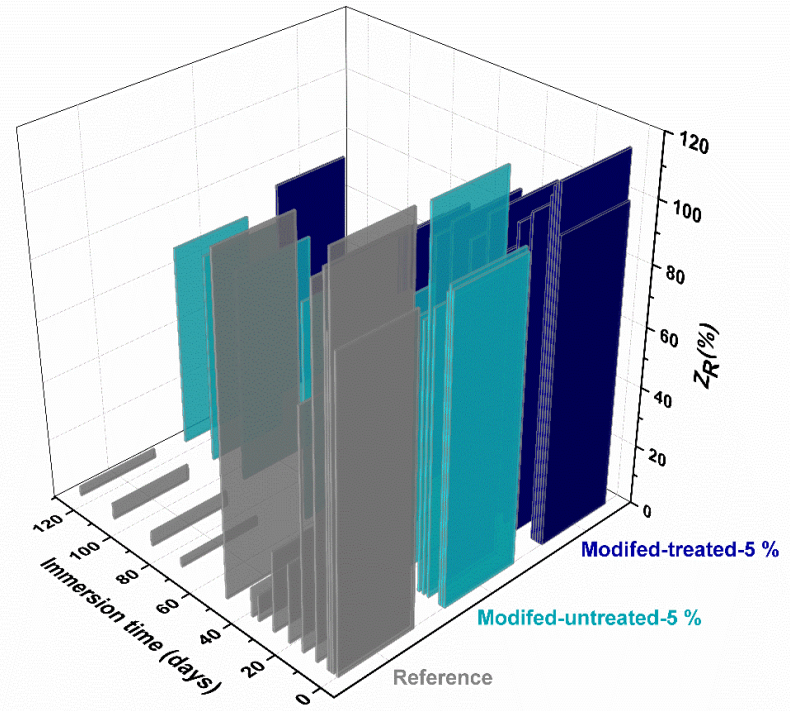

Figure 6.5 Evolution of ratio between initial low frequency impedance and the low frequency impedance measured at the certain time for polyolefin-based reference, modified-untreated-5 wt%, and modified-treated-5 wt%.

The $|Z|_{LF}$ values for reference, modified-untreated-5 wt%, and modified-treated-5 wt%, coatings after more than four months of immersion in 0.05 NaCl solution, were 1.16 × 10^{10} Ω cm^2, 5.2 × 10^{11} Ω cm^2, and 7.6 × 10^{11} Ω cm^2 respectively. These values are illustrated by colored triangles in Figure 6.6 and demonstrate the superior barrier property of both modified coatings, compared to reference ones. Now let´s compare these three systems with the most relevant work regarding the application of pH response carriers for smarter, self-healing coatings on steel, reported in Table 1.5.

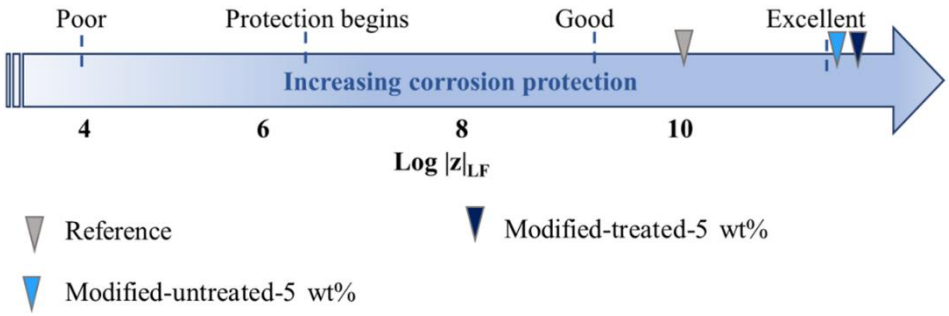

Figure 6.6 Log $|Z|_{LF}$ for polyolefin-based self-healing coatings, developed in this work, after approximately four months immersion in 0.05 M NaCl solution.

These systems were denominated as S1 to S25. A comprehensive comparison of those systems with the ones developed in this Thesis was reported in Appendix 1- Table A 1.12 – page 230. In that table $|Z|_{LF}$ values at the beginning and end of immersion were reported for each system. Moreover, to gain better insight on self-healing performance of the modified coatings, the low-frequency impedance moduli ($|Z|_{LF(modified)}$) at the end of immersion time, was compared with the same value for the reference coating ($|Z|_{LF(reference)}$) of each system ($\frac{|Z|_{LF\ (modified)}}{|Z|_{LF\ (reference)}}$). Figure 6.7 compares graphically, $|Z|_{LF}$ for the three systems developed in this Thesis, with the values of those systems reported in chapter 1- Table 1.5[14] (all $|Z|_{LF}$ values were normalized based on coating thickness).

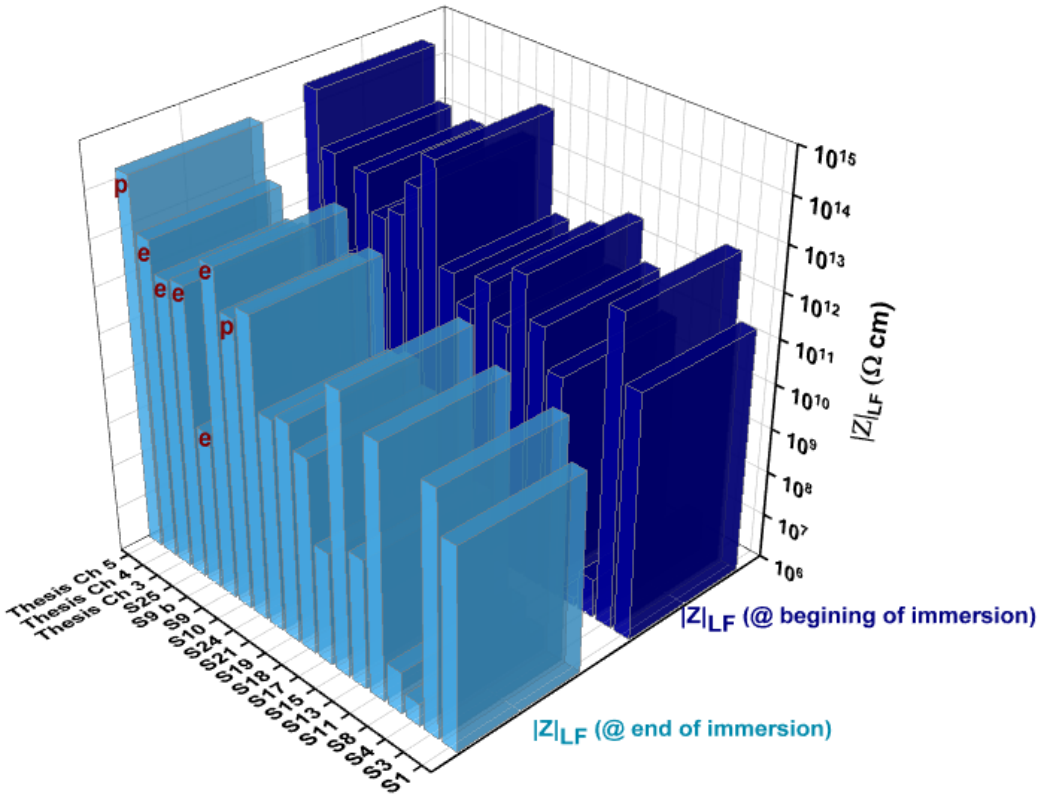

Figure 6.7 Comparison of low frequency impedance moduli mesured at the beginning, and at the end of immersion time, between systems developed in this Thesis and most relevant works reported in chapter 1 - Table 1.5. Letter (e), and (p) stand for epoxy-based and polyolefin-based coatings respectively.

14 As most of the time several systems were reported in one scientific article, the best result reported in each article, or the most similar system comparing to the systems reported in this Thesis were reported in both Figure 6.7 and Table A 1.12.

To date, the polyolefin-based coating modified with treated CeO_2-NPs developed in this work is the most promising self-healing system developed. Moreover, comparing $|Z|_{LF}$ values of reference and modified coatings at the end of immersion time ($\frac{|Z|_{LF\ (modified)}}{|Z|_{LF\ (reference)}}$), revealed 60% of improvement in the global protection properties (Appendix 1 – Table A 1.12). For the system denominated as S10 (the only polyolefin-based coating, with the same commercial polyolefin coating used in this Thesis - both marked with letter "p" in Figure 6.7), $|Z|_{LF}$ values were more than two orders of magnitude lower in comparison to the system reported in chapter 5. In S10 system, improvement of global protection properties ($\frac{|Z|_{LF\ (modified)}}{|Z|_{LF\ (reference)}}$) was about 11%.

The best epoxy system reported in this Thesis in chapter 4, also shows promising results when compared with similar systems (all marked with letter "e" in Figure 6.7). Regarding the self-healing system reported in chapter 3, even though IPDI-MCs, only target the epoxy matrix, the global protection properties of this system, are still comparable to those containing pH responsive particles, evidencing the excellent capacity of MCs in repairing the epoxy matrix.

To conclude, this PhD work goes beyond the state of the art by evidencing the high capability of IPDI-MCs to improve the global protection properties of commercial epoxy coatings. Moreover, these MCs, also impart self-healing ability to the commercial epoxy coating, which is a critical advantage that must be considered for the implementation of this solution. Therefore, synthesizing small, highly efficient, chemically stable, and long-shelf life IPDI MC and developing self-healing epoxy contributed to the current state of the art. Further improvement of the protective coating functionality was carried out with the addition of $Ce(DEHP)_3$, a corrosion inhibitor which is pH responsive. This smart coating offers excellent perspectives as primer for pipping structures.

This PhD work also reveals the efficiency of CeO_2 NPs, in improving both global protection properties and the self-healing ability of commercial polyolefin coatings. These properties enhanced drastically when CeO_2 NPs were treated with THEEDA, an organic corrosion inhibitor. To the best of the author's knowledge, this part of work is the first report related to the application of CeO_2 NPs in polyolefin coatings and is the first study on the use of THEEDA as a corrosion inhibitor in combination with CeO_2. The contribution of this smart coating to the current state of the art can be extremely impactful due to the excellent protection properties of the modified polyolefin-based coating.

6.2 Outlook

In this PhD work the ability of IPDI-MCs as promising carriers to offer self-healing ability to the commercial epoxy coating was validated using various characterization techniques. Also, the monitoring of all parameters involved in the synthesis of MCs was carried out. Later, MCs´ fabrication was scaled up. In this stage, around 5 % of produced MCs, showed lower shelf life. Although 5 % is not significant, further investigation is suggested, to optimize the scale-up parameters or to find the reason of this issue, which may improve our knowledge in microencapsulation of isocyanate.

Regarding the coatings modified with addition of Ce-based particles (CeO_2 NPs and $Ce(DEHP)_3$), pH-dependent release mechanism was proved indirectly. However, from the author's point of view, other characterization techniques, e.g., UV-Vis spectroscopy, may be employed to better establish the pH-dependent release mechanisms.

Additional surface characterization, such as Raman Spectroscopy and X-ray Photoelectron Spectroscopy (XPS), can assist in determining the exact composition of the corrosion products and protective layers formed over the artificially made defect. These further analyses can offer more precise knowledge to the current state of the art and are complementary to the findings reported in this PhD work.

Further evaluation of newly developed systems by localized techniques is suggested to gain insight on probability of repeated healing at the same location, specifically for pH sensitive release systems.

Moreover, investigating the effect of size/geometry of defects on self-healing performance of developed systems, provides valuable information on the capacity of each system for autonomously heal the defects.

To validate the performance of newly developed coatings, preparation of standard samples to perform salt spray test, and field test is necessary. It is worth mentioning that, for the part of the work presented in chapters 3 and 4, relatively large samples were prepared, and field tests were performed at the site of the end user in Qatar. As it was expected the system modified with addition of both DETA MCs, and $Ce(DEHP)_3$ was the most promising system among the epoxy-based coatings. However, salt spray test and field test for polyolefin-based system were interrupted due to pandemic situation. Therefore, these tests can be considered as a future work.

Evaluation of mechanical properties of developed coating also need to be performed in the future. The above referred tests will complement the wide variety of testing carried out and reported in this Thesis, with the final goal of validating this new technology.

6.3 References

[1] L.M. Muresan, Self-Healing Coatings for Corrosion Protection of Steel, in: M.A.S.H. Hosseini M. (Ed.), Industerial Appl. Intell. Polym. Coatings, Springer, Cham, 2016: pp. 479–492. https://doi.org/10.1007/978-3-319-26893-4_22.

[2] L.M. Muresan, Chapter 22 Self-Healing Coatings for Corrosion Protection of Steel, in: M. Hosseini, A.S. Makhlouf (Eds.), Industerial Appl. Intell. Polym. Coatings, Springer International Publishing Switzerland, 2016: pp. 479–492. https://doi.org/10.1007/978-3-319-26893-4_22.

[3] M.F. Montemor, Functional and smart coatings for corrosion protection: A review of recent advances, Surf. Coatings Technol. 258 (2014) 17–37. https://doi.org/10.1016/j.surfcoat.2014.06.031.

[4] D.G. Bekas, K. Tsirka, D. Baltzis, A.S. Paipetis, Self-healing materials: A review of advanced in materials, evaluation, characterization and monitoring techniques, Compos. Part B. 87 (2016) 92–119. https://doi.org/10.1016/j.compositesb.2015.09057.

[5] D. Grigoriev, E. Shchukina, D.G. Shchukin, Nanocontainers for Self-Healing Coatings, Adv. Mater. Interfaces. 4 (2017) 1600318. https://doi.org/10.1002/admi.201600318.

[6] S.B. Ulaeto, R. Rajan, J.K. Pancrecious, T.P.D. Rajan, B.C. Pai, Developments in smart anticorrosive coatings with multifunctional characteristics, Prog. Org. Coatings. 111 (2017) 294–314. https://doi.org/10.1016/j.porgcoat.2017.06.013.

[7] A. Stankiewicz, M.B. Barker, Development of self-healing coatings for corrosion protection on metallic structures, Smart Mater. Struct. 25 (2016) 084013. https://doi.org/10.1088/0964-1726/25/8/084013.

[8] S.R. White, N. Scottos, P. Geubelle, J.S. Moore, M.R. Kessler, S. Sriram, E.N. Brown, S. Viswanathan, Autonomic healing of polymer composites, Lett. to Nat. 409 (2001) 794-797.

[9] E.N. Brown, N.R. Sottos, S.R. White, Fracture testing of a self-healing polymer composite, Exp. Mech. 42 (2002) 372–379. https://doi.org/10.1177/001448502321548193.

[10] S.H. Cho, S.R. White, P. V. Braun, Self-healing polymer coatings, Adv. Mater. 21 (2009) 645–649. https://doi.org/10.1002/adma.200802008.

[11] J. Yang, M.W. Keller, J.S. Moore, N.R. Sottos, S.R. White, Microencapsulation

of Isocyanates for Self-Healing Polymers, Macromolecules. 41 (2008) 9650–9655. https://doi.org/10.1021/ma801718v.

[12] P.D. Tatiya, R.K. Hedaoo, P.P. Mahulikar, V. V. Gite, Novel polyurea microcapsules using dendritic functional monomer: Synthesis, characterization, and its use in self-healing and anticorrosive polyurethane coatings, Ind. Eng. Chem. Res. 52 (2013) 1562–1570. https://doi.org/10.1021/ie301813a.

[13] K. Thanawala, N. Mutneja, A.S. Khanna, R.K. Singh Raman, Development of self-healing coatings based on linseed oil as autonomous repairing agent for corrosion resistance, Materials (Basel). 7 (2014) 7324–7338. https://doi.org/10.3390/ma7117324.

[14] M. Behzadnasab, M. Esfandeh, S.M. Mirabedini, M.J. Zohuriaan-Mehr, R.R. Farnood, Preparation and characterization of linseed oil-filled urea-formaldehyde microcapsules and their effect on mechanical properties of an epoxy-based coating, Colloids Surfaces A Physicochem. Eng. Asp. 457 (2014) 16–26. https://doi.org/10.1016/j.colsurfa.2014.05.033.

[15] S. Zhang, H., Wang, J., Liu, X., Wang, Z., & Wang, High Performance Self-Healing Epoxy/Polyamide Protective Coating Containing Epoxy Microcapsules and polyanilin Nanofiber for Mild Carbon Steel, (2013) 10172–10180. https://doi.org/10.1021/ie400666a.

[16] W. Wang, L. Xu, X. Li, Y. Yang, E. An, Self-healing properties of protective coatings containing isophorone diisocyanate microcapsules on carbon steel surfaces, Corros. Sci. 80 (2014) 528–535. https://doi.org/10.1016/j.corsci.2013.11.050.

[17] S.J. García, J.M.C. Mol, A.E. Hughes, Y. González-García, P.A. White, H.R. Fischer, J. Mardel, Self-healing anticorrosive organic coating based on an encapsulated water reactive silyl ester: Synthesis and proof of concept, Prog. Org. Coatings. 70 (2011) 142–149. https://doi.org/10.1016/j.porgcoat.2010.11.021.

[18] M. Attaei, Microencapsulation of isocyanate compounds for autoreactive , monocomponent adhesive, Instituto Superior Technico Lisboa, MSc Thesis, Lisbon University, 2017.

[19] M. Attaei, M. V. Loureiro, M. Vale, J.A.D. Condeço, I. Pinho, J.C. Bordado, A.C. Marques, Isophorone diisocyanate (IPDI) microencapsulation for mono-component adhesives: Effect of the active H and NCO sources, Polymers (Basel).

10 (2018) 825. https://doi.org/10.3390/polym10080825.

[20] M.V. Loureiro, M. Attaei, S. Rocha, M. Vale, J.C. Bordado, R. Simões, I. Pinho, A.C. Marques, The role played by different active hydrogen sources in the microencapsulation of a commercial oligomeric diisocyanate, J. Mater. Sci. 55 (2020). https://doi.org/10.1007/s10853-019-04301-1.

[21] L.G.S. Gray, B.R. Appleman, EIS : Electrochemical Impedance Spectroscopy - A tool to predict remaining coating life?, J. Prot. Coatings Linings. 20 (2003) 66–74.

[22] S. Pourhashem, F. Saba, J. Duan, A. Rashidi, F. Guan, E.G. Nezhad, B. Hou, Polymer/Inorganic nanocomposite coatings with superior corrosion protection performance: A review, J. Ind. Eng. Chem. 88 (2020) 29–57. https://doi.org/10.1016/j.jiec.2020.04.029.

Appendix

Appendix 1 Supplementary information

Supplementary information of Chapter 3.

Table A 1.1 Summary of syntheses and combination of active H sources used to obtain high thermally - chemically stable, and highly efficient MCs.

Synthesis No.	Active H source	Shelf life (months)	Stability		
			Acetone	Ethanol	Hardener
SH-14, 37, 41	DETA	8.5	100	70	98
SH-20	PEI	«2	89	0	38
SH-21	Butanediol	«2	12	0	13
SH-31	PEI + HDMS	2		na	
SH-32, 43	DETA + HDMS	3		na	
SH-33, 38	HDMS	» 3	79	2	89
SH-35	PEI + n-OTES	«2		na	
SH-36, 39	n-OTES	4	80	2	88

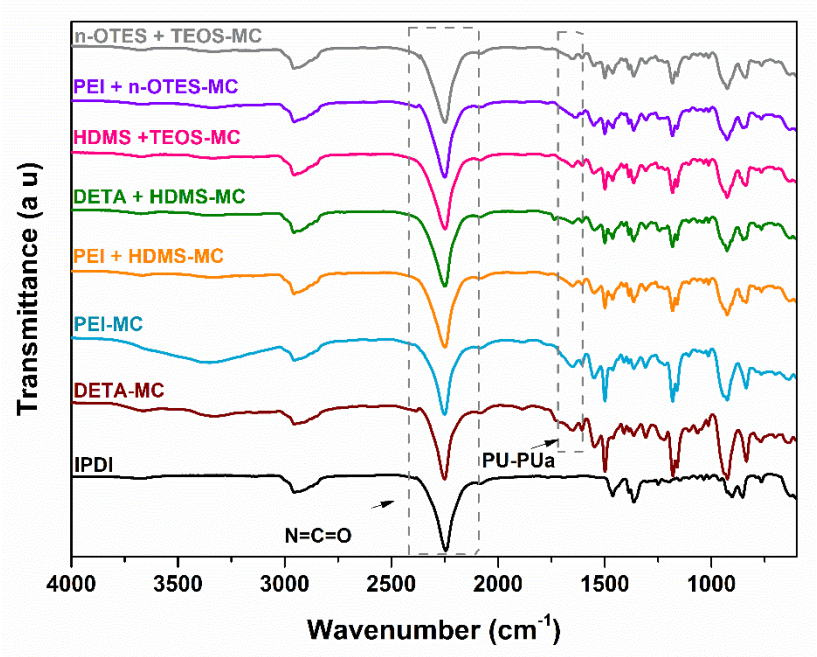

Figure A 1.1 First FTIR spectra of all MCs synthesized in the framework of this PhD work to obtain highly efficient and long shelf-life MCs (spectra were collected 3 days after synthesis).

Table A 1.2 Primary materials used for synthesizing IPDI MCs.

Material	Description	Supplier
Isophorone diisocyanate, IPDI	98 % purity	Covestro
Polyisocyanate (DRFE)	solution of tris (p-isocyanatophenyl) thiophosphate in ethyl acetate (NCO content of 7.2 ± 0.2)	Covestro
Triethoxyoctylsilane	-	Merck
Diethylenetriamine	with 99% purity	Alfa Aesar
Hexadecyltrimethoxysilane	-	Merck
Gum Arabic	-	Labchem

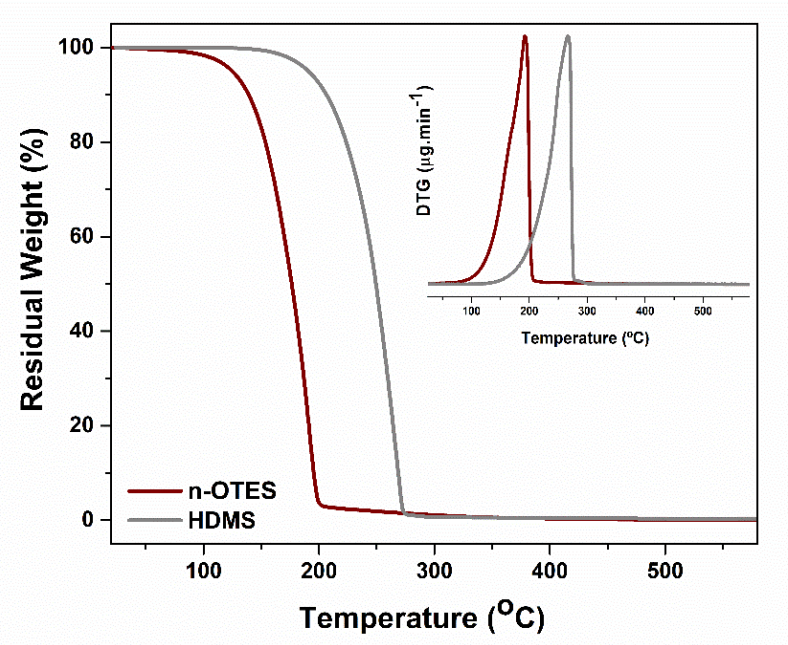

Figure A 1.2 TGA of HDMS and n-OTES. The inset shows the first derivative curves.

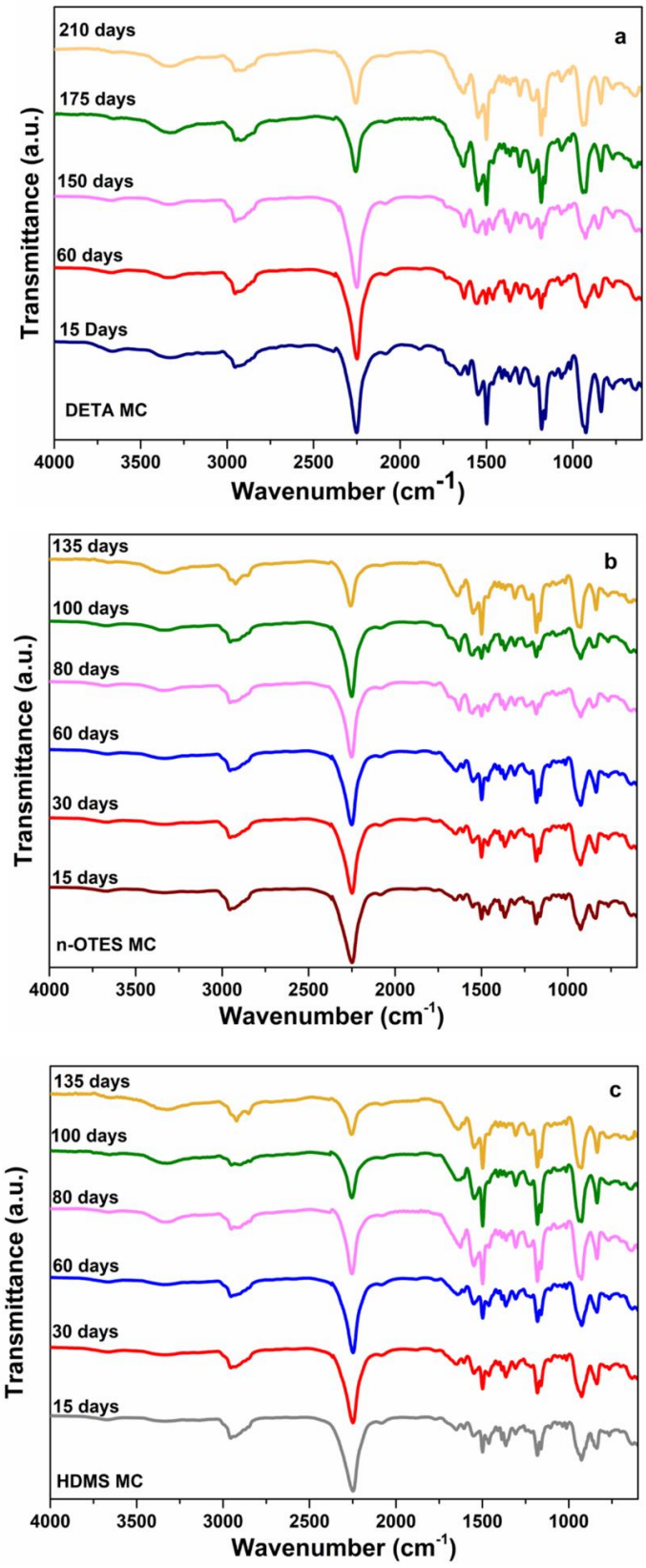

Figure A 1.3 FTIR spectra of a) DETA MCs, b) n-OTES MCs, and c) HDMS MCs for increasing storage times after synthesis.

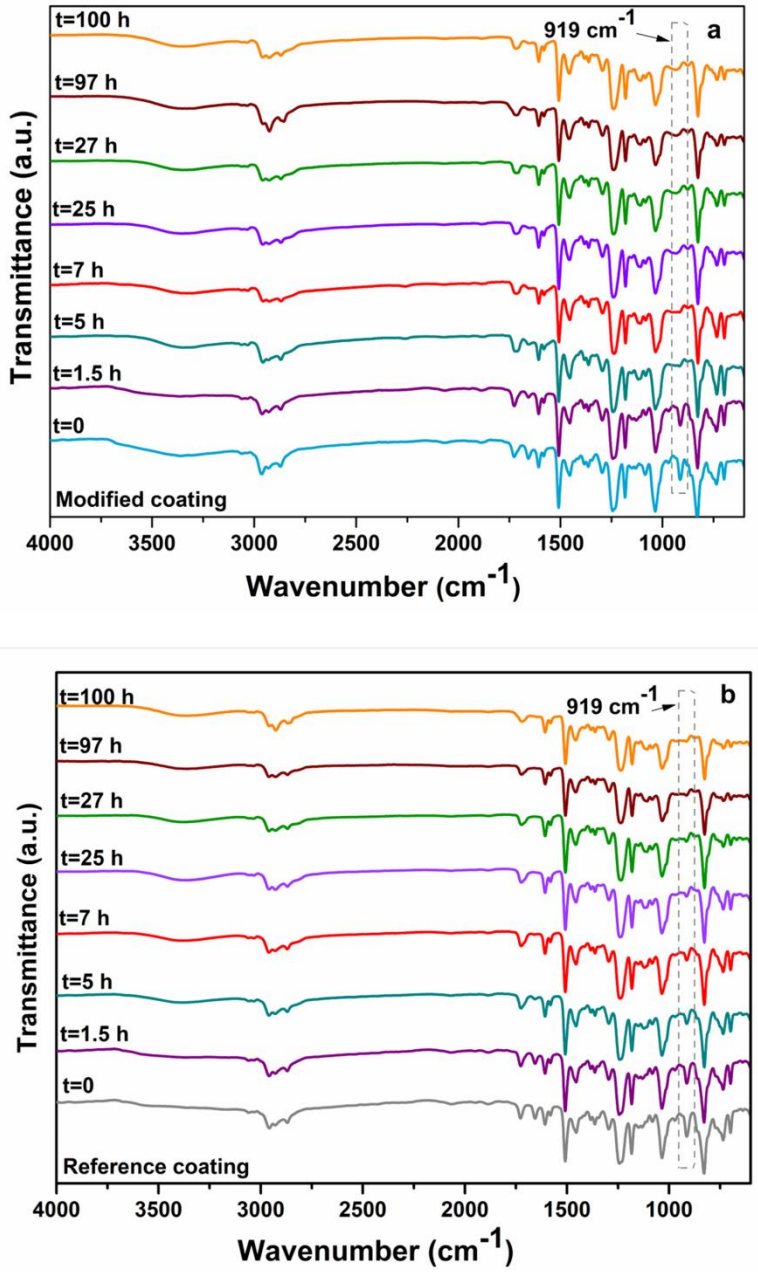

Figure A 1.4 Evolution of the FTIR spectra of a) modified, and b) reference coating when exposed to 40°C.

Table A 1.3 EEC parameters used to fit the EIS plots for the reference coating.

Reference							
	Element						
Time (days)	CPE-T_{Coat} ($F\ s^{n-1}\ cm^{-2}$)	n_1	R_P $\Omega\ cm^2$	CPE-T_{dl} ($F\ s^{n-1}\ cm^{-2}$)	n_2	R_{ct} $\Omega\ cm^2$	$\chi^2/10^{-3}$
1	1.9×10^{-10}	0.98	7.6×10^{8}	3×10^{-9}	0.56	2.5×10^{8}	21
6	1.8×10^{-10}	0.98	1×10^{9}	4×10^{-8}	0.65	2.3×10^{9}	35
10	1.7×10^{-10}	0.96	2.4×10^{8}	2×10^{-8}	0.45	4.2×10^{8}	22
15	2×10^{-10}	0.97	5.6×10^{8}	3×10^{-8}	0.36	6×10^{8}	21
30	2×10^{-10}	0.97	5.0×10^{8}	3×10^{-8}	0.33	1.2×10^{9}	2.9
45	2.1×10^{-10}	0.96	4.2×10^{8}	5×10^{-8}	0.61	5×10^{8}	3.1
70	1.8×10^{-10}	0.97	3.7×10^{7}	5×10^{-8}	0.84	2.5×10^{8}	1.2
100	2.1×10^{-10}	0.96	3×10^{7}	4×10^{-8}	0.47	3×10^{8}	3.9

Table A 1.4 EEC parameters used to fit the EIS plots for the modified coating containing 2 wt% of DETA-MCs.

Modified-MC-2 wt%							
	Element						
Time (days)	CPE-T_{Coat} ($F\ s^{n-1}\ cm^{-2}$)	n_1	R_P $\Omega\ cm^2$	CPE-T_{dl} ($F\ s^{n-1}\ cm^{-2}$)	n_2	R_{ct} $\Omega\ cm^2$	$\chi^2/10^{-3}$
3	2.6×10^{-11}	0.95	1.91×10^{8}	6.3×10^{-10}	0.34	1.1×10^{9}	1.4
5	2.6×10^{-11}	0.95	1.4×10^{8}	6.4×10^{-10}	0.32	1.4×10^{9}	1.6
11	2.9×10^{-11}	0.94	1.5×10^{8}	6.2×10^{-10}	0.39	1.5×10^{9}	3.4
15	3.1×10^{-11}	0.93	2.3×10^{8}	6.4×10^{-10}	0.42	1.3×10^{9}	1.2
60	3.08×10^{-11}	0.93	3.6×10^{8}	1.7×10^{-10}	0.53	1.9×10^{9}	2.1
80	3.12×10^{-11}	0.93	5.1×10^{8}	1.5×10^{-10}	0.56	2×10^{9}	4.5
120	2.15×10^{-11}	0.96	1.2×10^{8}	6.3×10^{-11}	0.58	9.2×10^{9}	0.1
180	2.13×10^{-11}	0.95	1.9×10^{8}	4.1×10^{-11}	0.62	1.7×10^{10}	1.2

Supplementary information of Chapter 4

Table A 1.5 Reagents used for synthesizing $Ce(DEHP)_3$ particles.

Material	Description	Supplier
2-(N-morpholino)-ethane sulphonic acid monohydrate	99.5 % purity	Carl Roth
Cerium (III) nitrate hexahydrate	99.5 % p.a purity	Sigma Aldrich
Sodium hydroxide	> 99.5 % purity	Carl Roth,
Petroleum benzene	Extra pure	Carl Roth
Bis (2-ethylhexyl)phosphoric acid	97 % purity	Merck

Synthesis of cerium organophosphate particles

In brief, 0.25 M bis(2-ethylhexyl) phosphate (DEHP) was added dropwise to 0.25 M of bis(2-ethylhexyl) phosphate salt (SDEHP), under continuous stirring. The prepared solution was left in the oven, at 50 ºC, during 48 h. Later, pH was adjusted to 12 with NaOH. Then, SDEHP was heated to 75 ºC and added under rigorous stirring to the mixture of $Ce(NO3)_3 \cdot 6H_2O$, 2-(N-morpholino)-ethane sulphonic acid monohydrate, and deionized water in a volume ratio of 6:2:3:9, respectively. After 1 h, the resulting aqueous suspension was separated and washed (several times by deionized water, and ethanol) by centrifugation at 13000 rpm. Particles were dried at 75 ºC for 7 days, before used.

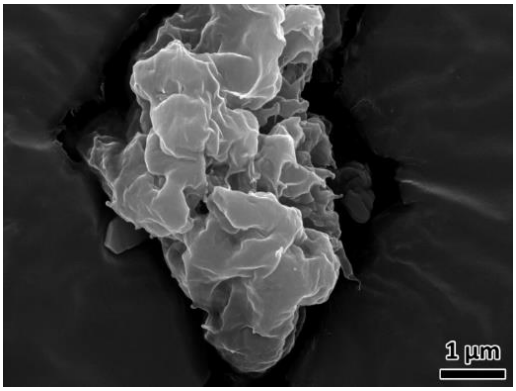

Figure A 1.5 SEM image of $Ce(DEHP)_3$.

Table A 1.6 EEC parameters used to fit the EIS plots for the modified coating containing 3 wt% of DETA-MCs.

Modified-MC-3 %							
Time	**Element**						
(days)	CPE-T_{Coat} ($F\ s^{n-1}\ cm^{-2}$)	n_1	R_P $\Omega\ cm^2$	CPE-T_{dl} ($F\ s^{n-1}\ cm^{-2}$)	n_2	R_{Ct} $\Omega\ cm^2$	$\chi^2/10^{-3}$
3	3.2×10^{-11}	0.94	3.5×10^{7}	1×10^{-10}	0.45	3.2×10^{9}	1.1
5	3.1×10^{-11}	0.94	7.8×10^{7}	2×10^{-10}	0.24	1.6×10^{9}	1.2
11	3.1×10^{-11}	0.94	8.6×10^{7}	8.6×10^{-10}	0.27	2.4×10^{9}	0.2
15	3.3×10^{-11}	0.93	7.9×10^{7}	9.4×10^{-10}	0.26	2.3×10^{9}	0.4
60	2.3×10^{-11}	0.98	8.4×10^{7}	1.8×10^{-10}	0.50	1.7×10^{9}	2.4
80	2.4×10^{-11}	0.96	1.2×10^{8}	1.4×10^{-10}	0.54	1.5×10^{9}	1.9
120	2.6×10^{-11}	0.95	6.5×10^{7}	7.2×10^{-11}	0.55	6.4×10^{9}	0.1
180	2.9×10^{-11}	0.94	3.1×10^{8}	5.4×10^{-11}	0.53	1.1×10^{10}	1.5

Table A 1.7 EEC parameters used to fit the EIS plots for the modified coating containing 3 wt% of DETA-MCs, and 1 wt% of $Ce(DEHP)_3$.

Modified-MC-3%-Ce-1%				
Time (days)	**Element**			
	CPE-T_{Coat} ($F\ s^{n-1}\ cm^{-2}$)	n_1	R_P ($\Omega\ cm^2$)	$\chi^2/10^{-3}$
1	7.8×10^{-11}	0.95	1×10^{11}	37
3	7.9×10^{-11}	0.95	9×10^{10}	28
7	9.1×10^{-11}	0.94	6.2×10^{10}	40
14	1×10^{-10}	0.93	4.7×10^{10}	52
16	1×10^{-10}	0.93	4.4×10^{10}	54
23	1×10^{-10}	0.93	4.2×10^{10}	43
30	9.8×10^{-11}	0.93	3.4×10^{10}	33
45	9.8×10^{-11}	0.92	7.2×10^{10}	35
50	1×10^{-10}	0.92	4.4×10^{10}	25
80	1×10^{-10}	0.92	5.02×10^{10}	23
100	9.2×10^{-11}	0.92	5.9×10^{10}	23

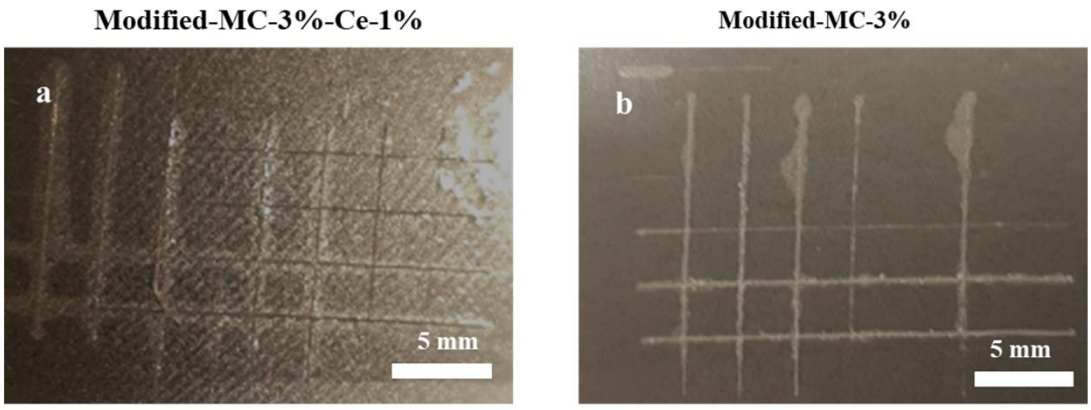

Figure A 1.6 cross-cut section of a) modified-MC-3%-Ce-1%, and b) modified-MC-3%; modified-MC-3%-Ce-1% shows excellent adhesion to substrate (5B - maximum adhesion) and modified-MC-3% shows very good adhesion (4B).

Supplementary information of Chapter 5

Table A 1.8 Primary materials used for synthesizing CeO_2 NPs.

Material	Description	Supplier
Ethanol	99.5 % purity	Carl Roth
Cerium (III) nitrate hexahydrate	99.5 % p.a purity	Sigma Aldrich
Ammonium hydroxide	30%	Carl Roth,

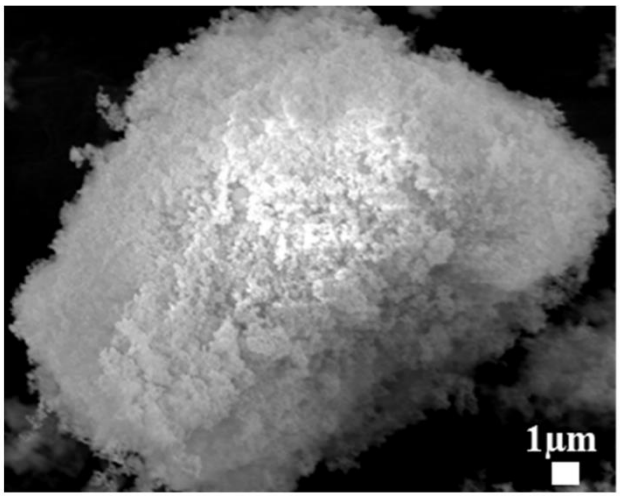

Figure A 1.7 SEM image of CeO_2 NPs.

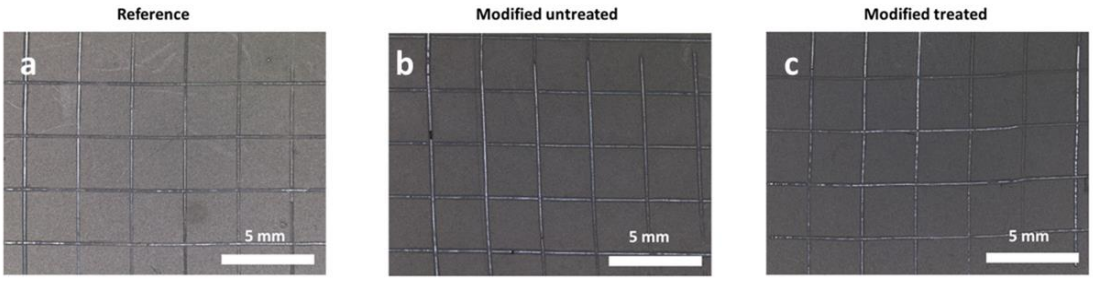

Figure A 1.8 cross-cut section of a) reference, b) modified untreated, and c) modified treated coating., all show excellent adhesion to substrate (5B - maximum adhesion).

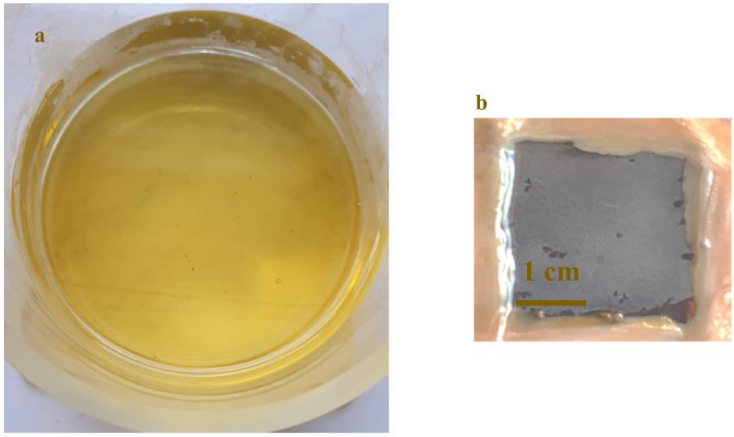

Figure A 1.9 a) Electrochemical cell containing 0.05 M NaCl solution and 1 wt% of THEEDA inhibitor after 150 h immersion of bare carbon steel, b) carbon steel after 150 h immersion inside 0.05 M NaCl solution containing 1 wt% of. THEEDA.

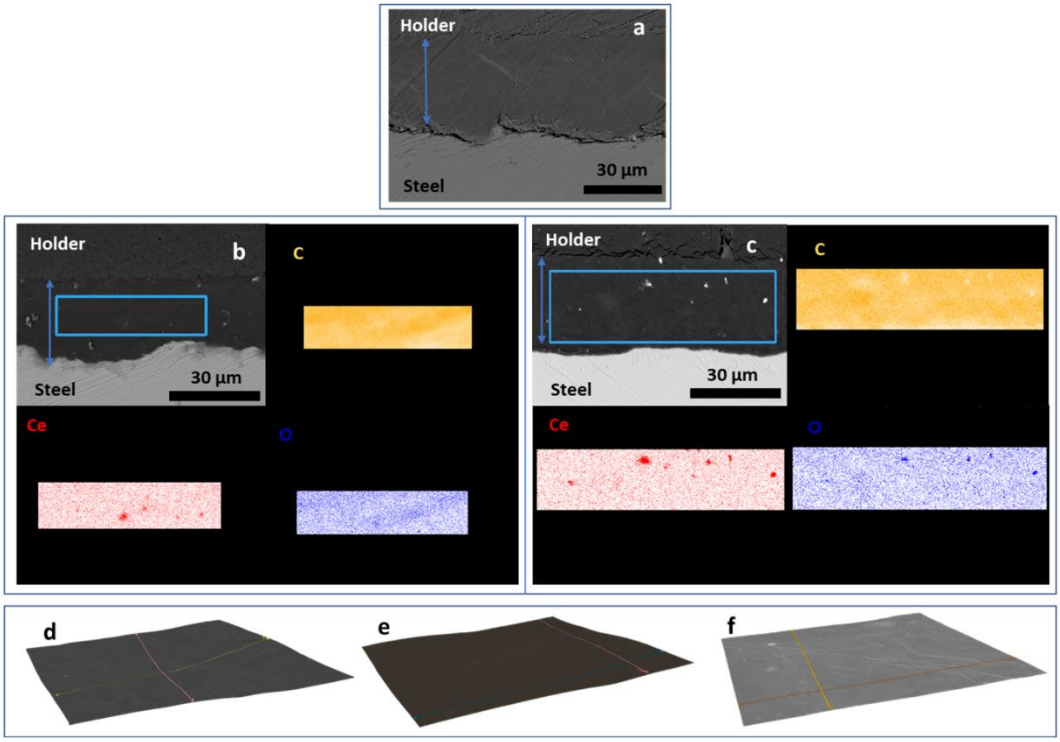

Figure A 1.10 SEM micrographs of a) reference, b) modified-untreated, c) modified-treated coating´s cross-section and corresponding EDS maps of C, Ce, and O for both modified coatings (b, and c); SEM image of surface topography of d) reference, e) modified-untreated, and f) modified treated coating.

Table A 1.9 EEC parameters used to fit the EIS plots of reference (polyolefin) coating.

Polyolefin-based Reference							
Time	**Element**						
(days)	CPE-T_{Coat} ($F\ s^{n-1}\ cm^{-2}$)	n_1	R_P $\Omega\ cm^2$	CPE-T_{dl} ($F\ s^{n-1}\ cm^{-2}$)	n_2	R_{ct} $\Omega\ cm^2$	$\chi^2/10^{-3}$
2	6.1×10^{-11}	0.98	5×10^{12}				4.3
3	6.3×10^{-11}	0.98	8.1×10^{11}				35
4	6.1×10^{-11}	0.98	6.1×10^{11}				4.3
5	6.7×10^{-11}	0.98	1.1×10^{12}				8.6
9	6.4×10^{-11}	0.98	3.1×10^{12}				4.8
15	6.6×10^{-11}	0.98	1.1×10^{12}				8.6
21	6.3×10^{-11}	0.98	3.7×10^{10}	0.14	0.74	3×10^{11}	7.2
28	6.3×10^{-11}	0.98	6×10^{9}	0.14	0.81	5.6×10^{11}	7.4
35	6.5×10^{-11}	0.98	2.8×10^{9}	0.6	0.92	4.2×10^{10}	16
38	6.4×10^{-11}	0.98	3.1×10^{9}	0.67	0.91	7.5×10^{10}	16
50	6.3×10^{-11}	0.98	2×10^{10}	0.16	0.62	3.5×10^{10}	3.0
72	6.0×10^{-11}	0.98	1×10^{9}	0.36	0.92	1.2×10^{10}	12
87	6.1×10^{-11}	0.98	5.6×10^{8}	0.46	0.90	1.8×10^{10}	5.9
107	5.8×10^{-11}	0.98	4.9×10^{8}	0.52	0.90	1.2×10^{10}	5.6

Table A 1.10 EEC parameters used to fit the EIS plots of modified polyolefin-based coating containing 5 wt% of CeO_2.

Modified-untreated-5 wt%-CeO_2				
Time	**Element**			
(days)	CPE-T_{Coat} ($F\ s^{n-1}\ cm^{-2}$)	n_1	R_P $\Omega\ cm^2$	$\chi^2/10^{-3}$
1	3.9×10^{-11}	0.98	1.1×10^{13}	1.7
2	3.9×10^{-11}	0.98	1.8×10^{13}	1.6
7	4.2×10^{-11}	0.98	2.1×10^{13}	1.9
9	3.3×10^{-11}	0.99	2.9×10^{13}	5.0
11	4.3×10^{-11}	0.97	1.6×10^{13}	2.0
22	4.6×10^{-11}	0.97	1.6×10^{13}	1.4
37	4.7×10^{-11}	0.97	1.5×10^{13}	3.3
63	4.8×10^{-11}	0.97	6.1×10^{12}	4.4
94	4.7×10^{-11}	0.97	9×10^{12}	4.9
110	4.9×10^{-11}	0.96	5.4×10^{12}	6.4
125	4.9×10^{-11}	0.96	4.3×10^{12}	7

Table A 1.11 EEC parameters used to fit the EIS plots of modified polyolefin-based coating containing 5 wt% of CeO_2 treated with THEEDA inhibitor.

Modified-treated-5 wt%-CeO_2				
Time	**Element**			
(days)	CPE-T_{Coat} ($F\ s^{n-1}\ cm^{-2}$)	n_1	$R_P/10^8$ $\Omega\ cm^2$	$\chi^2/10^{-3}$
1	2.7×10^{-11}	0.99	1.6×10^{13}	3.2
2	2.8×10^{-11}	0.99	3.3×10^{13}	1.0
3	2.8×10^{-11}	0.99	8.2×10^{13}	7.0
4	2.8×10^{-11}	0.99	1.1×10^{14}	1.5
11	3.0×10^{-11}	0.98	1.9×10^{13}	2.0
21	3.4×10^{-11}	0.97	1.4×10^{13}	3.0
28	3.2×10^{-11}	0.98	2.1×10^{12}	26
33	3.4×10^{-11}	0.97	1.6×10^{13}	3.2
43	3.2×10^{-11}	0.97	2.1×10^{13}	3.1
50	3.5×10^{-11}	0.97	1.8×10^{13}	4.0
65	3.7×10^{-11}	0.96	3.5×10^{12}	4.2
76	3.6×10^{-11}	0.98	1.1×10^{13}	6.5
89	3.9×10^{-11}	0.98	1.1×10^{13}	11
125	3.6×10^{-11}	0.96	5.2×10^{12}	7

Table A 1.12 Summary of most relevant work regarding the application of pH response carriers for smarter, self-healing coatings on steel

No.	Carrier	Corrosion Inhibitor	Coating	Coating Thickness (µm)	$\|Z\|_{LF}$ (Ω cm^2)		$\frac{\|Z\|_{LF\ (modifi}}{\|Z\|_{LF\ (refere}$
S1	HMZS	L-CAR	epoxy	30	1×10^9 (1 day)	1×10^8 (30 day)	100 ↑
S3	ZIF-8/GO	MBI	epoxy	40 ± 5	3.3×10^9 (1 day)	$\approx 10^9$ (20 days)	16700 ↑
S4	ZIF-7	BI	epoxy	50 ± 5	3.7×10^4 (1 day)	1.6×10^4 (3 day)	1.7 ↑
S8	$CaCO_3$	BTA/TA	epoxy	200	3.0×10^4 (1 day)	4.3×10^4 (20 day)	2.4 ↑
S11	Mesopores cerium oxide/Eudragit[a]	MBI	epoxy	70 ± 5	6×10^8 (6 h)	3×10^9 (1320 h)	6 ↑
S13	SiO_2	BTA	epoxy	110	7×10^9 (6 days)	9×10^6 (30 days)	1.1 ↑
S15	Multiwall CNT/Chitosan	DPA/Chitosan Zn cations	epoxy	75	3.69×10^{10} (48 h)	1.16×10^{10} (9 weeks)	1126 ↑
S17	HHNT	IM/DDA[b]	epoxy	200	5×10^9 (1 day)	7×10^6 (7 days)	2.3 ↑
S18	HHNT	BTA MBT	epoxy	200	2.8×10^{10} (7 days)	4.7×10^6 (90 days)	0.05 ↓
S19	Graphene sheet	BTA	epoxy	40 ± 3	1×10^9 (2 days)	3×10^8 (55 days)	28.5 ↑

S21	Graphene sheet/PANI	CeO_2	epoxy	75 ± 5	7×10^9 (1 day)	4×10^8 (70 day)	80 ↑
S22	CeO_2	cerium nitrate	Sol-gel	5.5	10^8 (24 h)	na	1000* ↑
S24	CeO_2/Ce_2O_3/Li	na	PMMA	17-20	2.9×10^{11} (1 day)	1×10^{10} (658 days)	na
S10	HAP	Ce-ions	polyolefin	39	1×10^{10} (1 day)	1×10^9 (140 day)	11 ↑
S9	$CaCO_3$	PEI	epoxy	26 ± 1	1.2×10^{10} (20 day)	5×10^{10} (280 day)	50 ↑
S9b	$CaCO_3$	PEI/TEA[b]	epoxy	23-30	8×10^9 (7 day)	1×10^7 (150 day)	1.42 ↑
S25	na	$Ce(DEHP)_3$	epoxy	31 ± 0.7	5×10^{10} (1 day)	1×10^{10} (402 days)	33 ↑
Ch4	na	IPDI-MCs + $Ce(DEHP)_3$	epoxy	53.5 ± 1.3	1×10^{11} (1 day)	6.2×10^{10} (285 days)	10 ↑
Ch5	CeO_2	THEEDA	polyolefin	35 ± 5	1.1×10^{12} (1 day)	6.1×10^{11} (130 days)	60 ↑

*Modified coating was reported to be five times thicker with compared to the reference coating. Blue and gray shadows show the same epoxy-based and polyolefin-based reference coatings, author of this Thesis used, to develop smart coatings reported in this PhD work. Therefore, these works considered to be the most comparable works with this Thesis.

Appendix 2 Tools and Equipment

In this subsection, tools and equipment employed to characterize synthesized particles and developed coatings during this PhD work are introduced. Specific parameters and conditions for each test are mentioned when necessary.

Scanning Electron Microscope (SEM)

Along this PhD work, SEM was employed to characterize morphology and size distribution of MCs, and NPs. Coating morphology, surface roughness of coating, and distribution of specific element inside the coating were also evaluated by SEM. Moreover, the corrosion products formed onto the surface of artificial defects were investigated by EDS.

Along Chapter 3, the morphology and size distribution of the MCs were studied by SEM, using a JEOL JSM7001F (JEOL, Tokyo, Japan) with a FEG-SEM (Field Emission Gun) microscope operating at 15 kV. The samples were coated previously with a conductive Au/Pd thin film, through sputtering, using a Quorum Technologies sputtering coater model Q150T ES. The same equipment was used to examine the coating surface and its cross section. Samples were previously coated with an Au/Pd thin film, using the same sputter coater machine.

Along Chapter 4, the same SEM (JEOL JSM7001F) was employed to analysis size and morphology of MCs, $Ce(DEHP)_3$, and coatings´ morphology.

Along Chapter 5, the same SEM (JEOL JSM7001F9, was utilized to analysis the morphology of CeO2 NPs.

A Phenom ProX G6 Desktop SEM was used to observe the cross-sections of reference and both modified coatings. The elemental analysis over the selected area of the coating cross-section was carried out using the Energy Dispersive Spectrometer equipped with integrated Element IDentification (EID) software. Moreover, the surface roughness of the reference and both modified coatings was evaluated using the same Phenom ProX G6 Desktop SEM equipped with the Phenom ProSuite software.

Optical Microscope (OM)

OM was frequently used during the synthesis of MCs, and during the coating preparation steps to ensure the intact shell of MCs. Moreover, morphology of developed coatings, and size, shape, and evolution of artificially made defects in the coatings, were frequently observed by OM. Although, OM was a handy tool, and was used frequently during this work, OM´s photos were rarely reported.

In Chapter 4, Leica DM2700 Material Microscope, was used to ensure intact shell of MCs after immersion inside the solution of $Ce(DEHP)_3$ inside the hardener part of coating during the 200 h.

Along Chapter 5, A Leica DMS300 Digital Microscope, was used to observe and to measure dimensions of artificially made scratches during the immersion in saline solution. These samples were further used to perform Micro-FTIR, and LEIS over the scratches.

Transmission Electron Microscope (TEM)

In Chapter 5, a Hitachi H8100 200kV TEM equipped with a thermionic emission gun, was used to characterize morphology and size of NPs, before and after treating with THEEDA inhibitor.

Fourier transformed infrared spectroscopy (FTIR)

Along this PhD work, FTIR was used frequently to characterize synthesized particles, and primary materials. As the analysis is quite fast, FTIR was the first characterization technique used to evaluate MCs, and NPs.

Along Chapter 3, FTIR was used to assess the chemical structure of the MCs, MCs' shell, and primary material used to synthesize MCs. To do so, Spectrum Two from PerkinElmer, equipped with a Pike Technologies MIRacle® ATR accessory was used. The spectra were taken in the range of 4000–500 cm^{-1}, with 8 cm^{-1} resolution and data collection of 16 scans.

The same equipment was employed to calculate the relative isocyanate encapsulation efficiency, to evaluate the shelf-life of MCs, and to assess the effect of addition of MCs into the epoxy, in curing time and curing behaviour of modified coatings.
To evaluate the stability of MCs inside various solvent and hardener part of coating formulation, a Spectrum Two from PerkinElmer (Waltham, MA) equipped with a UATR Two accessory was used. The spectra were obtained at 4 cm^{-1} resolution and 8 scans of data accumulation.

In Chapter 4, a Spectrum Two from PerkinElmer (Waltham, MA) equipped with a UATR Two accessory was used to analyze the chemical structure of MCs. The spectra were obtained at 4 cm^{-1} resolution and 8 scans of data accumulation. Chemical stability of MCs inside hardener part of coating formulation was evaluated by the same equipment.

In Chapter 5, a Spectrum Two from PerkinElmer (Waltham, MA) equipped with a UATR Two accessory, was used, to evaluate the chemical structure of THEEDA and of the NPs before and after treatment with THEEDA. Spectra were obtained in the range 4000 – 400 cm^{-1} with the 8 scans collection and a resolution of 8 cm^{-1}.

Micro-FTIR

In Chapter 5, Micro-FTIR was used to study the surface of the defects (scratches), artificially made on the surface of the studied coatings. Scratches with an approximate length of 6 mm were created with a sharp knife, exposing the bare metal, into 0.05 M NaCl solution. A Perkin Elmer Spotlight 200i FT-IR microscope with micro-ATR accessory was used, with a data collection of 32 accumulations in the range 4000 – 400 cm^{-1}.

Thermogravimetric analysis (TGA)

In this PhD work, TGA was utilized to gain insight on thermal stability of MCs and to calculate the amount of encapsulated healing agents inside the MCs, or to evaluate the quantity of inhibitor loaded into the NPs.

In Chapter 3, and 4, a TGA HITACHI STA 7200, Thermal Analysis System equipment, under a controlled nitrogen atmosphere with a flow of 200 ml/min, and a linear heating rate of 10 °C/min, from RT to 600 °C was used.

In Chapter 5, the same equipment was used to determine the quantity of THEEDA in the CeO_2 NPs. The studies were performed under a controlled nitrogen atmosphere with a flow of 200 ml/min, and a linear heating rate of 10 °C/min, from RT to 1000 °C.

Raman Spectroscopy

In Chapter 5, Raman Spectroscopy was conducted to evaluate the chemical structure of CeO_2 NPs, using LabRAM HR 800, equipped with an Olympus BXFM confocal microscope. Raman spectra were collected with the laser wavelength of 532 nm at the range of 200-1000 cm^{-1}, with maximum power of 20 mW, 10 scans per sample, and during the 30 seconds.

X-ray diffraction (XRD)

In Chapter 5, the powder crystallinity of CeO_2 NPs was analyzed by XRD. A Panalytical X'pert Pro diffractometer (θ/2θ) equipped with X'Celerator detector and with automatic data acquisition (X'Pert Data Collector (v2.0b) software) was used. The patterns were collected using unfiltered Cu Kα radiation, 40 kV−30 mA, and the Bragg−Brentano geometry over the 2θ range 10−90° with a 2θ-step size of 0.017° and a scan step time of 20 seconds.

Dip Coater Machine

A laboratory dip coater (RDC15, Bungard Elektronik) machine coupled to a SIEMENS SPS control unit, was used to apply coating on carbon steel substrate. For epoxy-based coatings (Chapter3, and 4) dipping and withdrawal speed were 19 mm/s, and 6 mm/s respectively. The carbon steel substrate was left for 4 seconds in the coating formulation, and then withdrawn. The dipping process was repeated 3 times for each sample. The coated samples were dried at 30-40 ºC for 5 days to ensure a fully cured coating structure.

For polyolefin-base coatings (Chapter 5), the same equipment was used. While the dip, and withdraw speeds maintained the same, the dipping process was repeated 2 times for each sample. The coated samples were dried and cured at 175-180 ºC for 5 minutes.

Electrochemical Studies

Electrochemical impedance spectroscopy (EIS)

The barrier properties of coated samples were evaluated by EIS. The measurements were carried out using the Gamry Instruments Reference 600+ apparatus during immersion in 0.05 M NaCl. Measurements were performed using a conventional three-electrode cell configuration: Saturated Calomel Electrode (SCE) as reference electrode, a platinum coil as counter electrode, and the coated steel as working electrode. Samples with a total exposed area of 3.63 cm^2 were immersed in 0.05 M NaCl, and the EIS measurements were carried out inside a Faraday cage, at open circuit potential under a 10 mV rms sinusoidal perturbation and in the frequency range from 50 kHz to 5 mHz. For all the polyolefin-based coatings an amplitude of 100 mv rms perturbation was used. Numerical fitting of the obtained EIS data was achieved with the ZView® software from Scribner Associates.

Localized Electrochemical Impedance Spectroscopy (LEIS)

LEIS measurements were performed using an Uniscan M370 scanning electrochemical workstation, connected to a Solartron 1286 Electrochemical Interface and a Solartron 1250 Frequency Response Analyzer. Measurements were conducted at the frequency of 10 Hz using a five-electrode configuration: SCE as reference electrode, platinum meshes (or carbon rods) as counter electrode, coated samples as working electrode, and platinum bi-electrode as LEIS probe. The measurements were carried out over an area of 12 × 12 mm^2 containing defects. While the scanned area for each sample was approximately 3 × 4 mm^2.

For epoxy-based coatings reported in Chapter 3, and 4, a pin-hole defect with approximate diameter of 320 µm was created with a sharp needle.

For polyolefin-based coatings reported in Chapter 5, defects (scratches) with an approximate length of 8 mm created with a sharp knife, exposing the bare carbon steel.

LEIS was conducted in admittance mapping mode at 10 Hz, probing the area under the test by the bi-electrode LEIS probe during immersion in 0.005 M NaCl. The scanned area for each set of coated samples were approximately 3 × 4 mm^2.

Scanning Vibrating Electrode Technique (SVET)

The evolution of localized corrosion activity for coated samples with point defect was monitored employing SVET. The SVET apparatus employed during this PhD work was a commercial system from Applicable Electronics™, based on the ASET program (Sciencewares™). SVET measurements were carried out using an insulated Pt-Ir microelectrode (supplied by MicroProbes) with platinum black deposited on a spherical tip to reach 16 µm diameter. The probe was placed approximately 120 µm above the surface, vibrating in the planes perpendicular (Z) and parallel (X) to the working electrode surface. The vibration frequencies of the probe were 124 Hz (Z) and 323 Hz (X). Only the vertical component was used for further analysis.

For epoxy-based coatings reported in Chapter 3, and 4, the evolution of the corrosion activity for coated samples was performed over an approximate area of 1.8 mm^2 containing a point defect with approximately 200 µm diameter during non-stop immersion in 0.05M NaCl solution.

For polyolefin-based coatings reported in Chapter 5, SVET prob was positioned approximately 100 µm above the surface. The evolution of the corrosion activity for these samples was performed over an approximate area of 3.14 mm^2 containing a point defect with approximately 80 µm diameter (made using a sharp needle to expose the steel substrate) during immersion in 0.05M NaCl solution.

Scanning Ion-Selective Electrode Technique (SIET)

The SIET apparatus was the same equipment used to perform SVET measurements. The localized pH measurements were carried out using pH-selective glass-capillary microelectrodes with a tip orifice diameter of 1.8 ± 0.2 µm. Silanized glass micropipettes were back-filled with the inner filling solution and tip-filled with the pH-selective ionophore-based membrane (pH working range 1.8-11.6). The pH-selective microelectrodes were calibrated using commercial pH buffers. For epoxy-based coatings reported in Chapter 3, and 4, the local pH was monitored 70 µm above the surface. The

same samples used to perform SVET, were scanned to detect localized pH over the 200 µm diameter point defect.

Scanning Fiber-optic Dissolved Oxygen (DO)

Scanning Fiber-optic DO was performed using the Workstage for localized measurements, produced by Sciencewares™ and Applicable Electronics™. Scanning was always performed 100 µm above the surface. DO scans were made according to a 31 × 31 grid (i.e. 961 points per scan). The movement of the commercial fiber-optic microsensor (PyroScience™) was controlled using ASET-LV4 software (Sciencewares™). Oxygen Logger software (PyroScience™) was used for DO concentration acquisition and recording. The diameter of the tip of the fiber-optic microsensor was 50 µm. The total area exposed to electrolyte was approximately 3.42 mm^2 for tested samples. This test was performed exclusively for three polyolefin-based coatings reported in Chapter 5.

Sample preparation procedure was identical for SVET, SIET, and Dissolved Oxygen concentration detection test, as following: the defect was produced on the coated samples using a needle shaped tool approached vertically at 90 degrees to the surface with the reproducible applied effort. Visual appearance of the defect was examined using microscope. Later, the sample with approximate dimension of ca. 10 × 10 mm^2 was fixed on the top of the mounting holder. Then the area around the defect was isolated using mixture of beeswax and colophony. Each type of the coated samples was examined by each technique at least in duplicate.

Adhesion test

Adhesion tests based on ASTM D3359-09 were performed employing Elcometer 107 Cross Hatch Cutter. The 6 teeth, 1 mm spacing tool was used to produce the pattern of 6 cross sections (≈ 20 mm) at right angles to the coated material until reaching the substrate. Then, Elcometer T1079358 adhesive tape was applied over the cut pattern, and it was removed. With the aid of a magnifying glass the detachment of the coating was evaluated. The surface of the coating was visually compared to the standard scale shown in ASTM D3359-09 and adhesion is graded according to the percentage of area removed.

Coating thickness measurement

A digital Elcometer 355 Coating Thickness Gauge was used to determine the thickness of the prepared coated coupons, considering an average of 10 measurements for each coating.

Appendix 3 Synthesis of PEI and CeO_2-SiO_2

As mentioned in Chapter 6, two more particles were synthesized to play a role of pH sensitive corrosion inhibitor for corrosion protection of carbon steel as following:

i) **Poly(ethyleneimine) (PEI)** was encapsulated in polymeric shell via interfacial polymerization in water-in-oil emulsion. Further MC´s shell was functionalized by addition of $CaCO_3$, to impart pH sensitivity into the MCs´shell. This is vital important for smart release of inhibitor (PEI). Encapsulation of PEI was performed in two phases, being encapsulation of PEI, and functionalization of MCs´shell by $CaCO_3$. However, at the end these two steps were merged to an easy one pot synthesis of PEI-MCs-$CaCO_3$, which is reported here.

ii) Moreover, **CeO_2-SiO_2** composite particles with various proportion of CeO_2/SiO_2, were synthesized as pH sensitive carriers. While both SiO_2 and CeO_2 are known as pH sensitive carriers, the objective of synthesis of these composite particles was to study and to select the best pH response carrier among CeO_2, SiO_2, and CeO_2-SiO_2. Although very promising results were obtained by addition of PEI-MCs to the epoxy-based coating, and addition of CeO_2-SiO_2 composite particle to polyolefin-based coating, the scientific articles related to these carriers are still unpublished, due to lack of the time. Therefore, here in two short subsections, synthesis of these carriers is reported in brief.

Encapsulation of Poly(ethyleneimine) (PEI)

PEI-MCs were prepared by interfacial polymerization in water-in-oil (W/O) emulsions. Firstly, an oil phase was prepared by addition of 4.9 wt % (total emulsion (W phase + O phase) of Span 80®, 3.6 wt% of IPDI, and 0.8 wt% of $CaCO_3$ in toluene. This solution was vigorously mixed at 5000 rpm and RT with an Ultra-Turrax (IKA T25 digital ULTRA TURRAX, Germany) to obtain homogenous phase. The water phase (9.4 wt. % of total emulsion) prepared by addition of 6.5 wt % of PEI to 3.25 wt % of (total emulsion) deionized water, was added to the oil phase. This solution also vigorously mixed at 8000 rpm for 5 min to obtain stable emulsion. The stable W/O emulsion was then stirred by mechanical stirring at 400 rpm. The temperature was increased from RT to 50°C and the reaction was stopped after 60 min. The solution was left to reach the RT and the MCs were separated from the solution and washed several times with acetone, using a centrifuge (OHAUS FC 5816R), at 4000 rpm. The final product was dried at atmospheric

pressure and RT for 24 h. The concentration of $CaCO_3$ as pH sensitive particles, was adjusted to obtain almost full coverage of MCs´ outer shell by $CaCO_3$ particles.

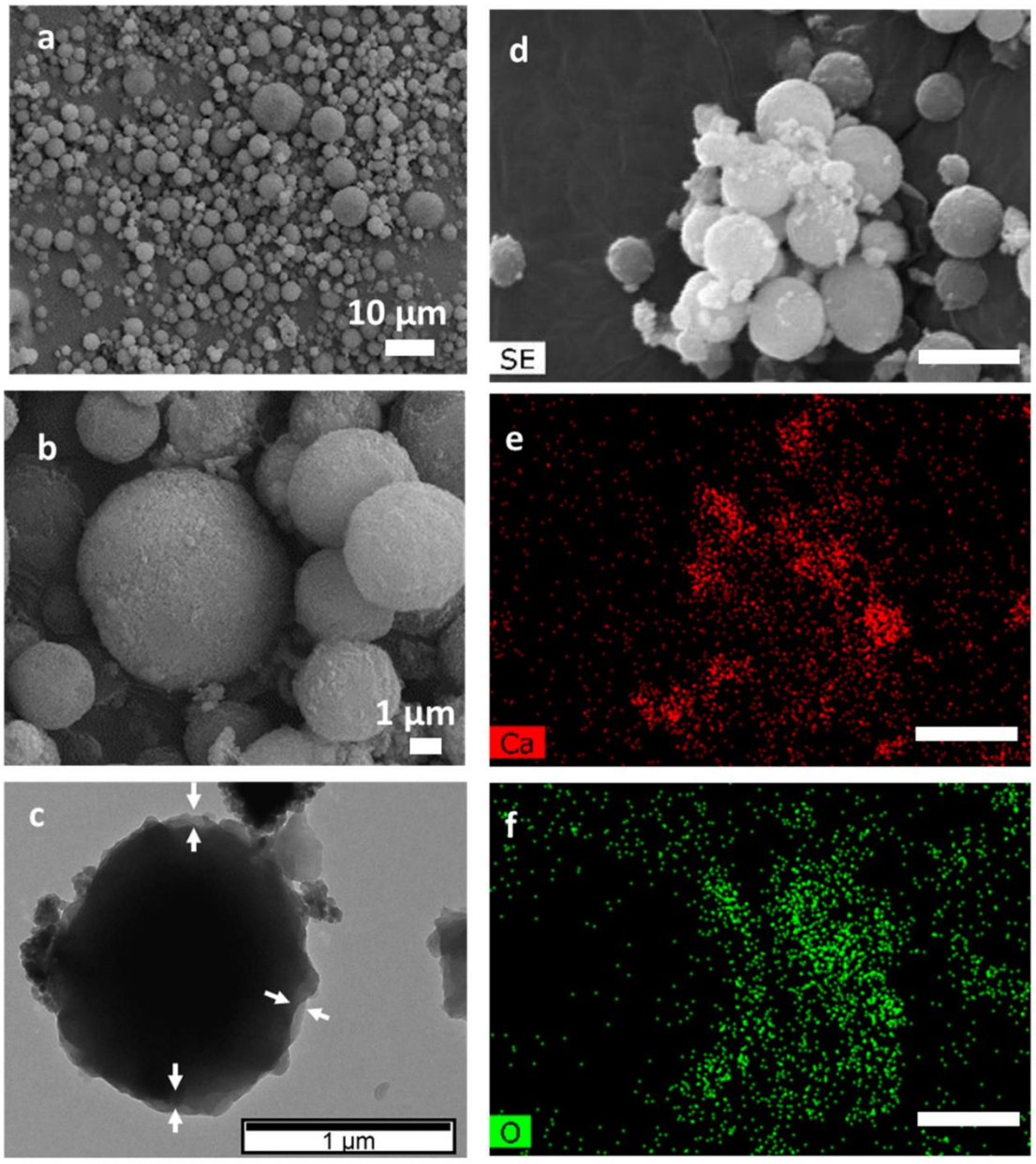

Figure A 1.11 a, b) SEM micrograph of MCs, c) TEM micrograph of MCs shows full coverage of $CaCO_3$ around MCs; EDS map of e) Ca, and f) O; d) the respective SEM image regarding these maps (scalebar = 10 µm)

Synthesis of CeO_2-SiO_2 nanoparticles

To synthesize the CeO_2-SiO_2 NPs three solutions were prepared:

i) A solution of 0.1 M of Tetraethyl orthosilicate (TEOS) (99%, Sigma-Aldrich) in ethanol (99.8%, Carl Roth) was prepared as a seed. The temperature was increased up to 70°C, and NH_4OH (30%, Carl Roth) was added dropwise to the seed solution until the seed solution attained pH ≈ 10.

ii) A solution of 0.7 M of TEOS in ethanol was prepared as Si-precursor. The solution was stirred for half an hour at RT to ensure complete dissolution of TEOS in Ethanol.

iii) Three different Ce-precursor concentrations, i.e. a solution of 0.49 M, 0.21 M, and 0.07 M of $Ce(NO_3)_3 \cdot 6H_2O$ (99%, Sigma-Aldrich) in pure Ethanol was prepared. Mixtures were stirred for half an hour to ensure complete dissolution. These three different concentrations were used further to synthesize composite NPs of CeO_2-SiO_2 with CeO_2/SiO_2 proportion of 70/30, 50/50, and 10/90 respectively.

To synthesize these composite NPs, firstly Ce-precursor was added dropwise into the seed solution at 70°C. After 15 minutes Si-precursor was added to the reactor. The mixture was continuously stirred (300 rpm) and after 60 min the reaction was stopped. The precipitate was then collected by centrifugation at 5000 rpm and washed several times with ethanol. The final product was dried at 50°C overnight.

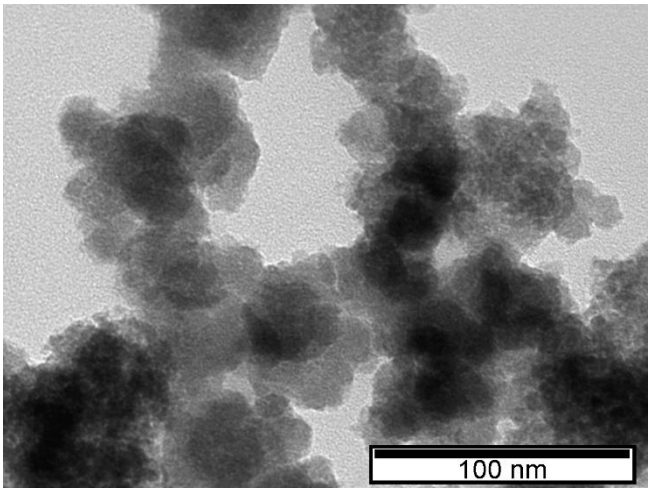

Figure A 1.12 TEM image of CeO_2-SiO_2 NPs (70/30).